United States Department of Commerce
National Institute of Standards and Technology

NISTIR 89-3915R

SUGGESTED METHODS AND STANDARDS FOR TESTING AND VERIFICATION OF ELECTROMAGNETIC BURIED OBJECT DETECTORS

William L. Gans
Richard G. Geyer
Wilfred K. Klemperer

National Institute of Standards and Technology
U.S. Department of Commerce
Boulder, Colorado 80303-3328

March 1990

NISTIR 89-3915R

SUGGESTED METHODS AND STANDARDS FOR TESTING AND VERIFICATION OF ELECTROMAGNETIC BURIED OBJECT DETECTORS

William L. Gans
Richard G. Geyer
Wilfred K. Klemperer

Electromagnetic Fields Division
Center for Electronics and Electrical Engineering
National Institute of Standards and Technology
U.S. Department of Commerce
Boulder, Colorado 80303-3328

March 1990

Sponsored by
U.S. Army Belvoir Research, Development, and Engineering Center
Fort Belvoir, Virginia 22060-5606

U.S. DEPARTMENT OF COMMERCE, Robert A. Mosbacher, Secretary
NATIONAL INSTITUTE OF STANDARDS AND TECHNOLOGY, John W. Lyons, Director

TABLE OF CONTENTS

LIST OF TABLES

LIST OF FIGURES

SUGGESTED METHODS AND STANDARDS FOR TESTING AND VERIFICATION OF ELECTROMAGNETIC BURIED OBJECT DETECTORS

William L. Gans, Richard G. Geyer, and Wilfred K. Klemperer
National Institute of Standards and Technology
Boulder, Colorado 80303

This is an interim report to sponsor on work performed by NIST personnel from January 1, 1985, to September 30, 1988. A brief overview of the theory of the electromagnetic properties of soils is presented, followed by an equally brief review of existing technologies for the detection of buried objects using electromagnetics. Suggested methods are then presented for realizing adequate target and soil standards and for testing procedures for buried object detectors that use these standards. Suggested instrumentation methodologies for verifying (calibrating) the target and soil standards are also presented along with an appendix containing reprints of selected relevant papers and an extensive bibliography.

Key words: buried object; conductivity; electromagnetic detection; mine; mine detector; permeability; permittivity; remote sensing.

1. INTRODUCTION

The purpose of this interim report is to provide documentation to U.S. Army Belvoir Research, Development and Engineering Center personnel describing the work performed by the National Institute of Standards and Technology under contract. This introduction summarizes the original work statement and contains a very brief description of the contents of the remaining chapters of this report.

Original Work Statement

The original work statement defining the tasks to be performed over approximately a four year period by NIST for the U.S. Army Belvoir Research, Development and Engineering Center is outlined below.

Phase I.

1. Create a joint National Academy of Sciences-NIST-U.S. Army review panel to review, annually, the work performed by NIST.

2. Review information provided by the Army pertaining to past and present mine detection systems, measurement methods, and standards, as necessary.

3. Provide the Army a suggested selection of standard test targets and soil backgrounds.

4. Provide the Army a preliminary set of definitions, parameters to be controlled, and standard test conditions.

5. Investigate the possibility of developing a performance effectiveness measure for mine detectors.

Phase II.

1. Recommend a final set of standard test targets.

2. Recommend a final set of standard test soils.

3. Recommend a set of measurement methods to ensure replication of test conditions.

4. Formulate (if possible) a definitive set of effectiveness measures.

Phase III.

1. Specify a measurement system to ensure standard test conditions.

2. Provide an error estimate for the measurement process.

Phase IV.

1. Provide initial guidance, training, and technology transfer.

What follows is a brief description of the contents of the remaining chapters of this report.

Chapter II contains a comprehensive review of the existing theory of the interaction of electromagnetic fields and materials relevant to soils and mine detection.

Chapter III contains selected information relative to NIST's review of present technology. Of particular interest is a brief review of Dr. David Hill's significant theoretical contributions to this project.

Chapter IV contains the results of NIST's studies and work on target standards and *Chapter V* contains the results of NIST's studies and work on soil standards.

Chapter VI contains the results of NIST's studies and work on test instrumentation and procedures required for calibrating standard soils and targets.

Chapter VII contains the results of NIST's studies and work on objective measures of detector performance, both detector-based and target-based.

Chapter VIII, finally, contains NIST's recommendations for future work necessary to complete this project.

Along with the references cited at the end of each chapter, there are a complete bibliography after Chapter VIII and a number of technical appendices. Also, the draft reports of work performed by Dr. Richard Geyer, under separate covers, are part of NIST's overall interim report to the Army.

II. ELECTROMAGNETIC CHARACTERISTICS OF RELEVANT MATERIALS

A. Physical Concepts Governing Electromagnetic Behavior

Any material is electromagnetically characterized by its permittivity, ϵ, in farads/meter (F/m), magnetic permeability, μ, in henries/meter (H/m), and electrical conductivity, σ, in siemenses/meter (S/m). Maxwell's equations, together with the constitutive equations relating field quantities in terms of material properties, completely govern electromagnetic wave propagation and behavior in that medium. Therefore, the use of electromagnetic energy to detect buried objects must involve detecting differences between the object and the surrounding medium in one or more of the above quantities.

The constitutive equations for a linear, homogeneous, and isotropic medium may be expressed in the frequency domain as

$$\begin{aligned} \vec{B} &= \mu \vec{H} , \\ \vec{J} &= \sigma \vec{E} , \\ \text{and} \quad \vec{D} &= \epsilon \vec{E} , \end{aligned} \tag{2.1}$$

where $\vec{B}$ is the magnetic flux density (webers/meter^2 or Wb/m^2) related to the magnetic field intensity, $\vec{H}$ (amperes/meter or A/m), by the magnetic permeability; $\vec{J}$ is the current density (amperes/meter^2 or A/m^2) related to the electric field intensity, (volts/meter or V/m), by the conductivity; and $\vec{D}$ is the electric flux density, (coulombs/meter^2 or C/m^2) related to the electric field by the permittivity. Any deviation from linearity is usually included by making ϵ, μ, or σ field dependent. For anisotropic media, ϵ, μ, and/or σ become 3 x 3 tensor matrices as opposed to constants or scalar functions of frequency.

The solution of Maxwell's equations yields all of the quantities that describe the propagation of electromagnetic waves in terms of the propagation constant, k, where

$$k^2 = \omega\mu(\omega\epsilon - j\sigma) . \tag{2.2}$$

In general, the constituent electrical properties may be written as complex quantities; that is,

$$\begin{aligned} \epsilon &= \epsilon' - j\epsilon'' , \\ \sigma &= \sigma' + j\sigma'' , \\ \text{and} \quad \mu &= \mu' - j\mu'' . \end{aligned} \tag{2.3}$$

The imaginary part of the propagation constant contains all necessary information about energy loss in a material medium during wave propagation. If, for the moment, magnetic properties are ignored, we may consider only the complex forms of ϵ and σ in eq. (2.2):

$$\omega(\epsilon' - j\epsilon'') - j(\sigma' + j\sigma'') = (\sigma'' + \omega\epsilon') - j(\sigma' + \omega\epsilon'') . \tag{2.4}$$

Here $(\omega\epsilon' + \sigma'')$ may be considered an effective permittivity and $(\sigma' + \omega\epsilon'')$ as an effective conductivity. The $(\sigma' + j\sigma'')$ physically represents carrier transport due to Ohmic and Faradaic diffusion mechanisms, whereas the $(\epsilon' - j\epsilon'')$ represents dielectric relaxation mechanisms. The loss tangent is defined from eq. (2.4) as

$$\tan \delta = \tan \left(\psi + \frac{\pi}{2}\right) \equiv \frac{\sigma' + \omega\epsilon''}{\sigma'' + \omega\epsilon'} , \tag{2.5}$$

where ψ is the phase angle between $\vec{E}$ and $\vec{J}$. If there are no dielectric losses, $\epsilon'' \rightarrow 0$. Similarly, if there are no Faradaic diffusion losses, $\sigma'' = 0$. Hence,

$$\tan \delta = \frac{\sigma'}{\omega\epsilon'} , \tag{2.6}$$

which describes physically the Ohmic losses.

What follows in this chapter is a detailed discussion of the dielectric and magnetic properties of those materials relevant to this project.

B. Dielectric Polarization Mechanisms

We can describe the dielectric properties of a material by the complex dielectric constant, $\epsilon = \epsilon' - j\epsilon''$, where ϵ' contains all the information about energy storage and ϵ'' contains all of the information about energy loss (both Ohmic and dielectric losses) in the material during wave propagation. The relative dielectric constant, or relative permittivity, of a soil is the permittivity of the soil normalized with respect to the permittivity of a vacuum, ϵ_0.

The quantity ϵ' is a measure of the amount of polarization in the material. There can be a number of different polarizing mechanisms present; each has a characteristic relaxation frequency and an associated dielectric dispersion centered around this relaxation frequency. Figure 2.1 illustrates the dispersions of dielectric constant and conductivity that are observed in materials in the frequency range of 10^3 to 10^{15} Hz. At the highest frequencies, the polarizing species in a material are the electrons. Electronic polarization occurs when an applied electric field causes a net displacement of the electron cloud of an atom with respect to its nucleus. At frequencies below about 10^{13} Hz, there is also a contribution from atomic polarization. Atomic polarization occurs in structures (molecules or solutions, for example) in which atoms do not share electrons equally and electric fields displace the electron clouds preferentially towards the stronger binding atoms. It also occurs when charged atoms are displaced with respect to each other. Dipolar polarization, that is, the orientation of polar molecules (molecules with asymmetric charge distributions), occurs at frequencies below about 10^{10} Hz [2.1].

At frequencies below about 10^5 Hz, various types of charge polarizations occur which may be collectively referred to as Maxwell-Wagner mechanisms [2.2, 2.3]. One of these, interfacial (space-charge) polarization, occurs when migrating charge carriers are trapped or impeded in their motion by local chemical or electric potentials, causing local accummulations of charge and a macroscopic field distortion. Another low-frequency mechanism that can occur in soils is due to mixtures of materials that have differing electrical properties (such as conducting spheres embedded in a dielectric). Several different equations are available to describe the resultant properties

[2.4, 2.5] for various geometries of the embedded conductor: conducting spheres or rods in a dielectric, alternating layers of dielectrics and conductors, for example. The common cause of these effects is the distributions of charge that occur at conductor-dielectric boundaries and the resultant action under applied electric fields which can yield very large, low-frequency dielectric constants. This mechanism, when we use synthetic soils whose conductivities are controlled by embedded conductors, is very important to examine and to relate to dispersion phenomena normally confronted in natural soil environments. This is true particularly when performance testing of broadband land mine detection systems is done and a relative detector figure of merit is estimated (broadband in this case means that the bandwidth extends into frequencies less than 1 MHz).

Still another dispersion mechanism for dielectric behavior at low frequencies, which is often distinguished from Maxwell-Wagner effects, is that which occurs in colloidal suspensions. Maxwell-Wagner effects are based on the assumption that the charge around conducting particles in a dielectric medium is a thin coating which is much smaller than the particle dimensions [2.5] and that the charge responds to an applied electric field independently of the charge on nearby particles. In colloidal suspensions, on the other hand, the charge layer is on the same order of thickness as or larger than the particle dimensions; hence it is affected by the charge distributions of adjacent particles. The theory of dispersion phenomena in colloidal suspensions is presently a fertile area of research. Dukhin [2.5] has shown that colloidal responses result in far higher low-frequency dielectric constants than those resulting from typical Maxwell-Wagner mechanisms, with dielectric constants on the order of 10^5 not uncommon. This could be an important phenomenon that spectrally increases the visibility of buried plastic land mines when broadband system performance is considered.

C. Dielectric Relaxation

Polarization processes occurring in material media as a result of electromagnetic wave propagation are physically damped by relaxation. This relaxation is analogous to a critically damped or overdamped oscillator. In the relaxation process, maximum energy is dissipated at a preferred relaxation

frequency, or resonance (which is the reciprocal of the relaxation time constant), with no dissipation at either zero or infinite frequency. Relaxation processes are the only ones observed in the natural soil environment at microwave frequencies and below. Thus, it would be useful to consider some relaxation models (cited in subsequent comments on soil specifications for broadband systems). The following relaxation models are based on the general equation of charge motion

$$\ddot{\underline{q}} + (\mu\sigma)^{-1}\,\dot{\underline{q}} + (\mu\epsilon)^{-1}\,\underline{q} = 0\,, \qquad (2.7)$$

where $\underline{q}$ is the charge and $\cdot$ represents differentiation with respect to time. All derivatives are with respect to time. An important current research area is considering diffusion of charged ions whose concentration is spatially variable. For this case, spatial derivatives must be taken in determining diffusion relaxation and this leads to generalized distributed impedances and nonlinear behavior [2.6].

C1. Debye Relaxation

Debye relaxation occurs in materials that have single relaxation time constants. The complex relative dielectric permittivity in a Debye material is given by [2.7, 2.8]

$$\epsilon' - j\epsilon'' = \epsilon_\infty \left[\frac{(\epsilon_s - \epsilon_\infty)/\epsilon_\infty}{1 + j\omega\tau} + 1\right] = \epsilon_\infty + \frac{\epsilon_s - \epsilon_\infty}{1 + \omega^2\tau^2} - j\,\frac{(\epsilon_s - \epsilon_\infty)\omega\tau}{1 + \omega^2\tau^2}\,, \qquad (2.8)$$

where ϵ_s is the measured relative dielectric permittivity at dc ($\epsilon_{dc} = \epsilon_s\epsilon_0$), ϵ_∞ is the relative dielectric permittivity at infinite frequency ($\epsilon_{infinite} = \epsilon_\infty\epsilon_0$), τ is the time constant of relaxation and ϵ_0 is the free space or vacuum permittivity (8.854×10^{-12} F/m).

C2. Generalized Relaxation Distributions

Wyllie [2.9] has given an expression for material media in which multiple relaxations or distributions of relaxations are found. Such behavior is more

typical of soils at frequencies below 1 MHz than Debye behavior, and the complex relative dielectric permittivity may be written

$$\epsilon' - j\epsilon'' = \epsilon_\infty + (\epsilon_s - \epsilon_\infty) \int_0^\infty \frac{D(\tau)(1 - j\omega\tau)}{1 + \omega^2\tau^2} \, d\tau \, , \qquad (2.9)$$

where $D(\tau)$ is the time constant distribution function normalized so that

$$\int_0^\infty D(\tau) \, d\tau = 1 \, .$$

A commonly observed simple relaxation distribution in soils is the Cole-Cole distribution [2.10]. In the Cole-Cole distribution, (2.9) reduces to

$$\epsilon' - j\epsilon'' = \epsilon_\infty + \frac{\epsilon_s - \epsilon_\infty}{1 + (j\omega\tau)^{1-m}} \, , \qquad (2.10)$$

where $0 \leq m \leq 1$. The $m = 0$ case corresponds to a Debye material that has a single relaxation. The $m = 1$ case corresponds to an infinitely broad, continuous distribution (one that has no relaxation). Usually $1 - m = c \leq 0.25$ for water-saturated soils, and the exact power-law exponential frequency behavior is critically dependent on water saturation, as discussed later in this report. (c is a constant defined in the next section and related to m as above.) This would necessitate methods for keeping c constant (as a function of frequency) in natural (or synthetic water saturated) soils when testing of land mine detectors is performed.

C3. Non-Debye Behavior of Rocks and Soils

Examples of studies showing the non-Debye behavior of rocks and soils are given by Saint-Amant and Strangway [2.11], Alvarez [2.12], Olhoeft et al. [2.13], Pelton et al. [2.14], Knight [2.15], and Lockner and Byerlee [2.16]. Observed deviations from Debye behavior have led to modifications of the Debye equation [2.12], including the Cole-Cole expression (eq. (2.10)) and the

corresponding Cole-Cole equivalent circuit [2.10]. The significant feature of the Cole-Cole circuit is the inclusion of a constant phase circuit element to model a distribution of relaxation times. The Cole-Cole expression has been found useful in fitting data from lunar soil samples [2.13], and an expression for the complex impedance of a material (as measured in the series mode) that contains a term analogous to the constant phase element in Cole-Cole [2.10] has been used in modeling the impedance of mineralized rocks [2.14, 2.17].

In addition to the Cole-Cole expression, there are three other empirical relations commonly used to describe a non-Debye response. These are the Cole-Davidson [2.18], the combined Cole-Cole, and the Williams-Watts [2.19] expressions. A characteristic feature of all these empirical relations, besides being based on eq. (2.7), is that at frequencies away from the relaxation frequency they reduce to expressions showing a power-law dependence on frequency for both ϵ' and ϵ''. This common characteristic led Jonscher [2.20, 2.21] to define this power-law dependence as the "universal dielectric response," that is,

$$\epsilon'(\omega) = K\omega^{-c} , \tag{2.11}$$

where K and c are constants that depend on the sample material and texture.

D. Dielectric Properties of Pure Water

Usually, natural soils contain water so the way in which dielectric constants combine is important in determining the bulk, or effective, dielectric constant of the soil at hand. The bulk dielectric constant of any soil (whether natural or synthetic) determines the electromagnetic visibility of buried land mines and, therefore, intrinsically affects the performance of any detection system. Before discussion of water saturation of heterogeneous soil mixtures, it is necessary to review fundamental dielectric behavior of pure and saline water.

The frequency dependence of the complex dielectric constant of pure water, ϵ_w, is well known and is given by the Debye equation [2.1, 2.7],

$$\epsilon_w(\omega) = \epsilon_{w\infty} + \frac{\epsilon_{wo} - \epsilon_{w\infty}}{1 + j\omega\tau_w} , \tag{2.12}$$

where

$\epsilon_{w\infty}$ = high frequency (or optical) limit of ϵ_w (dimensionless),

ϵ_{wo} = dc dielectric constant of ϵ_w (dimensionless),

τ_w = relaxation time of pure water (seconds), and

ω = frequency (radians/second).

Equation (2.12) may be simply written

$$\epsilon_w = \epsilon'_w - j\epsilon''_w = \epsilon'_w (1 - j\tan\delta_w) , \tag{2.13}$$

where $\tan\delta_w \equiv \epsilon''_w/\epsilon'_w$ is the loss tangent of water.

Rationalization of eq. (2.12) yields

$$\epsilon'_w(\omega) = \epsilon_{w\infty} + \frac{\epsilon_{wo} - \epsilon_{w\infty}}{1 + (\omega\tau_w)^2} \tag{2.14}$$

and

$$\epsilon''_w(\omega) = \frac{\omega\tau_w (\epsilon_{wo} - \epsilon_{w\infty})}{1 + (\omega\tau_w)^2} . \tag{2.15}$$

The magnitude of the high frequency dielectric constant, $|\epsilon_{w\infty}|$, has been determined by Lane and Saxton [2.22] to be

$$\epsilon_w \approx 4.9 \tag{2.16}$$

and is practically temperature independent. The relaxation frequency of pure water, $f_w = 1/(2\pi\tau_w)$, occurs in the microwave region and is temperature dependent. At 0°C, $f_w \approx 9$ GHz and at 20°C, $f_w \approx 17$ GHz. Equation (2.15) shows that ϵ''_w has its maximum value at $\omega = 2\pi f_w$. A plot of the frequency variation of ϵ'_w and ϵ''_w for pure water at 25°C is shown in figure 2.2 [2.4]. A Cole-Cole plot of ϵ''_w vs ϵ'_w, with f as a variable parameter, is shown in figure 2.3 for pure water at T = 0°C. This plot is a semicircle with end points defined by $\epsilon_w = \epsilon_{wo}$ in the low-frequency limit and by $\epsilon_w = \epsilon_{w\infty}$ in the high-frequency

limit. The point on the circle at which ϵ''_w is maximum occurs at the relaxation frequency, $f = f_w$, whose coordinates are simply given by

$$\epsilon'_w = (\epsilon_{wo} + \epsilon_{w\infty})/2 \text{ and } \epsilon''_w = (\epsilon_{wo} - \epsilon_{w\infty})/2 \ .$$

The dc dielectric constant of nonconductive water, ϵ_{wo}, is a function of temperature. Klein and Swift [2.24] have generated a regression fit for $\epsilon_{wo}(T)$ from dielectric measurements conducted between 1 GHz and 3 GHz

$$\epsilon_{wo}(T) = \epsilon'_{wo}(T) = 88.045 - 0.4147\ T + 0.6295 \times 10^{-3}\ T^{-2} \ , \qquad (2.17)$$

where T is in °C, and the loss term, ϵ''_{wo}, is zero.

E. Dielectric Properties of Saline Water

Although the dielectric properties of pure water and ice obey the Debye relaxation equations and are fairly well understood, ionic salts dissolved in water produce an electrolytic solution whose microwave dielectric properties may differ greatly from those of pure water. The salinity, S, of a solution is defined as the total mass of solid salt in grams dissolved in 1 kg of solution. Thus, S is normally expressed in parts per thousand by mass. Little will be said about broadband dielectric characterization of electrolytic solutions, except that the real and imaginary parts of the dielectric constant of a saline water solution are given by [2.23, 2.25]

$$\epsilon'_{sw} = \epsilon_{sw\infty} + \frac{\epsilon_{swo} - \epsilon_{sw\infty}}{1 + (\omega\tau_{sw})^2} \qquad (2.18)$$

and

$$\epsilon''_{sw} = \frac{\omega\tau_{sw}(\epsilon_{swo} - \epsilon_{sw\infty})}{1 + (\omega\tau_{sw})^2} + \frac{\sigma_i}{\epsilon_o\omega} \qquad (2.19)$$

where the subscript sw refers to saline water and σ_i is the ionic conductivity of the aqueous solution in S/m. The form of the complex permittivity for saline water differs from that of pure water only in the loss term, ϵ''_{sw}, where the added term, $\sigma_i/\omega\epsilon_o$, results from the ionic conductivity of the aqueous

solution is present. The ionic conductivity of saline water has a marked effect on the loss factor ϵ''_{sw} below 10 GHz. Therefore, high soil salinities will probably significantly affect the dielectric properties of wet soil. As Jedlicka [2.26] notes, few measurements and analyses have been reported relating soil salinity to effective soil dielectric constant. Consequently, the dependence of permittivity on soil salinity is not well understood. We do know, however, that the salinity of (free) pore water within a soil matrix depends directly on the cation exchange capacity of the matrix material. This fact should provide a direct relationship between soil type, amount of volumetric moisture present, and effective soil complex permittivity. Further work will enhance understanding between these physical soil parameters and measured electromagnetic properties.

Stogryn [2.27] points out that there is no evidence to indicate that $\epsilon_{sw\infty}$ depends on salinity; hence, we are safe to assume that $\epsilon_{sw\infty} = \epsilon_{w\infty} = 4.9$. He also empirically determines the dependence of permittivity on both the temperature and salinity of saline water by writing ϵ_{swo} as a factorable product, $\epsilon_{swo}(T,S) = \epsilon_{swo}(T)F(S)$. Polynomial fits to this relation have been obtained [2.24, 2.28] on measurements performed by Ho and Hall [2.29] and Ho, et al. [2.30] for $4 < S < 35$ parts per thousand to obtain the following functional (non-multiplicative) dependence of the dielectric constant of water with respect to salinity,

$$\epsilon'_{swo}(T,S) = \epsilon'_{wo}(T) - 0.1556 - 0.413 \times 10^{-3} S + 1.58 \times 10^{-6} S^2 \qquad (2.20)$$

and

$$\epsilon''_{swo}(T,S) = \epsilon'_{swo}\tan\delta_{swo} = 5.66 + 2.65 \times 10^{-3} S - 4.5 \times 10^{-6} S^2 . \qquad (2.21)$$

Equations (2.17), (2.20) and (2.21) will be used in subsequent development relating effective dielectric constant measurements (real part, ϵ', and loss tangent, $\tan\delta$) of a lossy fluid-saturated soil mixture to the in-situ fluid dielectric properties, as well as to the water-filled porosity of the soil mixture.

Several figures are included here to illustrate the relationship between the addition of salts to pure water and the dielectric properties of the

resulting solution. Figure 2.4 [2.31] is a plot of dc dielectric constant, ϵ_{sw}, versus solution concentration for three different salts. Figure 2.5 [2.31] is a plot of normalized relaxation time for a NaCl solution versus salt concentration at 25°C. Figure 2.6 [2.31] is a plot of the depression (change) of dielectric constant and relaxation time for a NaCl solution versus salt concentration at 0°C, 20°C and 40°C. These figures show that the presence of salt(s) in water (and thus in damp or wet soils) can drastically change the medium's dielectric constant.

F. Heterogeneous Soil Mixtures

By definition, natural soils are mixtures of host matrix mineral(s), air, and water. Generally, the real part of the effective relative dielectric constant, ϵ'_{eff}, of the mixture rarely exceeds 8 in the microwave region -- as long as there is no liquid water in the mixture. Similarly, the imaginary part, ϵ''_{eff}, usually does not exceed 1 in the absence of liquid water. By way of comparison, we see from figure 2.1 that ϵ'_w of liquid water is one order of magnitude larger than the relative permittivity of dry materials, whereas ϵ''_w is two orders of magnitude larger than that of dry materials, particularly at frequencies less than 2 GHz. Because of the large contrast between (complex) ϵ of the pore water and that of the host matrix in soils, the dielectric constant of the mixture is generally dominated by the dielectric behavior of water. For this reason, many investigators [2.22, 2.27, 2.32, 2.33] have generalized the Debye formulas given by eqs. (2.14) and (2.15) to mixtures in the following way,

$$\epsilon'_{eff} = \epsilon_{eff,\infty} + \frac{(\epsilon_{eff,o} - \epsilon_{eff,\infty})}{1 + (\omega\tau_{eff})^2}, \tag{2.22}$$

$$\epsilon''_{eff} = \omega\tau_{eff} \frac{(\epsilon_{eff,o} - \epsilon_{eff,\infty})}{1 + (\omega\tau_{eff})^2}, \tag{2.23}$$

where $\epsilon_{eff,o}$, $\epsilon_{eff,\infty}$ and τ_{eff} are functions of the dielectric constant of the matrix mineral(s), the water saturation, Sw, fraction in the pore space of the matrix, and the shape and orientation of the water inclusions. The dielectric constants of the matrix minerals are presumed to be nondispersive (frequency

independent or lossless) as well as independent of the applied direction (polarization) of the incident electric field. However, caution must be exercised in the use of eqs. (2.22) and (2.23) for soil mixtures over a broad range in frequency, since multiple relaxation phenomena not taken into account by the Debye rules can occur [2.1].

An example of a typical power-law variation of the dielectric constant as a function of water saturation for a consolidated sandstone is shown in figure 2.7 (recalling eq. 2.11). As the level of saturation decreases from full saturation, the power-law exponent, c, increases until at some critical saturation point (usually Sw $\doteq$ 0.2 for critical saturation) it drops rapidly to near zero. Most surface sands would probably fall below critical saturation, whereas most clay soils might fall in the region above critical saturation.

Typical behavior of ϵ' as a function of both water saturation and frequency is shown in figure 2.8. The observed dependence of ϵ' on Sw shows that ϵ' increases rapidly up to a critical water saturation, whereupon it increases more gradually and linearly with increasing saturation. For a completely dry soil and one which is only a single-component system, ϵ' goes to some threshold value independent of frequency. For a water saturation above critical saturation, ϵ' not only changes less with increasing frequency, but also has a lower value, almost by a factor of 4, from 50 kHz to 1 MHz. The significance of this observation is that mine detectors operating at differing frequencies are likely to be observing different contrasts in complex permittivity as long as water saturation (or equivalent metallic concentration in a synthetic soil) stays above critical with a greater dielectric contrast skewed toward lower detection frequencies.

Thus, there may be valid reasons to operate in this low frequency range for enhancing dielectric visibility contrast, even at the expense of spatial target resolution. The purpose of drawing attention to these phenomena is (1) to better compare detection systems that have different operating frequencies (whether fixed or broadband) in terms of the actual electrical contrast, $\epsilon'_H - \epsilon'_T$, seen between the host soil environment and buried land mine; and (2) to allow the removal of a variable nonlinear power-law frequency dependence of the soil's electrical properties in the case of water saturated

soils by keeping water saturation above the critical point for differing target size and burial depth parameters.

In summary, the functional dependence of c on water saturation in a porous medium is typified by figures 2.7 and 2.8. The actual power-law exponent observed depends on the texture (microgeometry) of the soil and resultant pore surface water or pore surface area-to-volume ratio.

G. Magnetic Susceptibility

Magnetic susceptibility is a fundamental physical property of a material medium. The degree to which a body is magnetized when placed in an external magnetic field is given by

$$\vec{M} = \chi_m \vec{H} \tag{2.24}$$

where $\vec{M}$ is the magnetization in amperes per meter, $\vec{H}$ is the applied external magnetic field intensity in amperes per meter and χ_m is the magnetic susceptibility (dimensionless) relating the applied field to the intensity of magnetization. We will use the International System of Units (SI) here.

For a magnetically linear, isotropic substance, the constitutive equation relating the magnetic flux density within a substance to the external magnetic field $\vec{H}$ due to magnetization is simply expressed by the vector equation,

$$\vec{B} = \mu_o (1 + \chi_m)\vec{H} = \mu\vec{H} \tag{2.25}$$

where μ_o is the permeability in vacuum ($4\pi \times 10^{-7}$ H/m) and χ_m is the dimensionless magnetic susceptibility defined in eq. (2.24).

The magnetic susceptibility of soils depends on the component magnetic minerals derived from chemical and mechanical breakdown of bedrock. Magnetic minerals of importance are few, and those most commonly encountered are the iron and titanium oxides which form several solid solution series in rocks (figure 2.9). Depending on the fractional composition of any solid solution series, the susceptibility may vary widely (figure 2.10). In addition to specific chemical composition, the susceptibility depends on grain size and the intensity of the magnetizing field. Thus, considerable variation in the susceptibility of rocks (and soils) can occur.

References (II)

[2.1] Geyer, R. G. Experimental parameters for land mine detection performance evaluations. (Nov. 1987) Report, Project 7232457 (100 pages).

[2.2] Maxwell, J. C. A treatise on electricity and magnetism. Dover Publ; 1891.

[2.3) Wagner, K. W. Erklarung der dielektrischen Nachwirkungsworgange auf Grund Maxwellscher vorstellungen. Archiv. Electrotechnik, Vol. 2: 371; 1914.

[2.4] Hasted, J. B. Aqueous dielectrics. London: Chapman and Hall; 1973. 302 p.

[2.5] Dukhin, S. S. Dielectric properties of disperse systems, in Matijevic, E., ed., Surface and colloid science, v. 3. New York, NY: Wiley Interscience; 1969. 83-166.

[2.6] Sluyters-Rehbach, M.; Sluyters, J. H. Sine wave methods in the study of electrode processes, in Electroanalytical Chemistry, Vol. 4, A. J. Bard, ed. New York, NY: Marcel Dekker; 1970. 1-128.

[2.7] Debye, P. Polar molecules. New York, NY: Chemical Catalog Co.; 1899.

[2.8] Smyth, C. P. Dielectric relaxation times in molecular relaxation processes. London: The Chemical Society; 1966. 1-14.

[2.9] Wyllie, G. Dielectric relaxation and molecular correlation in dielectric and related molecular processes. London; The Chemical Society; 1972.

[2.10] Cole, K. S.; Cole, R. H. Dispersion and absorption in dielectrics. J. Chem. Physics. 9: 341-351; 1941.

[2.11] Saint-Amant, M.; Strangway, D. W. Dielectric properties of dry geologic materials. Geophysics. 35: 624-645; 1970.

[2.12] Alvarez, R. Complex dielectric permittivity in rocks: a method for its measurement and analysis. Geophysics. 38: 920-940; 1973.

[2.13] Olhoeft, G. R.; Frisillo, A. L.; Strangway, D. W. Electrical properties of lunar soil sample 15301, 38. J. Geophys. Res. 79: 1599-1604; 1974.

[2.14] Pelton, W. H.; Ward, S. H.; Hallof, P. G.; Sill, W. R.; Nelson, P. H. Mineral discrimination and removal of inductive coupling with multifrequency IP. Geophysics. 43: 588-609; 1978.

[2.15] Knight, R. J. The use of complex plane plots in studying the electrical response of rocks. J. Geomag. Geoelectr. 35: 767-776; 1983.

[2.16] Lockner, D. A.; Byerlee, J. D. Complex resistivity measurements of confined rock. J. Geophys. Res. 90: 7837-7847; 1985.

[2.17] Madden, T. R.; Cantwell, T. Induced polarization, a review, in Mining Geophysics, Vol. 2, A. W. Musgrave, ed. Soc. Explor. Geophys; 1967. 373-400.

[2.18] Davidson, D. W.; Cole, R. H. Dielectric relaxation in glycerol, propylene glycol, and n-propanol. J. Chem. Phys. 29: 1484-1490; 1951.

[2.19] Williams, G.; Watts, D. C. Non-symmetrical dielectric relaxation behavior arising from a simple empirical decay function. Trans. Faraday. Soc. 66: 80-85; 1970.

[2.20] Jonscher, A. K. The interpretation of non-ideal dielectric admittance and impedance diagrams. Phys. Stat. Solutions (a). 32: 665-676; 1975.

[2.21] Jonscher, A. K. The universal dielectric response, a review of data and their new interpretation. Chelsea Dielectrics Group, University of London. 1979.

[2.22] Lane, J.; Saxton, J. Dielectric dispersion in pure polar liquids at very high radio frequencies, III. The effect of electrolytes in solution. Proc., Roy. Soc. 214(A); 1952. 531-545.

[2.23] Hasted, J. B. Liquid water: dielectric properties. Chapter 7 in Water--a comprehensive treatise, I, the physics and chemistry of water. New York: Plenum Press; 1972.

[2.24] Klein, L. A.; Swift, C. T. An improved model for the dielectric constant of sea water at microwave frequencies. IEEE Trans. Antennas Propag. AP-25; 1977. 104-111.

[2.25] Dobson, M. C.; Ulaby, F. T.; Hallikainen, M. T.; El-Rayes, M. A. Microwave dielectric behavior of wet soil, Part II: dielectric mixing models. IEEE Trans. Geosci. Remote Sensing. GE-23(1); 1985. 35-46.

[2.26] Jedlicka, R. P. Saline soil dielectric measurements. M.S. Thesis New Mexico State University, NM; 1978.

[2.27] Stogryn, A. Equations for calculating the dielectric constant of saline water. IEEE Trans. Microwave Theory Techn. MTT-19; 1971. 733-736.

[2.28] Wharton, R. P.; Hazen, G. A.; Rau, R. N.; Best, D. L. Electromagnetic propagation logging: advances in technique and interpretation. SPE of AIME Annual Technical Conference and Exhibition (Paper SPE 9267)1 1980 September. 21-24.

[2.29] Ho, W.; Hall, W. F. Measurements of the dielectric properties of sea water and NaCl solutions at 2.65 GHz. J. Geophys. Res. 78; 1973. 6301-6315.

[2.30] Ho, W. W.; Love, A. W.; VanMelle, J. J. Measurements of the dielectric properties of sea water at 1.43 GHz. NASA Contactor Report CR-2458. NASA Langley Research Center, Langley, VA; 1974.

[2.31] Debye, P. and Huckel, E. Z., Z. Phys. 24, 133, 305 (1923).

[2.32] Pottel, R. Water: A comprehensive treatise, Vol. II, Ed. F. Franks, Plenum Press, New York-London, ch. 17. 1973.

[2.33] Collie, C. H., Ritson, D. M. and Hasted, J. B. J. Chem. Phys., Vol. 16, n. 1. 1948.

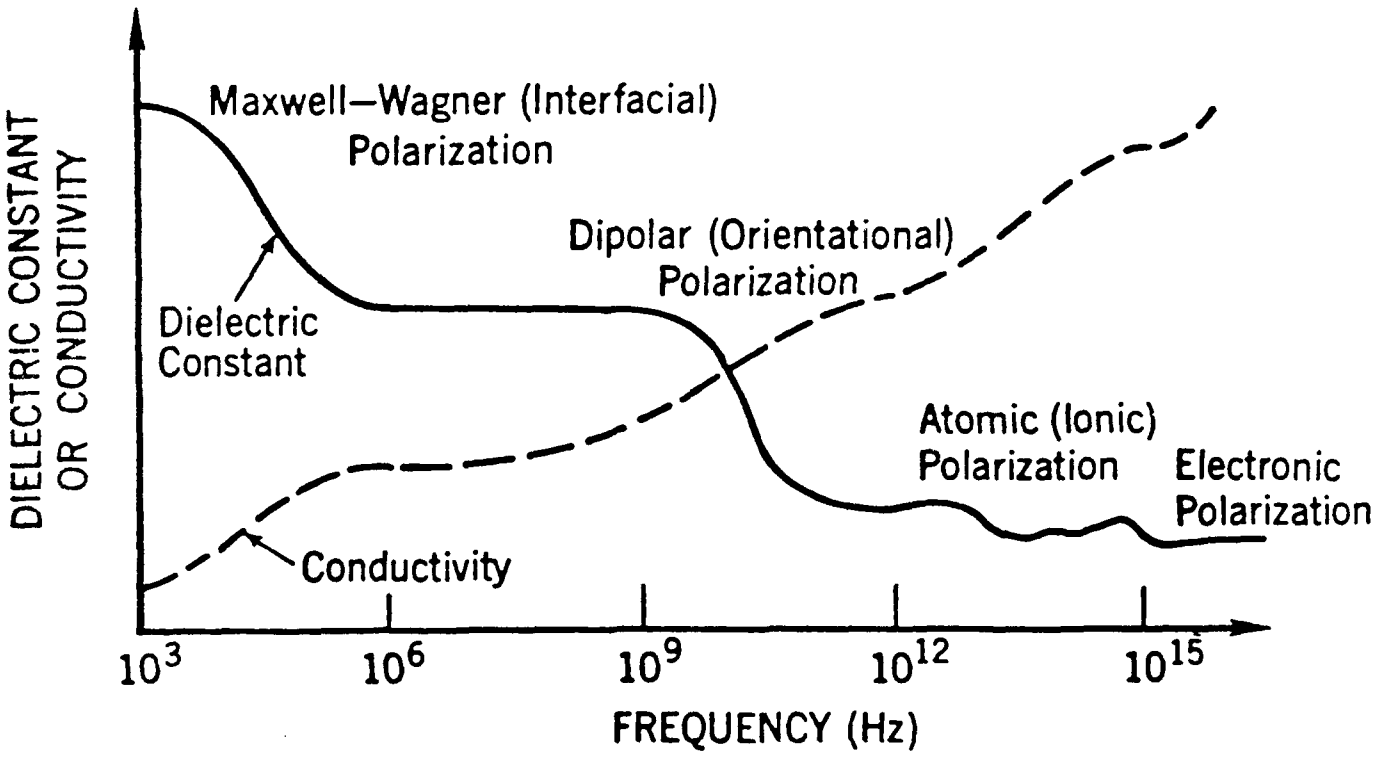

Figure 2.1 Dielectric dispersion for various types of polarization.

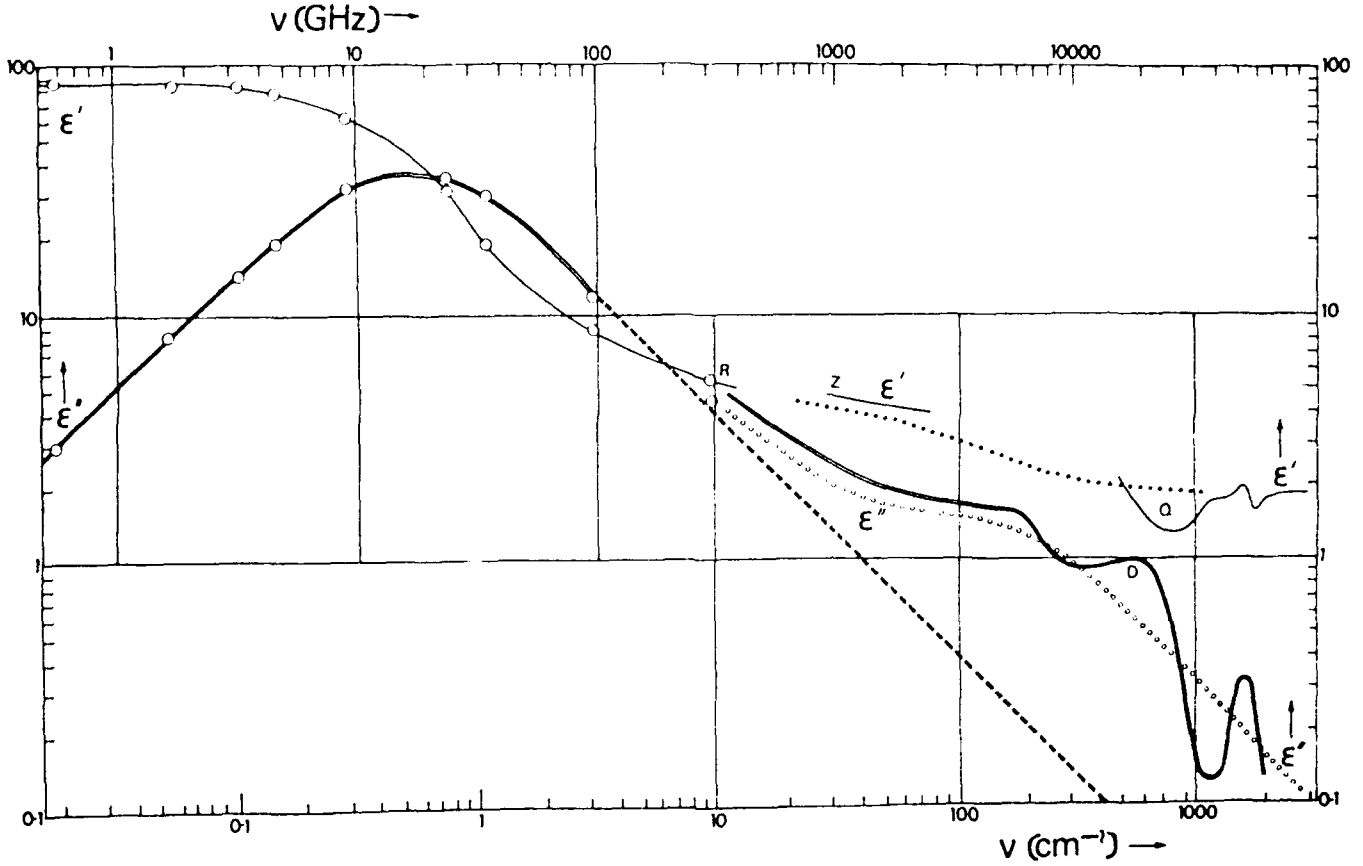

Figure 2.2 Frequency variation of ϵ_w' and ϵ_w'' for pure water at 25°C. Debye equation predicts linear 45° fall-off which appears, above, as the dashed line.

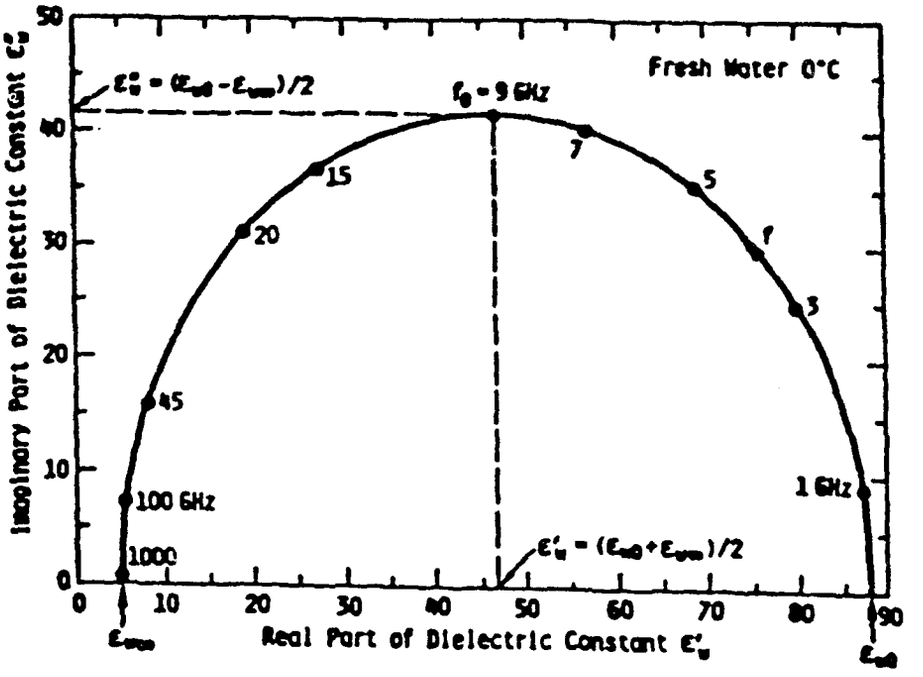

Figure 2.3 Cole-Cole diagram for the dielectric constant of pure water at 0°C.

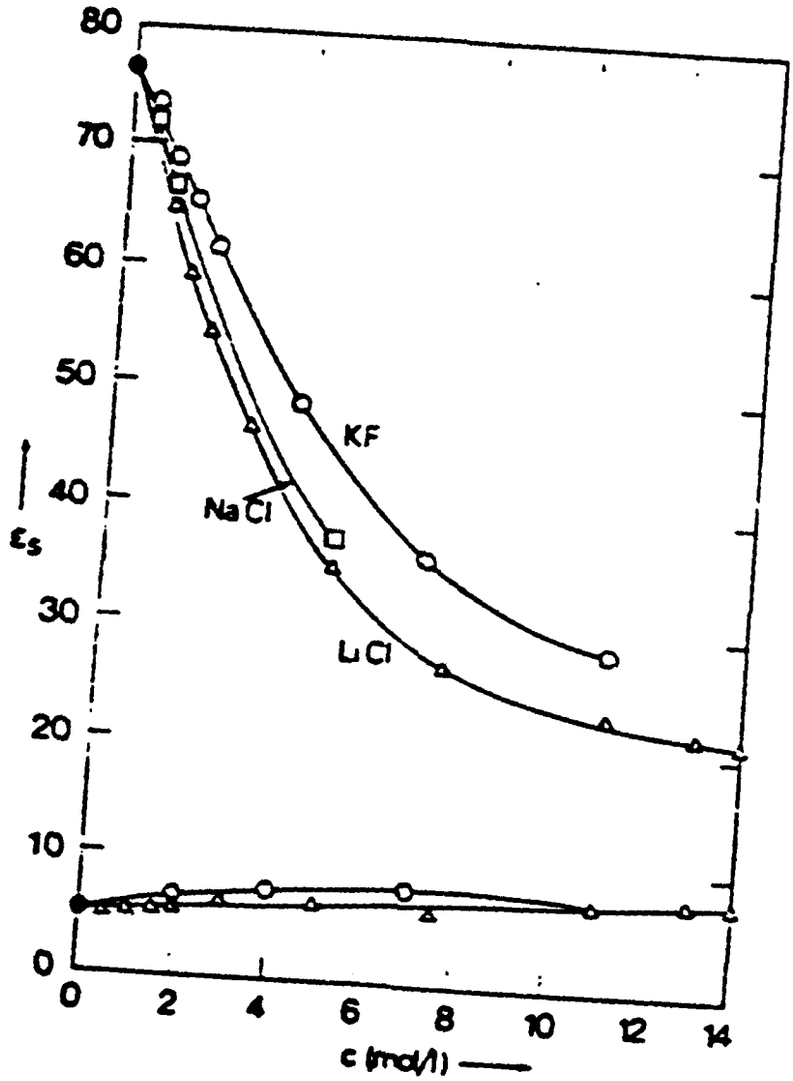

Figure 2.4 Measured concentration dependence of dc dielectric constants for three salts in highly concentrated water solution.

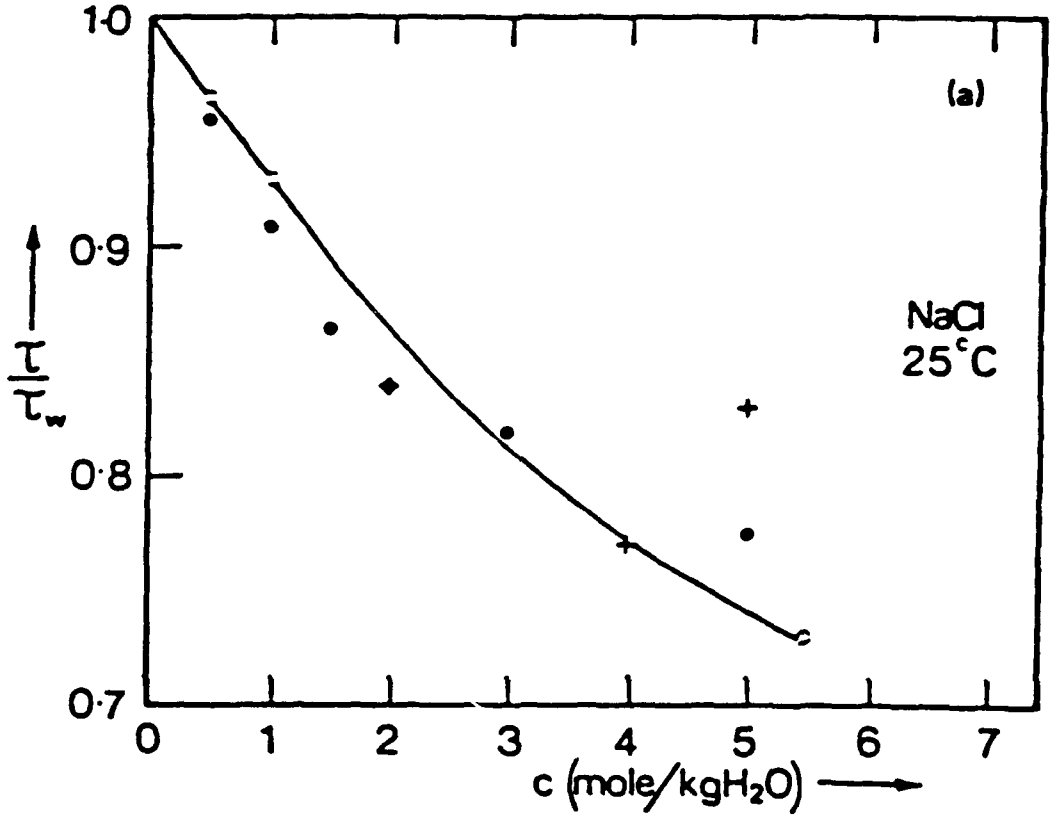

Figure 2.5 Measured concentration dependence of relaxation times of sodium chloride-water solution at 25°C.

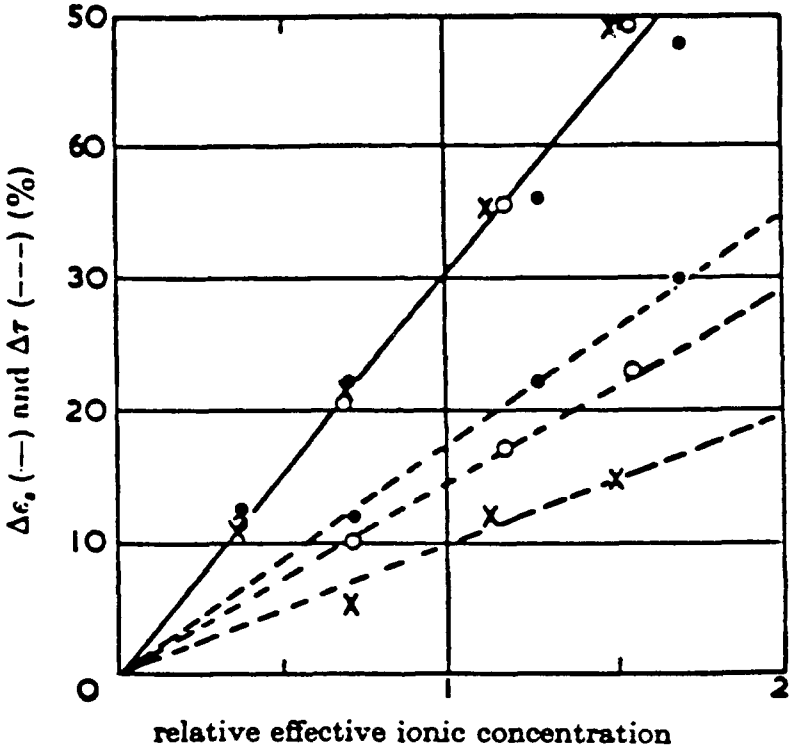

Figure 2.6 Depression of dielectric constant and relaxation time of sodium chloride solutions as a function of ionic concentration. • = 0°C; O = 20°C; x = 40°C.

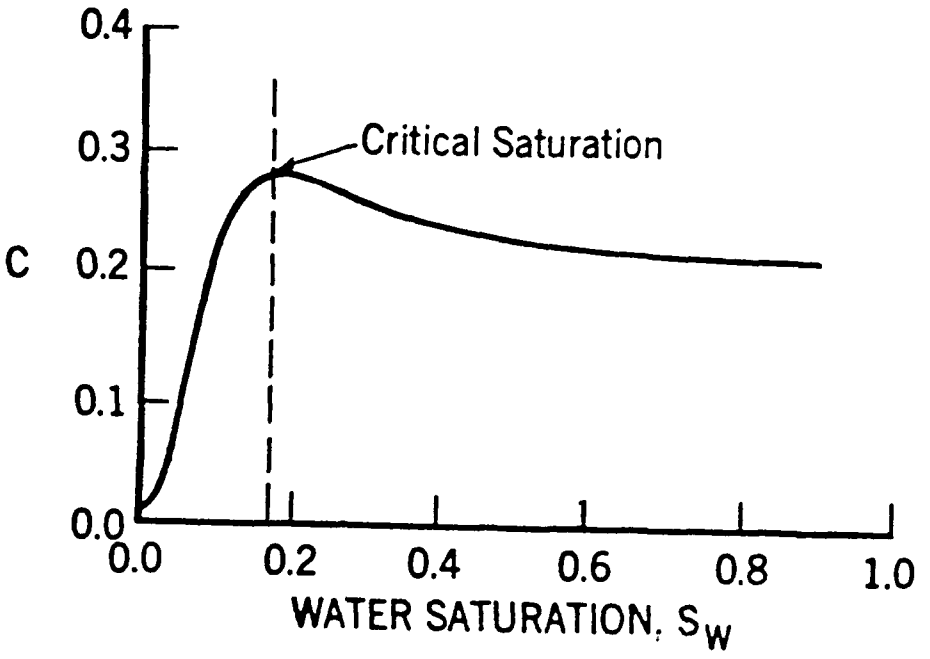

Figure 2.7 Typical power-law exponent variation of dielectric constant as a function of water saturation for a consolidated sandstone.

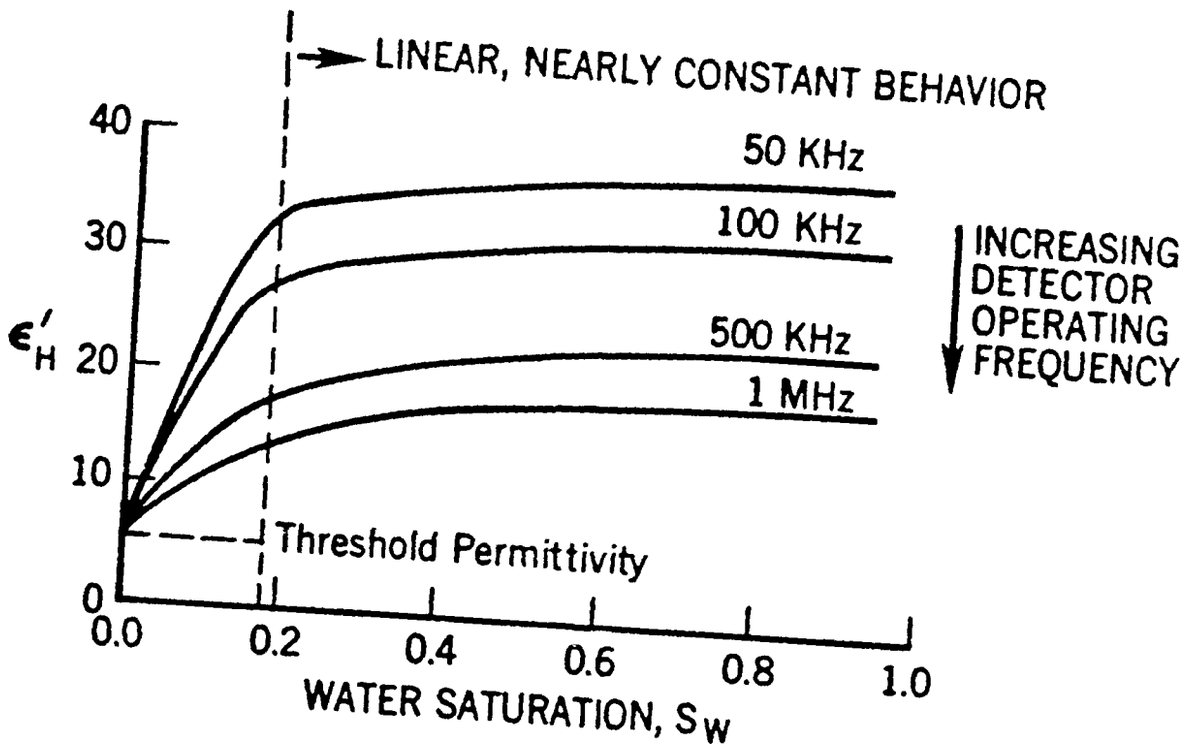

Figure 2.8 Dielectric constant as a function of water saturation for typical sandstone plotted parametrically as a function of frequency.

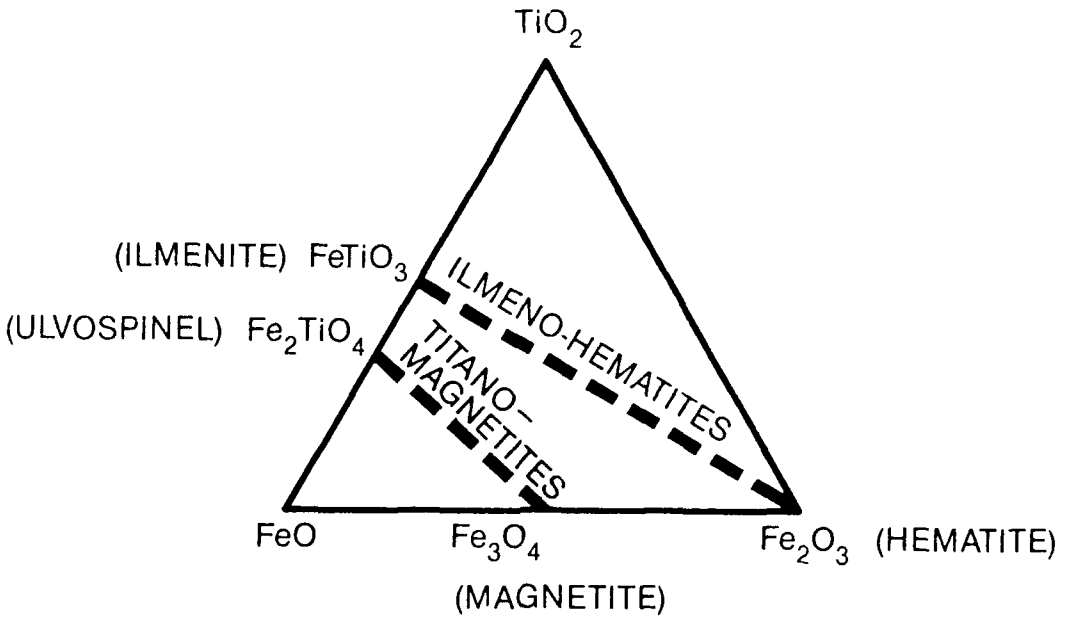

Figure 2.9 **Composition diagram of natural magnetic minerals.**

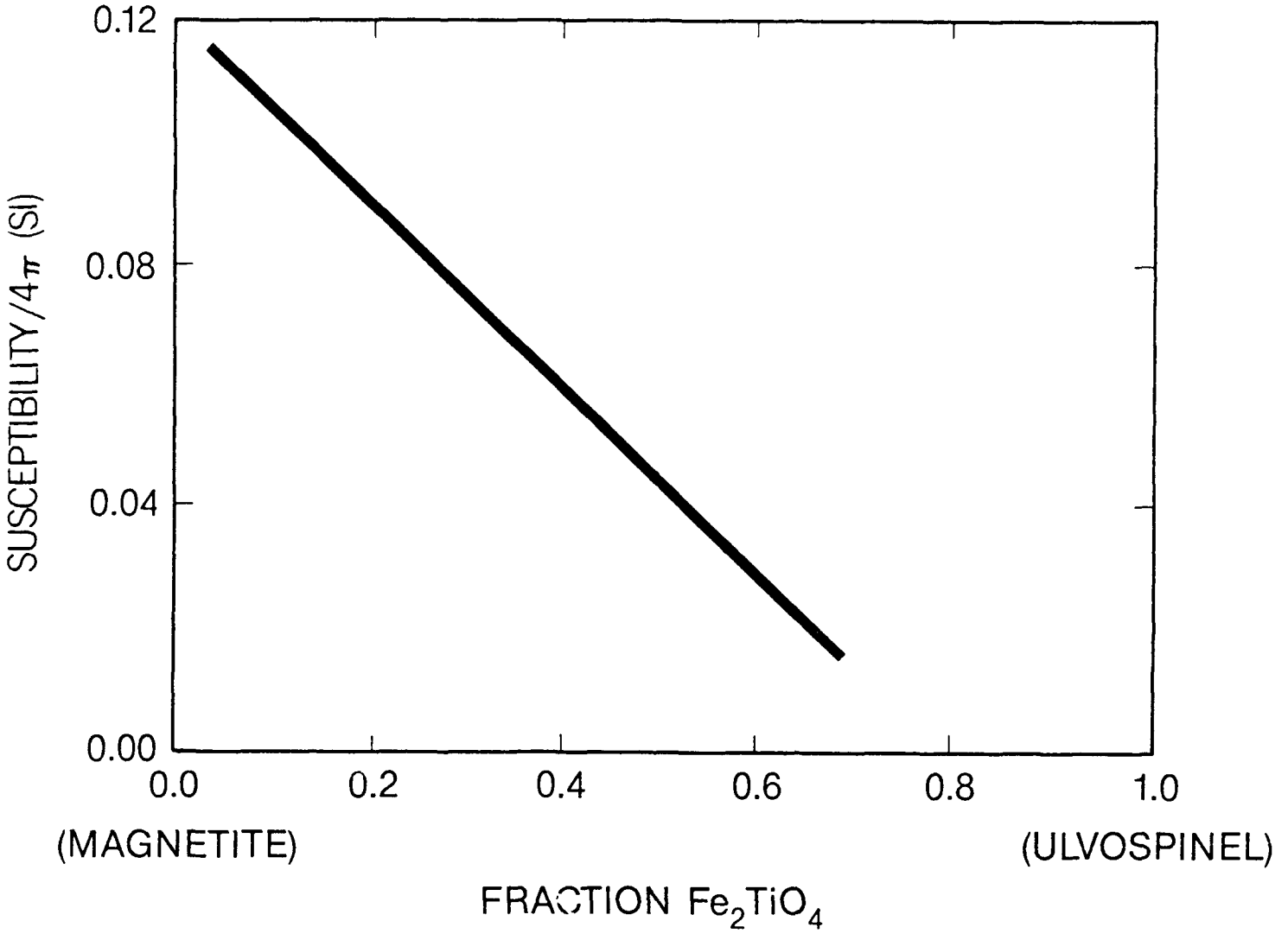

Figure 2.10 Magnetic susceptibility versus fractional composition of magnetite-ulvospinel solid solution.

III. REVIEW AND ANALYSIS OF EXISTING BURIED OBJECT DETECTOR TECHNOLOGY

A. Metal Detectors

Electromagnetic fields which oscillate in the kilohertz range cause eddy currents to flow in metallic objects. For metallic objects which are particularly good conductors, the currents are confined very closely to the object's surface. The "skin depth," δ, is related to the conductivity, the permeability, and the frequency by,

$$\delta = 1/\sqrt{\pi f \mu \sigma} \ , \qquad (3.1)$$

where, f = frequency in hertz

μ = magnetic permeability in henries/meter

σ = conductivity in siemens/meter

The magnitude of the eddy current decreases exponentially with distance from the surface of the conductor. The physical meaning of skin depth is the distance at which the currents have decreased to a value 1/e of what they are at the surface.

All low frequency metal detectors or treasure finders rely on the detection of eddy currents in metallic objects. The eddy currents are excited when an ac current in the search head coil generates time-varying magnetic fields in and above the ground. As eddy currents then flow in the buried metallic object(s), a small secondary magnetic flux (due to the eddy currents) is produced. This additional flux generates an additional signal voltage in the search coil which lags the detector-generated flux by 90 degrees. The resultant voltage in the search coil is, accordingly, shifted in magnitude and phase by an amount which depends on the conductivity of the buried object. Many of the treasure finders now available use this effect to discriminate between worthless aluminum or iron scraps and more valuable copper or silver coins.

It is customary to analyze the reactions of search heads (or eddy current test coils) with targets by means of normalized impedance diagrams on the complex plane. Figure 3.1 shows such a plot, with the reactance (X) on the y-axis and the resistance (R) on the x-axis. Both X and R have been normalized by the factor $2\pi fL_0$, the reactance of the search coil in air, in the absence of other metallic objects. For an excitation field frequency of 20 kHz, the impedance locus shows progressive changes in amplitude and phase as the conductivity of the target material is varied.

More than a dozen different metal detectors are manufactured in this country and at least an equal number of distinct types are available overseas. Different manufacturers exhibit considerable variety in their choice of features, operating modes, and detection sensitivity for metal detectors. The Army's Ft. Belvoir Research and Development Center lent us four AN/PSS-11's (standard detectors for metallic mines) for the duration of this project. The AN/PSS-11 is a hand-held metal detector with a unique search head geometry. A large coil around the periphery of the search head is the transmitting coil. Four smaller coils are arranged within and on the same plane as this transmitting coil. They are connected (in phase quadrature) to the receiving apparatus. The transmitting and receiving patterns for the search head are shown in fig. 3.2.

In addition to the four AN/PSS-11's, the Army also lent us a number of commercial treasure finders which had been tested previously at Ft. Belvior. We also acquired a German "search instrument" for locating metal objects hidden in the ground. This model is capable of locating nonmagnetic as well as magnetic objects. Unlike most metal detectors and treasure finders, this instrument uses a single coil for the excitation as well as the detection of eddy currents. It is similar to the manual, hand-held screening instruments used in airports to search for weapons. A voltage-to-frequency converter arrangement is employed to produce a frequency variation in the audio output, rather than a change in the loudness. A small change in audio frequency is easier to detect by ear than is a small change in audio signal strength.

B. Nonmetallic Object Detectors

Unlike the situation with the metal detectors (where several different types were available for study), only one type of plastic object detector was obtainable. We were lent three complete nonmetallic mine detector sets (standard AN/PRS-7's) for investigation and experimentation. This mine detection set has a planar four-layer search head fabricated by printed circuit techniques. The AN/PRS-7 has a transmitting antenna array which is composed of two capacitively end-loaded dipoles fed in opposing phase. The symmetrical arrangement produces a null in the radiation pattern in both the downward and upward direction. The metal tubing of the supporting stalk for the search head is located in this null plane, as is the receiving dipole. As long as the symmetry of this mechanical and electronic arrangement is carefully maintained (in particular, the feed arrangements for the various dipoles must be properly balanced), the receiver will respond to targets which are asymmetric with respect to the null plane. The receiver will not respond to a homogeneous or horizontally stratified earth. Objects which are electromagnetically dissimilar to the background material (either in conductivity or dielectric constant or both) can be detected as the search head passes over them. The receiver system amplifies and detects the RF signal, producing an audible loudness variation in a 1 kHz tone in response to these changes.

As with the AN/PSS-11 metal detector, considerable care must be taken in the manufacture of these devices to ensure that the required balance arrangements are maintained. Other approaches to the detection of plastic objects are described in the literature [3.1, 3.2].

C. Broadband (Pulsed) Systems

The AN/PRS-7 and the multi-frequency version of the AN/PRS-7, known as the AN/PRS-8, are CW systems -- that is, they do not operate as pulsed radars. We have consulted the literature on pulsed systems for the detection of buried objects. Earlier work on the subject is described in reports from MIT [3.3] and Ohio State University [3.4]. The former system was known as "GEODAR" and was mainly an effort to facilitate the detection of underground tunnels. A commercial version of the Ohio State University ElectroScience Laboratory's system was manufactured and sold commercially [3.5]. More recently, there are

references to work in Japan [3.6, 3.7] which demonstrate that some advantage can be gained by using a computer to enhance the detectability (on a color display) of target signals in the presence of background clutter and other noise. Less well publicized work by Dolph at SRI International [3.8] and by Alongi [3.9] is also applicable to the mine detection problem.

The advantage of most pulsed systems is that they gather information about the surface and subsurface regions over a broad range of frequencies. Indeed, the bandwidth of the echoes (if any) from the subsurface is generally limited by the transparency of the ground at UHF and microwave frequencies rather than by limitations of the transmitter and receiver equipment. This is because it avoids having to make any adjustments to the equipment. All of the information which could possibly be obtained by EM methods is made available pulse by pulse. On the other hand, the transparency of the ground for all but the most benign, very dry conditions severly limits the useable frequency range. This sets limits on the range resolution of the system, on the degree to which reflections from the air-ground interface can be suppressed, and on the detectability of targets. For a system operating over a frequency range from near dc to 1 GHz, the range resolution is no better than 15 cm. If the frequency range is further restricted to 500 MHz after the EM waves penetrate 20 cm of damp soil (a two-way path of 40 cm), the range resolution is no better than 30 cm. In particular, target signatures for mines which are buried very close to the surface cannot then be separated from the transmitter "main bang" or from the surface clutter signal. Likewise, target signatures attributed to targets buried some distance below the surface can no longer be separated from the clutter signal due to voids and other irregularities in the ground.

D. NIST Theoretical Work in Support of Buried Object Detector Evaluations

We thought that we needed a suitable theoretical framework to describe the transmitting and receiving characteristics of mine detectors as well as the interaction of radiowaves with buried objects. Dr. David Hill of NIST devised a particularly lucid theoretical model for the problem. His approach involves taking the Fourier transform of the distribution of complex electric

or magnetic field amplitude and then redefining the problem in terms of an angular spectrum of plane waves.

A description of radiowave fields in terms of their plane wave spectra is often advantageous, particularly for problems with planar geometry such as ours. An angular spectrum of plane waves may have only a few discrete spectral components or, more generally, it may be composed of a very large number of components or even a continuous distribution of waves. Each member (or any infinitesimal component) of the angular spectrum travels in the direction given by its propagation vector. Each of these components behaves exactly as an ordinary plane wave.

The more interesting and difficult problems that arise when a subsurface target is illuminated by an antenna above ground are conveniently described by the plane wave scattering matrix formalism of Kerns [3.10]. The plane wave spectral components radiated by the source antenna are reflected and refracted at the air-earth interface, and total fields above or below ground are calculated as integrals of these plane wave spectra. Specific sources such as a single plane wave or an electric or magnetic dipole are simply special cases of the general theory. The buried target is described by its plane wave scattering matrix, and the scattered plane waves are again reflected and refracted at the interface. All of the various interactions (the antenna interactions at the air-ground boundary, the target returns partially scattered and partially transmitted through the air-ground boundary, for example) are treated in a wholly self-consistent formulation, yet certain pieces of the problem can be extracted and studied separately. For example, the subsurface fields excited by an antenna over a lossy earth can be computed independently of the target. The actual plane wave transmission spectrum and scattering matrix are known for some simple antennas and targets. For more complicated cases, the scattering matrix formalism is still useful in showing what quantities are important and how they can be measured. Numerical results obtained by G. S. Smith [3.11], K. K. Mei [3.12], and others can be readily incorporated within this general theoretical framework.

A paper by Hill and Cavcey [3.13] (see Appendix III.A) showed how to derive expressions for che coupling between two antennas separated by an idealized, flat interface (the air-ground interface). This work extends the

generalized plane wave scattering formulation pioneered by Kerns to deal with the more interesting and difficult problems which arise when a subsurface target is illuminated by an antenna located above ground.

In a second paper [3.14] (see Appendix III.B), Hill showed how to use the Born approximation to describe EM scattering by buried objects of low dielectric contrast. Analytic expressions were obtained for three special shapes: (1) a sphere, (2) a cylinder, and (3) a rectangular box. Numerical results were given for the scattered near field and for the scattered far field, given plane wave illumination.

Hill also used the plane wave scattering matrix theory [3.15] (see Appendix III.C) to compute the far field E-field intensity in air and in the earth excited by oppositely-directed, transmitting antennas in the AN/PRS-7 mine detector. In pursuing this problem, a simple but general result was obtained for the front-to-back ratio of horizontal, linear antennas of arbitrary configuration located at the air-earth interface: Front-to-back ratio is proportional to $|\epsilon_r|^{1/2}$, where ϵ_r is the relative complex dielectric constant of the earth.

A good definition for the front-to-back ratio is the ratio of the far field E-field intensity in the earth to the far field E-field intensity in air in the two directions normal to the air-earth interface. This ratio is greater than 1 because of the focusing of the refracted fields in the earth and the partial cancellation of the fields in air. This simple formula can be derived from the plane wave scattering matrix theory or from reciprocity, and it is consistent with numerical results of G. S. Smith [3.11]. For elevated antennas, focusing in the earth still occurs, but the cancellation of the fields in air is less effective. For heights of about a quarter wavelength (the worst height), the front-to-back ratio is about 1, and this is also consistent with Smith's numerical results.

For angles away from the vertical, the enhancement in earth still occurs, but the magnitude of the enhancement depends on the specific antenna. Numerical results for the AN/PRS-7 transmitting antenna show a large enhancement in the earth even though the antenna produces a null in the vertical direction. The same relative enhancement (of the fields in the

earth) occurs when computing the near field of antennas above and below the air-earth interface.

In Hill's final paper on near field detection of buried dielectric objects [3.16] (see Appendix III.D), the plane wave scattering matrix theory was used to generate sweep curves for several different conditions with the AN/PRS-7 detector passed over a buried dielectric target. The search head for this mine detector is modeled as two oppositely directed transmitting dipoles and a single receiving dipole. The ratio of the received voltage, V_r, to the transmitter current, I_o, can be written as a product of matrices,

$$\frac{V_r}{I_o} = \bar{S}_{01} \; \bar{T}'_{12} \; \bar{S}'_{22} \; \bar{T}'_{21} \; \bar{S}_{10}. \qquad (3.2)$$

The right side of eq. (3.2) has a simple physical interpretation. $\bar{S}_{10}$ represents transmission from the detector into air, $\bar{T}_{21}$ represents transmission from air into the earth, $\bar{S}'_{22}$ represents scattering from the buried object, $\bar{T}_{12}$ represents transmission from the earth into air, and $\bar{S}_{01}$ represents reception at the detector. Various aspects of the overall detection problem (radiation, transmission, scattering, and reception) are treated in this paper. To our knowledge, this is the first time that the full plane wave scattering matrix theory has been used in near field calculations. The main results are sweep curves for various parameters (detector height, target depth, and horizontal target offset). All curves have a null directly overhead, a single peak on either side, and a smooth decay. A typical curve is shown in fig. 3.3.

E. NIST Tests, Instrumentation, and Procedures for Metal Detectors

Whenever possible, we performed unit testing of subsystems before testing of complete detector systems. For metal detectors and treasure finders, this meant starting with the search coil assembly and determining (from the pin-outs of the cable connector) the electrical characteristics of the transmitting as well as the receiving coils. An ordinary ohmmeter sufficed to check for continuity and the dc resistance of the coil windings. We used an ac impedance bridge to determine R, L, and C for the individual

coils. Shorted turns, coil balance, and so on were checked with a grid-dip meter or with a vector voltmeter and a search head known to be properly assembled. The search head was then connected to a laboratory version of the detector electronics. We call this our "brass board set-up." A schematic is shown in fig. 3.4. This equipment is capable of operating at any frequency in the range from 20 Hz to 20 kHz. If testing at higher or lower frequencies became necessary, a different power amplifier for the appropriate frequency band would be required.

The brass board detector is a broadband, linear system which can select (with the phase sensitive lock-in amplifier) any narrow-band signal for reception and plotting. This detector performs as well as or better than detectors provided with the mine detectors or treasure finders themselves. In particular, it is free of drift, it measures the phase of the received signal as well as the magnitude, and it has a very wide dynamic range. The first of these features is a convenience. The second feature (phase information) is used in some advanced metal detector systems to identify nonmagnetic material (such as stainless steel firing pins) in the presence of magnetic material (such as iron shrapnel or magnetite sand). Likewise, phase information can be used to discriminate (with the proper electronics) between aluminum alloy targets and copper coins. The last feature (wide dynamic range) means that adjustments for sensitivity, ground-balance, and so on are not required. Some disadvantages of this detector are that it weighs over 80 kg, operates over a very restricted temperature range (in an air-conditioned laboratory), and requires an extension cord to the ac mains. However, it should be possible to build small, portable units to similar or better performance specifications using modern manufacturing techniques.

With the search head mounted on a trolley or other positioning device, we obtained sweep curves using the brass board electronics. From these curves, we may judge the performance of a metal detector under controlled (repeatable) conditions. After preliminary tests of the search head with the brass board electronics system, we replaced it with the original battery-powered mine detector electronics package. Then we plotted sweep curves (with the complete system adjusted and ground-balanced exactly as suggested by the manufacturer) for a series of cylindrical copper test targets of progressively

smaller sizes. The testing terminated when test targets below a certain size could no longer be reliably detected. For these tests, the headphone output signal was run to a square-law detector and filtered with a 0.2 s time constant. We also found that it was useful to measure the sound pressure levels at the headphones. We referred the sound pressure level in dB with respect to a standard 2×10^{-5} N/m^2 rms pressure level at a frequency of 1 kHz. This 0 dB level is approximately the hearing threshold for young adults who have not attended very many rock concerts. We have demonstrated that very sensitive equipment can be employed to graphically display sweep curves at and below 0 dB. Perhaps some means could be devised to do likewise under field conditions.

Last, we estimated the dynamic range of the equipment by examining the detectability of large targets and targets in the presence of other disturbances (clutter). We also graded equipment on the basis of its ability to resolve small, closely spaced targets.

The detection of buried objects by electromagnetic means is difficult -- even when attenuation is not a limiting factor. Weak signals scattered by buried objects are typically well hidden in clutter. Clutter signals are the unwanted signals or noise which shows up as scattering from terrain surface features and from subsurface inhomogeneities. Certain poorly designed detectors are easily confused by radiation from other directions than the ground (nearby trees or vehicles, for example). Increases in transmitter power yield an improved signal-to-noise ratio for systems which are limited by receiver noise, natural noises (atmospheric or cosmic), or man-made interference. However, signal-to-clutter ratios are unaffected by such measures.

The clutter rejection capability of a given detector system is extremely difficult to estimate under field conditions. Clutter exhibits considerable variability. It is not a statistically well behaved signal. It shows up as a randomly phased signal which varies with the terrain and with the (invisible) features below the surface. To a certain extent, the clutter signal is also significantly influenced by the particular search pattern being used.

F. NIST Tests, Instrumentation, and Procedures for Nonmetallic Object Detectors

As with the metal detectors, we investigated the behavior of the search head alone before judging the performance of the complete system. For the AN/PRS-7 and similar detectors, this was difficult because parts of the transmitter as well as the receiver are built into the search head. We obtained a search head from which all of the electronic circuitry as well as the shielding tabs had been removed. We installed wide-band baluns at both the transmitting and the receiving antenna terminals and found that this head had a lower SWR at 432 MHz than at 380 MHz (the frequency at which its transmitter was expected to operate). A block diagram of the equipment used in these experiments is shown in fig. 3.5.

This brass board detector, unlike the unmodified AN/PRS-7, is a linear system. With the brass board, we can make stable, repeatable measurements weeks or even months apart. The 432 MHz transmitter is an ordinary signal generator of good spectral purity. The carrier frequency is 80% amplitude modulated by a 700 Hz sine wave to ensure that there is negligible clipping or distortion. A portion of the 700 Hz modulating signal is routed to the reference port of the lock-in amplifier. The receiver is a 400 MHz to 450 MHz broadband amplifier followed by a square-law detector. The lock-in amplifier is used to extract the weak 700 Hz component. The amplifier uses both the in-phase and the quadrature signal and forms the vector sum to yield an output directly proportional to the magnitude of the 700 Hz signal. This signal is fed to a measurement system. The final output is power in decibels vs. target displacement (see fig. 3.6). Comparison of this measured curve with the theoretically derived curve in fig. 3.3 indicates an excellent qualitative agreement.

References (III)

[3.1] Peters, Leon, Jr. and Young, J. D. Applications of Subsurface Transient Radar, Chapter 9 of book: Time-Domain Measurements in Electromagnetics, Van Norstrand Reinhold Co. Inc. (1986).

[3.2] Daniels, D. J. et al. Introduction to subsurface radar, IEE Proceedings 135, F, no. 4, pp 278-321 (1988).

[3.3] Chick, R. W. et al. "GEODAR," M.I.T. Lincoln Laboratory Report EPS-1 (Earth Propagation Studies), 1 August 1967. Prepared for ARPA under Electronic Systems Division Contract AF 19(628)-5167.

[3.4] Peters, Jr., L.; Burrell, G. A.; Tran, H. B. A scattering model for detection of tunnels using video pulse systems. The Ohio State University ElectroScience Lab., Dept. of Electrical Engineering (prepared under contract DAAG53-76-C-0179 for U.S. Army Mobility Equipment Research and Development Command, Ft. Belvoir, VA 22060); 1977; Technical Report 4460-3.

[3.5] Young, M. A. et al. "Underground Pipe Detector," U.S. Pat. No. 4062010 (1977).

[3.6] Osumi, N. and Veno, K. Microwave Holographic Imaging of Undergound Objects, IEEE Trans. Antennas Propagat. AP-33, pp 152-159 (1985).

[3.7] Tanaka, H. et al. Development of radio-based pipe locator, Proc. 16th World Gas Conference, 1985 Munich, Germany (Published by Int'l Gas Union).

[3.8] Dolphin, Lambert: Seminar talk given at University of Colorado 30 January 1986 on work done at SRI International (Palo Alto, CA).

[3.9] Alongi, A. V. A short-pulse high-resolution radar for cadaver detection, Proc. 1st Int'l Electronic Crime Countermeasure Conference (1973) pp 79-87.

[3.10] Kerns, D. M. Plane Wave Scattering Matrix Theory of Antennas and Antenna-Antenna Interactions, NBS Monograph 162, Washington, D.C. (U.S. Gov't Printing Office, 1981).

[3.11] Smith, G. S. Directive properties of antennas for transmission into a material half-space, IEEE Trans. Antennas Propagat. AP-32, pp 232-246 (1984).

[3.12] Chang, H. S. and Mei, K. K. Scattering of electromagnetic waves by buried and partly buried bodies of revolution, IEEE Trans. geosci. Remote Sensing GE-23, pp 596-605 (1985).

[3.13] Hill, D. A. and Cavcey, K. H. Coupling Between Two Antennas Separated by a Planar Interface, IEEE Trans. Geosci. Remote Sensing GE-25, pp 422-431 (1987).

[3.14] Hill, D. A. "Electromagnetic Scattering by Buried Objects of Low Contrast," IEEE Trans. Geosci. Remote Sensing GE-26, pp 195-203 (1988).

[3.15] Hill, D. A. "Fields of Horizontal Currents Located above the Earth," IEEE Trans. Geosci. Remote Sensing GE-26, pp. 726-732 (1988).

[3.16] Hill, D. A. "Near Field Detection of Buried Dielectric Objects," IEEE Trans. Geosci. Remote Sensing GE-27, pp. 364-368 (1989).

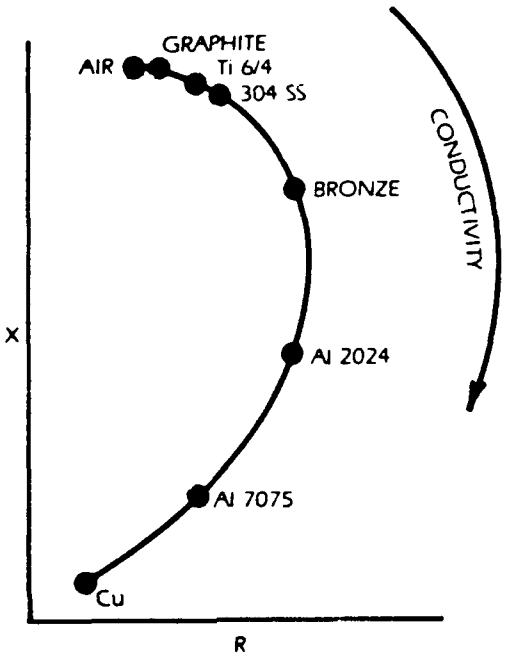

Figure 3.1 Normalized impedance for a search coil encircling cylindrical targets of different nonmagnetic materials (reactance, X, versus resistance, R).

Figure 3.2 Transmit and receive search head antenna patterns for the AN/PSS-11.

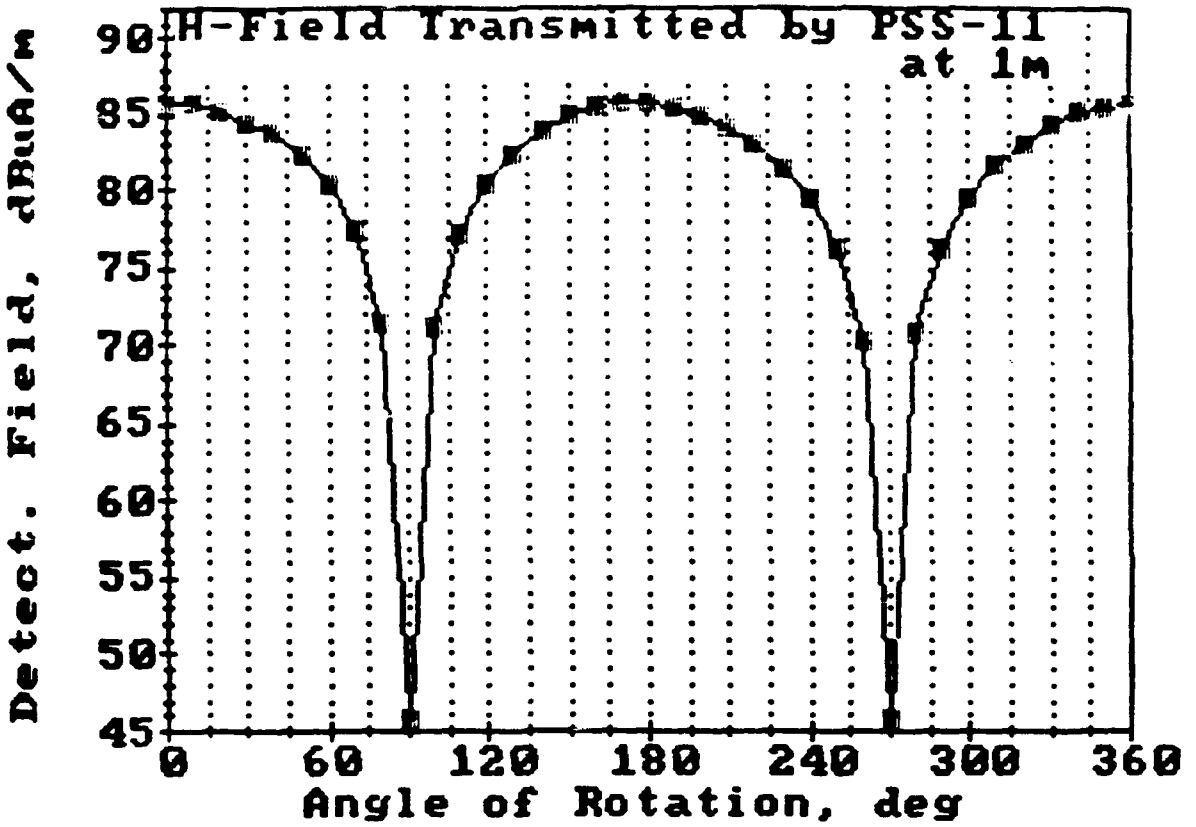

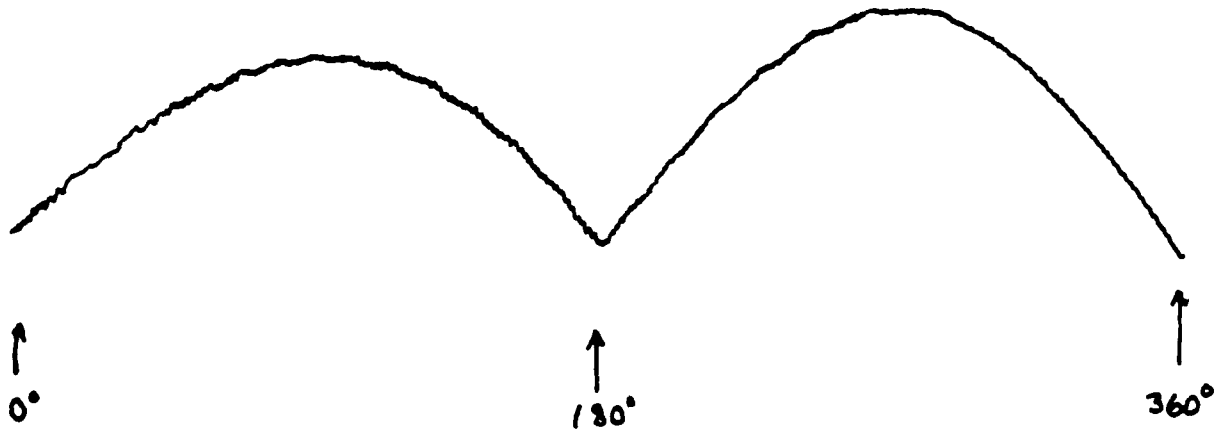

PSS-11, Receiver Pattern

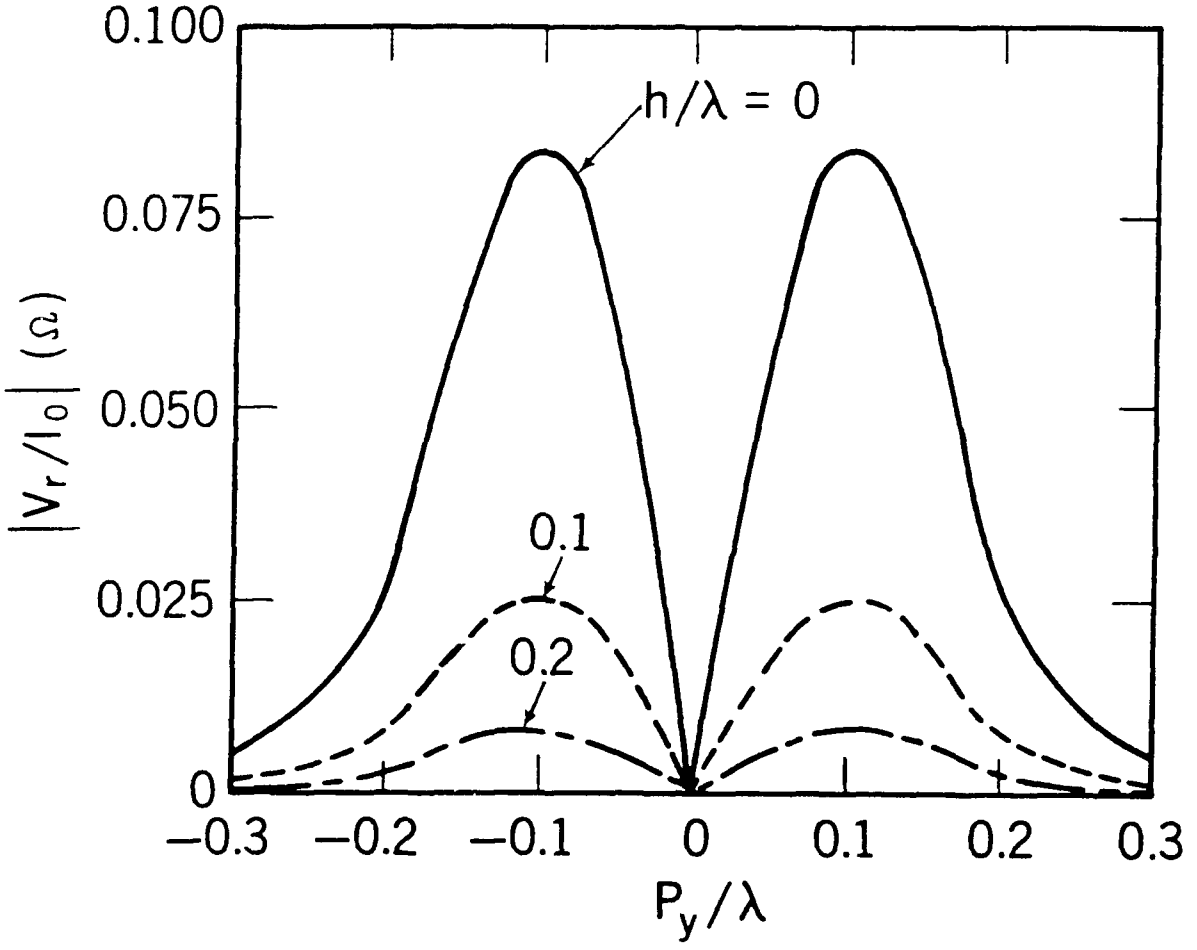

Figure 3.3 Theoretical sweep curves for the AN/PRS-7 for various detector heights, h. (ℓ/λ = 0.126)

BLOCK DIAGRAM of the BRASSBOARD AN/PSS-11

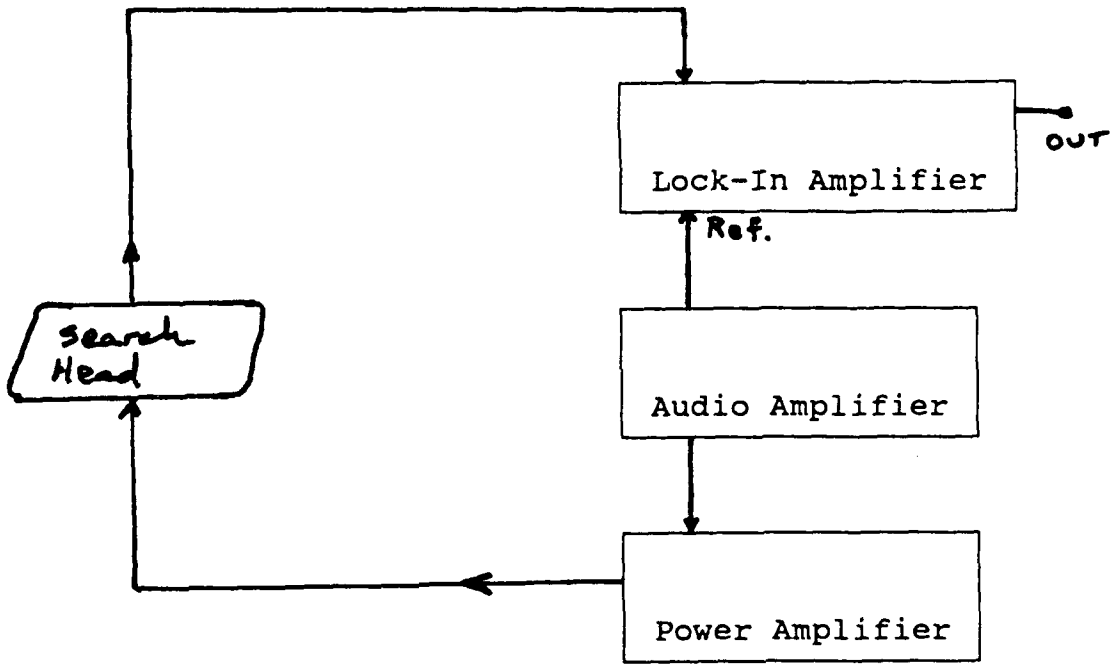

Figure 3.4 Block diagram for the AN/PSS-11 brassboard detector.

BLOCK DIAGRAM of the BRASSBOARD AN/PRS-7

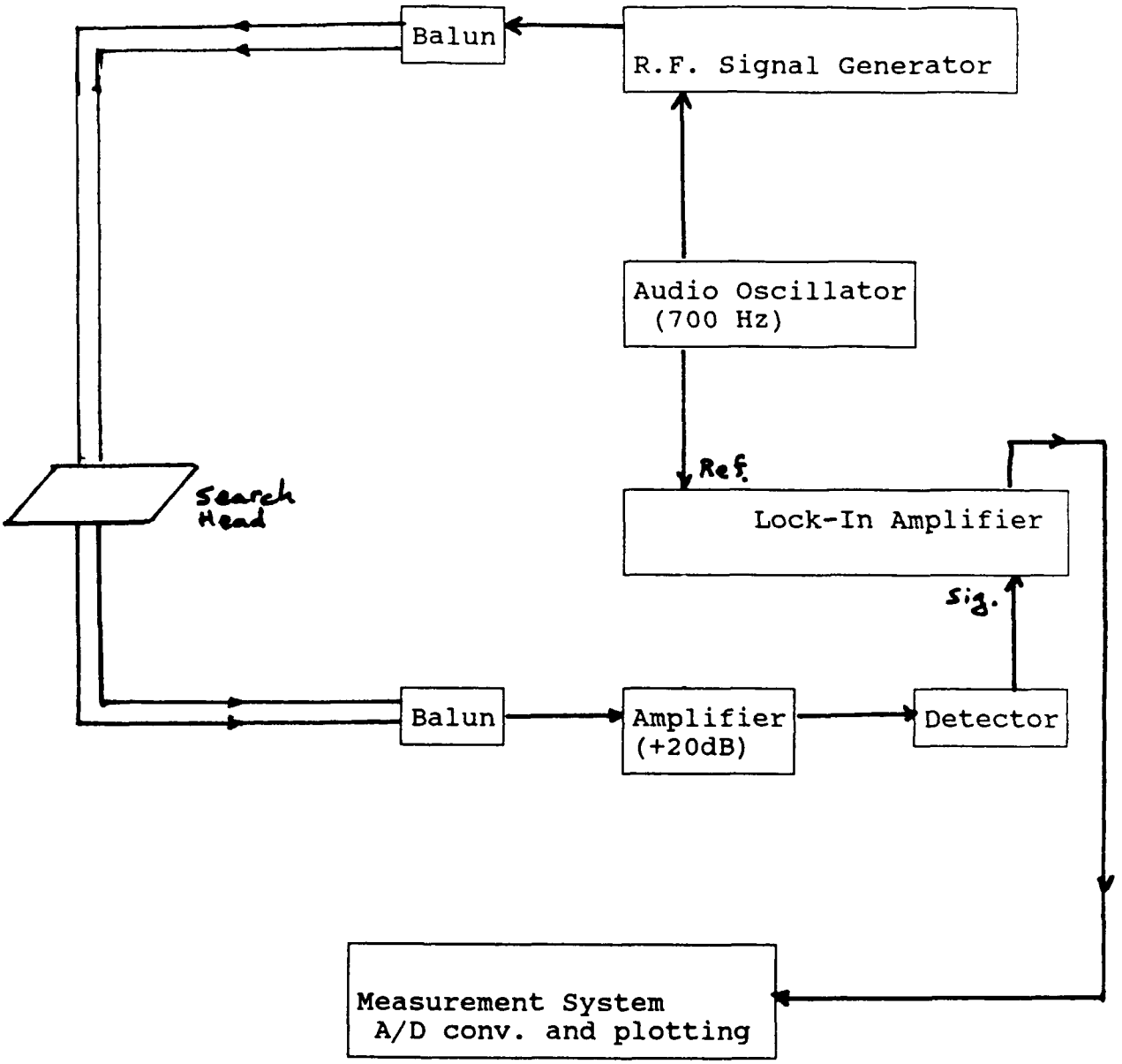

Figure 3.5 Block diagram for the AN/PRS-7 brassboard detector.

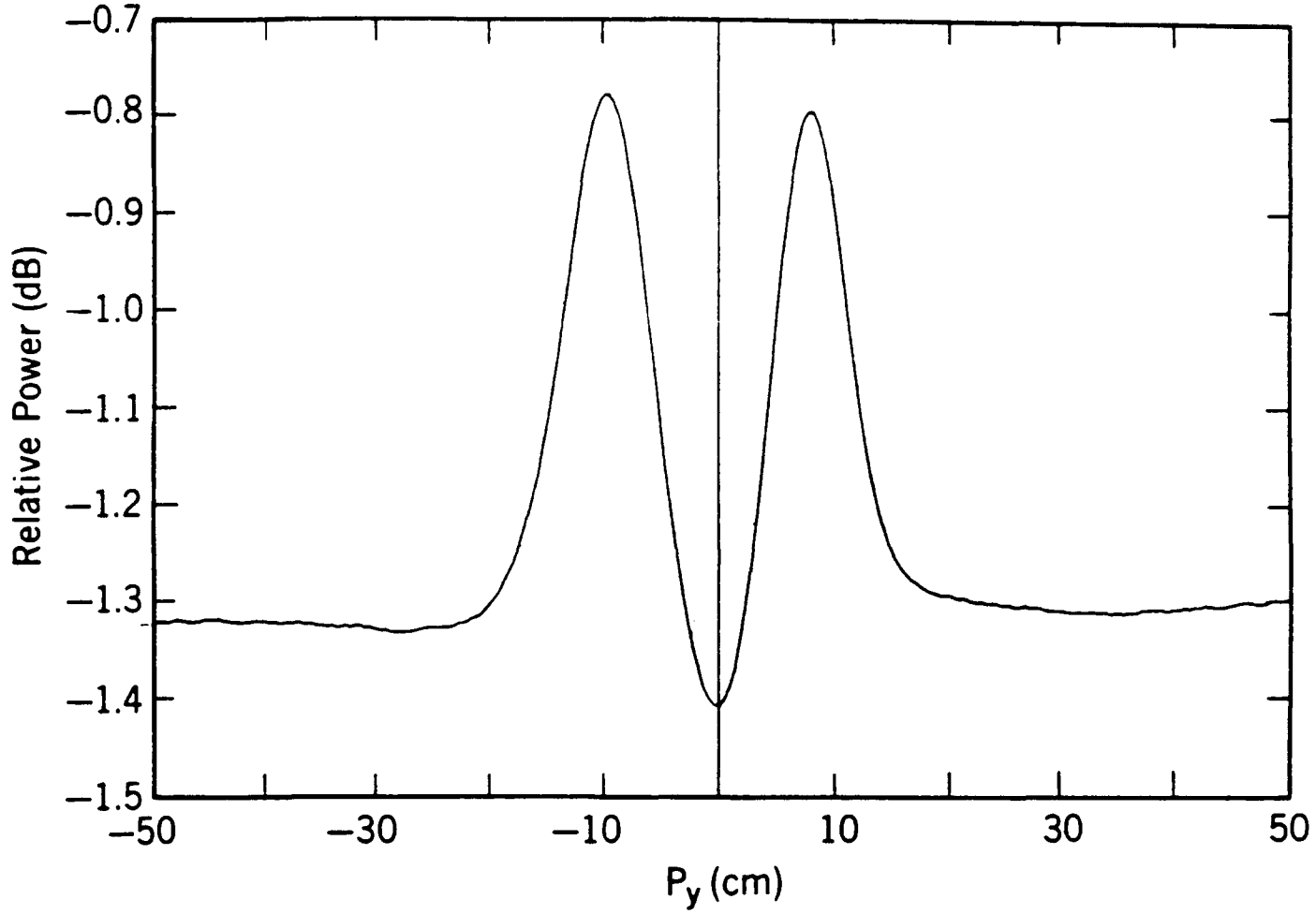

Figure 3.6 Experimental sweep curve for the AN/PRS-7.
Target: nylon sphere (in free space).
Frequency: 432 MHz.

IV. TARGET STANDARDS

A. Introduction

"Standard" targets should have certain desirable characteristics -- such as stability over time, reproducibility, and ease of fabrication. Unfortunately, some approaches to standardization involve particularly high costs; this tends to limit the use of good standards to a few well equipped laboratories. We distinguish two classes of standards:

1) standards based on some well established theory or on known, immutable physical properties, and

2) artifact standards which are reproducible and stable but for which a good theoretical model does not yet exist.

An example of the first class of standard is the voltage standard based on the ac Josephson effect. An example of the second class of standard is the standard Weston cadmium cell. The electromotive force produced by a Josephson junction irradiated at microwave frequencies can be precisely predicted from the theory of quantum electrodynamics (QED). A Weston cell yields an EMF of 1.01186 v, depending somewhat on its age and how it was made.

Where possible, we specify that testing of mine detectors be carried out with metallic and nonmetallic targets fabricated from pure or well analyzed materials. We also suggest that targets have simple cylindrical or spherical shapes. When, for purposes of realistic modeling, other target shapes and components must be used, at least the primary standards should be cylindrical or (preferably) spherical. Good theoretical models for the scattering of electromagnetic waves are available for these simple shapes. Also, the detection of spherical targets is not sensitive to target orientation. Furthermore, we suggest that the primary standard targets be molded or machined of single component materials without voids or simulated firing mechanisms. This can aid in further reducing the number of variables. Oxidation, water adsorption, and any surface or dimensional changes of the targets should be carefully monitored or entirely avoided if possible.

B. Metallic Standards

Testing metal detectors has traditionally involved checking whether they can succeed in finding an ordinary U.S. one-cent coin buried in various soils. This nicely illustrates one of the pitfalls of using artifact standards. The Government started minting copper-clad zinc pennies in October 1982. The weight of the coin decreased from approximately 3.1 g to approximately 2.55 g. To our knowledge, the copper alloy used is chosen on the basis of its durability -- its conductivity is not controlled. For careful work, avoid using ordinary coins as standard targets.

Objective testing of metal detectors can best be carried out with a set of known, repeatable metallic targets. Low frequency metal detectors transmit in the kilohertz range and sense eddy currents induced in buried metallic objects. The magnitude of these eddy currents varies as the -1/2 power of the conductivity of the target material and is directly proportional to target volume for simple shapes such as cylinders or spheres. It is important, when describing how these targets are made or copied, to specify the conductivity of the material. Certain materials, such as brass or aluminum alloys, exhibit very different conductivities depending on their composition and heat treatment. Highly purified elemental metals, especially those with the highest conductivity, show very little variation in conductivity from lot to lot. A further advantage is that their conductivity varies only slightly with changes in room temperature so this effect can be neglected when testing metal detectors. Accordingly, suitable standard test objects should have high conductivity. In increasing order of conductivity, this means gold, copper, or silver. We chose copper since it is the least expensive. "Five nines" purity electro-refined copper is readily available. The American Society of Metallurgists (ASM) of Metals Park, Ohio, lists the properties of various grades of wrought copper on page 248 of the 1981 edition of the Metals Handbook. Oxygen-free, electro-refined copper has a conductivity of 5.977×10^{-7} S/m at 20°C. The conductivity varies with temperature according to the formula:

$$\sigma = (5.977 \times 10^{-7})/(1 + \alpha T) \text{ S/m},$$

where $\alpha = 0.0068$,

and T = the positive or negative offset in °C from the reference temperature of 20°C.

The coefficient α for the change in resistivity with temperature is sufficiently small that corrections for the detectibility of copper targets at elevated temperatures (as in direct sunlight) are probably unnecessary.

Copper corrodes easily. We spray our copper test objects with a thin coating of spray laquer. If considerable wear and handling is likely to take place, a hard chromium plating over a nickel plating would be appropriate for these targets.

A set of seven copper cylindrical test objects were provided to the Countermine Technology Division at Ft. Belvoir in July 1986. The weights and other specifications are given in Table 4.1.

TABLE 4.1
Copper Test Objects

Material: Copper, electro-refined, 99.999% pure
Shape: Right-circular cylinders, diameter is twice the height
Density: 8.96 g/cm^3

Weight (g)	Diameter (mm)	Height (mm)
1	6.58	3.29
2	8.28	4.14
4	10.44	5.22
8	13.15	6.58
32	20.87	10.44
128	33.14	16.57
512	52.60	26.30

The smaller objects are suitable for calibrating the response of metal detectors (those operating at frequencies in the kilohertz range) to objects

as small as firing pins. The other objects in this set were provided to test the response of low-frequency metal detectors to significantly larger amounts of metal. Large metal objects (such as unexploded ordnance) must often be located using mine detectors optimized for very small metal objects. Test procedures are discussed in section VII of this report. Eddy currents die out slowly for the case of the large copper targets. Tests of target detectibility with the 32 g and larger cylinders should be performed with due regard for the long time constants involved (on the order of one-half second or more).

In addition to the copper cylinders, which we consider the primary targets for testing purposes, we have fabricated a small set of stainless-steel pins. We consider the pins to be secondary standards, useful for simulating the properties of firing pins in mines. Because of the difficulty of specifying the composition of stainless steel, results using these objects may show greater variability than those using the copper cylinders. The pins should, however, prove useful in tests of the detectors for plastic mines where the orientation of such pins may be important. Specifications for the pins are given in Table 4.2.

TABLE 4.2
Stainless Steel Test Objects

Material: Type 304 stainless steel
Shape: Cylindrical pins or narrow rods
Density: Approximately 7.9 g/cm^3

Weight (g)	Diameter (mm)	Height (mm)
1.56	3.175	25.4
0.39	1.5875	25.4
0.096	0.7938	25.4

All American Iron and Steel Institute (AISI) type 300 series steels are chromium-nickel austenitic steels in grades having up to 30% chromium and up to 20% nickel. Type 304 contains the following percentages:

Cr	.....	18.00 to 20.00
Ni	.....	8.00 to 12.00
C	.....	0.08 (max)
Mn	.....	2.00 (max)
Si	.....	1.00 (max)

The composition range is based on ladel analysis for standard AISI Type 304 as of 1959. It is not a specification. It is a classification which has been agreed upon and used by producers in the United States for grades which have attained an arbitrary annual minimum tonnage [4.1]. We do not recommend 304 stainless steel for the standard targets, although it is useful for secondary standards and for estimating the performance of mine detectors in locating objects such as firing pins.

C. Nonmetallic Standards

We fabricated some Teflon and nylon spheres as calibration targets for nonmetallic mine detectors and delivered these in July 1986. The weights and diameters for these objects are listed in Table 4.3, below.

Teflon and nylon were chosen for these reasons:

(1) nylon and Teflon are relatively impervious to moisture as well as to common alkaline, acidic, or salt components likely to be found in ordinary soils,

(2) these materials are readily available commercially in shapes and sizes suitable for further machining, and

(3) their dielectric constants (2.1 and 3.0) nicely bracket known values for many common explosives.

TABLE 4.3
Spherical Plastic Test Objects

Material:	Nylon	Material:	Teflon
Shape:	Spherical	Shape:	Spherical
Density:	1.15 g/cm^3	Density:	2.2 g/cm^3
Dielectric Constant:	3.0	Dielectric Constant:	2.1
Weight (g)	**Diameter (mm)**	**Weight (g)**	**Diameter (mm)**
36.0	39.0	68.4	39.0
72.0	49.2	136.8	49.2
144.0	62.0	273.6	62.0
288.0	78.2	547.2	78.2
576.0	98.5	1094.4	98.5

We decided to systematically vary the parameter of target volume rather than target weight, specifying five different sizes in each of the two materials. The volumes increase by a factor of 2 for each step up in size.

Discussions about test procedures for plastic mine detectors has focussed on two additional points: (1) the need for still larger test objects, and (2) whether the shape of the test objects could be made to conform more closely to that of known, real mines. We think that, at least for detectability threshold tests, small spheres are most likely to give the best, most repeatable results. Spherical targets do not require careful alignment with the surface of the ground -- only the depth matters. Spherical targets have a well defined radar cross section which does not depend on target orientation. They are also preferred on theoretical grounds, since the EM scattering cross section is well known even when the illuminating wavelength is much smaller than the diameter of the sphere [4.2]. We might wish to compare experimental data on the angular dependence of the scattered field with theory. Of course, nylon and especially Teflon are expensive plastics to use for very large test objects. The third theoretical paper by Hill (Appendix III.C of this report) outlines a method for calculating the scattering cross section for buried

spheres, cylinders, and rectangular parallelopipeds when the dielectric contrast between the target material and the background medium is low. We have fabricated both nylon and Teflon cylindrical targets of various sizes for use as secondary standards. They are similar to the dummy mines of Type I, class B, sizes 1, 2, and 3 [4.3]. However, they do not have air voids or replicas of firing mechanisms installed. Quantities delivered and dimensions for these mine replicas are given in Table 4.4.

TABLE 4.4
Cylindrical Plastic Test Objects

Quantity	Diameter	Height	Material
2	3"	1"	Nylon
2	6"	2"	Nylon
2	12"	3"	Nylon
2	3"	1"	Teflon
2	6"	2"	Teflon
2	12"	3"	Teflon

Certain thermoplastic materials would be useful in this respect, perhaps at least for secondary standards. An advantage of thermoplastic materials is that they can be cast, rather than machined, and that little additional finishing would be required. Also, testing the electromagnetic properties of such materials would be simpler (since wafers and/or coaxial shapes required for these tests could likewise be obtained without the requirement for any machining).

We have identified two thermoplastic materials which we think would make suitable test objects. One of these is amorphous sulfur with a dielectric constant of 3.65 and a melting point of 113°C. The other is paraffin with a dielectric constant of approximately 2.3 and a melting point of 37°C. Sulfur of adequate purity, uncontaminated with other material of different electromagnetic properties, is readily available. A suitably pure paraffin wax, for

which we could be sure that the properties were the same from lot to lot, would be the organic compound known as eicosane (a saturated, open-chain, acyclic hydrocarbon with a molecular weight of 282.54). The dielectric constant for this material is 2.25. Eicosane (99% pure) costs less than $30.00 per pound in small quantities.

D. Relationship of Standards to Realistic Targets

D1. Metallic Objects Relationships

For low-frequency treasure finders and metallic mine detectors, the tests with the cylindrical copper targets are more than adequate to establish detector sensitivity and other performance requirements. The response of low-frequency equipment (operating in the kilohertz range) shows little if any dependence on target orientation even for targets which are highly acicular (needlelike). The situation is very different for equipment operating at microwave frequencies, where polarization effects become important. When testing the ability of plastic object detectors to locate, say, metallic firing pins, target orientation must be carefully controlled for the resulting data to be useful and repeatable. In particular, the targets listed in Table 4.2 are likely to exhibit very different radar cross sections when placed parallel or perpendicular to the E-field of an operating AN/PRS-7.

D2. Nonmetallic Object Relationships

The primary plastic standard targets listed in Table 4.3 were delivered to Ft. Belvoir in July 1986. The secondary standards listed in Table 4.4 were delivered in August 1988. The materials from which these targets were machined were chosen to approximate the range of dielectric permittivities likely to be encountered in real mines. These targets (perfectly spherical or perfectly cylindrical) scatter electromagnetic waves in a very predictable fashion. An analytic solution for spherical objects is well known [4.2, 4.4]. Good approximations are available for the scattered fields from cylindrical objects [4.5]. The targets we have provided cover the range from anti-tank to smaller than anti-personnel. However, these standards do not mimic all features of real mines. Typical mines and mine replicas contain air voids,

firing mechanisms, pull rings, and other accessories which significantly modify the radar cross section. The Countermine Technology Division at Ft. Belvoir has made arrangements for the manufacture of a number of mine-like targets to address this issue [4.3]. Such targets cannot simultaneously satisfy two divergent requirements: (a) complete properties of real mines, and (b) precision in detector performance measurement and test repeatability. Realistic mine replicas possess radar cross sections which vary with changes in temperature and barometric pressure. Their nonuniform filler separates into layers or even deteriorates over time. Air voids (and light-weight foam inserts to simulate voids) distort or change shape permanently. Nevertheless, they are interesting test objects which certainly look like mines; it should be possible to use them as secondary or tertiary standards so long as their radar cross sections are frequently compared with those of the primary standards. We have not yet been given any of these generic mines. We look forward to comparing them with our standards at some future date.

The detection of buried, nonmetallic objects is a difficult task [4.6]. As we have seen, their typically low contrast ratio in sandy soil or loam leads to their becoming nearly invisible to electromagnetic waves. Because of their small size, carefully made anti-personnel mines (those without air voids or metal pins) are often completely undetectable with present-day equipment.

E. NIST Recommendations and Conclusions

Accurate testing of treasure finders and mine detectors is notoriously difficult. When performance tests are carried out, the degree to which meaningful, repeatable data can be obtained is critically dependent on the targets being used. At UHF and higher frequencies, target orientation must also be carefully established unless the targets are spherical. What follows are NIST's recommendations for target standards that should be used to test metal detectors and nonmetallic object detectors.

E1. Targets for Metal Detector Testing

It is difficult or impossible to obtain consistent results with mine replicas or coins. The coated pure copper standards that NIST has provided to the Army should be used as primary standard targets for the testing of

low-frequency metal detectors; their permeability and conductivity are known very accurately and their masses and volumes have been carefully controlled. For more realistic target detection testing, the Type 304 stainless steel cylinders that have also been provided to the Army should be used. Although the permeability and conductivity are not known to the accuracy of the copper standards, they should prove sufficiently accurate and repeatable for all but the most demanding tests.

E2. Targets for Nonmetallic Object Detector Testing

Sets of standard spherical and/or cylindrical nylon and Teflon targets should be utilized for the most accurate tests of nonmetallic object detectors. Several of these have been provided to the Army by NIST. The spherical standards should be used whenever errors due to target orientation must be avoided in the tests. The cylindrical standards, being somewhat more realistic in shape, should suffice for the majority of the tests as described in chapter VII. The principal reason that NIST recommends the use of these targets for most of the tests is that they are homogeneous, have well known constituent electromagnetic properties, and, most important for theoretical modeling purposes, have known scattered electromagnetic field signatures. As is stated in chapter VII, these standards do not preclude using more realistic mine replicas as targets for other tests.

For a more robust testing strategy, NIST recommends fabricating targets using the same rigid-matrix technology as is being proposed for soil standards. With little additional effort, standard targets can be molded with known electromagnetic properties that can cover a wide range of values. Thus, for example, targets for a set of tests to measure permittivity contrast ratio could be constructed with incrementally varying permittivity. Using the nylon or Teflon targets, on the other hand, would require varying the permittivity of the soil standards which would be more difficult and expensive as well as less realistic. In addition, using this technology would allow the fabrication of extremely realistic mine replica targets with such features as air gaps, inhomogeneities (explosives with a plastic shell, for example), and firing pins.

References (IV)

[4.1] Metals Handbook, vol. 1, 8th Edition, p. 408, (1961), American Society of Metallurgists.

[4.2] Mie, G. Amalen der Physik 25, p. 377, (1908).

[4.3] Brown, D. et al. Mine Detector Targets, VSE Corp. Report ASD/0047-87/35RD, (October 1987).

[4.4] Van deHulst, H. C. Light Scattering by Small Particles, N.Y.: J. Wiley & Sons, 1957.

[4.5] Hill, D. A. Electromagnetic Scattering by Buried Objects of Low Contrast, IEEE Trans. Geosci. Remote Sensing GE-26, pp. 195-203 (1988).

[4.6] Pear, Robert. Returning Afghan Refugees Face Peril of Millions of Land Mines, NY Times, 13 August 1988.

V. SOIL STANDARDS

A. Typical Electromagnetic Properties of Real Soils

Knowledge of the electromagnetic properties of typical real soils is necessary before it is possible to identify candidate methods for realizing soil standards. Several cases may be listed and generally characterized in terms of conductivity and permittivity contrasts as representative of the differing electrical environments likely to be encountered in either plastic or metallic mine detection.

Case 1: Dry Beach Sands (Plastic Mine Detection)

One type of host soil environment is that in which either no pore water or very little pore water (water saturation Sw < 0.01) exists within a magnetically impermeable, unconsolidated, and electrically resistive soil grain matrix having low cation exchange capacity. Such a situation exists in a dry beach sand or dry gravel host medium and probably presents the most difficult plastic mine detection test environment.

The host soil conductivity, σ_H, in this case is generally low ($\sigma_H \leq 10^{-3}$ S/m) and the host dielectric constant, ϵ_H', is low and probably less than the target (mine) dielectric constant ($\epsilon_H' = 2.70$ when referenced to dry sand consisting of clean quartz grains having diameters greater than 0.03 mm but less than 0.60 mm where the water saturation, Sw, is 0 and the frequency is 300 MHz). If we take a nylon sphere as representative of our plastic mine target (where the target conductivity, σ_T, is much less than 10^{-3} S/m and the target dielectric constant, ϵ_T', remains fixed at 3.00), then $\epsilon_H'/\epsilon_T' \doteq 0.90$ and $\sigma_H/\sigma_T \doteq 1$.

Case 2: Wet Fresh Water Beach Sands (Plastic Mine Detection)

This situation is characterized by moderately fresh (deionized) pure water saturation (Sw $\doteq$ 0.14) in a magnetically impermeable, unconsolidated, and electrically resistive ($\sigma_H \leq 10^{-3}$ S/m) soil grain matrix of low cation exchange capacity. Due to increased water saturation, the host soil

dielectric constant at a typical UHF detection frequency of 300 MHz would be approximately 10, leading to dielectric and conductivity ratios of $\epsilon'_H/\epsilon'_T \doteq 3.3$ and $\sigma_H/\sigma_T \doteq 1$. Because of the higher permittivity contrast at the chosen operating frequency, this case probably presents a less difficult detection test than Case 1.

Case 3: Wet Clay Soils and Wet Marine Beach Sands (Plastic Mine Detection)

The wet clay soil environment is characterized by highly brackish or saline pore water saturation ($Sw \geq 0.20$) in a magnetically impermeable, unconsolidated, and electrically conductive soil grain matrix of high cation exchange capacity. In such a case, both the measured host soil conductivity and host soil dielectric constant at 300 MHz are relatively high ($0.1\ S/m \leq \sigma_H < 1\ S/m$ and $\epsilon'_H \doteq 20$); this leads to significant dielectric and conductivity ratios where $\epsilon'_H/\epsilon'_T \doteq 6.7$ and $\sigma_H/\sigma_T >> 1$ for a nylon spherical target. Such a situation is likely to be that most commonly encountered; therefore it is one which should be simulated in any validation testing.

These electrical properties would also characterize a magnetically impermeable, unconsolidated, and electrically resistive soil grain matrix of low cation exchange capacity having highly saline pore waters, such as might be encountered in wet marine beach sands. All other factors being equal, target visibility in terms of dielectric contrast is greatest for this case; but because of the conductive (lossy) nature of the host medium, test target detection at increasing depths of burial for UHF operating frequencies is expected to be sharply limited.

Case 4: Magnetically Impermeable Host Soils (Metal Mine Detection)

Because the contrast in conductivity between a metallic mine target in either an electrically resistive dry beach sand or an electrically conductive wet clay remains very high (for analysis purposes, infinite), and because most metal mine detectors operate in the VLF region (affording little attenuation for expected burial depths) and sense secondary magnetic fields due to induced eddy currents within the buried mine, two test soils would seem to bracket those situations commonly encountered in the field. These are a magnetically

impermeable or magnetically permeable host medium. The magnetically impermeable host soil may be simulated by quartz sand grains having no magnetite-ilmenite, which are the common naturally occurring magnetic minerals [5.1]. Hence, the host soil medium in this case would have a magnetic permeability, μ_H, equal to that of free space, μ_0 ($4\pi \times 10^{-7}$ H/m). Conductive losses in the host medium can be controlled either by adding known amounts of saline pore water or aluminum powder.

Case 5: Magnetically Permeable Host Soils (Metal Mine Detection)

Attenuation rates for a plane electromagnetic wave in a uniform, magnetically permeable earth are greater than in a uniform, magnetically impermeable earth -- all other factors being equal. In fact, the plane-wave skin depth (distance within the earth at which amplitudes of the electric and magnetic field vectors are equal to $1/e = 0.3679$ of their respective values at the surface) of a magnetically permeable host soil decreases by $(\mu_r\mu_0)^{-\frac{1}{2}}$ where μ_r is the relative permeability and μ_0 is the permeability of free space or vacuum. The U.S. Army Belvoir Research and Development Center (BRDC) already has a test lane simulating this case that consists of a silica sand magnetite mixture (70 percent dry sand, 30 percent magnetite grains, -30 mesh size) whose relative magnetic permeability was measured and found to be 1.35 [5.1]. Because not all metallic land mine detectors employ ground signal removal techniques, a logical test procedure for evaluating differing systems would be to simulate both Case 4 and 5 in the test lane environment. See Table 5.1, below, for a list of the magnetic susceptibility of naturally occurring rocks and minerals.

Table 5.1
Magnetic Susceptibility of Rocks and Minerals (from Reference [5.2])

Magnetic Minerals	Susceptibility $k/4\pi$ (SI)
Magnetite Crystals	6.3 to 24.0
Magnetite	0.04 to 2.0
Ilmenite	0.03 to 0.14
Franklinite	0.036
Pyrrhotite	0.007 to 0.028
Specularite	0.003 to 0.004
Chromite	0.002
Major Rock Types	
Basic Effusive	0.001 to 0.004
Basic Plutonics	>0.0001 to <0.004
Granites and Allied Rocks	>0.0001 to <0.001
Gneisses, Schists, and Slated	>0.0001 to <0.001
Sedimetaries	>0.0001 to <0.001
Specific Rock Types	
Igneous Rocks	
Basalt	0.00068 to 0.0063
Diabase	0.000078 to 0.0042
Gabbro	0.00044 to 0.0041
Granite	0.00003 to 0.0027
Porphyry	0.000023 to 0.0005
Metamorphic Rocks	
Serpentine	0.00025 to 0.014
Slate	0.000039 to 0.0030
Gneiss	0.00001 to 0.0020
Schist	0.000026 to 0.00024
Sedimentary Rocks	
Shale	0.00004 to 0.0005
Clay	0.0002
Sandstone	0.000005 to 0.000017
Dolomite	0.0000009 to 0.000014
Limestone	0.000004
Iron Ores and Minerals	
Siderite	0.0001 to 0.003
Limonite	0.0001 to 0.0002
Hematite	0.00004 to 0.0001
Ankerite	0.00002 to 0.0001

Table 5.1
Magnetic Susceptibility of Rocks and Minerals (from Reference [5.2]) (Cont.)

Typical Sulfide Minerals	Susceptibility $k/4\pi$ (SI)
Arsenopyrite	0.000005 to 0.0002
Chalcopyrite	0.000005 to 0.0002
Chromite	0.000005 to 0.0002
Markasite	0.000005 to 0.0002
Pyrite	0.000005 to 0.0002
Diamagnetic Minerals and Rocks	
Anhydrite and Gypsum	-0.0000011 to -0.00001
Quartz	-0.0000011 to -0.0000012
Sylvite	-0.0000009 to -0.0000011
Calcite	-0.0000006 to -0.0000010
Rock Salt	-0.0000004 to -0.0000013

B. Dielectric Mixing Rules

Soils are mixtures of minerals that are the weathered by-products of rocks. Usually, natural soils contain some water so the way in which dielectric constants combine is important in determining the bulk, or effective, dielectric constant of the soil at hand. The bulk dielectric constant of any soil (whether natural or synthetic) determines the electromagnetic visibility of buried land mines and, therefore, intrinsically affects the performance of any detection system. Once a range of suitable dielectric background characteristics, relatable to conditions actually encountered in the field, is accepted, mixing rules provide the easiest and most pragmatic approach to specification of standard test soils.

Geyer [5.3] has noted that some mixing rules have little broadband applicability for soils since they are based on systems where little or no conduction takes place. For example, when one of the components in a composite dielectric is conductive, large (frequency-, temperature-, and salinity-dependent) polarizations can occur that can be attributed to interfacial polarizations at the boundaries of the conductive phase. A mixing rule that does not account for these interfacial polarizations has little broadband

applicability. Despite the fact that most mixing rules fail in a broadband sense (since they do not account for all relaxation effects), it is nonetheless useful to be able to predict the effective electromagnetic properties of soils of different lithologies and porosities even over narrower frequency ranges -- 100 MHz to 2 GHz in this case -- that affect the signal levels measured by UHF land mine detection systems.

The purpose of a mixing rule is to allow estimation of the dielectric properties of a soil (either test standard or soil encountered in the field) when given measurements of that soil's physical properties only. Its usefulness will be limited by its dependence on adjustable soil- and frequency-specific parameters. An efficacious mixing rule, then, will provide a convenient means for predicting a test soil's dielectric behavior in microwave land mine performance testing and in signal level determination. It will also provide a physically based mixing model that is dependent on measurable soil parameters and can be used for subsequent development and research.

Generally, all materials can be classified into one of three dielectric groups. The first of these, to which pure water and ice belong, is homogeneous substances. A second group, in which ionic salts are dissolved in solution (usually water) is electrolytic solutions. The third group, heterogeneous mixtures, includes that of wet, lossy soils or multicomponent (lossy or nonlossy) media of interest here for test soil lanes. The merits of any chosen background material (standard) for mine test lanes depend not only on correlation with actual field conditions likely to be encountered but also on the ease with which its (complex) dielectric properties can be predicted and controlled for the operational frequency range of interest.

B1. Function-Theoretic Rules

In general, the average dielectric constant of a heterogeneous mixture consisting of two or more substances is related to the dielectric constants of the individual substances, their volume fractions, their spatial distributions, and their orientations relative to the direction of the incident electric field vector [5.4]. In order to determine the functional dependence of the average dielectric constant of a mixture to these variables, the average electric field within the mixture as a whole must be related to the

electric fields within the inclusions [5.5]. The problem is that if the inclusions are randomly dispersed throughout the host medium, it is not generally possible to derive an exact solution for the fields within the inclusions since the mutual electromagnetic interactions of the inclusions are dependent on their positions with respect to each other. Tinga [5.6] gives a review of various approximations that have been proposed for solving the interaction problem. These approximations vary from those that ignore short-range interactions between inclusions (by restricting the validity of the dielectric mixing model to only those mixtures characterized by a low concentration of inclusions) to relations that account for first-order inclusion interactions by the solution of Maxwell's equations and appropriate boundary conditions [5.6, 5.7]. In all cases, the dimensions of the inclusions are much smaller than the propagation wavelength in the host medium. Böttcher [5.8] gives a comprehensive review of dielectric mixing models that includes both empirical (or semi-empirical) formulations for specific mixtures as well as theoretical models developed for highly specialized media that contain either ellipsoidal particle inclusions (spheres, disks, needles) or confocal ellipsoidal spheroids.

B2. Generalized Heuristic Rules for Soil Mixtures

Natural soils are mixtures of matrix minerals, air, and water. As noted in [5.3], water in the pore spaces of surface soils consists of two phases. One of these phases is the bulk (free) pore water. The other is adsorbed water that is adjacent to the matrix grain surfaces and usually several molecular layers thick. This adsorbed water is called surface (or bound) water. The saturation level at which the dielectric constant becomes less sensitive to water saturation is entirely a function of the amount of surface water in soil pore spaces; this explains the dependence of the dielectric constant on soil texture types (particle size and shape distributions) as well as on the intrinsic porosity of the soil mixture. Of course, the porosity is simply related to the bulk density, and the degree of conductive loss responsible for electromagnetic wave attenuation is dependent on the salinity of the pore water which, in turn, depends quite naturally on both the matrix cation exchange capacity and the soil temperature. The fact that the electrical

properties of water-saturated soils are frequency dependent is also not physically surprising since we expect polarization, that is, the orientation of polar molecules (molecules with asymmetric charge distributions), to occur in an applied electric field. The mobility of any polar molecule (such as water) will always depend on the time rate of variation of that field.

Bound water adsorbed to a solid surface has a dielectric response significantly different from that of free water. This is so because the molecular mobility of the water molecules has been reduced by physical bonding to the matrix grain surfaces [5.9, 5.10, 5.11]. Most of the measurement evidence to date seems to indicate that the restricted mobility causes a reduction of the static dielectric constant of water adsorbed to the surface from 80 for free water to about 6 for sorped water [5.10] which is greater than an order-of-magnitude reduction. Furthermore, surface-bound water exhibits a relaxation frequency of about 10^4 Hz instead of 100 GHz, which is seven orders of magnitude lower than that of bulk water [5.3, 5.12].

Such observations have led McCafferty and Zettlemayer [5.11] to suggest that dielectric dispersion in the VLF region in systems composed of a solid and adsorbed water may principally be due to relaxation of the adsorbed water. However, an equally plausible explanation is that conductivity inhomogeneities in a soil matrix are responsible for dielectric dispersion and it is not the rotational mobility of water molecules in the surface water that is important, but rather the conductivity of the surface layer [5.13, 5.14].

Thus the most general form of a heuristic, predictive dielectric mixing rule that might be used for soil specifications would separate the volumetric percentages of bound and free water. The soil mixture is then described electrically as a four-component system whose constituent components are linearly combined in terms of the respective volume fractions as

$$\epsilon_{soil}^{\alpha} = v_m\epsilon_m^{\alpha} + v_a\epsilon_a^{\alpha} + v_{bw}\epsilon_{bw}^{\alpha} + v_{fw}\epsilon_{fw}^{\alpha} , \qquad (5.1)$$

where v represents volume fraction; the subscripts m, a, bw, and fw represent soil matrix, air, bound water, and free water; and α is a constant.

Here we recognize that

$$\phi \;=\; \text{total porosity} \;=\; (\rho_m - \rho_b)/\rho_m \;=\; 1 - \rho_b/\rho_m \;,$$

where ρ_m and ρ_b denote the matrix (solid material) and bulk (air, water, material mixture) density, respectively, and,

$$\begin{aligned} v_m &\equiv 1 - \phi \\ v_a &\equiv \phi - Sw \\ Sw &= v_{bw} + v_{fw} \;. \end{aligned} \tag{5.2}$$

The two terms involving bound and free water are often combined into a single term with an empirically determined multiplicative factor of the free water permittivity in the soil [5.15]. That is,

$$v_{bw}\epsilon_{bw}^{\alpha} \;+\; v_{fw}\epsilon_{fw}^{\alpha} \;\doteq\; Sw^{\nu}\,\epsilon_{fw}^{\alpha} \;, \tag{5.3}$$

where the exponent, ν, of total water saturation, Sw, is empirically derived.

Substituting eqs. (5.2) and (5.3) into (5.1) and recognizing that $\epsilon_a^{\alpha} \equiv 1$ yields the following relation in terms of porosity and water saturation

$$\epsilon_{soil}^{\alpha} \;=\; (1 - \phi)\,\epsilon_m^{\alpha} \;+\; \phi - Sw \;+\; Sw^{\nu}\,\epsilon_{fw}^{\alpha} \;. \tag{5.4}$$

In terms of the bulk and soil matrix densities, eq. (5.4) may be written

$$\epsilon_{soil}^{\alpha} \;=\; (1 - 1 + \rho_b/\rho_m)\,\epsilon_m^{\alpha} \;+\; 1 - \rho_b/\rho_m \;+\; (Sw^{\nu}\,\epsilon_{fw}^{\alpha} - Sw)$$

or

$$\epsilon_{soil}^{\alpha} \;=\; 1 \;+\; \frac{\rho_b}{\rho_m}\,(\epsilon_m^{\alpha} - 1) \;+\; (Sw^{\nu}\,\epsilon_{fw}^{\alpha} - Sw) \;, \tag{5.5}$$

where $\rho_b/\rho_m = v_m/v_b$ is the soil matrix volume fraction.

For $\alpha = 1$, eq. (5.5) is known as a <u>linear</u> model; for $\alpha = 1/2$ as a <u>refractive</u> model (since $\epsilon^{1/2} \equiv n$ is the refractive index); and for $\alpha = 1/3$ as the <u>cubic</u> model.

The results of over 500 measurements made by Dobson, et al. [5.15], on five differing soil types at nine frequencies (from 4.0 GHz to 18 GHz) and for volumetric moistures, Sw, ranging from 0.01 to total saturation gave values of ν between 1.0 and 1.16 and suggested a refractive model ($\alpha = 1/2$) as most suited for soil-water mixtures. This was observed earlier by Shutko and Reutov [5.16]. Hence $Sw^{\nu} \doteq Sw$ and

$$\epsilon_{soil}^{1/2} \doteq 1 + \frac{\rho_b}{\rho_m} (\epsilon_m^{1/2} - 1) + Sw\ (\epsilon_{fw}^{1/2} - 1) . \qquad (5.6)$$

Combining the effects of bound and free water into one term (eq. (5.3)) reduces the implicit dependence of ϵ_{soil} on soil type [5.4]; this is not surprising since clays are expected to have more bound water than, say, sand grains. In general, however, ϵ_{soil} and ϵ_{fw} in eq. (5.6) are complex quantities, since attenuative loss due to electrolytic conduction is fundamentally implicit in natural soils and therefore must be incorporated into test lane soils for realistic performance testing. In fact, the loss tangent of soil pore water, which depends on salinity (and temperature), is essentially an in situ parameter and cannot be ascertained correctly by pore fluid extraction. These complicating facts will be addressed below.

B2.1 Dry Soil Mixture

For a dry soil mix eq. (5.6) simplifies to

$$\epsilon_{soil}^{1/2} = 1 + \frac{\rho_b}{\rho_m} (\epsilon_{matrix}^{1/2} - 1) \qquad (5.7)$$

since $Sw \equiv 0$. Or, in terms of the porosity ϕ of the soil mix,

$$\epsilon_{soil}^{1/2} = (1 - \phi)\ \epsilon_{matrix}^{1/2} + \phi\ \epsilon_{air}^{1/2} \qquad (5.8)$$

or

$$\epsilon_{soil}^{1/2} = (1 - \phi)\ \epsilon_{matrix}^{1/2} + \phi ,$$

since $\epsilon_{air}^{1/2} = 1 - j0$. In this case the soil mixture will have a real dielectric constant (or exhibit no conductive losses). Therefore, essentially

no electromagnetic attenuation will be imposed on field behavior by the background soil medium in the frequency range of interest and detection systems operating at higher relative frequencies would be expected to perform best, all other factors being equal [5.3]. Examples of dielectric, nonlossy test soils are dry sands (SiO_2 or SiC). Frequency-domain measurements of the dielectric constant on these soils have been reported previously [5.3].

B2.2 Lossy, Fluid-Saturated Soils

For lossy, fluid-saturated soils the dielectric mixing rule becomes more complicated since both the bulk soil mixture and the pore water become electrically lossy and attenuate electromagnetic fields. In this case the electromagnetic fields of a mine detection system operating at a higher relative frequency would suffer greater attenuation. If the effective skin depth is too small relative to the burial depth of a buried mine, the detection system would perform more poorly than a system operating at a lower frequency. There are two cases to consider: one where background soils are only partially water saturated and the other where soils are fully saturated.

B2.2.1 Partially-Saturated Soil Mixtures

The complex dielectric constant of the soil may be written

$$\epsilon_{soil}^{1/2} = (1 - \phi)\, \epsilon_{matrix}^{1/2} + (\phi - Sw)\, \epsilon_{air}^{1/2} + Sw\, \epsilon_{water}^{1/2}, \qquad (5.9)$$

where

$$\epsilon_{matrix}^{1/2} = \sqrt{\epsilon'_{matrix}} \quad \text{(nonlossy)},$$

$$\epsilon_{air}^{1/2} \equiv 1 \quad \text{(nonlossy)},$$

$$\epsilon_{water}^{1/2} = [\epsilon'_{water} - j\, \epsilon''_{water}]^{1/2} \quad \text{(lossy)}, \qquad (5.10)$$

$$= [\epsilon'_{water}\, (1 - j\, \tan\delta_{water})]^{1/2}, \quad \tan\delta_{water} \equiv \frac{\epsilon''_{water}}{\epsilon'_{water}},$$

and

$$\epsilon^{1/2}_{soil} = [\epsilon'_{soil} - j\,\epsilon''_{soil}]^{1/2} \qquad \text{(lossy)}$$

$$= [\epsilon'_{soil}\,(1 - j\,\tan\delta_{soil})]^{1/2}, \quad \tan\delta_{soil} \equiv \frac{\epsilon''_{soil}}{\epsilon'_{soil}} .$$

Use of the half-angle relation

$$\tan\delta = \frac{2\,\tan\,\delta/2}{1 - \tan^2\,\delta/2}$$

allows a complex dielectric constant $\epsilon = \epsilon'\,(1 - j\,\tan\delta)$ to be written as

$$\epsilon^{1/2} = \frac{\sqrt{\epsilon'}}{(1 - \tan^2\frac{\delta}{2})^{1/2}}\,(1 - \tan^2\frac{\delta}{2} - 2j\,\tan\frac{\delta}{2})^{1/2}$$

$$= \frac{\sqrt{\epsilon'}}{(1 - \tan^2\frac{\delta}{2})^{1/2}}\,[(1 - j\,\tan\frac{\delta}{2})^2]^{1/2} \qquad (5.11)$$

or

$$\epsilon^{1/2} = \frac{\sqrt{\epsilon'}}{(1 - \tan^2\frac{\delta}{2})^{1/2}}\,(1 - j\,\tan\frac{\delta}{2}) .$$

Use of eqs. (5.11) and (5.10) in (5.9) then yields

$$\frac{\sqrt{\epsilon'_{soil}}}{(1 - \tan^2\frac{\delta_{soil}}{2})^{1/2}}\,(1 - j\,\tan\frac{\delta_{soil}}{2}) = (1 - \phi)\,\sqrt{\epsilon'_{matrix}} + (\phi - Sw)$$

$$+ \frac{Sw\,\sqrt{\epsilon'_{water}}}{(1 - \tan^2\frac{\delta_{water}}{2})^{1/2}}\,[1 - j\,\tan\frac{\delta_{water}}{2}] .$$

Separating real and imaginary parts yields

$$\frac{\sqrt{\epsilon'_{soil}}}{(1 - \tan^2 \frac{\delta_{soil}}{2})^{1/2}} = \sqrt{\epsilon'_{matrix}} + \phi (1 - \sqrt{\epsilon'_{matrix}}) - Sw + \frac{Sw \sqrt{\epsilon'_{water}}}{(1 - \tan^2 \frac{\delta_{water}}{2})^{1/2}} \quad (5.12)$$

and

$$\frac{\sqrt{\epsilon'_{soil}} \tan \frac{\delta_{soil}}{2}}{(1 - \tan^2 \frac{\delta_{soil}}{2})^{1/2}} = \frac{Sw \sqrt{\epsilon'_{water}} \tan \delta_{water}/2}{(1 - \tan^2 \frac{\delta_{water}}{2})^{1/2}} . \quad (5.13)$$

Both eqs. (5.12) and (5.13) must be satisfied simultaneously. ϵ'_{soil}, $\tan\delta_{soil}$, and ϵ'_{matrix} are known from measurements. The total porosity, ϕ, and water and air saturations, Sw, and ϕ - Sw, respectively, may be determined by using a value for the water salinity, S, which is based on the cation exchange capacity of the matrix soil type. The dielectric constant of the pore water, ϵ'_{water}, is computed from eqs. (2.17) and (2.20). The loss tangent of the pore water is then calculated from eq. (2.21). Substituting these values and the measured ϵ'_{soil} and tan ($\delta_{soil}/2$) into eq. (5.13) allows the determination of Sw from which the total porosity is computed (eq. (5.12)).

B2.2.2 Saturated Soil Mixtures

A more expedient approach is to relate the complex dielectric constant of the soil mixture to the water-filled porosity ϕ_w so that we may write

$$\epsilon^{1/2}_{soil} = (1 - \phi_w) \epsilon^{1/2}_{matrix} + \phi_w \epsilon^{1/2}_{water} . \quad (5.14)$$

Use of eqs. (5.10) and (5.11) now yields

$$\frac{\sqrt{\epsilon'_{soil}}}{(1 - \tan^2 \frac{\delta'_{soil}}{2})^{1/2}} = (1 - \phi_w) \sqrt{\epsilon'_{matrix}} + \frac{\phi_w \sqrt{\epsilon'_{water}}}{[1 - \tan^2 \frac{\delta_{water}}{2}]^{1/2}} \quad (5.15)$$

and

$$\frac{\epsilon'_{soil} \tan\frac{\delta_{soil}}{2}}{(1 - \tan^2\frac{\delta_{soil}}{2})^{1/2}} = \frac{\phi_w \sqrt{\epsilon'_{water}} \tan\frac{\delta_{water}}{2}}{[1 - \tan^2\frac{\delta_{water}}{2}]^{1/2}} \quad (5.16)$$

Again, ϵ'_{soil}, $\tan\delta_{soil}$, and ϵ'_{matrix} are known from measurements. A value for the salinity, S, of the pore water is then taken. The real part of the pore water permittivity, ϵ'_{water}, at temperature T (°C), is then computed from

$$\epsilon'_{water} = \epsilon'_{wo}(T) - 0.1556 - 4.13 \times 10^{-4} S + 1.58 \times 10^{-6} S^2 \quad (5.17)$$

where

$$\epsilon'_{wo}(T) = 88.045 - 0.4147 T + 6.295 \times 10^{-4} T^2 . \quad (5.18)$$

Next the loss tangent of the pore water is calculated from

$$\tan \delta_{water} = [\epsilon'_{water}]^{-1} [5.66 + 2.65 \times 10^{-3} S - 4.5 \times 10^{-6} S^2] . \quad (5.19)$$

This initial value of $\tan \delta_{water}$ is substituted into eq. (5.15) to determine ϕ_w. A corrected value of $\tan(\delta_{water}/2)$ is determined from eq. (5.16) which is then used to determine a new value for the water salinity and porosity, ϕ_w, until they converge to constant values. This approach is one commonly used in geophysics and reservoir engineering to determine both the water-filled porosity and pore water salinity of rocks from <u>in situ</u> dielectric measurements. For our purposes here, these are the fundamental parameters that allow us to predict, from a mixing relationship, how attenuative a background soil is. The important point is that the complex permittivity (both nonlossy and lossy parts) of the background test medium be the same in performance evaluations of mine detector systems operating at the same frequency. While various synthetic substances can be thought of that can simulate the real field situation of water-saturated soils in terms of the complex permittivity at a single frequency, there are few synthetics which, in combination, can simulate the dielectric behavior of water-saturated soils over a broad range in frequency.

B3. Application to Granular Soil Mixtures

As an application to dielectric property prediction of soil mixtures, consider a two-phase mixture of air and dry sand, where sand consists of washed quartz grains that have diameters ranging from 0.027 and 0.60 mm. Recalling eq. (5.7) we write

$$\epsilon_{soil}^{1/2} = 1 + \frac{\rho_b}{\rho_m} (\epsilon_{matrix}^{1/2} - 1)$$

For this mixture, Geyer [5.3] and Jesch [5.17] have reported a measured mean relative dielectric constant, ϵ'_{soil}, of 2.702 at 300 MHz and for a mean bulk density, ρ_b, of 1.540 g/cm^3. Standard deviations for the relative dielectric constant and mean bulk density were 0.0486 and 0.022 g/cm^3, respectively. Bussey [5.18, 5.19] has reported ϵ' of silica equal to 3.822, measured at 9 GHz with the use of cavity resonators. Von Hippel [5.20] has reported ϵ' of (fused) silica at 25°C and at 300 MHz equal to 3.78. Von Hippel's results show fused silica essentially dispersionless over the frequency range of 100 Hz to 25 GHz, with tan $\delta_{silica} = 0.5 \times 10^{-4}$ at 300 MHz. Clark [5.21] and Morey [5.22] give the matrix density of pure silica, ρ_m, to be 2.203 g/cm^3.

In summary, use of the two-phase refractive dielectric mixing rule yields a predicted relative dielectric constant

$$\epsilon_{soil,\ predicted} = [1 + 0.699\ (\epsilon_{matrix}^{1/2} - 1)]^2$$

$$= [1 + 0.699\ (3.780^{1/2} - 1)]^2$$

$$\epsilon_{soil,\ predicted} = 2.756\ .$$

This result differs by 2.1 percent from observed measurements using an open-ended transmission line with a vector automatic network analyzer. This difference is probably due to impurities in the quartz sand, which would affect both ρ_m and ϵ_{matrix}.

B4. NIST Measurements of Electromagnetic Soil Properties

B4.1 Natural Soils

A large number of dielectric measurements on soils have been made by NIST over the past decade. Jesch [5.17], using frequency domain open-circuit coaxial transmission line techniques (described in detail in Chapter VI), has made dielectric measurements of five different natural soil types. The textural types were sand, sandy loam, silt loam, clay loam, and clay. Sand is defined as washed quartz grains having diameters from 0.027 mm to 0.60 mm, whereas silt is washed quartz grains having diameters between 0.0033 mm and 0.021 mm. The clay used was inorganic (kaolin or bentonite) with plate diameters less than 0.0033 mm.

The soils used by Jesch [5.17] were constructed as follows:

Sand Texture - 9.5 parts sand, 0.5 parts clay, 0.3 parts silt;
Sandy Loam - 6.4 parts sand, 3.6 parts clay, 2.5 parts silt;
Silt Loam - 2 parts sand, 8 parts clay, 6.8 parts silt;
Clay Loam - 3.2 parts sand, 6.8 parts clay, 3.3 parts silt; and
Clay - 2 parts sand, 8 parts clay, 2 parts silt.

These soil types, which are classified according to particle size and distribution, are illustrated in fig. 5.1 and 5.2.

The natural soil measurements for the above five soil types were accomplished for moisture levels ranging from 0 to 48 percent and for test frequencies from 300 to 9300 MHz. A small but representative sample of the results are shown in Tables 5.2, 5.3, 5.4, 5.5, and 5.6. Little dispersion is observed for all soils when $Sw \doteq 0.00$. However, as water saturation increases, greater dispersion in ϵ' occurs, particularly as the matrix particle diameters decrease. From previous discussion, this is expected, since the ratio of surface water to bulk pore water dramatically increases by several orders of magnitude.

Table 5.2 Experimental Results of Dielectric Measurements on Sand as a Function of Water Saturation Sw and Frequency f [5.17]

SAND						
f (MHz)	Sw = 0.00 ϵ'		Sw = 0.04 ϵ'		Sw = 0.14 ϵ'	
	(Mean)	(Std. Dev.)	(Mean)	(Std. Dev.)	(Mean)	(Std. Dev.)
300	2.702	0.0486	4.225	0.168	10.458	0.413
500	2.694	0.0492	4.079	0.162	10.641	0.415
1000	2.693	0.0515	4.019	0.165	11.179	0.349
2000	2.695	0.0515	3.940	0.142	9.951	0.334
4000	2.656	0.0419	3.946	0.148	10.544	0.441
9300	2.737	0.0660	3.373	0.198	10.179	1.140

Table 5.3 Experimental Results of Dielectric Measurements on Sandy Loam as a Function of Water Saturation Sw and Frequency f [5.17]

SANDY LOAM						
f (MHz)	Sw = 0.00 ϵ'		Sw = 0.06 ϵ'		Sw = 0.24 ϵ'	
	(Mean)	(Std. Dev.)	(Mean)	(Std. Dev.)	(Mean)	(Std. Dev.)
300	2.650	0.040	5.967	0.076	24.527	0.326
500	2.642	0.047	5.407	0.062	24.328	0.185
1000	2.660	0.079	4.909	0.028	22.705	0.625
2000	2.680	0.102	4.408	0.035	21.156	1.072
4000	2.691	0.125	4.301	0.019	15.549	1.560
9300	2.663	0.027	3.813	0.084	9.884	2.400

Table 5.4 Experimental Results of Dielectric Measurements on Silt Loam as a Function of Water Saturation Sw and Frequency f [5.17]

SILT LOAM						
f (MHz)	Sw = 0.00 ϵ'		Sw = 0.05 ϵ'		Sw = 0.10 ϵ'	
	(Mean)	(Std. Dev.)	(Mean)	(Std. Dev.)	(Mean)	(Std. Dev.)
300	2.340	0.049	4.453	0.097	9.151	0.186
500	2.321	0.051	4.038	0.083	8.083	0.182
1000	2.318	0.059	3.692	0.078	7.458	0.343
2000	2.343	0.085	3.391	0.080	5.573	0.157
4000	2.325	0.044	3.319	0.108	5.275	0.048
9300	2.408	0.094	3.170	0.092	4.065	0.268

Table 5.5 Experimental Results of Dielectric Measurements on Clay Loam as a Function of Water Saturation Sw and Frequency f [5.17]

CLAY LOAM						
f (MHz)	Sw = 0.00 ϵ'		Sw = 0.06 ϵ'		Sw = 0.12 ϵ'	
	(Mean)	(Std. Dev.)	(Mean)	(Std. Dev.)	(Mean)	(Std. Dev.)
300	2.775	0.024	5.667	8.719	0.183	0.186
500	2.760	0.027	5.108	0.138	8.083	0.182
1000	2.773	0.037	4.649	0.101	7.363	0.223
2000	2.771	0.051	4.151	0.065	5.702	0.018
4000	2.758	0.048	4.024	0.156	5.682	0.005
9300	2.708	0.076	3.826	0.122	4.657	0.418

Table 5.6 Experimental Results of Relative Dielectric Measurements on Clay as a Function of Water Saturation Sw and Frequency f [5.17]

CLAY						
f (MHz)	Sw = 0.00 ϵ'		Sw = 0.06 ϵ'		Sw = 0.12 ϵ'	
	(Mean)	(Std. Dev.)	(Mean)	(Std. Dev.)	(Mean)	(Std. Dev.)
300	2.717	0.052	6.030	6.034	10.676	0.204
500	2.703	0.053	5.399	0.015	9.402	0.186
1000	2.721	0.065	4.952	0.058	9.871	0.807
2000	2.721	0.068	4.187	0.005	6.294	0.124
4000	2.732	0.105	4.289	0.085	5.642	0.823
9300	2.677	0.052	3.754	0.053	5.185	0.950

B4.2 Synthetic Soils

A further extensive study of permittivity measurements has recently been accomplished at NBS for synthetic soil materials that might be used in land mine validation testing. These measurements were also performed in the frequency domain, using open-circuit coaxial transmission-line techniques. Data were collected for wetted sands and various silicon carbide (60-grit) and sand mixtures, as well as for silicon carbide and aluminum powder mixtures, over the frequency range of 50-750 MHz. A brief summary of the results is given here.

Initially, the coaxial line was filled with tap water at 20°C in order to verify the experimental procedure and calculations. Calculated permittivity and loss tangent from 50 MHz to 1.20 GHz are shown in figure 5.3, validating laboratory procedures.

Dielectric dispersion curves for wetted sand samples (water saturations varying from 4 percent to 14 percent) are given in figures 5.4, 5.5, and 5.6. The dielectric constant predictably increases as water saturation increases, with dispersion evident principally at frequencies less than 150 MHz. In addition, the permittivities at 600 MHz of a 5 cm section of various water-

saturated sands were measured as a function of drying time at approximately 20°C. These results, illustrated in figure 5.7, show that host soil permittivities can vary by as much as a factor of 2 over a 72 h drying time. Hence, if wetted soils are used for test beds, the host permittivity should be measured at the time of validation testing so as to properly compare different detection systems.

Various mixtures of silicon carbide and sand were also examined and the results are given in figures 5.8, 5.9, 5.10, 5.11, and 5.12. The loss tangent increases slightly with increasing frequency as opposed to the case of wetted sands, where the loss tangent either remained constant or decreased with frequency. Provided these silicon carbide mixtures have little conductive (lossy) material in them, almost no dispersion is evident. Therefore, by controlling the sand-silicon carbide mix, we may simulate a host medium whose effective permittivity ranges from 3 to 13 but remains constant over the 50-750 MHz range (for any given mix) for plastic land mine validation tests.

The addition of conductive aluminum powder to silicon carbide yielded expected dispersion, as seen in figure 5.13. In fact, addition of even 5 percent aluminum powder (by mass) caused dispersion to be evident at frequencies as high as 500 MHz. Hence, if conductive constituents such as aluminum powder are added to host test lanes, the dispersion characteristics of the lossy test media should be known a priori so that detection systems operating at different frequencies may be compared properly (just as for wetted soils).

C. Use of Loose Matrix Synthetic Soils for Narrowband or Fixed Frequency Test Lanes for Nonmetallic Buried Objects

The point of the discussion on polarization mechanisms and relaxation processes is to provide insight into the frequency dependence of ϵ_H' for soil materials. Because the frequency dependence of ϵ' for most soil materials is generally flat from 1 MHz to 1 GHz, there is valid justification for specifying synthetic test soils since their constituent electromagnetic properties may be more controllable. A preliminary suggested set of standard background media is given in Table 5.7 for plastic mine detector validation testing.

Table 5.7 **Preliminary Set of Standard Background Media for Plastic Mine Detector Validation Testing**

Background Medium	Dielectric Constant, ϵ'	Loss Tangent, $\sigma/\omega\epsilon'$
Dry Silica Sand	2.8 ± 0.05	0.01
Mixture: 40% SiC, 60% Dry Sand	5.0 ± 0.2	0.013 ± 0.002
Mixture: 80% SiC, 20% Dry Sand	10.0 ± 0.4	0.018 ± 0.003

In the natural soil environment encountered by the foot soldier, both conduction and dielectric mechanisms influence mine detector signals. The common factor affecting both conduction and dielectric mechanisms is the water saturation, Sw. Thus, in standard background test media it is critical to control and/or to know water saturations. As a matter of test procedure, mine lanes for UHF detectors should not only be enclosed in an electromagnetically anechoic environment (to avoid spurious noise reflections off metallic objects), but also one which is shielded from the varying influences of outside weather that affect Sw.

D. <u>Use of Loose Matrix Natural Soils for Test Lanes for Metallic Buried Objects and Broadband Systems</u>

The use of synthetic soils for test lanes for single-frequency metal land mine detectors may also be justified in terms of greater control of constituent properties governing detector signals. Since these detectors generally operate at a frequency around 2500 Hz, there are usually no significant attenuation problems in sensing metallic mine signals at burial depths that may be as great as 1 m, even for a relatively conductive ($\sigma_H \doteq 0.1$ S/m) soil or for that which is magnetically permeable ($\mu_H = 1.4\ \mu_0$). Suggested background media for single-frequency metal mine detectors are given in Table 5.8. Because the conductivity contrast between a metallic mine and almost any conceivable natural soil is so high (effectively infinite for analysis purposes), requirements on testing environments for metal mine detectors are much less stringent. That is, test lanes for VLF or ELF single-

frequency metal mine detectors need not be in an anechoic environment nor do they need to be shielded from the influences of outside weather.

Table 5.8 Preliminary Set of Standard Background Media for Metal Detector Validation Testing

Background Medium	Relative Magnetic Permeability, μ/μ_0
Dry Sand	1.00
Mixture: Dry Sand with 30% Magnetite	1.35

Signals measured by both single-frequency plastic mine UHF and metal mine VLF detectors are sensitive only to the volume of the buried land mine. In order to gain shape information (and therefore minimize false alarms due to ground clutter), future detectors must be developed that are broadband in design and measurement -- a fact well recognized in radar work. As such development proceeds, the sensitivity to complex permittivity contrasts (mine visibility), affected by dielectric relaxation processes, becomes relevant in understanding detector performance and in specifying optimal system bandwidth.

The use of synthetic or natural soils in test lanes for broadband system validation should be approached with caution. Natural soils often depart drastically from Debye behavior (single relaxation dielectric dispersion) at frequencies less than 1 MHz. Furthermore, broadband dispersive characteristics of synthetic soils (in the ELF or VLF frequency range) may not compare to that of natural soils commonly encountered by the field soldier.

Thus, although it would be desirable to have background test material that is electromagnetically analogous to those situations commonly encountered in the field, it is equally desirable to have test soils that can be accurately specified, and whose properties can be closely controlled and measured. On account of these two requirements, it is expedient to examine in more detail the dielectric characteristics of water saturated soils with a view toward understanding those parameters that can be controlled and are responsible for governing electromagnetic field behavior. At the very least, such an examination should provide insight into how natural soils might be

used in performance testing of broadband mine detection systems or in predicting how they may differ from the suggested set of standard background media given in Tables 5.7 and 5.8.

E. NIST Recommendations and Conclusions

E1. Natural Loose-Matrix Soil Standards

Natural loose-matrix soil standards have the advantage of possessing identical electromagnetic properties (μ_r, ϵ_r and σ) to soils found in the field. However, these natural soils have the following disadvantages.

1. Water Content Variation -- It is very difficult (if not impossible) to consistently control the water content of a natural loose-matrix soil. Even small changes in water saturation, Sw, can have a very large effect on the dielectric constant of the soil.

2. Water Gradient Variation -- Even if some method were eventually determined for accurately and consistently controlling Sw, there is still a problem with the fact that Sw is a function of depth in the soil. This function is, in general, unknown but is related to gravity and soil texture and type.

3. Reproducibility -- It would be very difficult to find sources of natural soils which would be sufficiently uniform to serve as standards.

4. Soil Density Variation -- It is also very difficult to control the soil density (compaction) of a natural loose-matrix soil. These variations lead to an undesirable inhomogeneity in the electromagnetic properties of the background medium.

5. Soil Density Gradient Variation -- Similarly to the water gradient problem, the effects of gravity will lead to soil density stratification with a resulting increase in the values of the electromagnetic constituent properties of a natural loose-matrix soil as a function

of increasing depth. Although, for some tests, it may be desirable to simulate realistic soils by purposefully introducing this gradient variation, it should be controllable.

6. Target Position and Orientation -- The use of natural loose-matrix soil standards makes it very difficult to place targets in the medium with precisely controlled depths and orientations. Thus, reproducible tests would be almost impossible to conduct.

7. Surface Irregularities -- The use of natural loose-matrix soil standards would make it very difficult to control the surface smoothness (or profile) of the medium. Tests demanding smooth surfaces as well as those with purposefully irregular surface profiles (surface clutter tests) would be difficult or impossible.

8. Contamination -- It would be very difficult, over time, to prevent contamination of loose-matrix natural soil standards or even to detect that contamination had taken place.

E2. Synthetic Loose-Matrix Soil Standards

Synthetic loose-matrix soil standards would be an improvement over natural soils in that disadvantages 1, 2, and 3, above, could be eliminated. However, disadvantages 4 through 8 still apply, and, in addition, these synthetic soils have other disadvantages as follows:

1. Property Deviation with Frequency -- Although it is possible to synthesize a given natural soil's electromagnetic properties over a narrow frequency range with a mixture of dry materials, such as silica sand and silicon carbide, it is not possible to synthesize a natural soil that would duplicate the natural soil's properties over a broad range of frequencies. (A range of 100 kHz to 5 GHz would be desirable.) Therefore, for adequate detector testing, a number of different synthetic soil lanes would be required to simulate the properties of just one natural soil.

2. Temperature Dependence -- Since there is a wide variation in the dielectric constant of water as a function of temperature, it would be very difficult to create a dry synthetic material mixture which would track damp or wet natural soils over even a small range of ambient temperatures.

E3. Liquid Soil Standards

NIST's conclusion with respect to liquid soil standards is that, although this approach is probably not impossible, it is impractical. It is very likely impossible to simulate all desired electromagnetic properties of natural soils with liquids, and simply the mechanics of attempting to perform detector tests over a large tank filled with liquids would be extremely difficult and, perhaps, dangerous.

E4. Rigid-Matrix Soil Standards

NIST recommends that, as future work, a set of rigid matrix soil standards be developed and installed at Ft. Belvoir. (See Chapter VIII.) These soil standards, as presently envisioned, would consist of portable bricks (with or without standard or realistic targets embedded within) fabricated from mixtures of epoxy (or some other suitable binder), water, salts, silica sand and/or polystyrene beads. These standards would possess none of the disadvantages of loose-matrix natural or synthetic soils. In addition, preliminary experiments at NIST indicate that a very wide range of values for electromagnetic properties can be obtained with these bricks, and these properties should track those of natural soils over a very wide band of frequencies and temperatures.

References

[5.1] Geyer, R. G. Magnetic Susceptibility Measurements for Mine Detection: Some General Comments. Report, U.S. Army Belvoir Research and Development Center, Fort Belvoir, VA, 1987, 10 p.

[5.2] Heiland, C. A. Geophysical Exploration. Englewood Cliffs, New Jersey: Prentice Hall 1940, pp. 310-314.

[5.3] Geyer, R. G. Experimental Parameters for Land Mine Detection Performance Evaluations. Report, U.S. Army Belvoir Research and Development Center, Fort Belvoir, VA, (Proj. 7232457); 1987 November, 100 p.

[5.4] Ulaby, F. T.; Moore, R. K.; Fung, A. K. Microwave Remote Sensing, Vol. III: From Theory to Applications. London, England: Addison-Wesley Publishing Co., 1982.

[5.5] Hasted, J. B. Liquid Water: Dielectric Properties. Chapter 7 in Water -- A Comprehensive Treatise, I, The Physics and Chemistry of Water. New York: Plenum Press, 1972.

[5.6] Tinga, W. R. Generalized Approach to Multiphase Dielectric Mixture Theory. J. Appl. Phys. 44; 1973, pp. 3897-3902.

[5.7] Ho, W. W.; Love, A. W.; VanMelle, M. J. Measurements of the Dielectric Properties of Sea Water at 1.43 GHz. NASA Contactor Report CR-2458. NASA Langley Research Center, Langley, VA, 1974.

[5.8] Böttcher, C. J. F. Theory of Electric Polarization. Amsterdam: Elsevier, 1952.

[5.9] Kurosaki, S. The Dielectric Behavior of Water Sorbed in Silica Gel. J. Phys. Chem. 58; 1954, pp. 320-324.

[5.10] Bockris, J.; Gileady, E.; Muller, K. Dielectric Relaxation in the Electric Double Layer. J. Chem. Physics. 44; 1966, pp. 1445-1456.

[5.11] McCaffer y, E.; Zettlemayer, A. C. Adsorption of Water Vapor on α-Fe_2O_3. Faraday Soc. Discussions, Vol. 52; 1971, pp. 239-254.

[5.12] Hasted, J. B. The Dielectric Properties of Water in Progress in Dielectrics, Vol. 3., J. B. Birks and J. Hart, ed. New York: John Wiley & Sons; 1961, pp. 101-149.

[5.13] Nair, N. K.; Thorp, J. M. Dielectric Behavior of Water Sorped in Silica Gels, Part 1, Commercial Silica Gels and the Elimination of Dielectric Hysteresis. Trans. Faraday Soc. 61, pp. 962-974, 1965.

[5.14] Kenyon, W. E. Texture Effects on Megahertz Dielectric Properties of Calcite Rock Samples. J. Appl. Phys. 55, pp. 3151-3159, 1984.

[5.15] Dobson, M. C.; Ulaby, F. T.; Hallikainen, M. T.; El-Rayes, M. A. Microwave Dielectric Behavior of Wet Soil, Part II: Dielectric Mixing Models. IEEE Trans. Geosci. Remote Sensing. GE-23(1), 1985, pp. 35-46.

[5.16] Shutko, A. M.; Reutov, E. M. Mixture Formulas Applied in Estimation of Dielectric and Radiative Characteristics of Soils and Grounds at Microwave Frequencies. IEEE Trans. Geosci. Remote Sensing. GE-20, 1982, pp. 29-32.

[5.17] Jesch, R. L. Dielectric Measurements of Five Different Soil Textural Types as Functions of Frequency and Moisture Content. Nat. Bur. Stand. (U.S.) NBSIR 78-896, 1978, 26 p.

[5.18] Bussey, H. E. International Comparison of Complex Permittivity Measurement at 9 GHz. IEEE Trans. Instr. Meas. IM-23(3), 1974, pp. 235-239.

[5.19] Bussey, H. E.; Gray, J. E.; Bamberger, E. C.; Rushton, E.; Russel, G.; Petley, B. W.; Morris, D. International Comparison of Dielectric Measurements. IEEE Trans. Instr. Meas. IM-13, 1964, pp. 305-311.

[5.20] Von Hippel, A. R. Dielectric Materials and Applications. New York: The Technology Press of M.I.T. and John Wiley & Sons, 1954. 438 p.

[5.21] Clark, S. P. Handbook of Physical Constants. Geol. Soc. Am. Memoir 97, 1966, 587 p.

[5.22] Morey, L. Properties of Glass. New York: Reinhold Press, 1954.

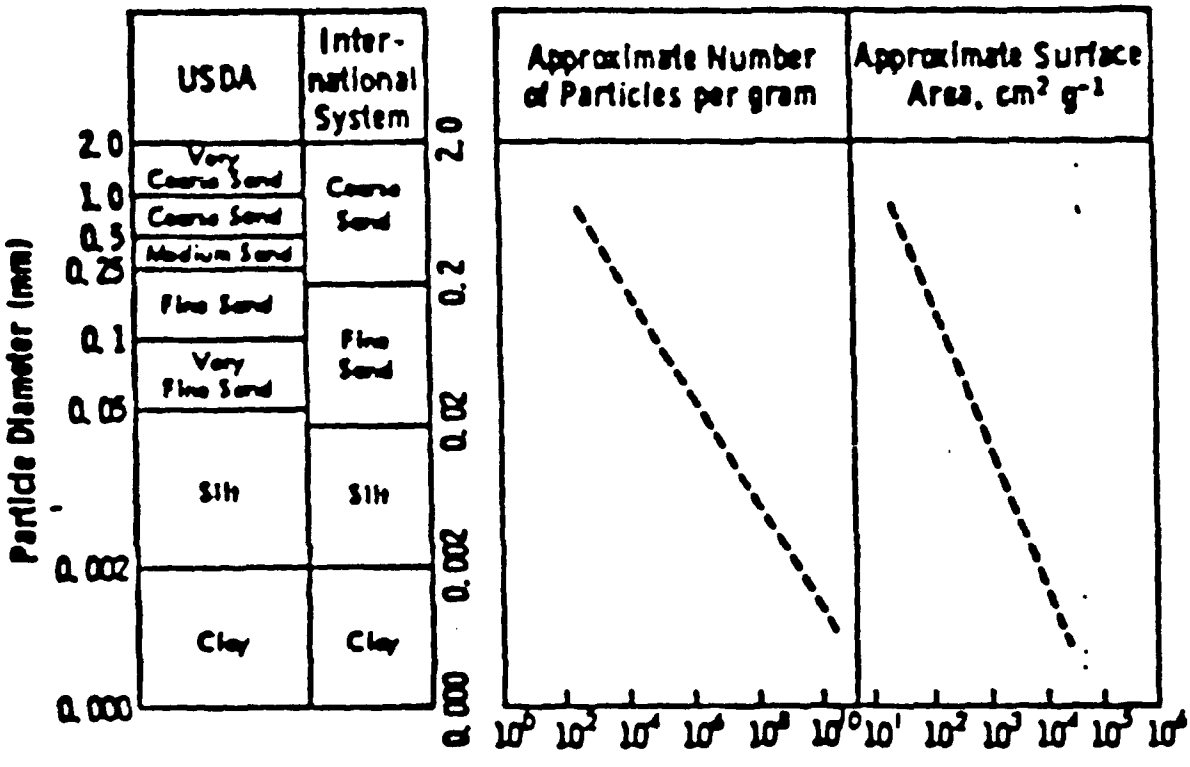

Figure 5.1 Particle properties for different soil types.

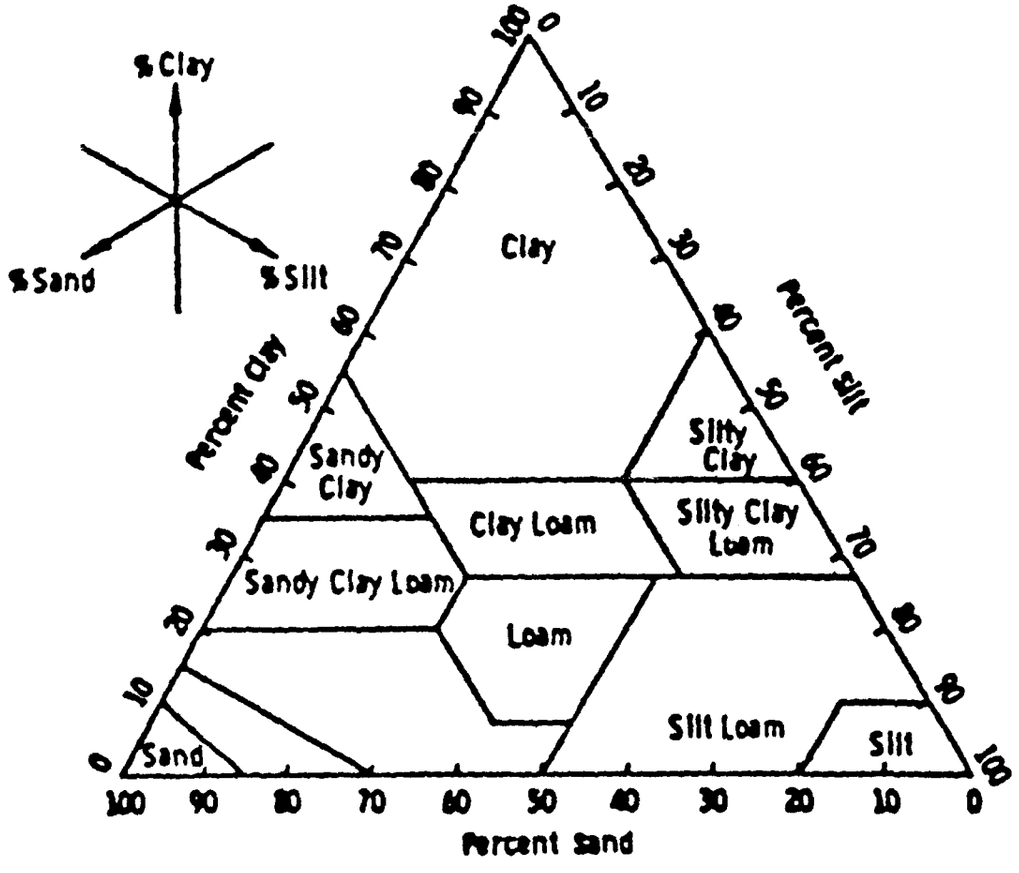

Figure 5.2 Particle distribution for different soil types.

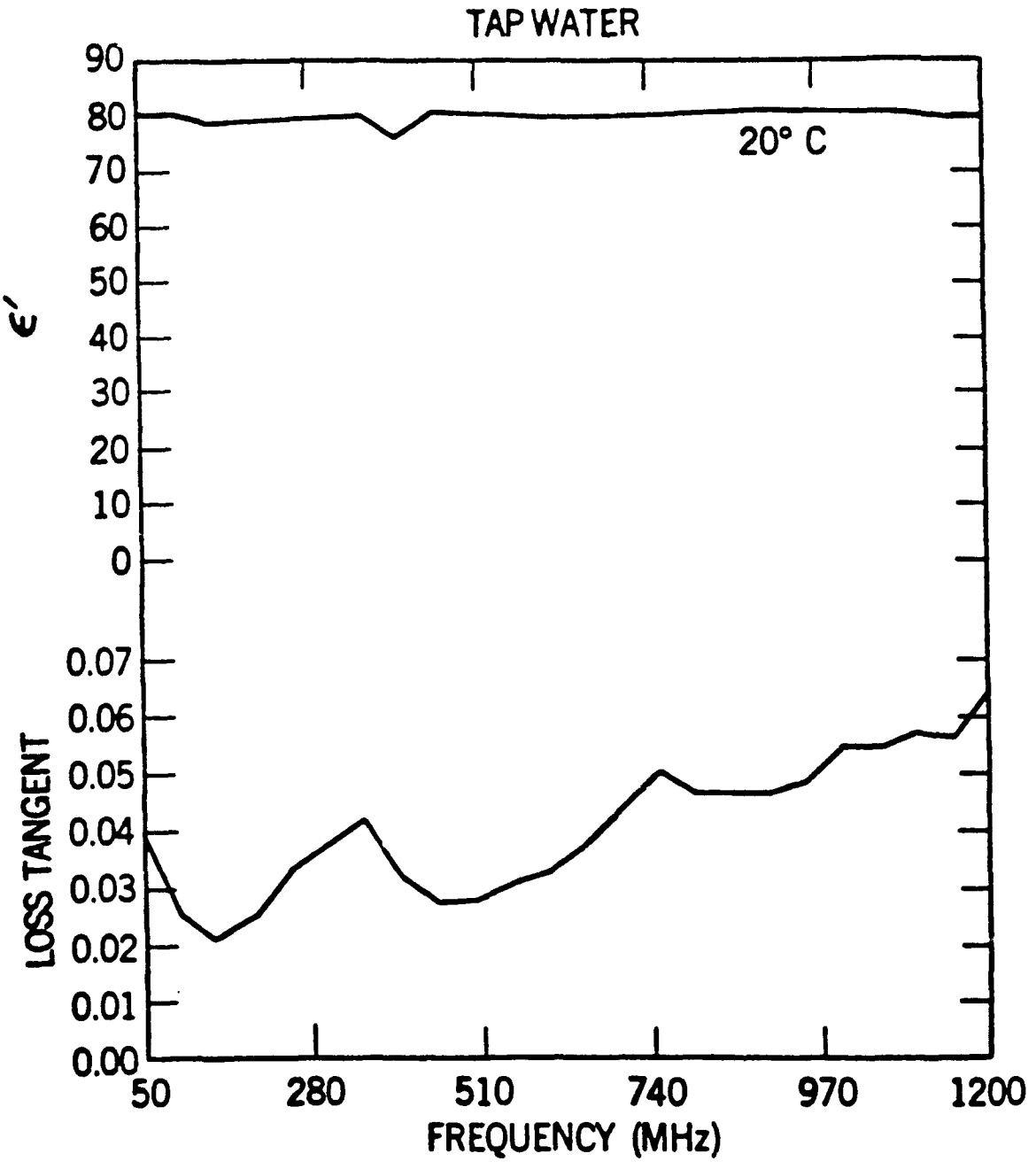

Figure 5.3 Measured permittivity and loss tangent vs frequency for tap water at 20° C.

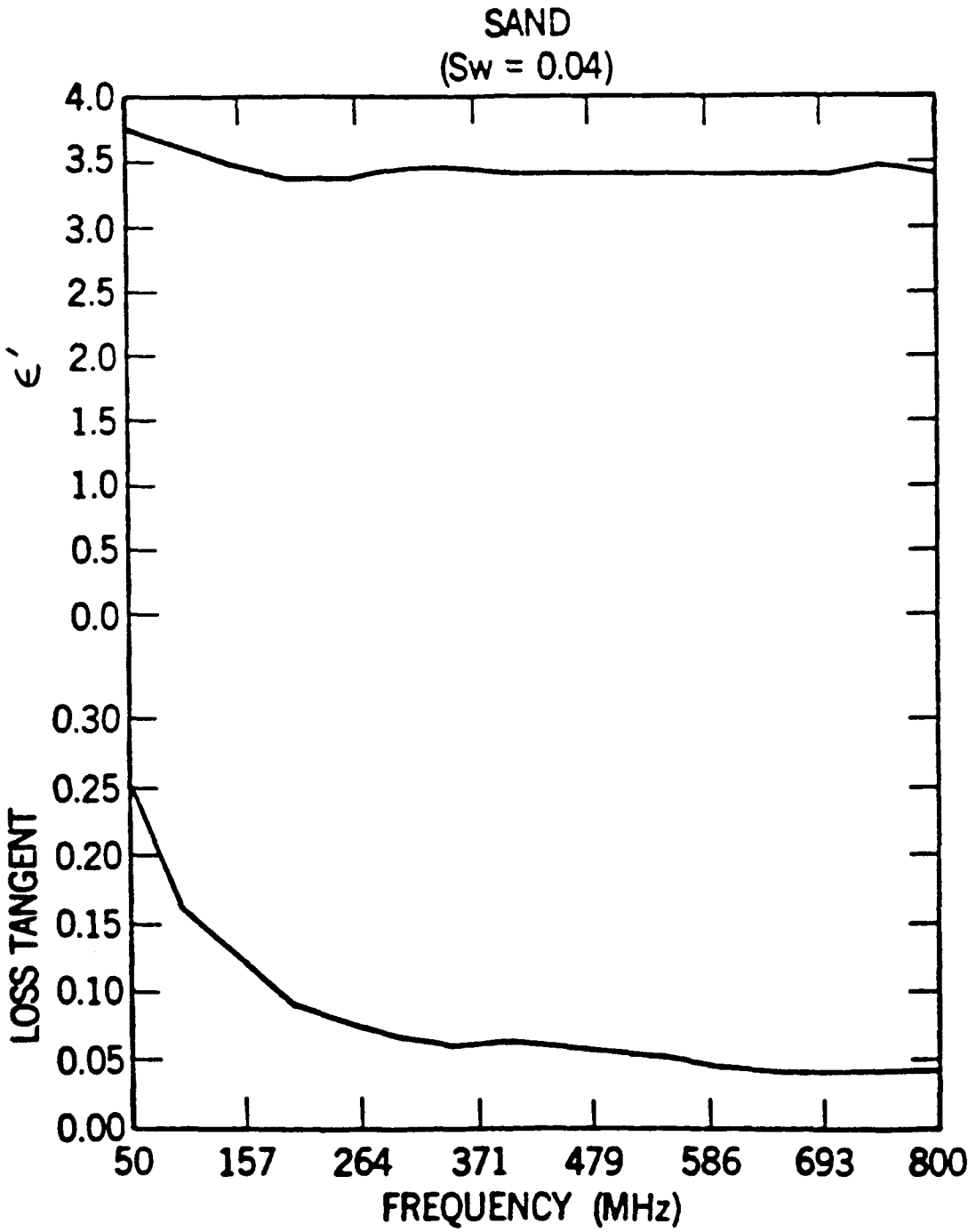

Figure 5.4 Measured permittivity and loss tangent vs frequency for sand with 4% water.

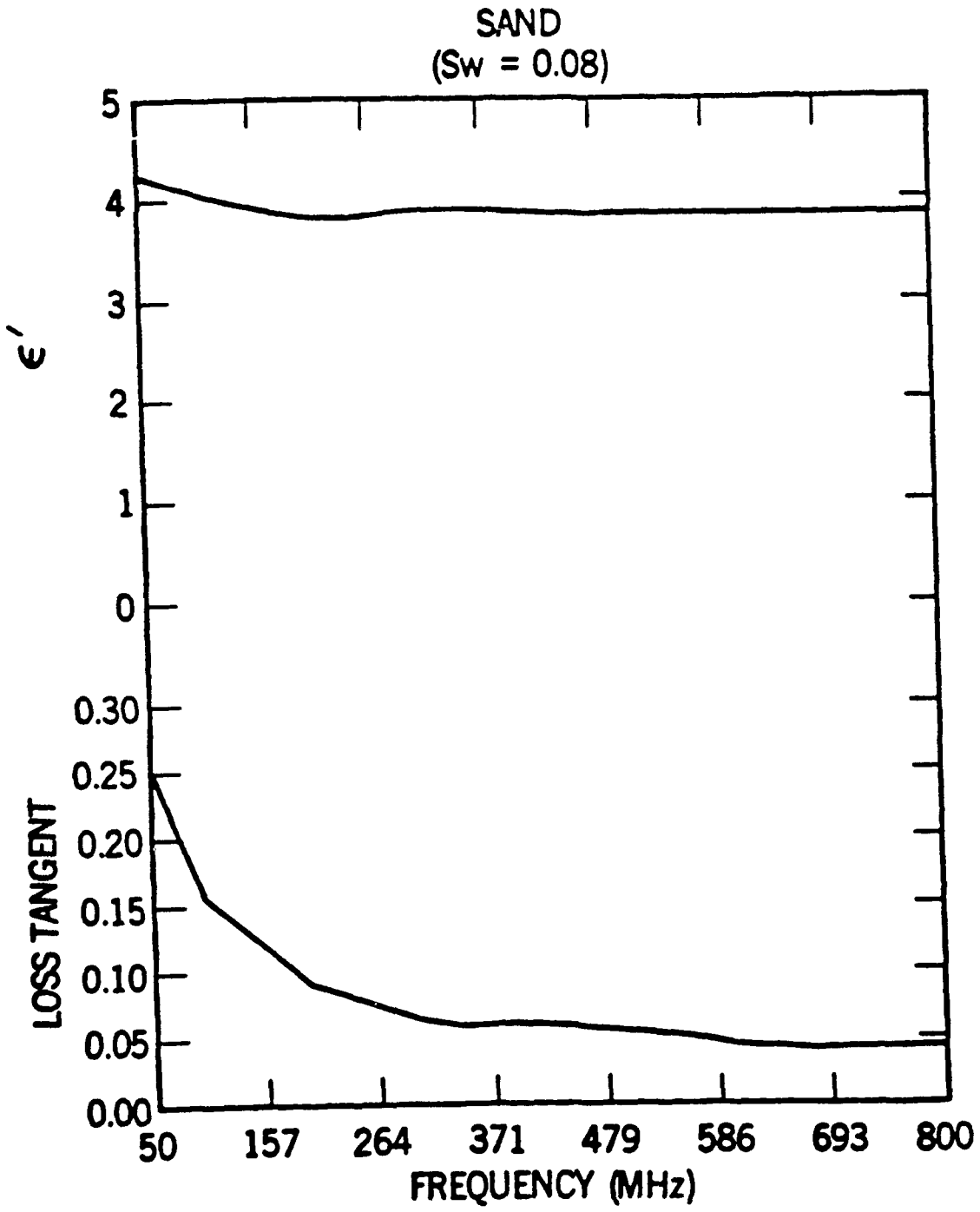

Figure 5.5 Measured permittivity and loss tangent vs frequency for sand with 8% water.

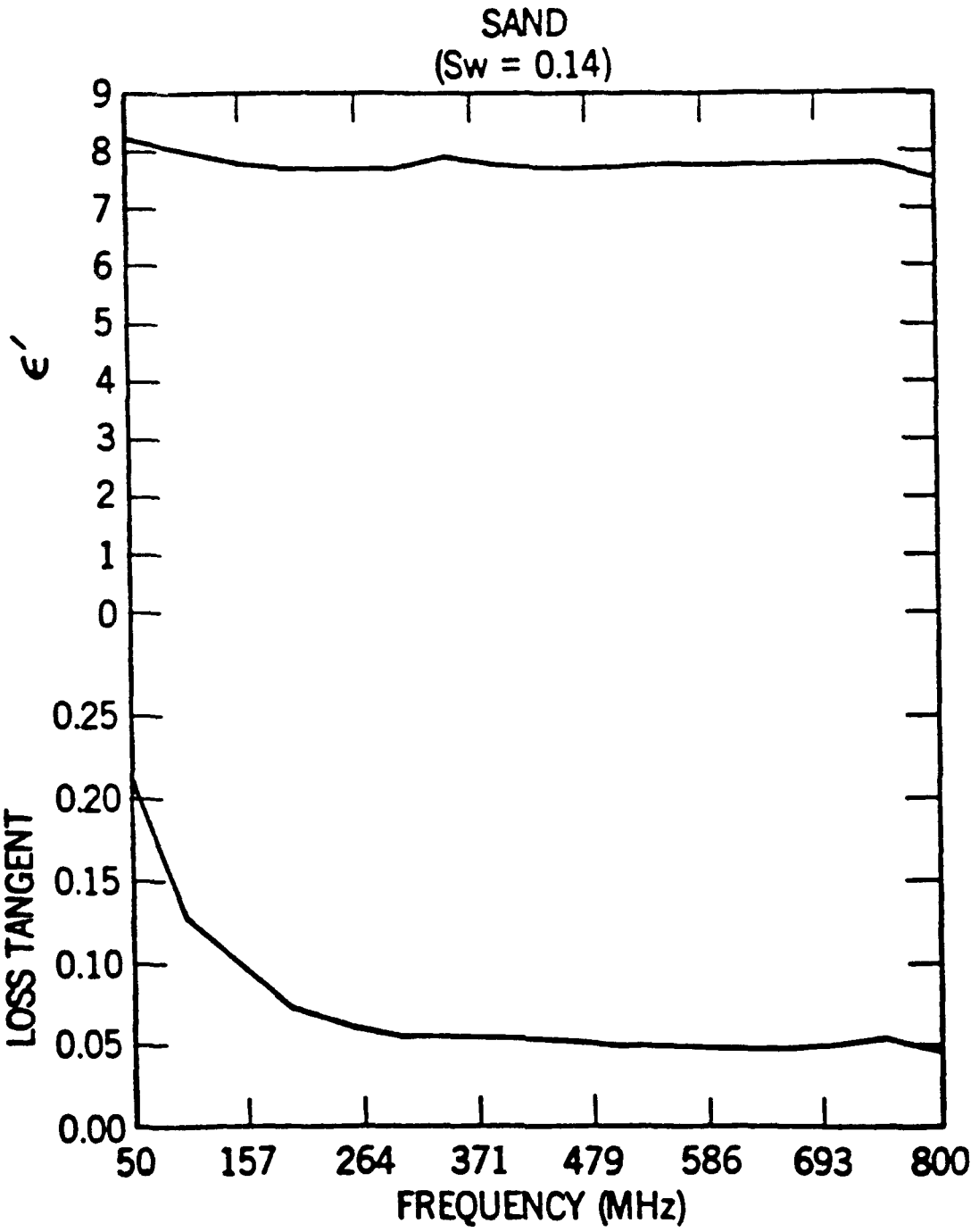

Figure 5.6 Measured permittivity and loss tangent vs frequency for sand with 14% water.

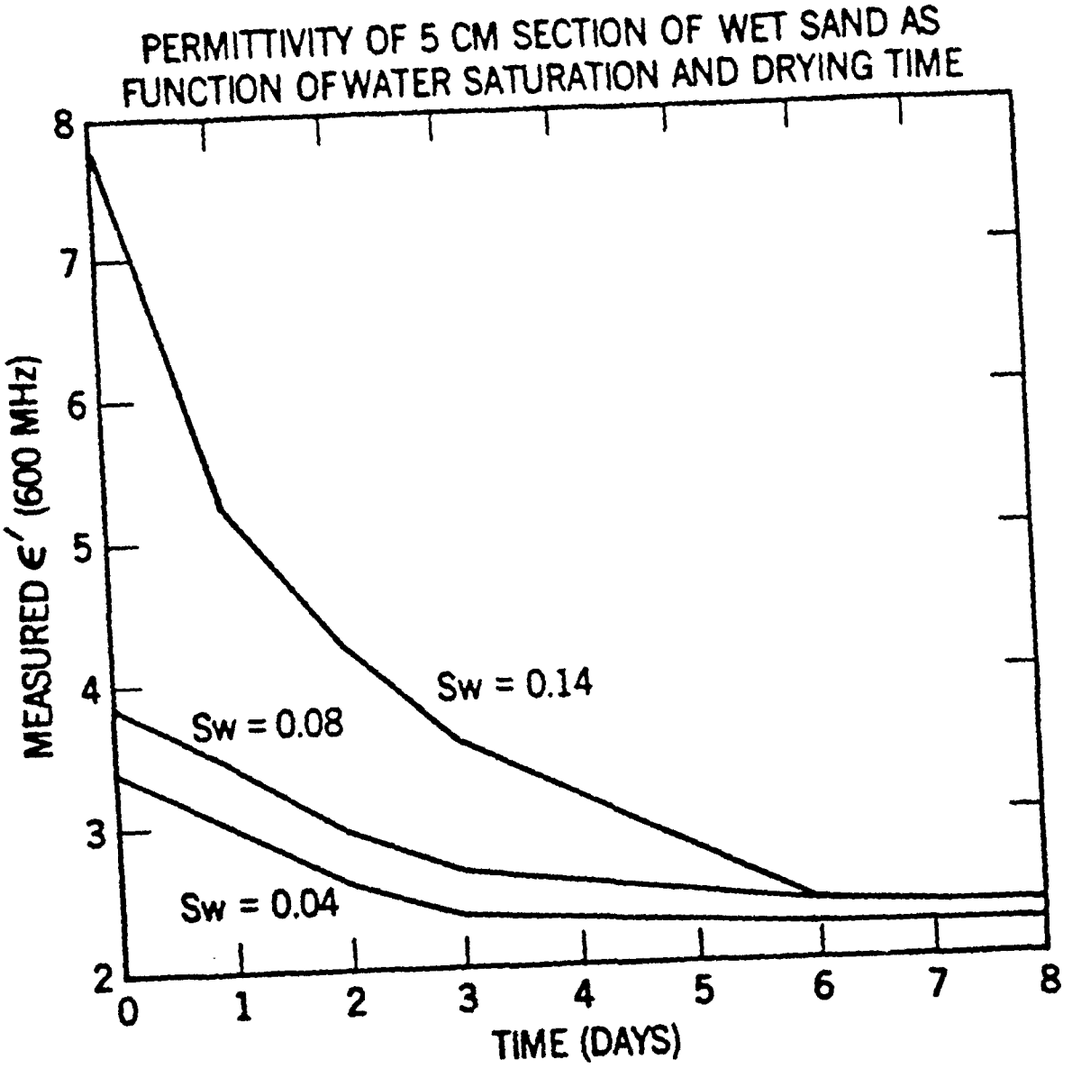

Figure 5.7 Measured permittivity at 600 MHz vs drying time at 20° C for various sand & water mixtures.

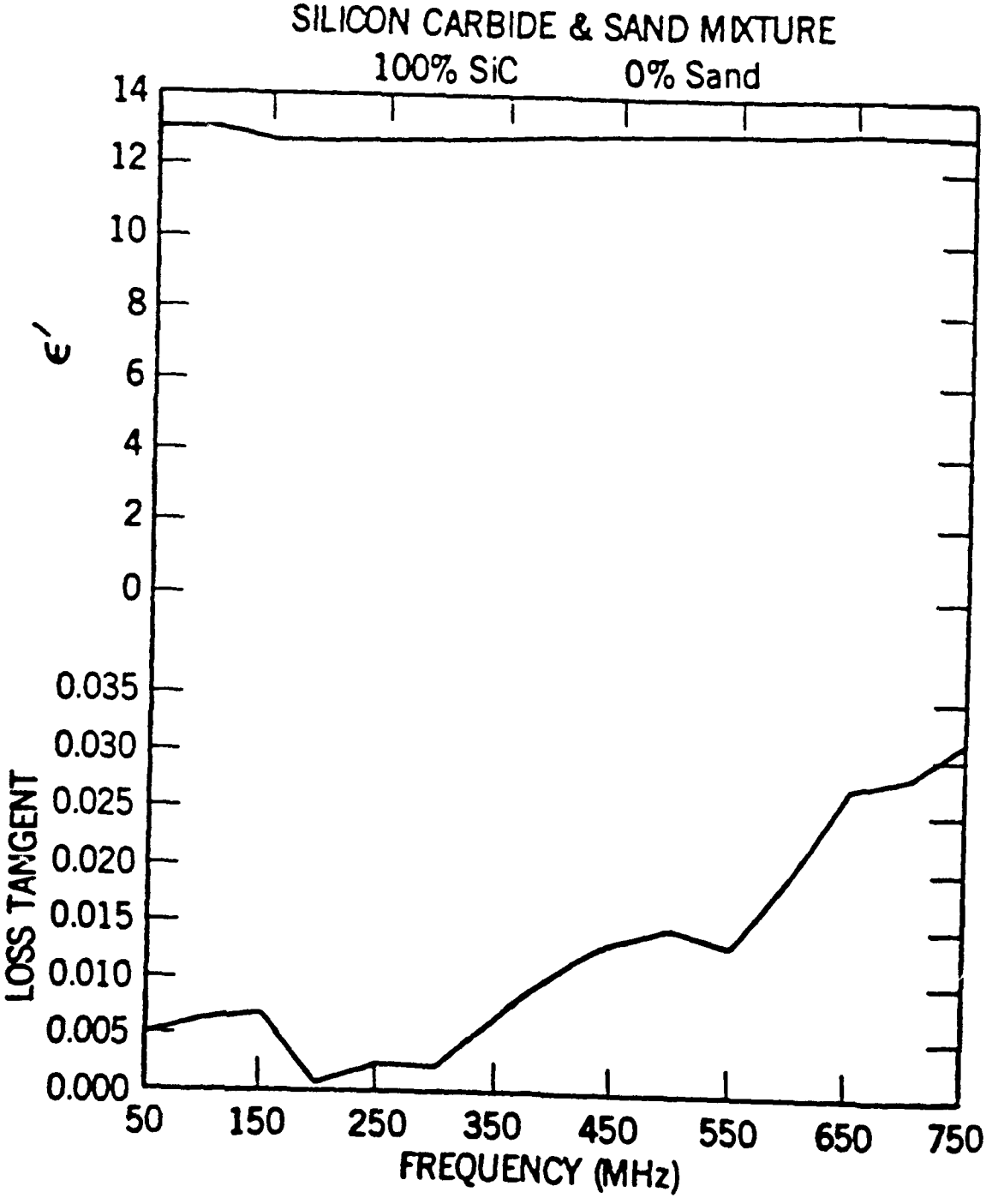

Figure 5.8 Measured permittivity and loss tangent vs frequency for 100% silicon carbide.

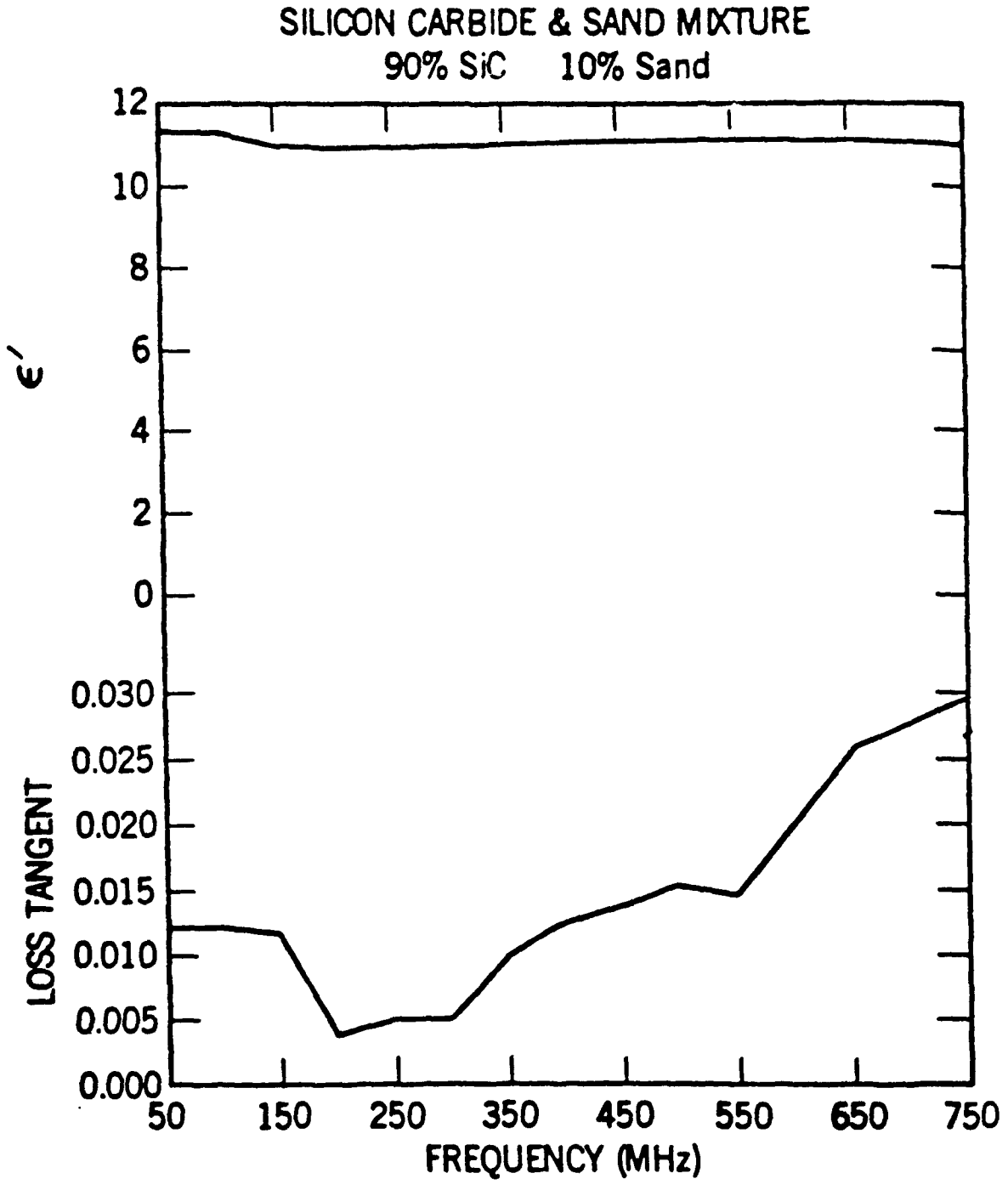

Figure 5.9 Measured permittivity and loss tangent vs frequency for 90% silicon carbide 10% sand mixture.

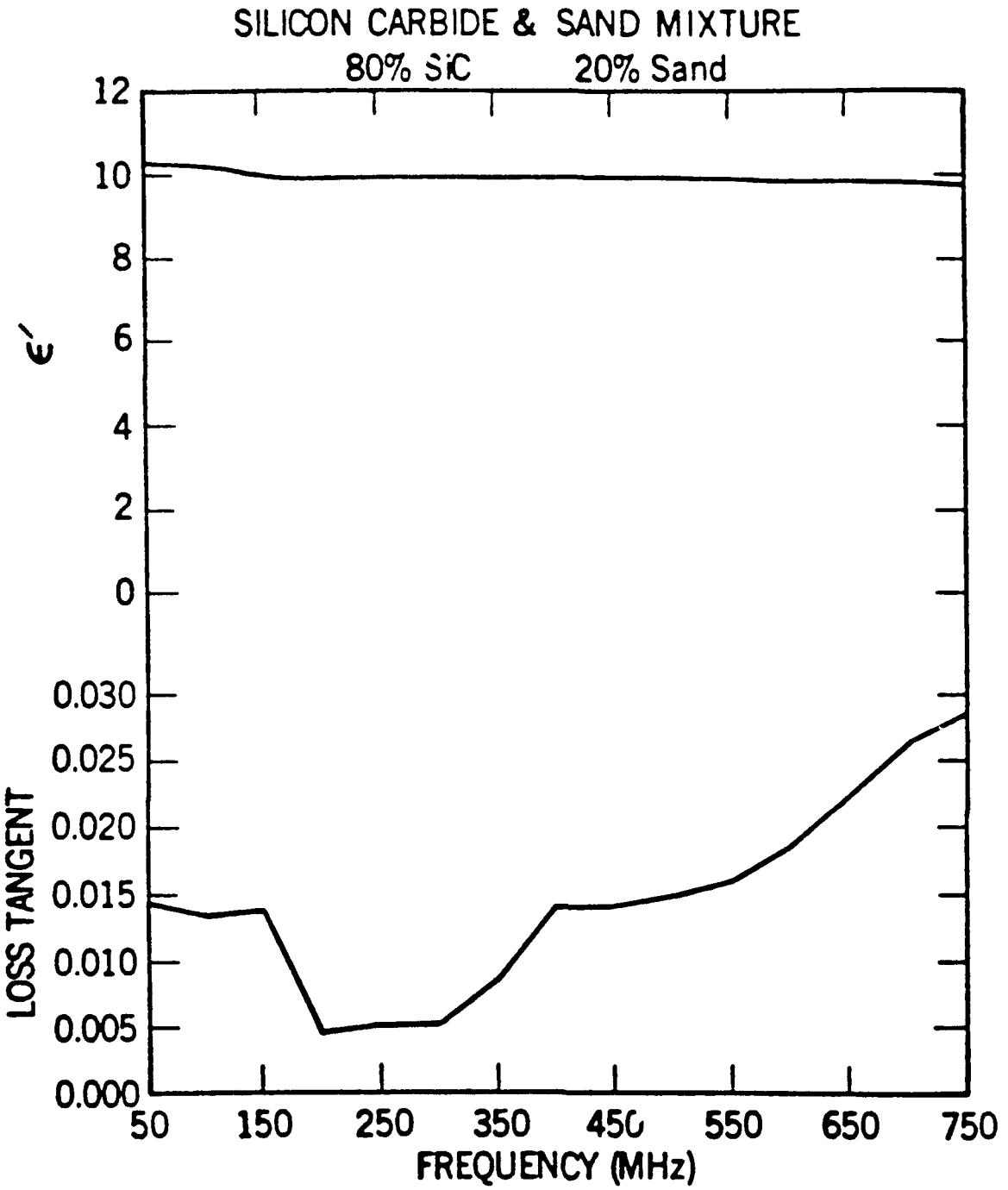

Figure 5.10 Measured permittivity and loss tangent vs frequency for 80% silicon carbide 20% sand mixture.

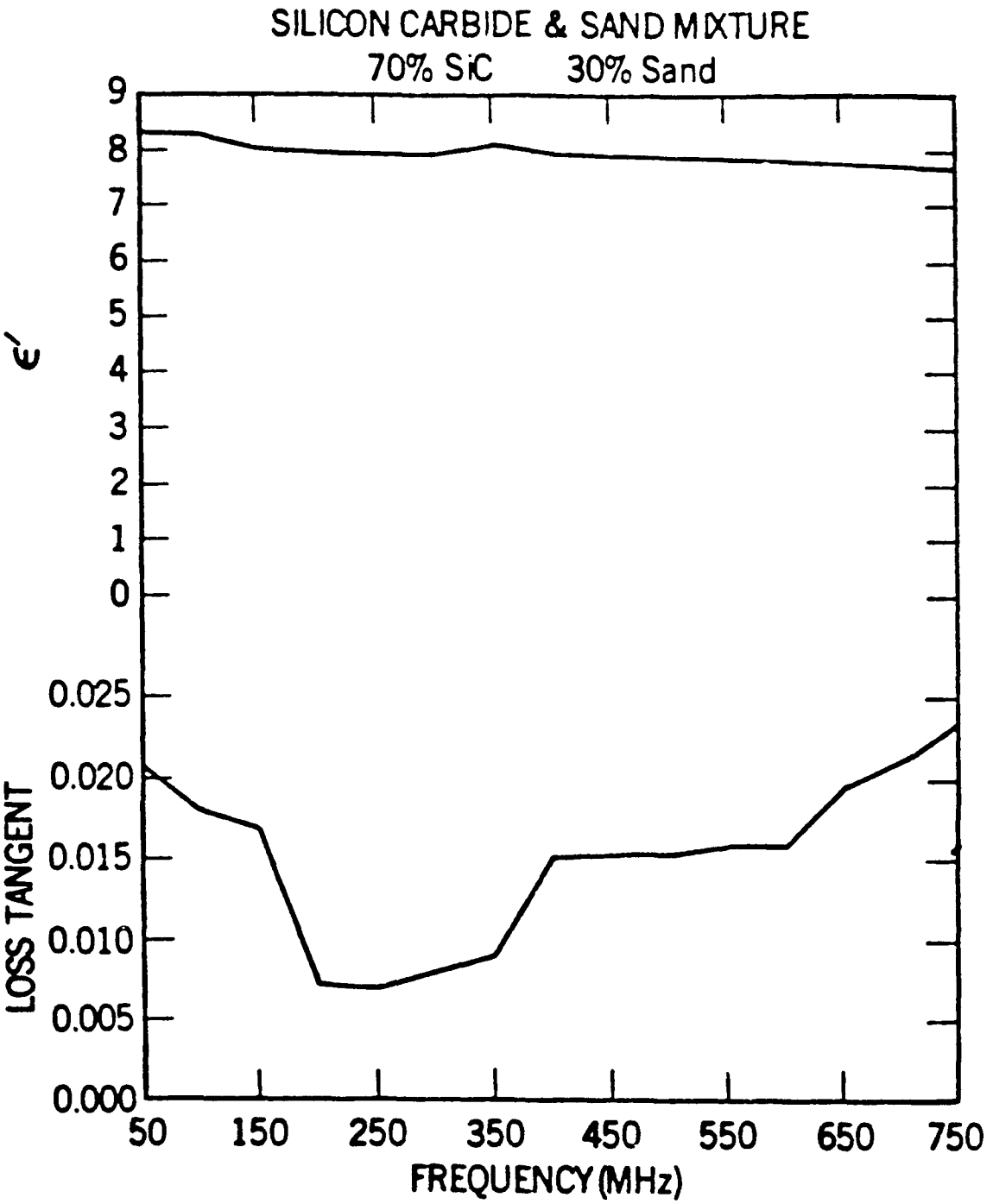

Figure 5.11 Measured permittivity and loss tangent vs frequency for 70% silicon carbide 30% sand mixture.

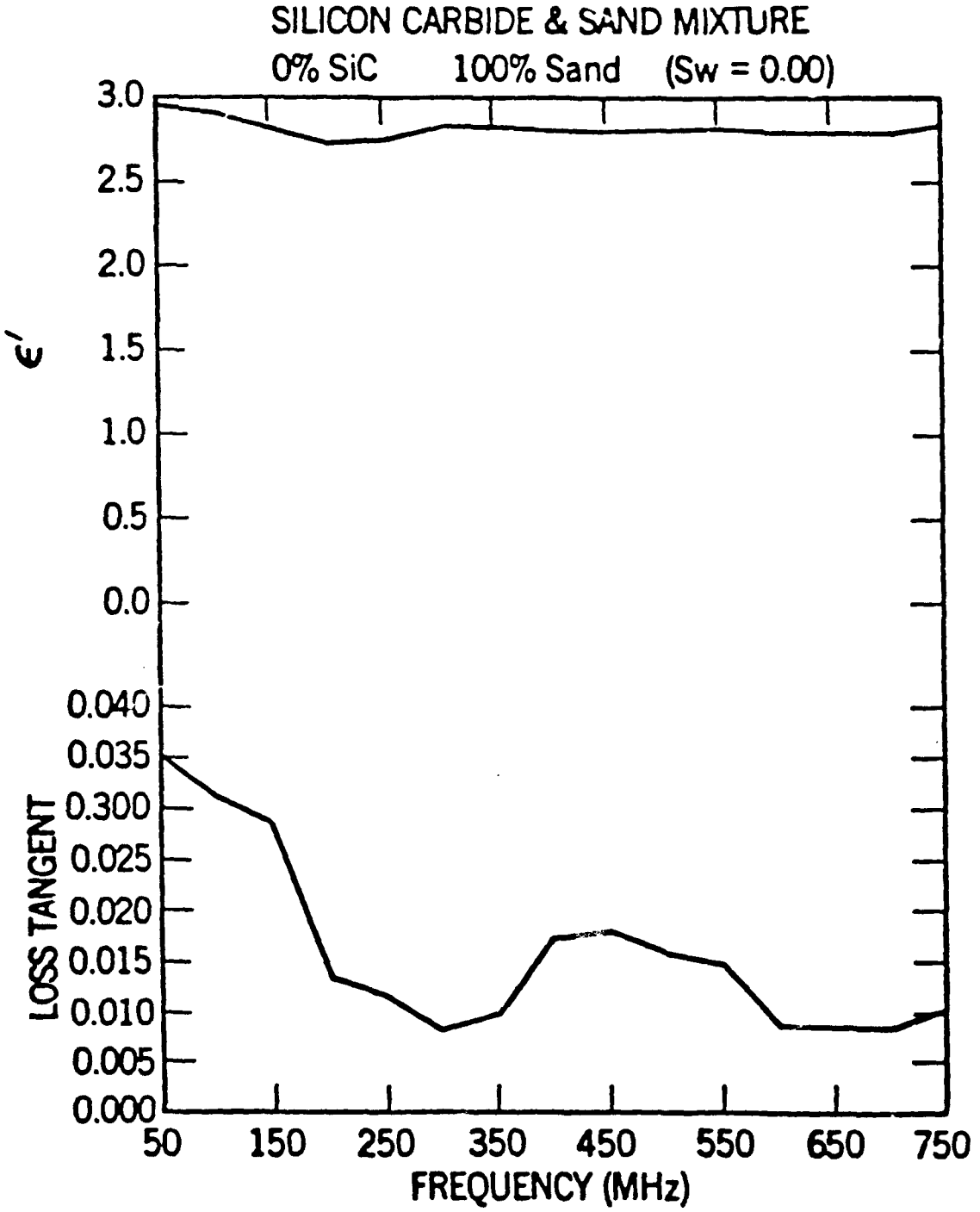

Figure 5.12 Measured permittivity and loss tangent vs frequency for 100% sand.

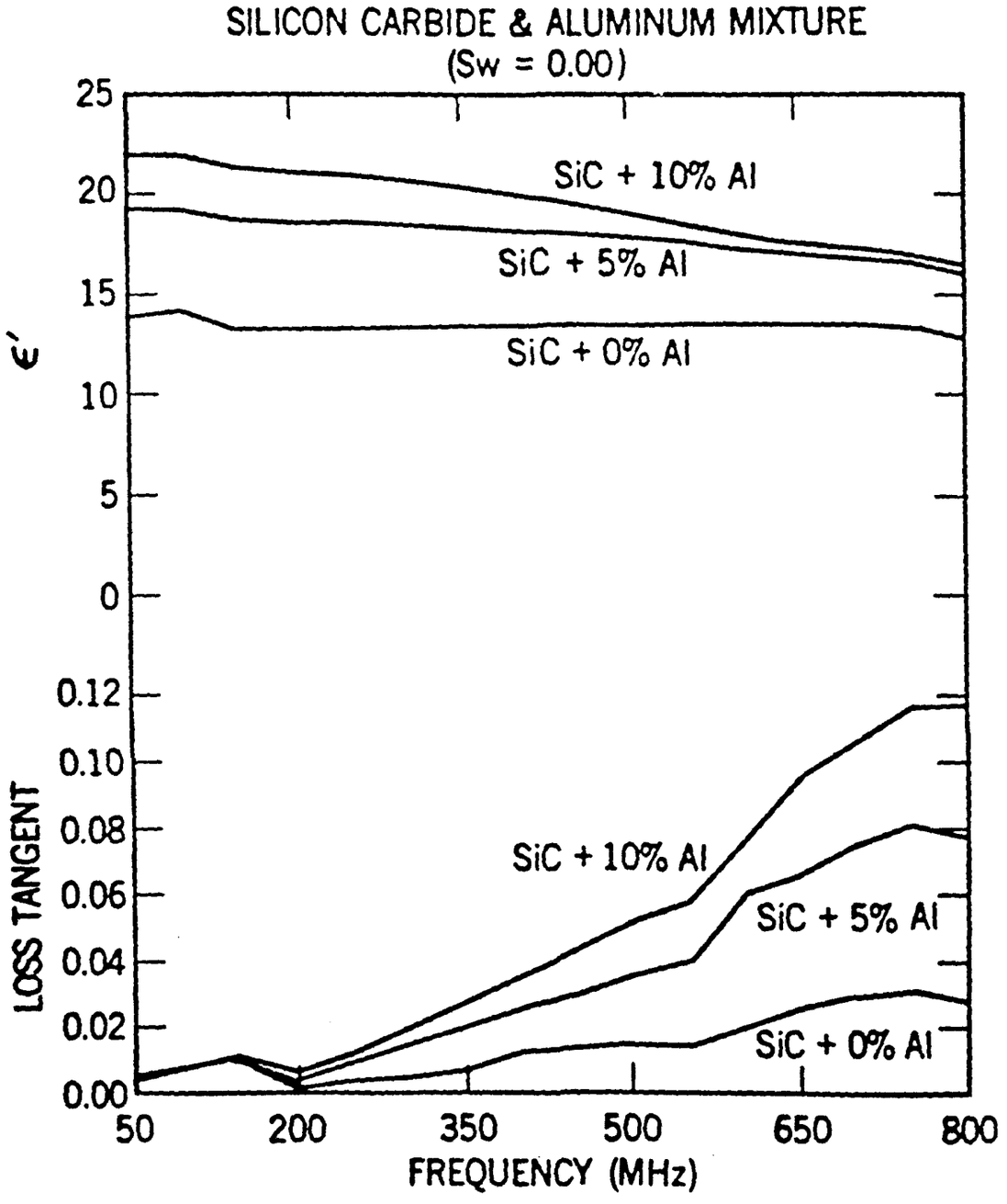

Figure 5.13 Measured permittivity and loss tangent vs frequency for various silicon carbide & aluminum powder mixtures.

VI. TEST INSTRUMENTATION AND PROCEDURES FOR STANDARDS

A. Introduction

The measurement of mine detector performance generally requires that certain specified tests be carried out with test targets buried in a carefully controlled environment or test lane. For tests of plastic object detectors that use UHF or microwave frequencies, the returned signals are very much weaker than the transmitted signals. This makes it imperative that the test procedures be designed so that we can obtain consistently similar results for the returns from a given combination of test target and background medium. Unfortunately, test conditions vary over time -- especially if the test lane contains damp soil. In this section of the report, we briefly review various laboratory methods for determining the electromagnetic properties of target and background materials. We then describe methods for simulating the electromagnetic properties of damp, sandy soils with dry materials. We also describe methods for accurately determining the electromagnetic properties of such dry materials and for the long-term monitoring of the properties of test lanes composed of such materials.

Dielectric measurement techniques have a long history [6.1-6.3] and will be briefly mentioned here. Afsar, Birch, and Clarke [6.4] give a comprehensive review of techniques developed over the past two decades to measure dielectric properties of materials in the frequency range 1 MHz-1500 GHz.

Frequency domain laboratory techniques often employ propagation measurements in a waveguide transmission line containing the dielectric. Measurements of the input admittance of a shielded open-circuited coaxial line filled with the material are common [6.5]. Depending on the frequency range of interest, the admittance at the plane of the sample holder connector is measured by a capacitance bridge (kilohertz range), Schering or twin T bridges [6.6] (up to 200 MHz), or an Automatic Network Analyzer (ANA) (0.5 MHz-18 GHz). These admittance values are then converted by suitable formulas into complex permittivity, loss tangent, and so on. Closed cavity resonator techniques are also used for permittivity measurements in the microwave region [6.7-6.11]. As the frequency range of interest becomes still higher (greater than 20 GHz) open cavity resonator techniques are used [6.12-6.21], since at

the higher frequencies the open resonator can be made fairly small and the high Q values required for the measurement of low dielectric loss are easily attained.

Time domain laboratory methods for dielectric spectroscopy are also undergoing rapid development [6.22-6.28]. These methods typically make use of a reflected wave off a length of air line, part of which is filled with the material to be tested. The complex permittivity is determined from the measured reflection coefficients.

B. Laboratory Sample-Holder Measurements of the Electromagnetic Properties of Materials

B1. Dielectric Measurements Using Open-Circuit Coaxial Lines

Bussey [6.5] and, more recently, Jesch [6.29] have made measurements of the dielectric properties of materials using open, coaxial sample holders. The design of the sample holders, fabricated from 14 mm, 50 Ω precision coaxial air line and equipped with a 900-BT precision coaxial connector, is shown in fig. 6.1. Essentially, soil conductivity and permittivity is determined by the construction of a section of coaxial transmission line, as illustrated in fig. 6.1, with the soil serving as the lossy dielectric environment for the electromagnetic fields produced within the transmission line.

The impedance, z_{in}, at the input end of a transmission line has a characteristic impedance z_o and termination impedance z_e, given by

$$z_{in} = z_o \frac{z_e + z_o \tanh\gamma\ell}{z_o + z_e \tanh\gamma\ell}, \tag{6.1}$$

where $\gamma = \alpha + j\beta$ is the complex propagation constant of the transmission line, α and β are the respective attenuation and phase constants of the transmission line, and ℓ is the length of the transmission line. When the termination impedance is 0 (short circuit at the termination), eq. (6.1) becomes

$$z_{in,\ \text{short circuit}} = z_o \tanh\gamma\ell \tag{6.2}$$

whereas when the termination is an open circuit we have

$$z_{in,\ open\ circuit} = z_o\ [\tanh\gamma\ell]^{-1}\ . \qquad (6.3)$$

Dividing the short circuit input impedance by the open circuit input impedance yields

$$\frac{z_{in,\ short\ circuit}}{z_{in,\ open\ circuit}} = \tanh^2\ (\gamma\ell)$$

or

$$\gamma = \frac{1}{\ell}\ \tanh^{-1}\sqrt{\frac{z_{in,\ short\ circuit}}{z_{in,\ open\ circuit}}} \qquad (6.4)$$

or

$$\gamma = \frac{1}{2\ell}\ \ell n\ \frac{1 + \sqrt{z_{in,\ short\ circuit}/z_{in,\ open\ circuit}}}{1 - \sqrt{z_{in,\ short\ circuit}/z_{in,\ open\ circuit}}}$$

$$= \frac{1}{2\ell}\ \ell n\ \left|\frac{1 + \sqrt{z_{in,\ short\ circuit}/z_{in,\ open\ circuit}}}{1 - \sqrt{z_{in,\ short\ circuit}/z_{in,\ open\ circuit}}}\right|$$

$$+ \frac{j}{2\ell}\ \text{phase}\ \frac{1 + \sqrt{z_{in,\ short\ circuit}/z_{in,\ open\ circuit}}}{1 - \sqrt{z_{in,\ short\ circuit}/z_{in,\ open\ circuit}}} + 2n\pi\ , \qquad (6.5)$$

$n = 0, \pm1, \pm2, \ldots.$

Hence the attenuation constant α of the transmission line is

$$\alpha = \frac{1}{2\ell}\ \ell n\ \left|\frac{1 + \sqrt{z_{in,\ short\ circuit}/z_{in,\ open\ circuit}}}{1 - \sqrt{z_{in,\ short\ circuit}/z_{in,\ open\ circuit}}}\right| \qquad (6.6)$$

and the phase constant β is

$$\beta = \frac{1}{2\ell} \text{ phase } \frac{1 + \sqrt{z_{in,\ short\ circuit}/z_{in,\ open\ circuit}}}{1 - \sqrt{z_{in,\ short\ circuit}/z_{in,\ open\ circuit}}} + \frac{n\pi}{\ell} . \tag{6.7}$$

The TEM characteristic impedance z_o of the coaxial transmission line is

$$z_o = \sqrt{\frac{j\omega\mu}{\sigma + j\omega\epsilon}} \frac{\ell n(b/a)}{2\pi} , \tag{6.8}$$

where b,a are the outer and inner diameters of the coaxial line, respectively.

From Ampere's law,

$$\nabla \times \vec{H} = (\sigma - j\omega\epsilon) \vec{E} , \tag{6.9}$$

and Faraday's law,

$$\nabla \times \vec{E} = j\omega\mu \vec{H} , \tag{6.10}$$

we see that

$$\gamma^2 = j\omega\mu (\sigma - j\omega\epsilon) , \tag{6.11}$$

so that from measurements of α and β conductivity and permittivity are easily obtained,

$$\sigma(\omega) = 2 \alpha\beta/(\omega\mu) , \tag{6.12}$$

$$\epsilon(\omega) = (\alpha^2 - \beta^2)/(\omega^2\mu) . \tag{6.13}$$

The results of a series of measurements using this open-ended coaxial holder technique are shown in fig. 6.2. The technique is well-suited to making measurements of the dielectric properties of granular mixtures. Figure 6.2 shows data obtained at 600 MHz for various mixtures of sand and silicon carbide as the percentage of sand is varied.

B2. Permittivity and Permeability Measurements with a Two-Port Measurement Technique

As described more fully in Appendixes VI.A and VI.B, the complete electromagnetic proportion of materials can be obtained over a wide range of frequencies with a two port measurement set-up. We made a large number of measurements using an Automatic Network Analyzer (ANA). This particular system [6.30] is composed of an S parameter test set, sweep frequency generator, and a control computer. The system is capable of determining S parameters over the frequency range of 45 MHz to 26.5 GHz. We made all of our measurements between 50 MHz and 1.05 GHz. Before taking any data, calibrations were carried out with three standards: a precision short, an open circuit, and a 50 Ω matched load. These standards were all terminated in 3.5 mm connectors on the S parameter test set. We used a sample holder made from a 10 cm length of precision beadless 14 mm air line. The holder was terminated with GR-900 connectors. Samples of plastic material were machined on a lathe so that they fitted very precisely between the inner and outer conductors of the holder. Samples of the Teflon and nylon used to make test targets were prepared in this way. To measure the properties of a given sample, one of the GR-900 connectors was removed from the line and the machined sample was then inserted. The distance from the end of the holder to the sample was measured with a depth gauge and recorded before reattaching the GR-900 connector. The holder was then carefully connected to the ANA. See fig. 6.3.

Measurements of all four S parameters were taken over the frequency range from 50 MHz to 1.05 GHz for each material at 5 MHz intervals. This yielded 201 data points per plastic sample. The time required typically did not exceed 15 minutes per plastic sample -- including the time required to store data on a floppy disk. The data are stored as nine numbers for each frequency: four complex S parameters (two numbers each) and the frequency (one additional number).

All data are analyzed using a program* written in BASIC. The program prompts the user to input the following quantities: (1) the number of data

---

*Appendix VI.A, attached.

points, (2) the length of the sample holder in meters (0.0994), (3) the length of the sample, (4) the distance from the S_{11} end of the sample holder to the sample, and (5) the distance from the S_{22} end of the sample holder to the sample. The values given in (2)-(5) above are used to rotate the electrical phases from reference planes located at the GR-900 connectors to corresponding planes located at the S_{11} and S_{22} ends of the sample located inside the holder.

The program asks the user for a file name before retrieving the information from the disk. Values for S_{21} and S_{12} (after reference plane rotation) are displayed on the screen, as well as magnitude and phase differences. Since the system should be symmetrical after phase plane rotation, these differences should be close to 0. A set of differences significantly greater than zero indicate that one or more of the lengths entered in (2)-(5) above need adjustment, or that various system calibrations have not been properly performed.

The user can request that either the S_{11} S_{21} products or the S_{22} S_{12} products be used in the calculations. We used both sets of data; accordingly, there are pairs of overlapping curves for each of the four quantities shown in figures 6.4 and 6.5. The program calculates values of the complex permittivity and permeability for the sample according to formulas given in Appendix B. At this point the program will, at the user's option, print the results before saving them on the disk. The stored values are used later to produce graphs.

B3. Procedures for Determining EM Properties of Test Soils

Measurements of the permittivity and permeability of granular samples (such as dry sand and SiC sand mixtures) are done with methods similar to those described earlier in the section on plastic test targets. Two thin plastic washers are used to confine the material inside the sample holder. The procedure we have adopted involves first inserting a Teflon washer (14 mm diameter, 1.5 mm thickness) into one end of the beadless air line. A measured volume of the sample is then poured in from the other end while gently tapping the body of the holder to allow the sample to settle. A second 1.5 mm Teflon washer is inserted and pushed firmly into place using a metal tube. The distance from the end of the holder to each of the Teflon washers is then

measured with a depth gauge and recorded. The GR-900 precision coaxial connectors are reattached to the sample holder which is subsequently connected to the ANA (using GR-900/SMA adaptors and precision coaxial cables). Figure 6.3 shows the measurement setup. Examples of the measurements made on dry sand and on a 60%/40% mixture of dry sand and SiC are shown in figures 6.6 and 6.7.

Errors can be reduced by exercising care in sample preparation. The material between the Teflon washers must be free of voids or air gaps. The washers must be machined so that they present a flat face to the air on one side and to the particulate material on the other side. Washers must be placed correctly in the holder with the plane of the washer perpendicular to the center conductor. We tried to make the washers we used as thin as possible -- yet with sufficient material to maintain adequate rigidity. The washers are considered to be a part of the sample by the analysis program; their use may introduce errors if the material under test is electromagnetically very dissimilar. The method used for calculating permittivities and permeabilities also requires that the sample be less than one-quarter of a wavelength long. This limits the length of the sample which can be used or limits the frequency range which can be analyzed for materials of high dielectric constant. Very lossy materials (for which no significant transmission through the sample holder takes place) would also be difficult or impossible to characterize. Finally, for solid samples, care must be taken to insure that the samples fit tightly in the holder to minimize contact resistance.

C. In Situ Methods

A number of investigators have, with varying degrees of success, attempted to develop probe methods for determining the electromagnetic properties of soils. A report [6.31] outlines the measurement technique and the construction details for a two-frequency, *in situ* probe which can be inserted into holes bored into clay or loose soil. The instrument is reliable and easy to use. It is powered by two nine-volt transistor radio batteries and is portable. Measurements at UHF frequencies should be accurate to within 10% for conductivity and permittivity. Dalton *et al*. [6.32] used a parallel-

electrode probe on the end of a parallel wire transmission line, with time domain reflectometer equipment for a read-out of soil moisture and electrical conductivity. The analysis assumes that the permittivity and the conductivity are independent of frequency, that the soil has a low loss tangent, and that the end of the parallel-electrode probe is a perfect open circuit at all frequencies. There are conditions (such as in dry, salt-free sand) for which the method might give some useful, qualitative information.

There are a number of other methods for determining the electromagnetic properties of materials in situ [6.33-6.37]. More recently, Scott and Smith [6.38, 6.39] have shown how to use monopoles and more complicated probes to measure the electromagnetic properties of granular and liquid materials. Another approach, used in the petroleum industry, involves placing cavity-backed antennas on borehole instruments. With this technique, the transit-time and the attenuation of the electromagnetic waves are measured -- from which the complex permittivity can be determined at a fixed frequency.

We have studied the information available and concluded that the four-terminal ANA method -- although less convenient than in situ schemes -- is still the best measurement scheme for general use. We recommend that this method be used to measure not only the electromagnetic properties of test targets but also that of the background media.

D. Measuring the Electromagnetic Properties of Magnetic Materials

Many techniques for the measurement of the magnetic properties of materials are available [6.40-6.42]. Most techniques for determining magnetic susceptibility involve placing the sample in a weak uniform and time-varying source field (less than 4×10^{-3} A/m) which does not saturate the sample, so the initial susceptibility obtained is independent of the magnetizing field and hysteresis effects are avoided. As Anderson [6.43] has noted, measurement techniques often involve balancing a Maxwell inductance bridge with the sample inserted into one solenoidal inductance arm of the bridge (figure 6.8). Another approach is to note the change in mutual reluctance between two coils set up in a coaxial or orthogonal relation to each other when the magnetic sample material is placed near the coils, calibrating the system with a standard of known susceptibility and normalizing sample size to an equivalent

half-space composed of material of identical susceptibility to the sample's. One paramagnetic standard often used for calibrating susceptibility bridge measurements is ferrous ammonium sulfate $FE(NH_4)_2\ (SO_4)_2 \cdot 6H_2O$, with a molecular weight of 392.15. The susceptibility of this salt is $32.6 \times 10^{-6} \times 4\pi$ SI units/g.

Figure 6.8 shows a typical susceptibility bridge which detects an inductance change in test coil, C_2, by action of the coil's field on a sample having unknown susceptibility. Coils C_1 and C_2 are solenoids carefully matched for inductance. M_1 and M_2 are identical variable inductors. In operation, the bridge is balanced with no specimen in either coil through variable resistor R and inductor M_1. The specimen is then inserted into C_2 (test coil) and the bridge balanced with inductor M_2 where the inductance adjustment is proportional to the susceptibility. Calibration of the inductance M_2 may be achieved by balancing the bridge with a test tube containing a known weight of a paramagnetic compound such as ferrous ammonium sulfate of known susceptibility in the coil C_2. Calibration is simply accomplished by balancing the bridge with inductor M_2 when the test standard is placed in C_2. The test tube is then removed and bridge balanced with variable inductor M_1. The same test tube with the same amount of the same standard substance is again inserted into coil C_2 and the bridge balanced with M_2. This process is repeated throughout the inductance range of C_2 so as to obtain a calibration curve referred to the known standard. If ferrous ammonium sulfate is used, it should be kept in a fresh, sealed bottle since the salt is slightly hygroscopic.

In these techniques, the sample is energized with a low-frequency field. This field must have a low-enough frequency that no conductivity response of the sample will be observed. A model which provides a general rule of thumb for the highest usable ac frequency is that of a conducting permeable sphere in a uniform alternating magnetic field,

$$H = H_0 e^{-j\omega t}\ , \qquad (6.14)$$

as shown in figure 6.9. Ward [6.44] has slightly rewritten (for $e^{-j\omega t}$ time dependence) Wait's [6.45] original results for the in-phase M and out-of-phase

N components of the induced dipole moment of a sphere in a uniform alternating magnetic field when the wavelength in the external host medium is much greater than the radius of the sphere ($|\gamma_1 a| \ll 1$ where $\gamma_1 = [j\omega\mu_1\sigma_1 + \omega^2\mu_1\epsilon_1]^{1/2}$):

$$M - jN = \left[\frac{2\mu_2(\tan\alpha - \alpha) - \mu_1(\alpha - \tan\alpha + \alpha^2\tan\alpha)}{2\mu_2(\tan\alpha - \alpha) + 2\mu_1(\alpha - \tan\alpha + \alpha^2\tan\alpha)} \right] ,$$

$$\alpha = (j\omega\mu_2\sigma_2)^{1/2}a. \qquad (6.15)$$

The in-phase and quadrature components of the induced dipole moment of a sphere are shown plotted as a function of the response parameter of a sphere, $\theta = (\omega\sigma_2\mu_2)^{1/2}a$, in figure 6.10. These components are shown in parametric fashion for $\mu_2/\mu_1 = 1$ (free space) to $\mu_2/\mu_1 = 1000$ (steel sphere).

In order that the conductivity response of the sample be small, fig. 6.10 shows that $\theta^2 = (\omega\mu_2\sigma_2)a^2$ should be $\ll 1$. In the case of pure magnetite, the permeability μ_2 is approximately $1.5 \times 4\pi \times 10^{-7}$ H/m and the conductivity σ_2 is about 1.5×10^4 S/m. Thus, for a 2.5 cm diameter sphere and the condition that $\theta = 0.1$, we find that the maximum allowable frequency is approximately 400 Hz. The maximum allowable frequency for samples that are considerably less conductive than pure magnetite may be higher while still avoiding sample conductivity response. Wait's work [6.45] can also be used to quantitatively assess detection limits for both conductivity and permeability contrasts.

A susceptibility meter was used in measuring the susceptibility of a sand and magnetite mix provided to NIST by Lee Anderson of BRDEC (Belvoir Research, Development and Engineering Center). The sample consists of silica sand and magnetite of about 30 mesh size. The susceptibility meter is quite portable (0.5 kg with dimensions of 190 x 80 x 30 mm, operating on one disposable 9 V battery).

The meter contains two coils placed orthogonally to each other in the detector head, which is mounted in the bottom of the instrument case (circuit diagram shown in fig. 6.11). In a nonmagnetic environment the voltage induced in the receiver coil by the transmitter coil is zero. When a sample is brought near the coils, a voltage proportional to the magnetic susceptibility

of the sample is induced in the receiver coil. The received signal is detected by a phase-locked amplifier and after rectification is sent to drive an analog panel meter, which is thermally compensated and directly calibrated for susceptibility. Field strengths are less than $4\pi \times 10^{-3}$ A·turns/m at 1000 Hz so that with the phase sensitive receiver circuit the influence of electric conductivity in most samples is usually eliminated. As indicated by Anderson [6.43], calibration is usually done for a half-space geometry, which is convenient when measurements are performed in the field. When laboratory samples are measured, a multiplicative correction factor should be applied according to the soil sample size. A chart indicating this half-space correction factor is given in figure 6.12 from information provided by the manufacturer.

The silica sand-magnetite mixture's susceptibility (~330 g sample, ~50 mm diameter) was measured and found to be approximately 175000×10^{-6} SI units uncorrected for sample size. Using a correction factor of 2.0 from fig. 6.12, the susceptibility of the 330 g sample is about 350000×10^{-6} SI units. For mine detection standards, such measurements can provide the practical property range limits for which detection feasibility of various mine detection systems can be judged. Similar comments can be made about other physical property contrast limits, such as complex permittivity (as a function of frequency), density, and acoustic velocity.

E. Recommendations and Conclusions

We have stressed the importance of accurate test instrumentation for characterizing the electromagnetic properties of target materials and test lane media. Time domain methods show considerable promise for rapid and straightforward measurement of complex permittivity and complex permeability. We recommend that either time domain or frequency domain Automatic Network Analyzers (ANAs) be used for this purpose. A considerable body of commercial, off-the-shelf hardware and software already exists. The listing for a program which we have been using is provided as Appendix VI.A.

We are aware of the Army's desire for *in situ* measurements of μ and ϵ. The need for such measurements in areas far from laboratory facilities and where mine detectors are to be subjected to field testing is well established.

We suggest that for permeability measurements the method described in Section D of this chapter be used -- and that a laboratory network analyzer be used to calibrate all such portable instruments beforehand. We are not aware of any in situ techniques for measuring μ and ϵ which are both accurate and wide-band. Perhaps some can be developed in the future. In the meantime, we recommend that the permittivity measurements continue to be performed with coaxial sample holders as described in Section B.2 and Section B.3.

References (VI)

[6.1] von Hippel, A. R. Dielectric materials and applications. Cambridge Massachusetts Inst. Technology; 1954, 438 p.

[6.2] von Hippel, A. R. Dielectric and waves. New York, NY: John Wiley & Sons; 1954, 284 p.

[6.3] Hill, N. E.; Vaughn, W. E.; Price, A. H.; Davies, M. Dielectric properties and molecular behavior. London: Van Nostrand; 1969, 480 p.

[6.4] Afsar, M. N.; Birch, J. R.; Clarke, R. N. The measurement of properties of materials. Proc. IEEE; 1986; 74(1), pp. 183-199.

[6.5] Bussey, H. E. Dielectric measurements in a shielded open circuit coaxial line. IEEE Trans. on Instr. Meas.; 1980; IM-29(2), pp. 120-124.

[6.6] Jones, R. N.; Bussey, H. E.; Little, W. E.; Metzker, R. F. Electrical characteristics of corn, wheat, and soya in the 1-200 MHz range; 1978; Nat. Bur. Stand. (U.S.) NBSIR 78-897.

[6.7] Birnbaum, G.; Franeau, J. Measurement of the dielectric constant and loss of solids and liquids by a cavity perturbation method. J. Appl. Phys.; 1949; 20, pp. 817-818.

[6.8] Horner, F. Resonance methods of dielectric measurement at centimeter wavelengths. J. IEEE; 1946; 93(III), pp. 55-57.

[6.9] Bethe, H. A.; Schwinger, J. Perturbation theory of resonant cavities; 1943; NDRC, Rpt. D2-117.

[6.10] Cook, R. J. Microwave cavity methods, in high frequency dielectric measurements; 1973; J. Chamberlain and G. W. Chantry, ed., IPC Science & Technology Press, pp. 12-27.

[6.11] Bussey, H. E. Measurement of RF properties of materials: a survey. Proc. IEEE; 1967; 55, pp. 1046-1053.

[6.12] Culshaw, W.; Anderson, M. V. Measurement of permittivity and dielectric loss with a millimeter wave Fabry-Perot interferometer. Proc. IEEE; 1962; 109(B), Suppl. 23, pp. 820-826.

[6.13] Degenford, J.; Coleman, P. D. A quasi-optics perturbation technique for measuring dielectric constants. Proc. IEEE; 1966; 54, pp. 520-522.

[6.14] Degenford, J. A quasi-optic technique for measuring dielectric loss tangents. IEEE Trans.; 1968; IM-17, pp. 413-417.

[6.15] Cullen, A. L.; Yu, P. K. The accurate measurement of permittivity by means of an open resonator. Proc. R. Soc. A; 1971; 325, pp. 493-509.

[6.16] Conbau, G.; Schwering, F. On the guided propagation of electromagnetic wave beams. IRE Trans.; 1961; AP-9, pp. 248-256.

[6.17] Cullen, A. L.; Nagenthiram, P.; Williams, A. D. Improvement in open resonator permittivity measurement. Electron. Letters; 1972; Vol. 8, pp. 577-579.

[6.18] Cullen, A. L.; Nagenthiram, P.; Williams, A. D. A variational approach to the theory of the open resonator. Proc. R. Soc. A.; 1972; 329, pp. 153-169.

[6.19] Kogelnik, H.; Li, T. Laser beams and resonators. Proc. IEEE; 1966; 54, pp. 1312-1329.

[6.20] Cook, R. J.; Jones, R. G.; Rosenberg, C. R. Comparison of cavity and open resonator measurements of permittivity and loss angle at 35 GHz. IEEE Trans.; 1974; IM-23, pp. 438-442.

[6.21] Jones, R. G. Precise dielectric measurements at 35 GHz using an open microwave resonator. Proc. IEEE.; 1976; 123(4), pp. 284-290.

[6.22] Van Gemert, M. J. C. High-frequency time-domain methods in dielectric spectroscopy. Phillips Res. Rpts; 1973; 28, pp. 530-572.

[6.23] Gans, W. L.; Andrews, J. R. Time-domain automatic network analyzer for measurement of RF and microwave components; 1975; Nat. Bur. Stands. (U.S.) Tech. Note 672.

[6.24] Nicolson, A. M.; Ross, G. F. Measurement of the intrinsic properties of materials by time-domain techniques. IEEE Trans. Instr. Meas.; 1970; IM-14(4).

[6.25] Peyrelasse, J.; Boned, C.; LePetit, J. P. Setting up of a time-domain spectroscopy experiment. Application to the study of the dielectric relaxation of pentanol isomers. J. Phys. Sci. Instr.; 1981; 14, pp. 1002-1008.

[6.26] Nakamura, H.; Mashimo, S.; Wada, A. Precise and easy method of TDR to obtain dielectric relaxation spectra in the GHz region. Japanese J. Appl. Phys.; 1982; 21(7), pp. 1022-1024.

[6.27] Suggett, A. Time-domain methods, dielectric and related molecular processes. Chem. Soc. London; 1972; Vol. 1, pp. 101-120.

[6.28] Bottreau, A. M.; Dutuit, Y.; Moreau, J. On a multiple reflection time-domain method in dielectric spectroscopy: Application to the study of some normal primary alcohols. J. Chem. Phys.; 1977; 66(8), pp. 3331-3336.

[6.29] Jesch, R. L. Dielectric measurements of five different soil textural types as functions of frequency and moisture content; 1978; Nat. Bur. Stand. (U.S.) NBSIR 78-879.

[6.30] Measuring Dielectric Constant with the HP 8510 Network Analyzer. Product Note No. 8510-3, Hewlett-Packard Corp., Palo Alto, CA; August 1985.

[6.31] Caldecott, R.; et al. A radio frequency probe to measure solid electrical parameters; January 22, 1985; Final Report 715616-4; Ohio State University ElectroScience Lab., Columbus, Ohio.

[6.32] Dalton, F. N.; et al. Time-domain reflectometry: Simultaneous measurement of soil water content and electrical conductivity with a single probe. Science; June 1, 1984; 224, pp. 989-990.

[6.33] King, R. W.; Smith, G. S. Antennas in matter; Fundamentals, theory, and applications. Cambridge, MA: M.I.T. Press; 1981.

[6.34] Smith, G. S.; King, R. W. P. Electric field probes in material media and their application in EMC. IEEE Trans. Electromagn. Compat.; 1975; EMC-17, pp. 206-211.

[6.35] Smith, G. S.; King, R. W. P. Electric field probes in material media and their application in EMC. IEEE Trans. Electromagn. Compat.; 1976; EMC-18, p. 130.

[6.36] Smith, G. S.; Nordgard, J. D. Measurements of the electrical constitutive parameters of materials using antennas. IEEE Trans. Ant. prop.; 1985; 33(7), pp. 783-792.

[6.37] Scott, W. R. Dielectric spectroscopy using shielded open-circuited coaxial lines and monopole antennas of general length. Ph.D. thesis, Georgia Inst. Tech.; 1985, 228 p.

[6.38] Scott, W. R. and Smith, G. S. Dielectric spectroscopy using monopole antennas of general electrical length. IEEE Trans. on Antennas & Prop.; July 1986; AP-34(7), pp. 919-929.

[6.39] Smith, G. S. and Scott, W. R. A simple method for the in situ measurement of the electrical properties of the ground. Paper JA02-3, pages 242-245, 1987 IEEE AP-S International Symposium Digest, June 15th-19th at Virginia Tech. (IEEE Catalog No. CH2435-6/87).

[6.40] Nagata, T. Rock magnetism. Tokyo: Maruzen Press; 1961, 350 p.

[6.41] Akimoto, S. Magnetic properties of ferromagnetic oxide minerals as a basis of rock magnetism. Adv. Phys.; 1957; 6(288).

[6.42] Heiland, C. A. Geophysical exploration. Englewood Cliffs, New Jersey: Prentice Hall; 1940, pp. 310-314.

[6.43] Anderson, L. Private Communication; 1985.

[6.44] Ward, S. H. Electromagnetic theory for geophysical applications. Mining Geophys.; 1967; II, p. 78.

[6.45] Wait, J. R. A conducting sphere in a time varying field. Geophys.; 1951; 16, p. 666.

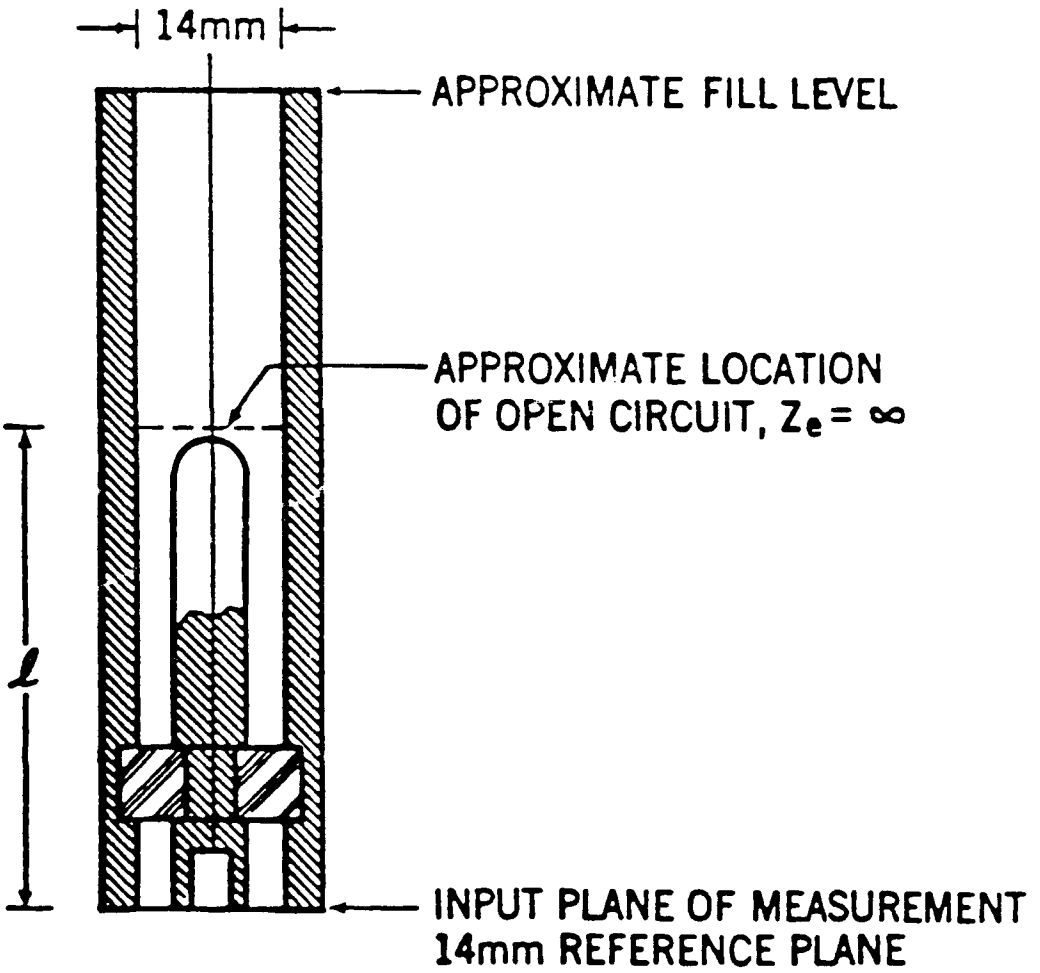

Fig. 6.1 Cross-sectional drawing of the coaxial transmission line sample holder for the single-port measurement scheme.

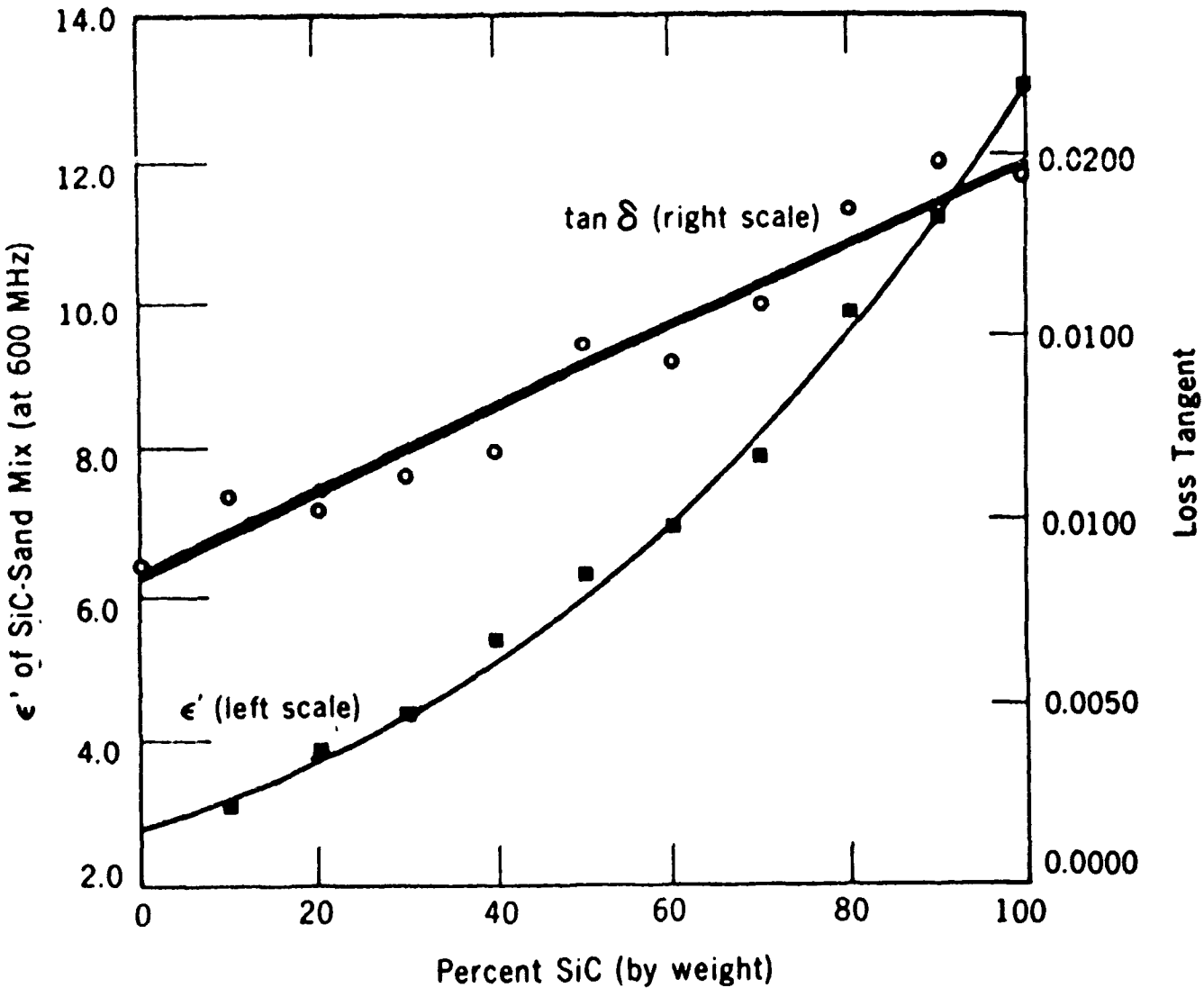

Fig. 6.2 Electromagnetic properties (at 600 MHz) of a blend of SiC and silica sand for various percentages (by weight) of SiC.

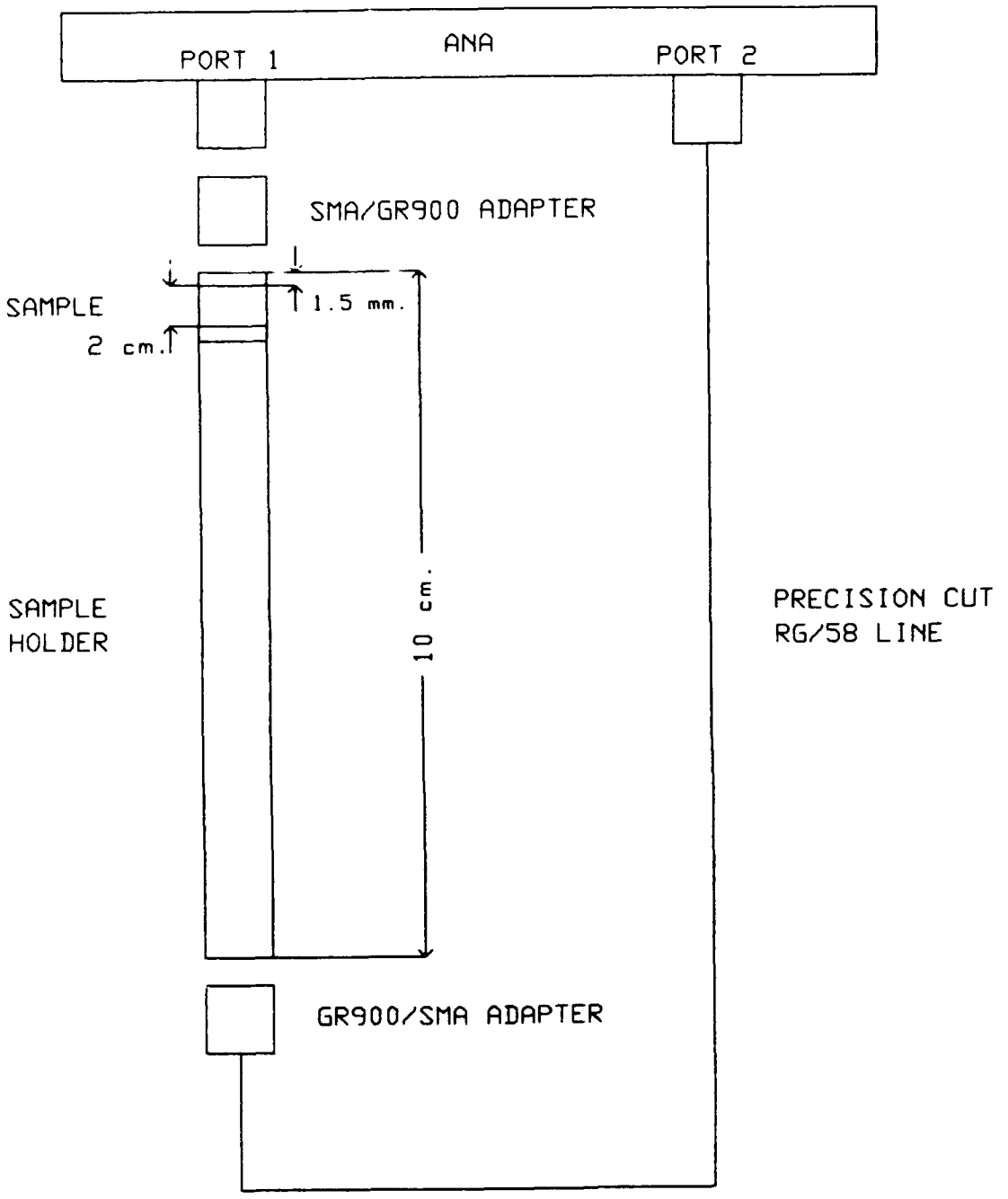

Fig. 6.3 **Schematic of the ANA materials measurement system.**

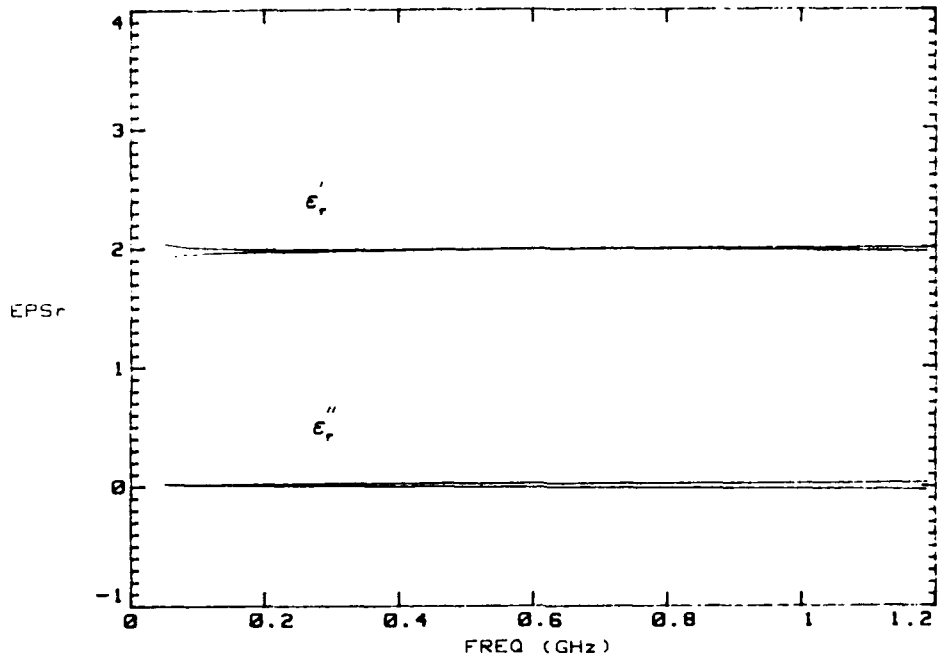

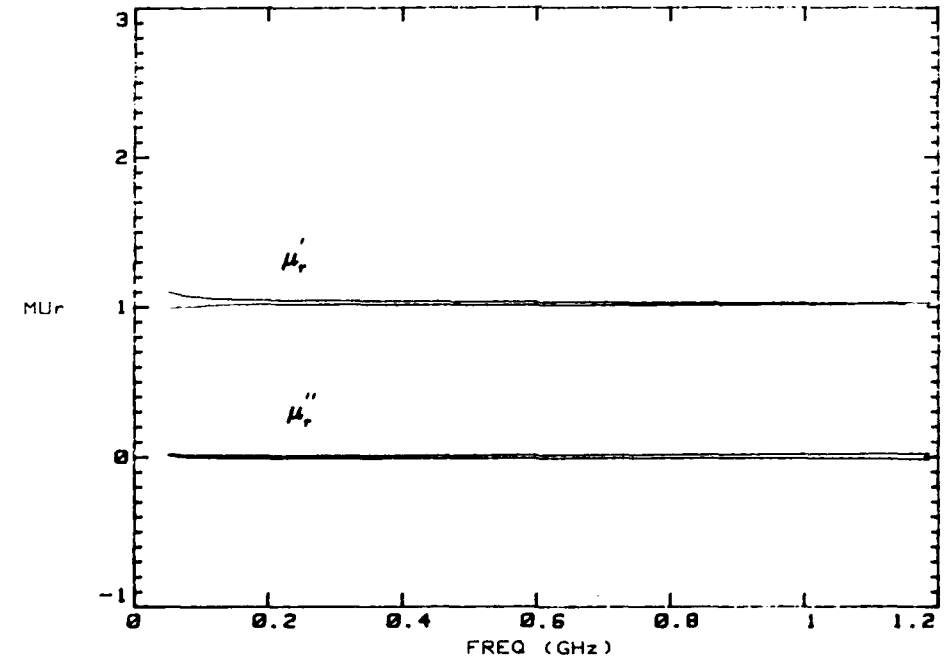

Fig. 6.4 Complex permittivity and permeability of Teflon as measured with the ANA.

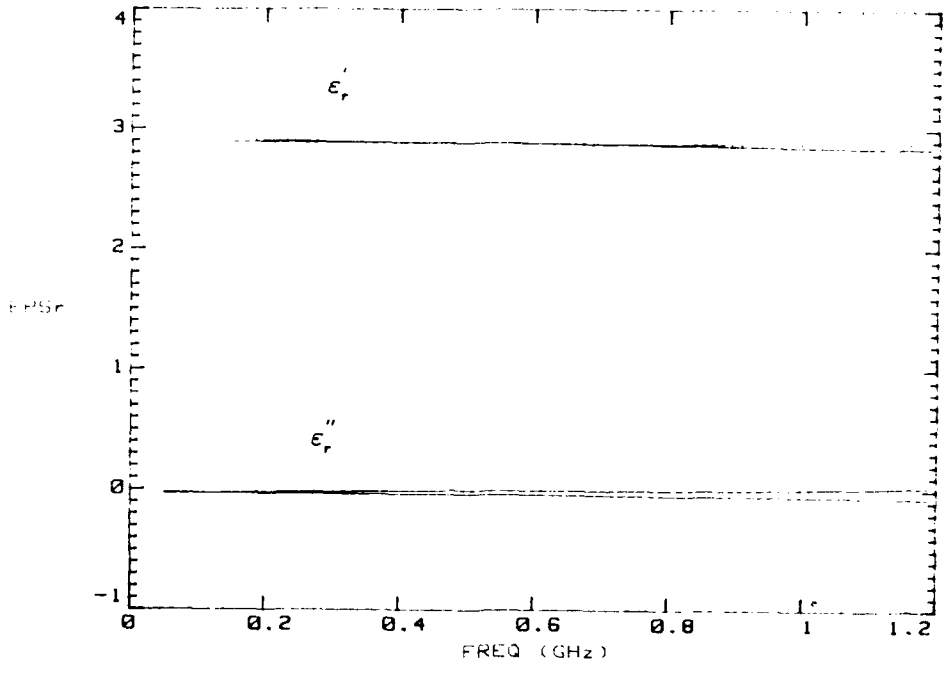

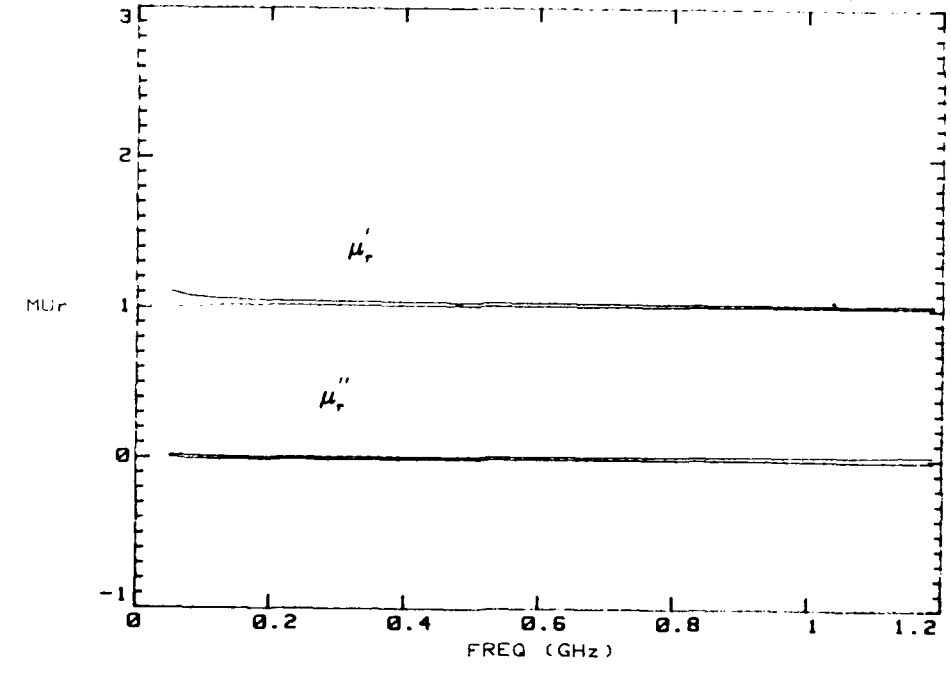

Figure 6.5 Complex permittivity and permeability of nylon as measured with the ANA.

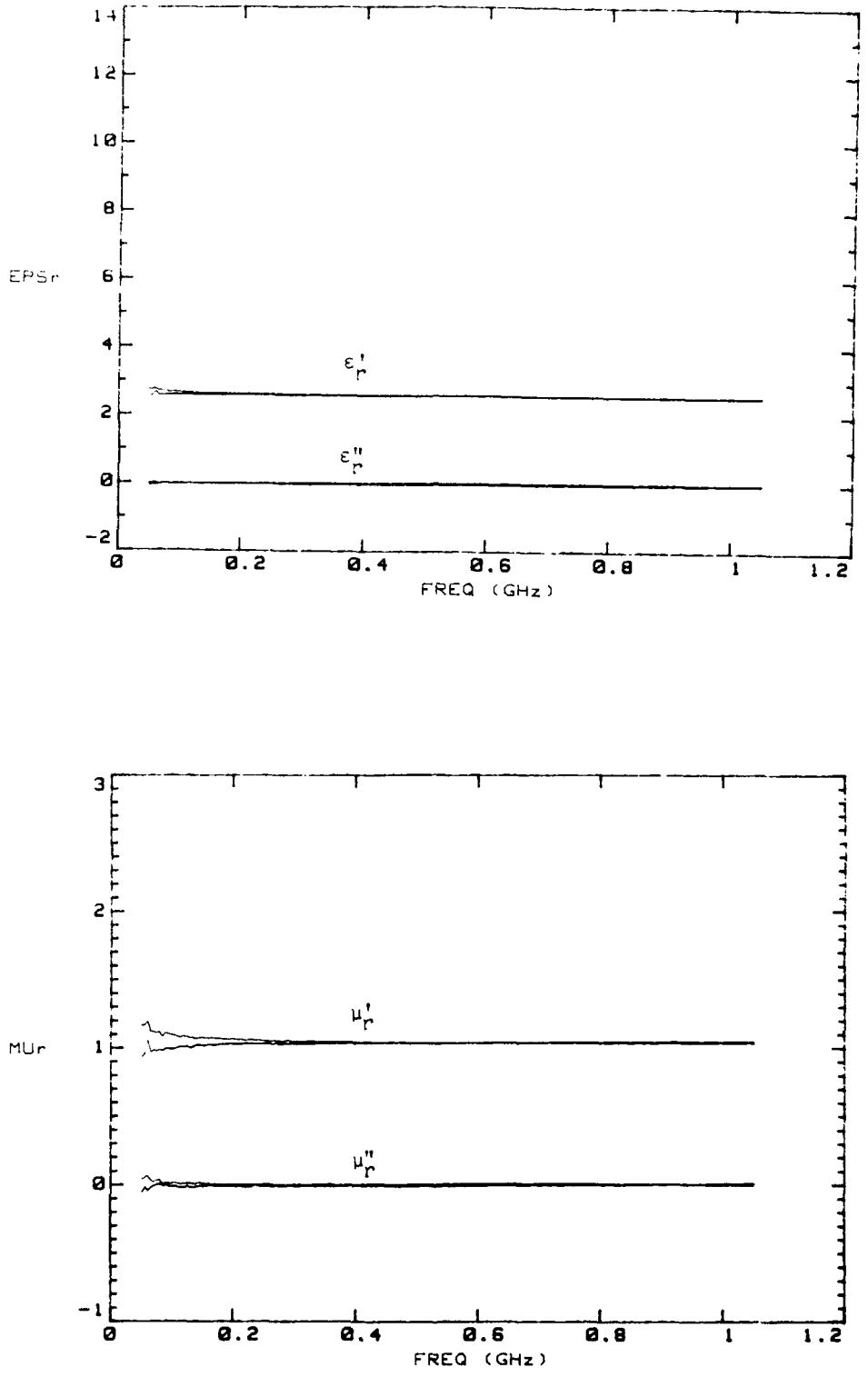

Fig. 6.6 Complex permittivity and permeability for dry sand as measured with the ANA.

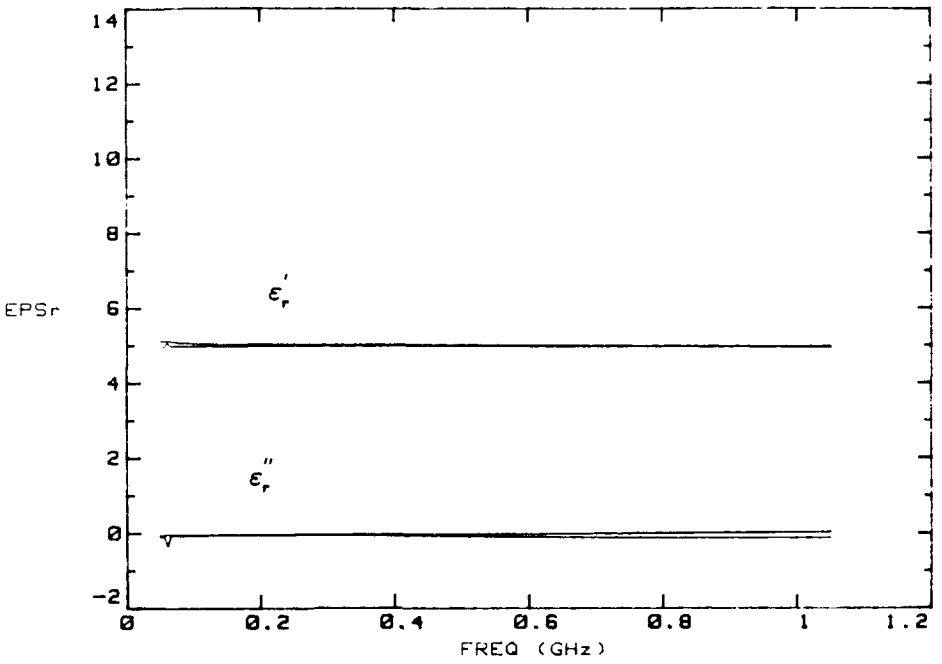

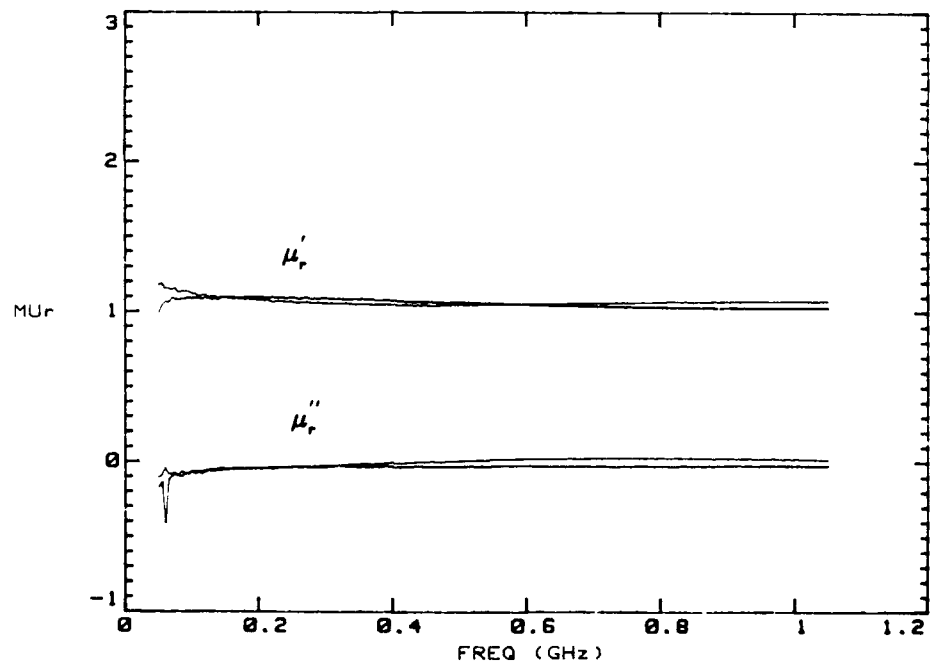

Fig. 6.7 Complex permittivity and permeability of a 60% dry sand and 40% SiC (by weight) mixture as measured with the ANA.

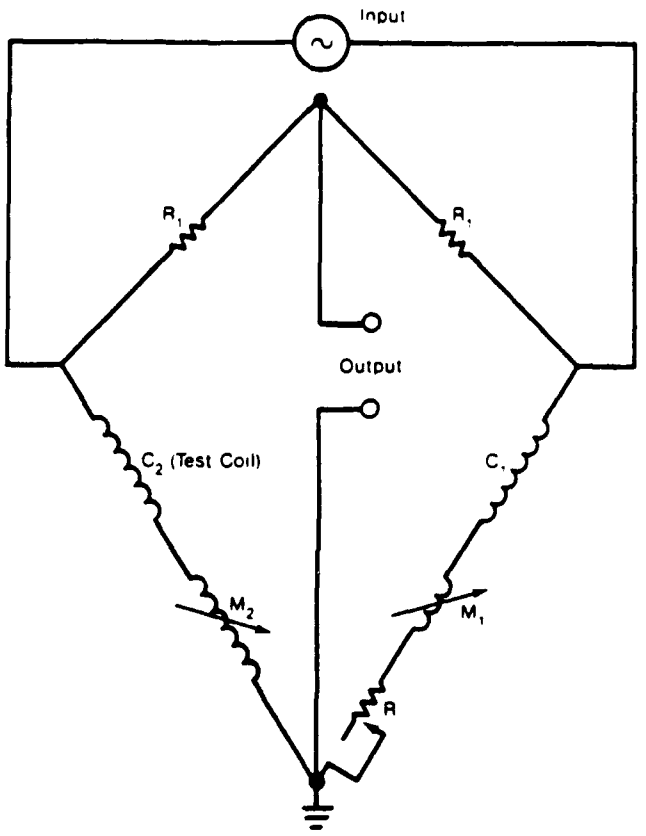

Fig. 6.8 Schematic diagram for a typical susceptibility bridge.

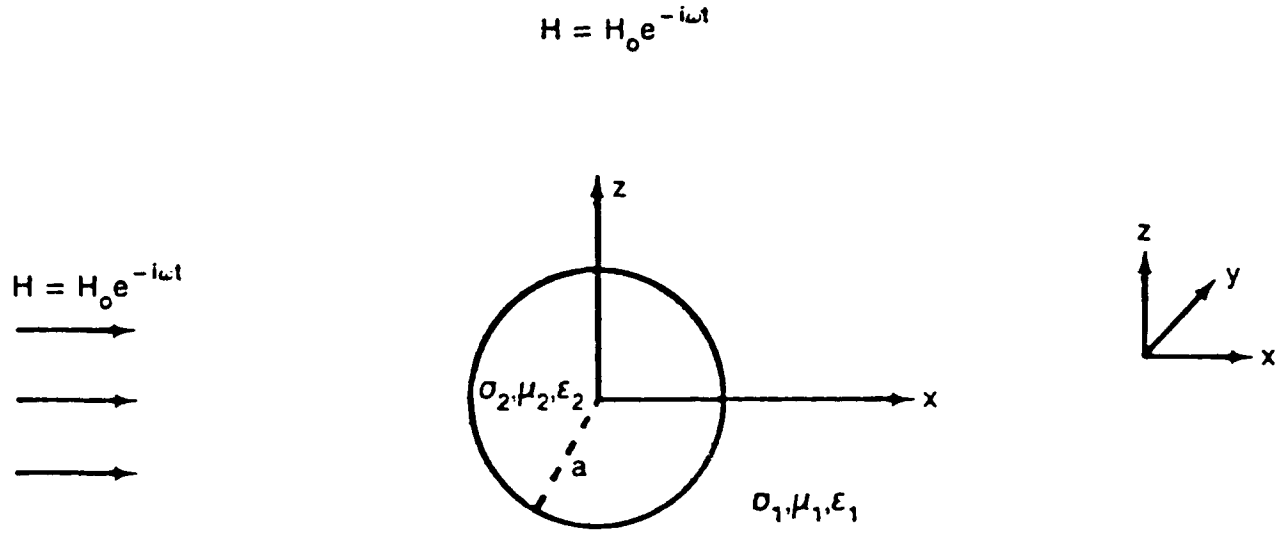

Figure 6.9 Conducting permeable sphere of radius a in a uniform alternating magnetic field. The conductivity, permeability, and permittivity of the host medium are σ_1, μ_1, and ϵ_1, respectively. The conductivity, permeability, and permittivity of the sphere are σ_2, μ_2, and ϵ_2, respectively.

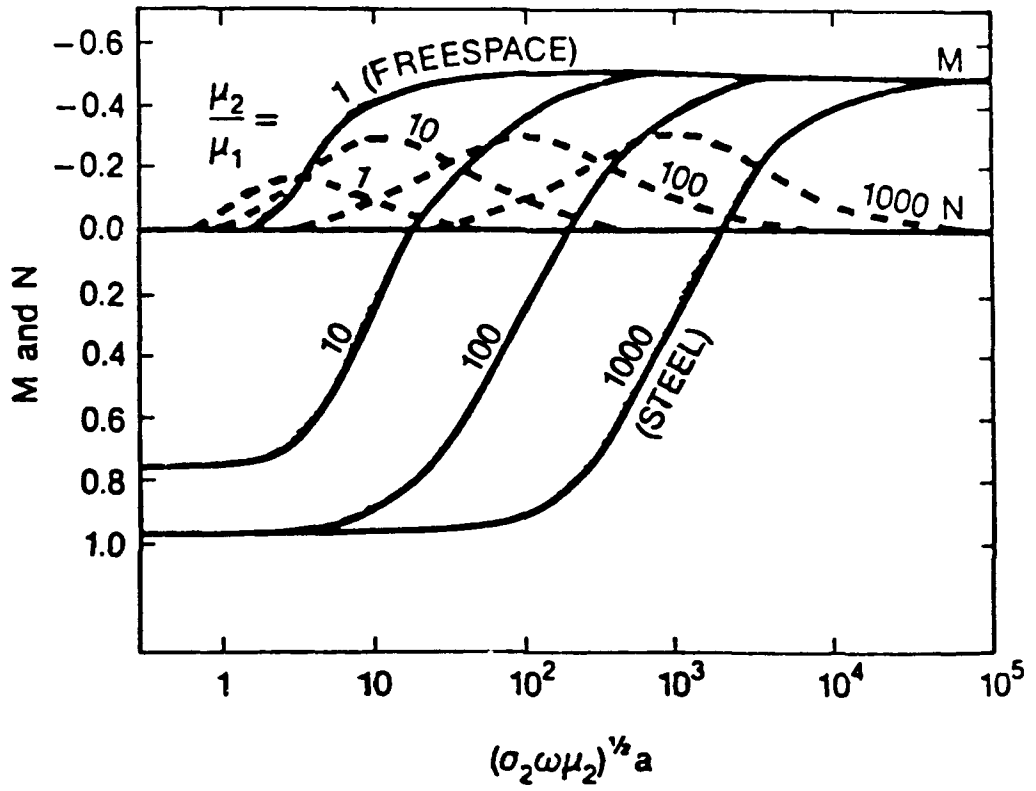

6.10 In-phase (M) and out-of-phase (N) components of the induced dipole moment for a sphere in a uniform alternating magnetic field for the case $|\gamma_1 a| << 1$. See reference [6.44].

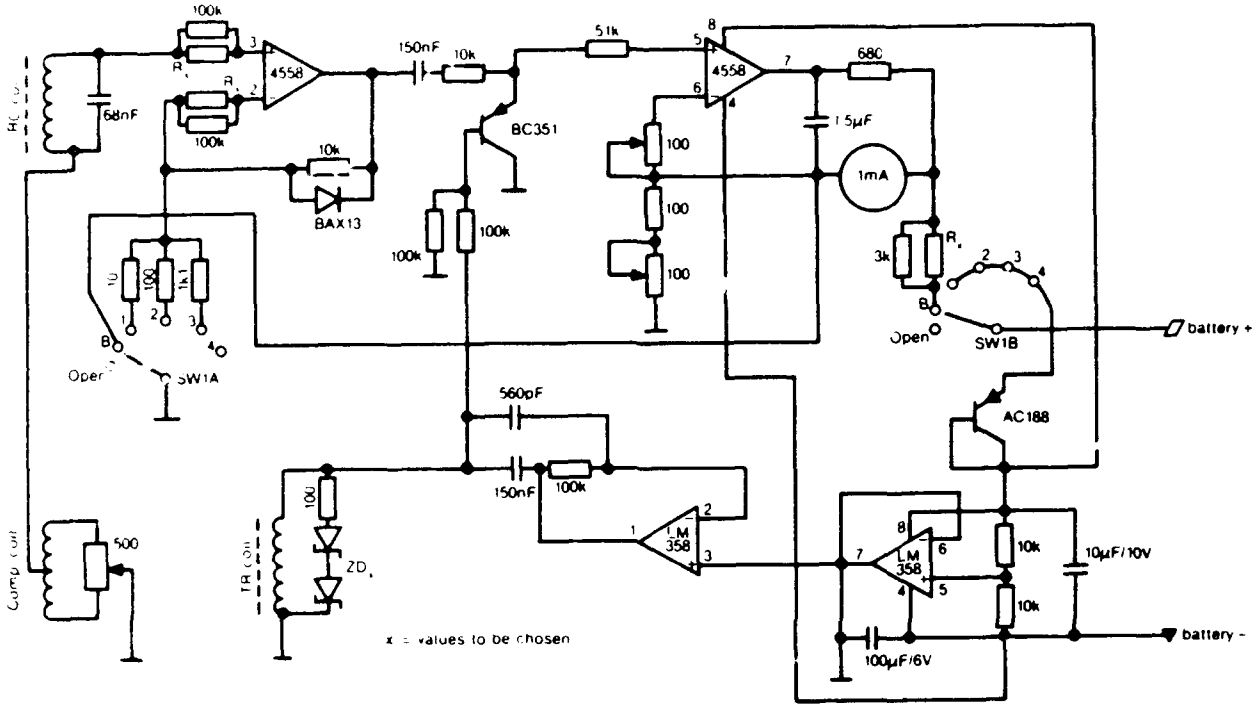

Figure 6.11 Circuit diagram for the susceptibility meter.

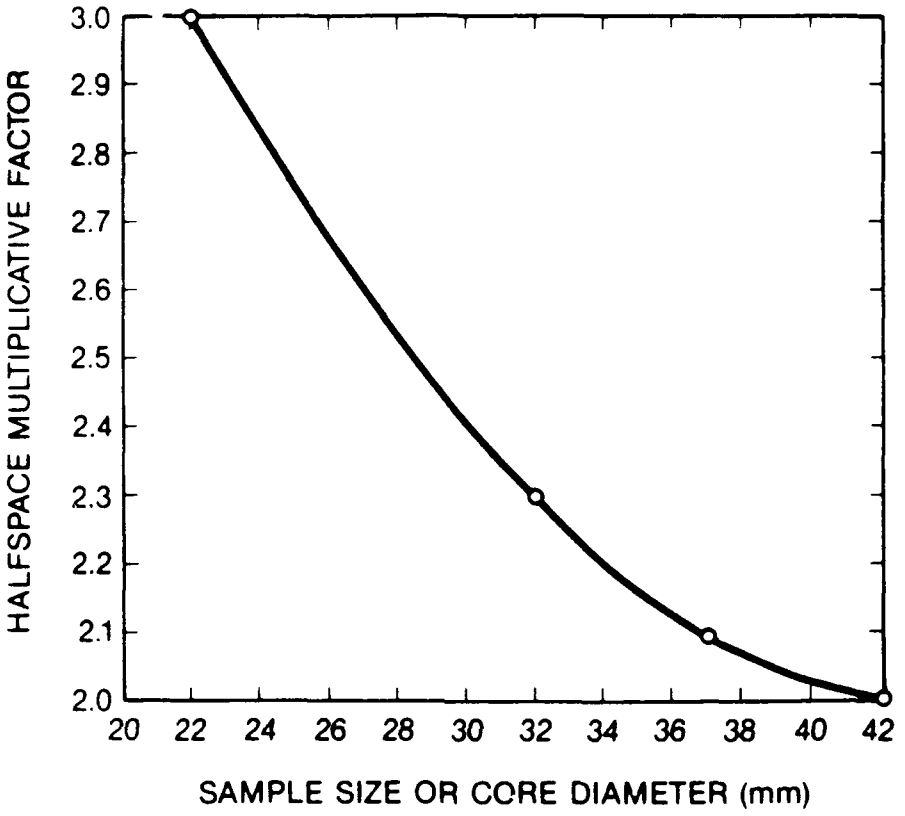

Fig. 6.12 Half-space multiplicative correction factor for susceptibility measurements.

VII. OBJECTIVE MEASURES OF DETECTOR PERFORMANCE

A. Introduction

Parameters affecting performance evaluations of electromagnetic mine detection systems may be divided into two main categories. In the first category are those factors that are not directly concerned with the detector's ability to find targets. Some of these parameters are cost, weight, battery life, reliability, ease of operation, and ease of repair. Any attempt to assign an overall figure of merit to a detector system should include weighting factors for this category of parameters, but this task is not within the expertise of NIST personnel and is best left to the Army.

The second category consists of those factors that do affect the detector's ability to find targets. Within this category, we may consider two different classes of performance measures. The first class addressed in this chapter is detector-based performance measures. These include such parameters as noise levels, detector dynamic range, operating frequency, bandwidth, sensor height and tilt angle. The second class addressed is target-based performance measures. These measures are essentially detector-independent and include such parameters as target-earth permittivity (or conductivity or permeability) contrast ratio, target size, target depth, and target shape. What follows in this chapter is a discussion of detector-based performance measures, target-based performance measures, and recommendations for detector tests within both classes.

B. Detector-Based Performance Measures

B1. Noise Factor of Mine Detectors

If there were no noise at the receiver input of the mine detector and none were generated by the receiver, sufficient amplification would result in the detection of any signal, even for a small contrast between the electromagnetic properties of the land mine and host soil. In reality, noise is always present; consequently, amplification of a signal results in amplification of noise as well. Furthermore, the minimum detectable signal power in the receiver is limited by noise which can be attributed to the following

internal and external sources: (a) equipment noise (amplifier or sensor noise); (b) cosmic and atmospheric noise picked up by antenna; (c) man-made interference (machinery, other radio transmitters), and (d) ground clutter. If these noise sources were the only limiting factors affecting mine detection, then a suitable requirement would be that the secondary electromagnetic fields due to the presence of a land mine would not be exceeded by these noise sources.

B1.1 Ideal System Noise Factor

The system noise factor of any ideal receiver may be simply defined as a measure of the degradation of the signal-to-noise ratio as the signal passes through the receiver (which depends on the design of the input stages and frequency of operation of the receiver). The system noise factor, SNF, of a mine detector is defined, therefore, as the power ratio of $(S/N)_{in}$ to $(S/N)_{out}$; that is,

$$SNF \equiv 10 \log_{10} \frac{(S/N)_{in}}{(S/N)_{out}} . \qquad (7.1)$$

For an ideal receiver $(S/N)_{in} = (S/N)_{out}$, so SNF = 0 dB. Equation (7.1) is a measurable quantity for evaluating mine detector performance and, in general, depends both on operating frequency and another measurable quantity of the system, its dynamic range.

B1.2 Overall Operating Noise Factor

For a general receiving system free from the spurious effects of ground clutter, the operating system noise factor [7.1-7.3] is given by

$$f = f_a + (\ell_c - 1)(\frac{T_c}{T_o}) + \ell_c(\ell_t - 1)(\frac{T_t}{T_o}) + \ell_c\ell_t(f_d - 1) , \qquad (7.2)$$

where f_a = the external noise factor defined as

$$f_a = p_n/KT_ob = T_a/T_o \qquad (7.3)$$

p_n = noise power available from an equivalent loss-free antenna in watts,

K = Boltzmann's constant = 1.38×10^{-23} J/K,

T_o = reference temperature, taken as 288 K,

b = effective noise power bandwidth of the receiving system in hertz,

T_a = effective antenna temperature in presence of external noise,

ℓ_c = antenna circuit loss (available input power/available output power),

T_c = actual temperature, in kelvins, of the antenna system and nearby ground,

ℓ_t = transmission line loss (available input power/available output power),

T_t = actual temperature, in kelvins, of the transmission line,

f_d = noise factor of the receiver,

F_a = the external noise figure defined as

$$F_a = 10 \log f_a \text{ (dBW)} ,$$

F_d = the noise figure of receiver defined as

$$F_d = 10 \log f_d \text{ (dBW)} .$$

If $T_c = T_t = T_o$, eq (7.2) becomes

$$f = f_a - 1 + \ell_c \ell_t f_d , \tag{7.4}$$

where

$$f_c = 1 + (\ell_c - 1)\left(\frac{T_c}{T_o}\right) \tag{7.5}$$

is the noise factor associated with the antenna circuit losses and

$$f_t = 1 + (\ell_t - 1)\left(\frac{T_c}{T_o}\right) \tag{7.6}$$

is the noise factor associated with transmission line losses. For no antenna circuit or transmission line losses, f is given by

$$f = f_a - 1 + f_d . \tag{7.7}$$

Internal system noise can be closely controlled by the manufacturer for most mine detection systems and may be quickly determined by BRDEC in validation testing. External noise sources are less controllable; of these, atmospheric and ground clutter are the least controllable.

B1.3 Atmospheric Noise

Spaulding [7.3] has given the minimum and maximum external noise figure due to expected atmospheric noise as a function of frequency (from 0.1 Hz to 10^8 Hz). These are shown in figures 7.1 and 7.2 and take into account the entire earth's surface, all seasons, and times of day. In the frequency range 0.1 Hz-10 kHz (that of most operating metal mine detection units), there is very little seasonal, diurnal, or geographic variation. The variability in the 100-120 kHz range is principally due to the variability of the earth-ionosphere waveguide cutoff.

Relation (7.3) can be written

$$P_n = F_a + B - 204 \text{ dBW} , \tag{7.8}$$

where $P_n = 10 \log p_n$, $B = 10 \log b$, and $10 \log KT_o = -204$. Lauber [7.4] has given the expression for the vertical component of the rms electric field strength for a half-wave dipole in free space.

$$E_n = F_a + 20 \log f_{MHz} + B - 99.0 \text{ dB } (\mu V/m) . \tag{7.9}$$

If we use a conversion factor of 1 μV/m = 33 pT for relating electric field strengths to orthogonal magnetic field strengths and note that figures 7.1 and 7.2 may be used for vertical as well as horizontal magnetic field strength noise levels [7.5] at any frequency and any effective antenna temperature, an approximate value for the magnetic field strength atmospheric noise is given by

$$H_n \doteq 4\pi \times 10^{-9} \sqrt{b} \tag{7.10}$$

or

$$H_n \doteq 0.1 \text{ nT } \sqrt{b} \ .$$

Cohn [7.6] has used the above nominal value for H_n to plot primary coil ampere-turns-per-coil diameter required to achieve a specified detection range for a normalized target size of unity when external atmospheric noise is the only limiting factor. An operating metal detector frequency of 2.5 kHz is close to a local minimum of the external noise figure shown in figure 7.1 (127 dB), which takes into account the entire surface of the earth, all seasons, and all times of day. Therefore, it is an optimal operating frequency with respect to noise figures based on atmospheric sources. Figures 7.1 and 7.2 may be used in specifying the external atmospheric noise figure for any operating frequency and effective antenna temperature.

A report [7.7] on the noise factor for mine detection systems where signals due to ground clutter are specifically excluded has been written. In this paper, an example is taken to show how analytic work may be used with external atmospheric noise measurements to predict whether a given system operating at a specified frequency and effective temperature would allow detection of metal mine targets of specified sizes. In another report [7.8], Geyer has pointed out that there are optimal operating frequencies that maximize the quadrature-induced multipole moments of buried metallic spheres for any permeability and conductivity contrast between the sphere and host soil and for a buried sphere with any diameter. Thus, there is a means in metal-mine detection to choose an operating frequency that maximizes the quadrature response for a given size mine target. Together with the results described here, signal-to-noise ratios could then be determined so as to predict whether that size target, at a given depth of burial, would yield a threshold detection signal (signal exceeding overall operating noise factor by at least 2 or 3 dB).

B2. Detector Dynamic Range

One of the most important measures to be considered in the evaluation of mine detection systems is the mine detection probability that can be ascribed

to a given system when the electromagnetic characteristics of the test target and background soil are specified. The detection probability is defined as the probability that the (target) signal, if present, will be detected. Given the electromagnetic characteristics of metallic (or plastic) test standards and background soil(s), as well as the overall operating noise factor of the detection system, a threshold detectability level may be ascertained in principle for any burial depth and size of the test standard.

The function of a mine detection system is to determine the presence or absence of a buried mine. The maximum sensitivity of any system is governed by the threshold of detection. This threshold in turn is set at a level based on a tolerable false alarm rate. A false alarm results from an occasional level of noise exceeding the system threshold. Since system sensitivity is of prime importance, it is necessary to examine the relationship among noise (for the types of noise previously categorized), bandwidth, threshold, and false alarm rate.

Threshold and signal-to-noise requirements for mine detection are reviewed by Geyer [7.7]. The probability of a false alarm can be ascertained once a tolerable false alarm rate and the bandwidth of the detection system are determined. From the estimated false alarm probability and noise variance, a detection threshold may be simply calculated. Finally, minimum acceptable signal-to-noise ratios for any probability of successful detection and any false alarm probability can then be evaluated. Any mine detection system having a high threshold of detection (or low sensitivity) would be given a low figure of merit. Conversely, any detection system that has high sensitivity, or at least variable threshold levels of detection, would be given a higher performance rating. High sensitivity for variable detection thresholds usually mean that the system intrinsically has greater dynamic range.

A minimal detection requirement is that the signal output from measured electromagnetic fields perturbed by a land mine (for systems with earphones) be at least 2 or 3 dB above the overall operating noise factor of the system in order to be resolvable. Systems that depend on the normal hearing threshold (approximately a rms sound pressure of 2×10^{-5} N/m^2 at 1 kHz), as well as the smallest discernable change in audible level (2 or 3 dB), are therefore

inherently limited in sensitivity. This is a critical systems engineering requirement that should be addressed.

Ensuring signal levels that are at least 2 or 3 dB over the overall operating noise factor of the system (defining signal as that due to the presence of a mine) may or may not always be possible, even when the mine is electromagnetically visible. Such assurance will demand a thorough broadband analysis of the ground clutter problem, since system internal noise can be controlled and since system engineering considerations can be used to overcome external atmospheric noise sources.

B3. Susceptibility to Ground Clutter

While it is possible to evaluate the performance of any mine detection system under controlled circumstances having minimal or no ground clutter, it is more difficult to predict the operation of that system on the battlefield. A mine detection system can be tested and shown to have the highest overall figure of merit based on weighted experimental parameters discussed to this point -- but could fail to detect a mine in the field where the external noise due to ground clutter is high.

Ground clutter includes the natural effects of an inhomogeneous and/or dispersive host medium in which the mine target resides, as well as effects of surface roughness. Other types of ground clutter could stem from surface or buried cultural debris such as spent shells or artillery (see fig 7.3).

Unwanted signals due to ground clutter can be the most important contributor to the overall operating noise factor. This source of noise, which can give large numbers of nuisance or false alarms, is currently difficult to quantify in a meaningful way. Only if there is spatial or temporal resolvability of the signal in the presence of clutter can there be hope of taking fruitful measures to minimize the effects of interfering signals on target signals. Furthermore, it would be useful to know whether, if any mine detection system incorporated an optimally matched filter as part of its system design, spectral resolvability exists between the mine target signal $S(\omega)$ and unwanted noise signals $N(\omega)$ -- and, if so, under what conditions. Thus it would be desirable to have a generalized solution to the model illustrated in figure 7.3 which (1) is broadband (not frequency limited); (2)

incorporates ground clutter; (3) allows spatially variant and dispersive $\mu_H(r;\omega)$, $\epsilon_H(r;\omega)$, $\sigma_H(r;\omega)$; and (4) can be applied to weak or strong scattering targets.

Such an analysis would provide insight into system design specifications and lead, in general, to the ultimate goal -- better detection capability. It is difficult to conceive how present mine detection systems undergoing test validation would perform better in a cluttered environment than in highly controlled, standardized test environments as previously discussed. Consequently, the BRDEC approach of highly controlled validation testing is probably sufficient for comparative performance evaluations of existing detection systems. Geyer [7.8] has outlined an exact deterministic approach to the analysis of ground clutter for an arbitrary dispersive and spatially variant background medium and for an arbitrary incident source field.

B4. Optimally Matched Filter Characteristics

One approach to attacking the ground clutter problem and to increasing the detection probability is to know the (near-field) frequency spectrum $S(\omega)$ (or averaged frequency spectrum $\langle S(\omega)\rangle$) of the input target (land mine) signal. Once $S(\omega)$ is given for an ensemble of specified targets, it is not only possible to incorporate adaptive thresholding, but also to design an optimally matched filter transfer function, $H(\omega)$, for a mine detection system operating in the presence of white Gaussian noise; that is,

$$H(\omega) \equiv S^*(\omega) \ , \tag{7.11}$$

where $S(\omega)$ is the frequency spectrum of the input (target) signal $s(t)$ and $S^*(\omega)$ is the complex conjugate of $S(\omega)$. A mine detection device that has a system response given by eq (7.11) is the optimal detection system in the sense of maximizing signal relative to average noise power. We could therefore place a higher figure of merit on a mine detector configured such that the output response $O(\omega)$ for a given test standard $S(\omega)$ is given by

$$O(\omega) \equiv S(\omega)\ S^*(\omega) \tag{7.12}$$

Ground clutter may or may not be white Gaussian in character. If not, it would be possible to design a Wiener-Hopf filter, optimal in the least squares sense; that is,

$$H_{opt}(\omega) = \frac{\Phi_S(\omega)}{\Phi_N(\omega) + \Phi_S(\omega)} \tag{7.13}$$

when noise is uncorrelated with the desired signal output and where $\Phi_S(\omega)$, $\Phi_N(\omega)$ are the signal and noise power spectra. Future detection systems may well incorporate a Wiener-Hopf filter. Such incorporation will await more definitive work on characterizing $\Phi_N(\omega)$.

B5. Sensitivity to Detector Height above Earth's Surface and Pattern Signatures

Smith [7.9] has investigated the directive transmission characteristics of horizontal electric and magnetic dipoles over a dielectric half-space by expressing the field of a general antenna over that half-space as a spectrum of plane waves [7.10]. He then asymptotically evaluates the integrals representing the far field so as to define pattern function, gain, and directivity of the horizontal electric or magnetic dipole antenna as a function of height above the earth.

More recently, Hill [7.11] has considered the specific case of oppositely directed horizontal electric dipole antennas, such as are found in the AN/PRS-7 plastic mine detector (see fig 7.4). A null always exists for the AN/PRS-7 in the directions normal to the air-earth interface from the detector head (spatially midway between the oppositely directed dipole antennas) -- in the absence of a lateral change in complex permittivity.

We can, however, examine the effect of antenna height on the field for fixed observation points either in the earth or in the air. This is illustrate in figures 7.5 and 7.6, which clearly show the desirable and expected increase in subsurface fields (and decrease in the fields in the air), as the antenna is brought closer to the earth's surface. Generally, electromagnetic field enhancement in the earth will always occur as the source antenna is brought closer to the air-earth interface, regardless of the type of source

excitation or antenna configuration. The actual enhancement will depend on the specific antenna. Proper comparisons in land mine validation testing should maintain the same detector head height above the earth's surface.

Hill [7.12] has also shown the far-field H-plane multiple-lobe pattern that can occur over a uniform half-space having high dielectric contrast, $\epsilon'/\epsilon_0 = 80$ (see fig 7.7). For $1 \leq \epsilon'/\epsilon_0 \leq 4$, this complex pattern does not occur. This H-plane multiple-lobe pattern (more nulls than at $\theta = 0°$, 90°, and 180°) is undesirable in any plastic mine detection system and should be avoided, since it would be difficult to distinguish several closely spaced targets from single buried ones. Any mine detector that has a multiple-lobe signature pattern (more than two side lobes) for the maximum expected ratio of ϵ'/ϵ_0 should be ascribed a lower figure of merit.

The variations in sensor head height over a given sweep time (which are likely to occur in field operations) could lead to signals greater than what might be expected from a buried weak scattering target (such as a plastic mine in dry sand). One seemingly simple systems approach for handling this problem would be to incorporate within the detection head an ultrasonic or infrared range finder that would allow feedback system signal corrections to be made in real time in accordance with theoretical near-field analysis [7.12].

C. Target-Based Performance Measures

C1. Sensitivity to Specified Complex Permittivity Contrasts

One of the important parameters needed in evaluating the performance of any land mine detection system is that system's sensitivity to specified complex permittivity contrasts. For example, a preliminary set of background media for validation testing of both plastic and metal mine detectors has already been submitted and will be reviewed below. Because mine detectors may have differing operating frequencies or be broadband operationally, it is important to understand dielectric dispersion in test soils so as to be cognizant of various dielectric relaxation processes affecting the validation testing. It is also important to recognize these processes so that standardized test conditions may be properly controlled and so that mine

detector performance evaluations are properly made (that is, mine detectors correctly compared) in the light of actual measured electrical contrasts.

Several cases may be listed and generally characterized in terms of conductivity and permittivity contrasts as representative of the differing electrical environments likely to be encountered in either plastic or metallic mine detection.

C2. Sensitivity to Target Size

Previous analytic studies performed for BRDEC [7.13, 7.14] have demonstrated that anomalous signals generated by a buried land mine, whether metal or plastic, are proportional to target volume in the frequency range used by most detection systems. Most cw mine detection systems currently available operate in the Rayleigh scattering region insofar as mine detection is concerned; that is, the electrical size of the target mine is small compared to the wavelength in the surrounding medium. Hence, shape information, which could lead to a reduction in the false alarm rate, cannot be directly ascertained from signals measured by most mine detectors.

Hill [7.14] has used the Born approximation to derive the plane wave scattering matrix [7.10] for objects of low dielectric contrast. He has also considered the shape dependence of scattered (plane wave) electromagnetic fields for the cases of a sphere, a cube, and a cylinder whose electrical properties simulated a plastic (nylon) land mine. These shapes bracket all those likely to be encountered in land mines. Although some shape dependence in the scattered field was determined (see fig 7.8), it would be difficult to determine and use in the field as a basis for discriminating against unwanted ground clutter signals without a priori knowledge of the target volume itself -- even with conceivable multiple look angles of the target with spatially variable transmitter-receiver configurations.

For this reason, we have submitted copper right circular cylinders that might be used as metallic test object standards and both nylon and teflon spheres that might be used as plastic test object standards. These standards can be used in a discriminatory fashion in mine detector validation tests by parametrically changing the target volume for a given burial depth and host-target electrical property contrast. If a mine detection system is unable to

detect the largest standard, it will be unable to detect smaller standards (all other factors being equal). Similarly, if a mine detector cannot sense the presence of a buried land mine where the electrical property contrast is high, it surely will not sense mine when the contrast is low (all other factors being equal).

3. Sensitivity to Burial Depth

One of the more important parameters to be considered in assigning a figure of merit to any mine detection system is its detection sensitivity to a prescribed burial depth of a given land mine. The functional dependence with depth of plane electromagnetic waves traveling in a uniform, isotropic earth is exponential, that is, proportional to $e^{-\gamma z}$ (+z is positive downward), or

$$e^{-\gamma z} = e^{-(\pi f \mu \sigma)^{1/2} z} \; e^{-j(\pi f \mu \sigma)^{1/2} z} , \tag{7.14}$$

where μ is the (real) magnetic permeability, σ is the (real) conductivity, and f is the operating frequency. The well-known skin depth, that is, the distance within the earth at which the amplitudes of the electric and magnetic field vectors are attenuated to 1/e = 0.3679 of their respective values at the surface, is

$$z_{\text{skin depth}} \equiv \left(\frac{1}{\pi f \mu \sigma}\right)^{1/2} = \frac{1}{\mathrm{Re}(\gamma)} , \quad \sigma >> \omega\epsilon . \tag{7.15}$$

The plane-wave skin depth gives an effective depth of penetration and can be used as a rule of thumb for effective search depths of a mine detector in conductive soils, even though field excitation is not plane wave.

For a nominal ground conductivity of 0.1 S/m and magnetic permeability approximately equal to that of free space ($4\pi \times 10^{-7}$H/m), we see that the skin depth is roughly 30 m at 2500 Hz. Hence, highly conducting soils would not be expected to inhibit search depths of most metal mine detectors. However, the effective search depth of a plastic land mine detection unit operating at 250 MHz in the same conductive soil environment would only be about 0.1 m, a depth which is less than the maximum probable depth of mine burial (0.3 m). Effective search depths should at least be 0.3 m in the worst case likely to

be encountered -- that of an electrically lossy environment -- for all cw mine detection systems. The easiest way to control this is to lower the operating frequency.

Dispersion phenomena are evident whenever the host medium is lossy. Therefore, two mine detection units operating at widely different frequencies would sense differing electrical property contrasts, all other factors being equal. It is important to be able to predict when favorable electrical contrast between the mine and the background medium can be expected. Such information allows proper comparisons among various mine detection systems to be made.

Although the expected dielectric contrast and hence visibility of a (plastic or metallic) land mine increases with decreasing frequency (which would increase the detection range performance), spatial resolution and shape definition do not. In this regard, Cohn [7.6] has considered the quasistatic effects of variation in height of the search head on measured signals and detection range, assuming that the attendant signal variations (due to conductive or magnetically permeable ground) remain uncancelled. It would be desirable, if practical, to have as broadband a detection response as possible under the attenuation constraints imposed by a lossy background test medium.

It is advisable to make sensitivity tests of land mine burial depth in a conductive host soil environment at the maximum probable depth of mine burial. If any mine detection system is unable to sense a given mine at the surface (or in free space), it will be unable to do so when buried in a lossy medium.

C4. Sensitivity to Target Shape

Anomalous signals generated by a buried land mine, whether metal or plastic, are proportional to target volume in the frequency range used by most detection systems. A means for discriminating among different target shapes (target classification) is vital to reducing the false alarm rate at any given detection threshold and for increasing the detection probability. Such a discrimination capability is closely akin to the susceptibility of that system to unwanted ground clutter in the external noise factor. Any mine detection system having shape discrimination capability would, all other factors being equal, command a high figure of merit.

Target classification may be viewed as a crude form of inverse scattering that determines which of many body shapes is most consistent with the measured scattered field data. The scattered electromagnetic field produced by either a conducting or dielectric body in the presence of an incident wave is described by Maxwell's equations. Since these fields are determined by the relative positions of the constituent parts of scattering body surface (the boundary condition), it might be expected that, in general, the characteristics of the scattered field would be different for different object geometries. The most desirable mine classification scheme would produce an image displaying the shape and size of the object being illuminated. Such a detection system would effectively solve the inverse scattering problem, which is determining the boundary conditions from the received waveform.

As expected, there are preferred frequencies for indicating the shape and size of a target. In the theory of scattering, three roughly defined frequency regions are of interest: the Rayleigh, the resonance, and the optical regions, where the wavelength of the incident field is much larger, of the same order, or much smaller than the size of the target, respectively. With illumination in the Rayleigh region, the scattered field describes the volume of the target [7.15]. The character of the backscattered field in the optical region, on the other hand, is indicative of the principal curvatures of the target's specular points. Illumination in the resonance region gives rise to surface currents that circulate the body surface (into what would be the optical shadow areas) and reradiate. Resonance region illumination is generally considered most efficacious for target shape and size determination using multiple frequency measurements.

Chan and Peters [7.16], in an elegant attempt to characterize the effects of buried cultural debris and to distinguish such effects from the expected signals of buried land mines, have examined some target resonant phenomena using broadband (short pulse ground radar) detection systems. Preliminary results suggest that schemes either to eliminate or to process found clutter will rely on broadband detection systems. Of course, the principal limitations in deducing shape information from resonance phenomena are the attenuation constraints imposed by the lossy background test medium when a validation test is performed at the maximum expected depth of burial (0.3 m).

In conclusion, shape discrimination is one of the more important attributes that could give future (broadband) mine detection systems a high figure of merit in validation tests. Because few of the land mine detection systems presently available have demonstrated capability for shape discrimination, however, it will probably have a low weight in any performance matrix that BRDEC decides upon.

D. NIST Recommendations and Conclusions

Although it may eventually be possible to develop a set of performance measures that are solely detector-based, we have concluded that this approach is not feasible at this time. Using a "radar equation" approach, whereby the measurement of such detector characteristics as antenna gain and beam pattern, detector noise factor, operating frequency and bandwidth, and dynamic range, would yield a quantitative estimate for probability of target detection and/or false alarm rate, is not considered possible with present knowledge. The designers of detectors, of course, must concern themselves with parameters such as these, and qualitative relationships among these parameters and probability of detection do exist. However, all the necessary quantitative, functional relationships are not now known, and, in any event, the measurement of all of the necessary detector parameters would prove excessivly difficult, time consuming, and expensive. Fortunately, there is a better procedure which, for the most part, avoids the necessity for measuring any detector parameters. This procedure is described below.

D1. Recommended Target-Based Tests

The ability to comparatively measure the efficacy of electromagnetic mine detectors (existing models as well as future ones) may simply be realized by ethe construction of a set of target-earth test lanes. Chapter VIII (Suggested Future Work) contains our plans for implementing such lanes; described here is an outline of the basic concept. Input from the Army will be required in order to design the specifics of these tests to achieve the most realistic test conditions.

Listed below are some recommended target-based tests that use our concept of rigid-matrix soil and target standards. The advantages of this system have

already been addressed in chapters IV, V, and VI. Also, another advantage of this rigid-matrix approach is that future additional tests, such as additional soil types or different targets, can be added to this system quite easily.

D1.1 Contrast Ratio Tests

For the five background rigid-matrix soil standards initially recommended, target standards (spheres or cylinders) of equal volume would be embedded that have varying contrast ratios of permittivity, conductivity and/or permeability. By burying the targets with equal depths and orientations, and analogous to a physician's eye chart, the objective of this test would be to see how many of the targets could be detected as they vary in contrast from high to practically transparent.

D1.2 Burial Depth Tests

These tests would involve embedding sets of the same standard target at increasing burial depths. The objective of these tests, again, would be to see how many of these targets could be detected. The size, shape, orientation, and contrast ratio of the targets would be constant.

D1.3 Target Volume Tests

These tests would involve embedding targets with incrementally decreasing volumes (sizes) while holding the depth, contrast ratio shape, and orientation constant. The objective, as with virtually all of these tests, would be simply to record how many of these targets could be detected.

D1.4 Target Shape Tests

These tests would consist of varying the shape of targets with constant volume, depth, orientation and contrast ratio. One example of this test would be to vary the target shape from flat disks to thin rods. Again, the objective would be to see how many of these targets could be detected.

D1.5 Target Orientation Tests

These tests would consist of varying the orientation of a target of fixed size, shape, depth and contrast ratio. For example, the targets could be a set of identical cylinders which are embedded in the rigid-matrix soil standards at incremental angles from 0° to 90° from horizontal. As usual, the objective would be to see whether the detector could find any or all of the targets.

D1.6 Target Resolution Tests

These tests would consist of varying the distance between two targets (either identical or differing in some parameter) and measuring the detector's ability to individually resolve the two targets. The objective of these tests would be to determine the minimum target spacing at which the detector could indicate that two targets are present.

D1.7 Realistic Mine Target Tests

In addition to using standard targets with somewhat idealized shapes, as in the six tests above, more realistic replicas of actual known mines could be embedded in the rigid-matrix soil standards with varying depths, orientations, spacings, and so on, to test the detector's ability to find realistic targets. Fabricating these replicas can also be accomplished with the same rigid-matrix techniques as are developed for making the soil standards. Also, along with controlling the electromagnetic constituent properties of the replicas, it would not be difficult to add other realistic properties such as firing pins and air gaps.

D1.8 Surface Clutter Tests

As a more sophisticated set of tests, the surfaces of the rigid-matrix bricks could be cut or molded to simulate earth surfaces that are not flat and smooth. Both periodic and random surface profiles could easily be realized with this rigid-matrix technique. Since the surface profiles, once cut or

molded into the bricks, would remain constant, the repeatability of the tests would be ensured.

D1.9 Volume Clutter Tests

Again, for a more sophisticated set of tests, other benign objects such as rocks, tree roots, or metal shrapnel, could be embedded in the rigid-matrix soil standard bricks along with targets to test the ability of the detector to discriminate between actual targets and other volume inhomogeneities.

D1.10 Earth Stratification Tests

A more sophisticated set of tests would be stratifying the electromagnetic constituent properties of the rigid-matrix soil standards in order to test the detector's ability to "see through" the discontinuities introduced by these differing strata. Fabricating stratified rigid-matrix bricks should pose little more difficulty than that involved with homogeneous bricks.

These tests listed above are intended to be only indicative of the possibilities that would be realizable with our rigid-matrix soil (and target) standard approach. Practically all of the undesirable characteristics associated with the use of natural soils, synthetic loose-matrix soils and liquids, as listed in chapter V, would be eliminated by our recommended approach. Discussions with Army Belvoir personnel will be required to ascertain the exact parameter values and test target configurations that best suit the Army's needs.

D2. Detector Test Methodologies

Once the mine target test range has been designed, specified and installed, a set of actual detector test methodologies must be specified. What follows is a list of possible detector tests that we think will be required in order to adequately compare the performance of various mine detectors under realistic conditions. Any of the following tests can be performed for any of the target configurations.

D2.1 Sensor Velocity Tests

Over any or all of the target tests, the velocity of the detector sensor (search head) would be incrementally varied over a reasonable range (as dictated by the Army's needs and the detector manufacturer's operating specifications). In this manner, the detector's sensitivity to sensor velocity variations could be evaluated simply by observing the number of targets detected at each velocity.

D2.2 Sensor Tilt Angle Tests

Again, during the target tests, the tilt angle of the detector sensor would be incrementally varied over a reasonable range. Similarly to the velocity tests, the detector's sensitivity to tilt angle variations could be evaluated simply by observing the number of detected targets.

D2.3 Pendulum Tests

As somewhat more realistic motion test, it might be desirable to combine the above two tests by moving the detector sensor over the desired targets along the arc of a circle or some other curve, such as might occur when an operator swings the detector back and forth. The implementation of the motion tests is addressed in chapter VIII.

D2.4 Spatial Accuracy Tests

With knowledge of both the target position and detector sensor position at the moment of target detection, it is possible to measure the detector's ability to locate the position of the target accurately in both X and Y coordinates. As stated in chapter VIII, this can be accomplished by modifying and automating the Army's existing overhead trolley system.

D2.5 Detector Sensor Height Tests

In combination with the velocity, tilt angle and/or pendulum tests described above, the height of the detector sensor above the surface would be varied over a reasonable range (again determined by the detector manufacturer's operating specifications and the needs of the Army). Again, all of

these tests could be accomplished by modification of the Army's existing trolley system as outlined in chapter VIII.

Almost certainly, the Army will consider some of these tests unnecessary, and think other tests are necessary. One of the key advantages to our approach to test standardization is its flexibility. Once the basic system of rigid-matrix soil standards, standard and realistic targets, and automated trolley motion is installed, it should be quite easy and cost effective to make changes or add tests as future experience and needs dictate.

References (VII)

[7.1] Barsis, A. P.; Norton, K. A.; Rice, P. L.; Elder, P. H. Performance predictions for single tropospheric communication links and for several links in tandem; 1961; Nat. Bur. Stand. (U.S.) Tech. Note 102.

[7.2] International Radio Consultative Committee. Characteristics and applications of atmospheric radio noise data; 1983; Report No. 3220-2.

[7.3] Spaulding, D. A. International Radio Consultative Committee. Worldwide minimum external noise levels, 0.1 Hz to 100 GHz; 1982; Report No. 670.

[7.4] Lauber, N. R. Preliminary urban UHF/VHF radio noise intensity measurements in Ottawa, Canada. Proc., 2nd Symp. on EMC; 28-30 June, 1977; Montreux, Switzerland; 1977.

[7.5] Spaulding, D. A. Private communication; 1987.

[7.6] Cohn, G. I. Low frequency electromagnetic induction techniques; 1973; Tech. Essays, Army Countermine Study Report.

[7.7] Geyer, R. G. Noise factor for mine detection systems: A performance measure; 1987; Report to U.S. Army Belvoir Research and Development Center, Fort Belvoir.

[7.8] Geyer, R. G. Suggested experimental parameters for land-mine detection performance evaluations; 1987; Report to U.S. Army Belvoir Research and Development Center, Fort Belvoir.

[7.9] Smith, G. J. Directive properties of antennas for transmission into a material half-space. IEEE Trans. Ant. Prop. AP-32(3), 1984, pp. 232-246.

[7.10] Kerns, D. M. Plane-wave scattering-matrix theory of antennas and antenna-antenna interactions; 1981; Nat. Bur. Stand. (U.S.) Monogr. 162.

[7.11] Hill, D. A. Near-field detection of buried dielectric objects (to be published) 1988. See Appendix III.D.

[7.12] Hill, D. A. Fields of horizontal currents located above the Earth. (To be published) 1988. See Appendix III.C.

[7.13] Hill, D. A.; Cavcey, K. H. Coupling between two antennas separated by a planar interface. IEEE Trans. Geosci. Remote Sensing; July 1987; GE-25(4); pp. 422-431.

[7.14] Hill, D. A. Electromagnetic scattering by buried objects of low contrast. IEEE Trans. Geosci. Remote Sensing; March 1988; GE-26(2), pp. 195-203.

[7.15] Crispin, J. W.; Siegel, K. M. Methods of radar cross-section analysis. New York, NY: Academic Press; 1968.

[7.16] Chan, L. C.; Peters, L., Jr. Subsurface electromagnetic mine detection and identification; 1978; Technical Report, Department of the Army, U.S. Army Mobility Equipment Research and Development Command, Fort Belvoir, VA; 76. p.

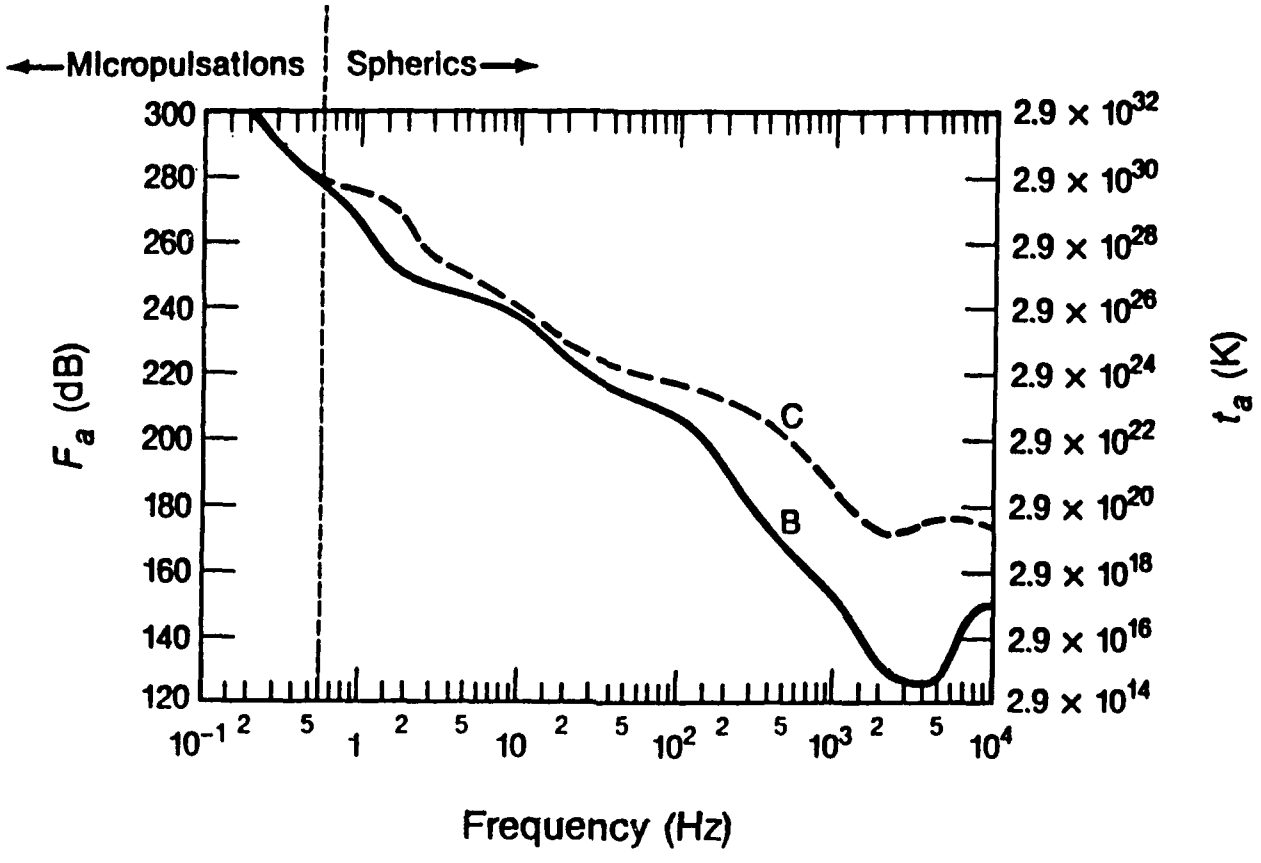

Figure 7.1 Minimum (B) and maximum (C) atmospheric noise figure vs frequency.

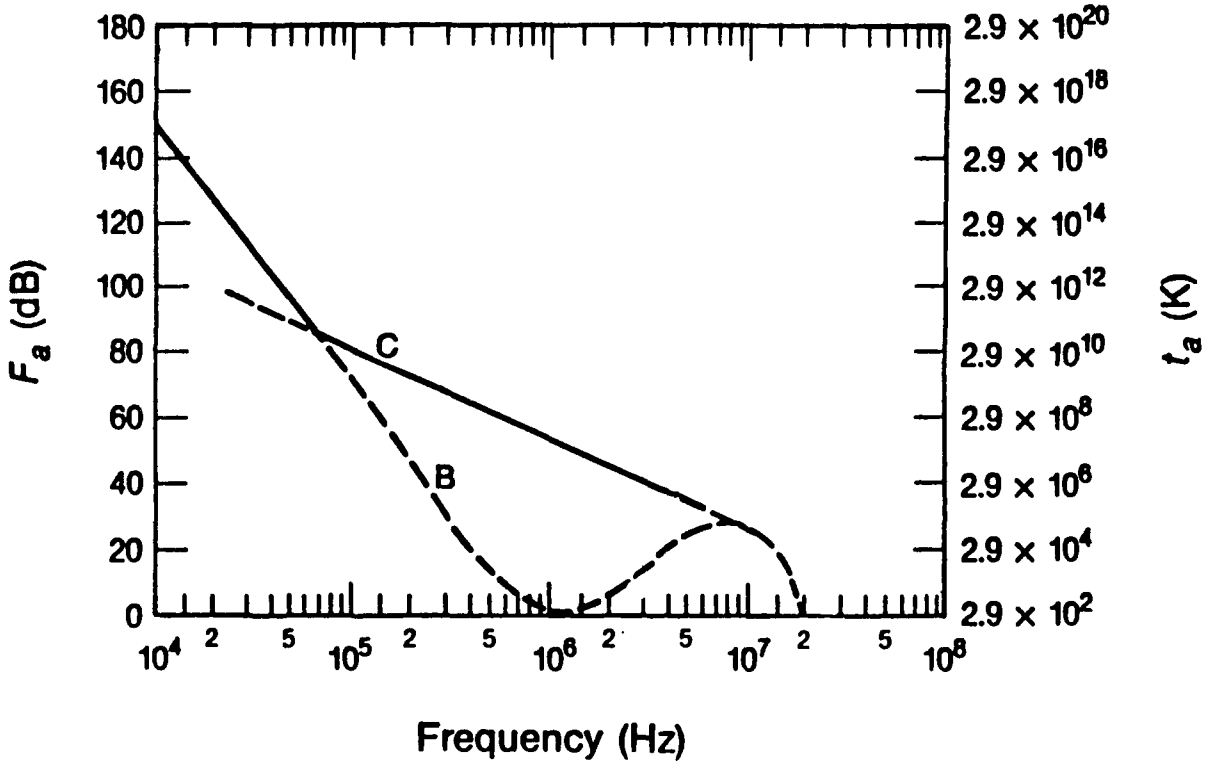

Figure 7.2 Minimum (B) and maximum (C) atmospheric noise figure vs frequency.

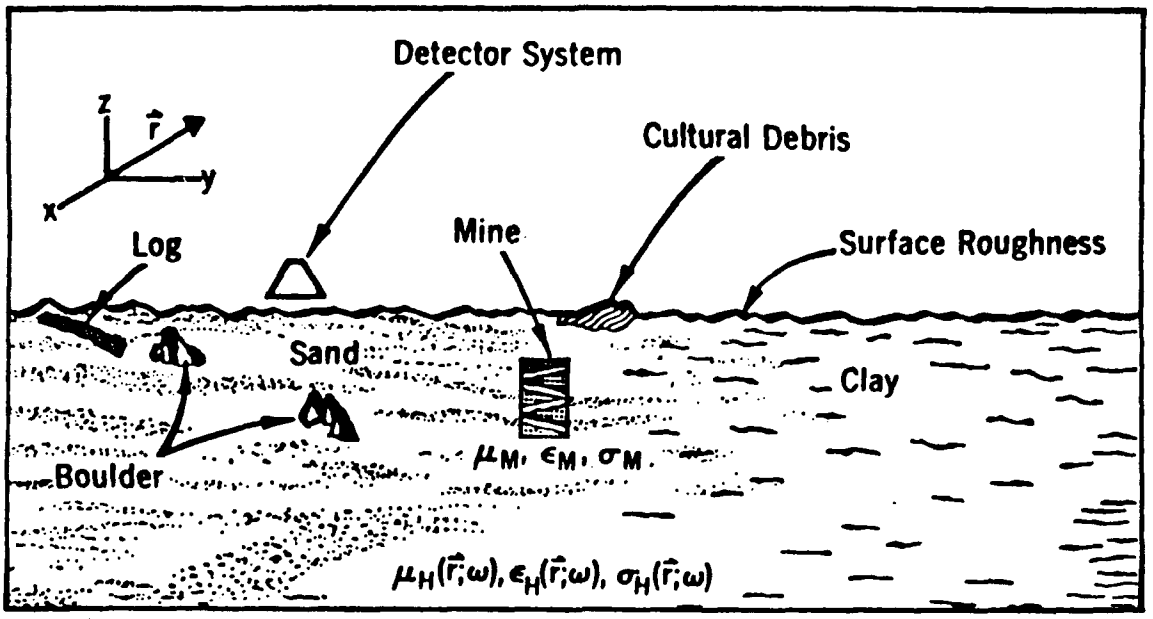

Figure 7.3 Sources of ground clutter.

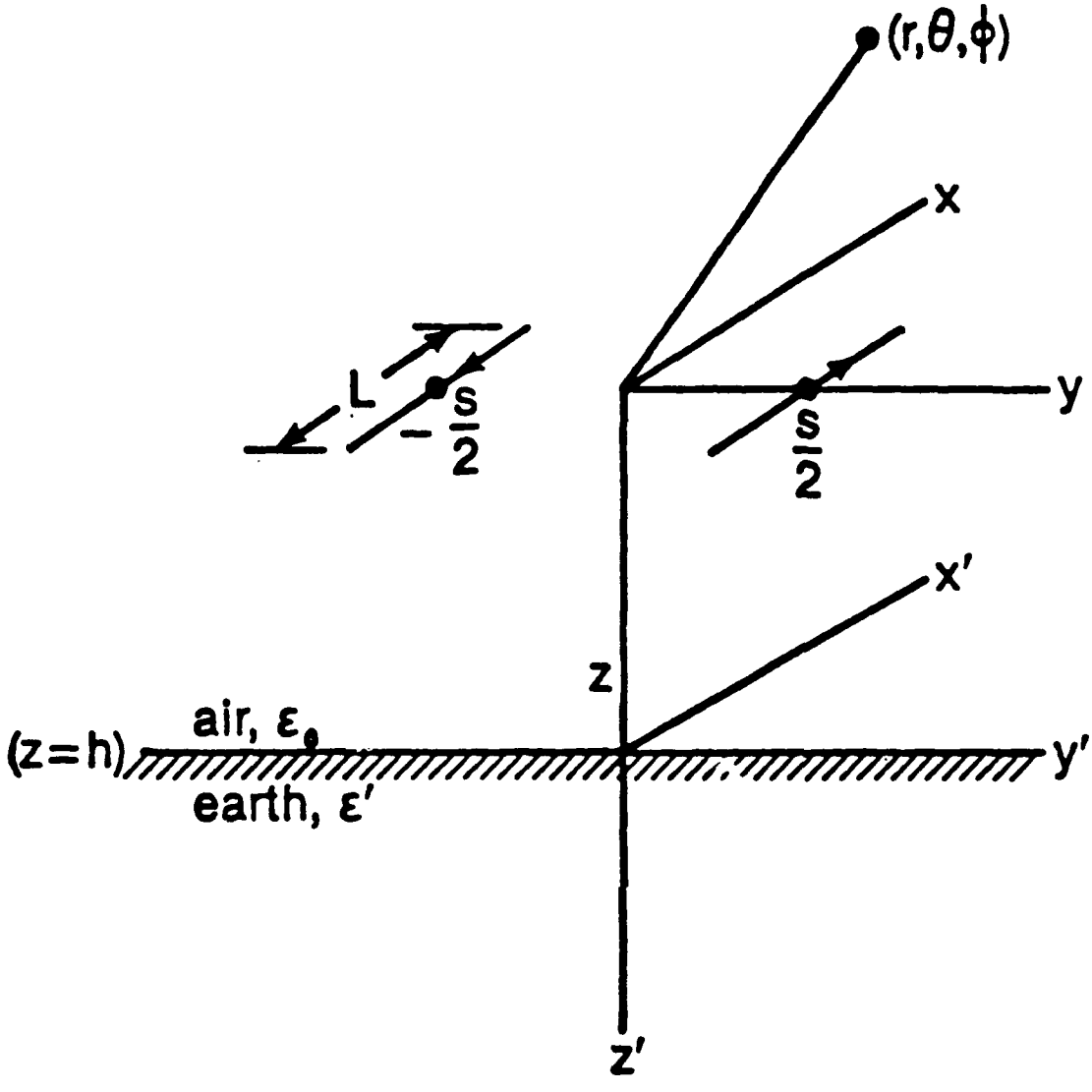

Figure 7.4 Oppositely directed dipoles at height h above the earth.

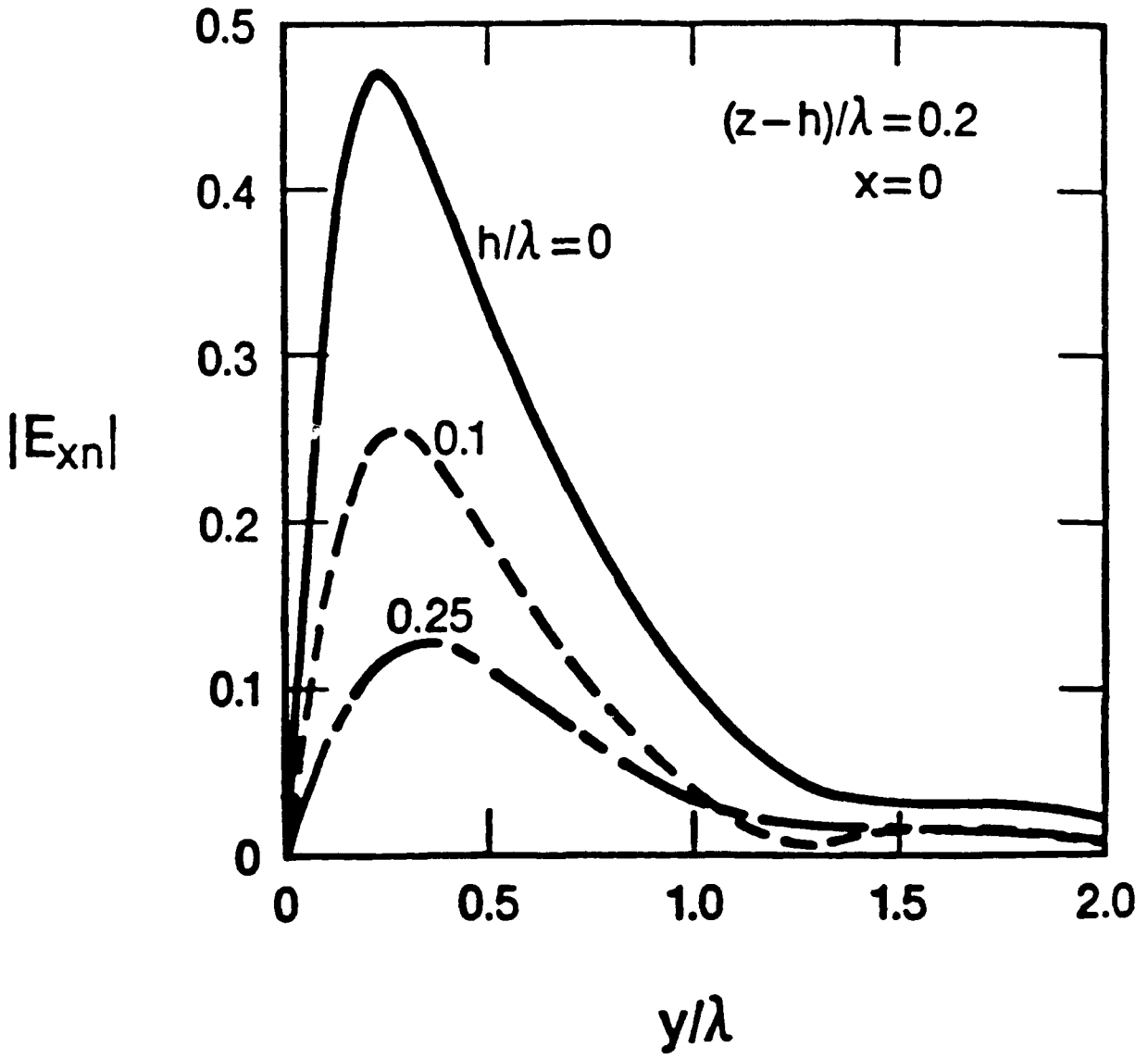

Figure 7.5 Normalized electric field at various heights in air for a fixed observation point in the earth.

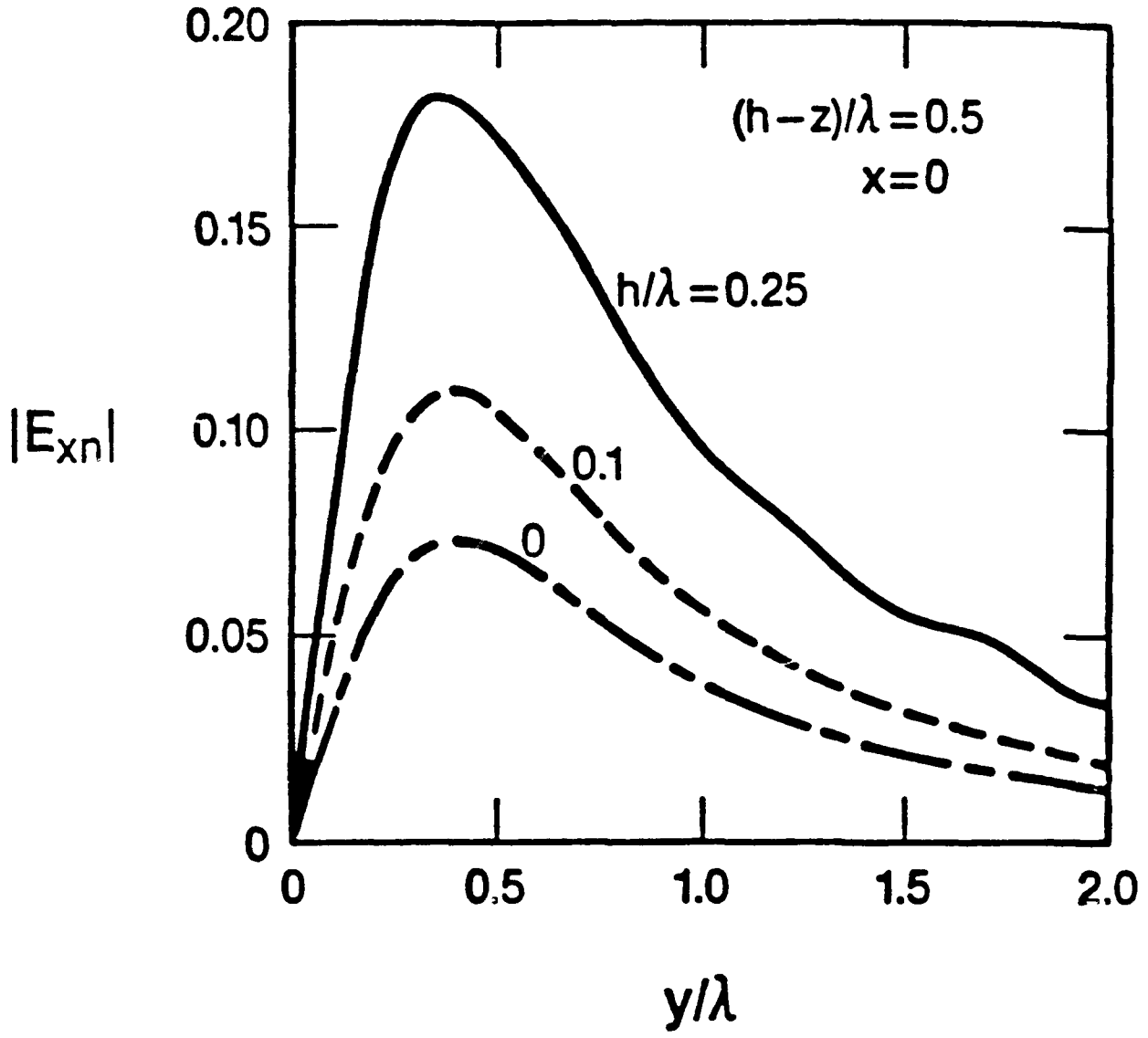

Figure 7.6 Normalized electric field at various heights in air for a fixed observation point in the air.

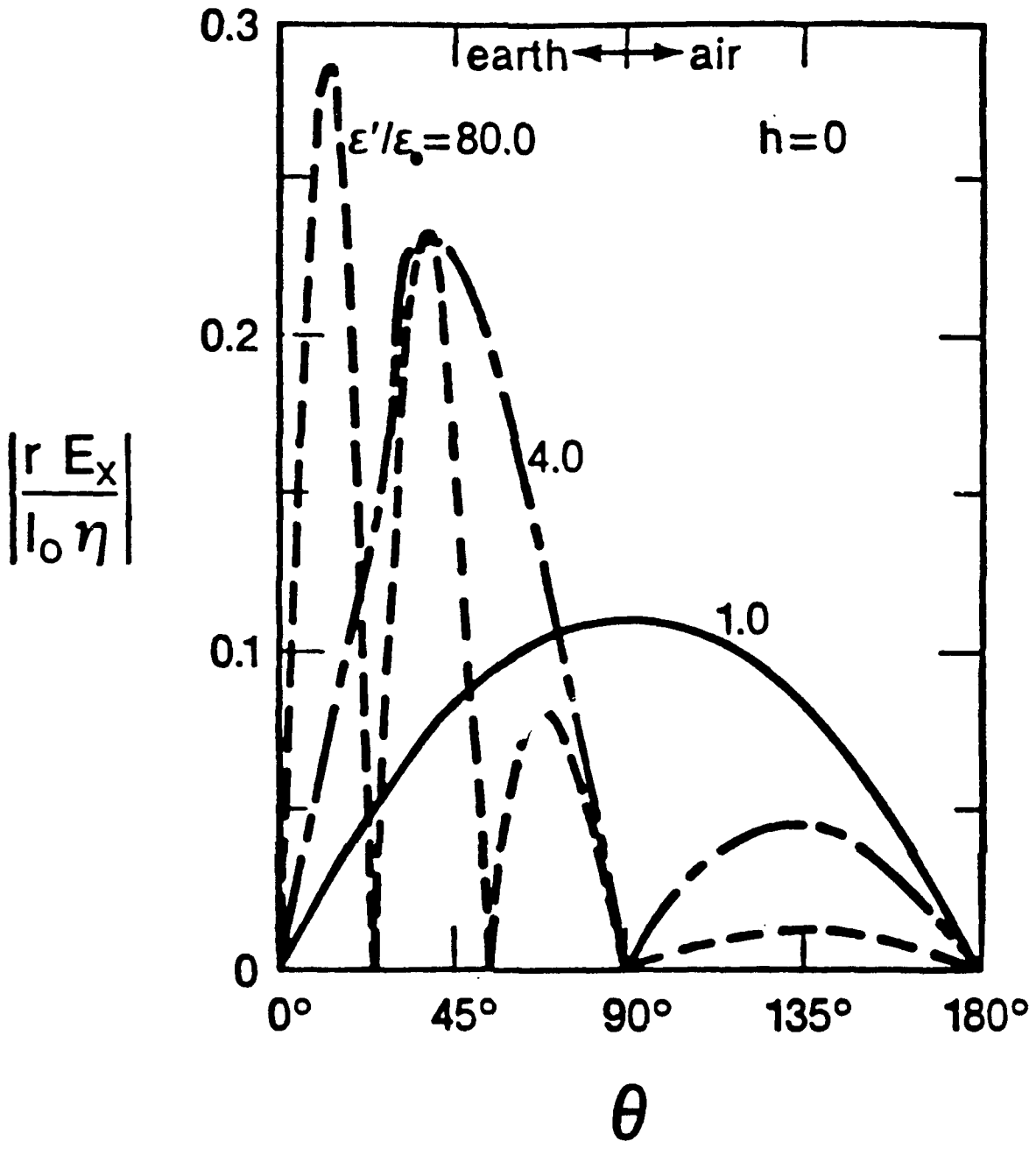

Figure 7.7 H-plane pattern of oppositely directed dipoles located at air/earth interface for various earth permittivities.

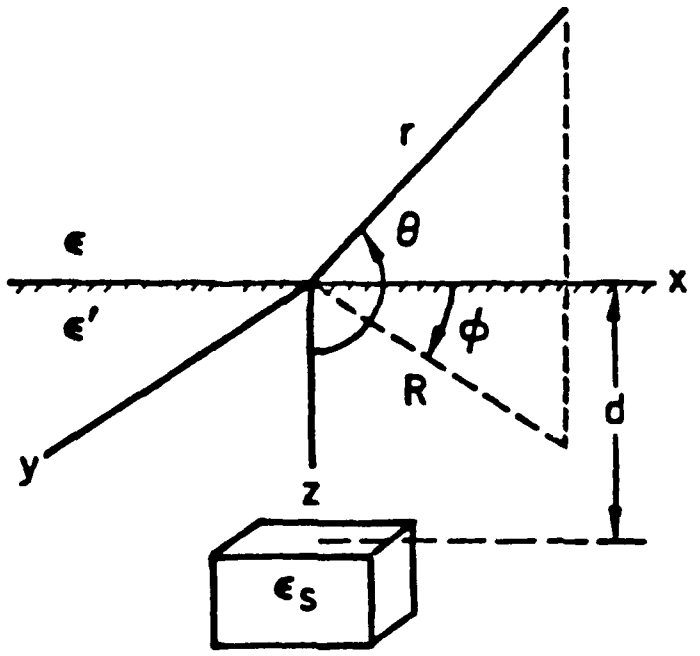

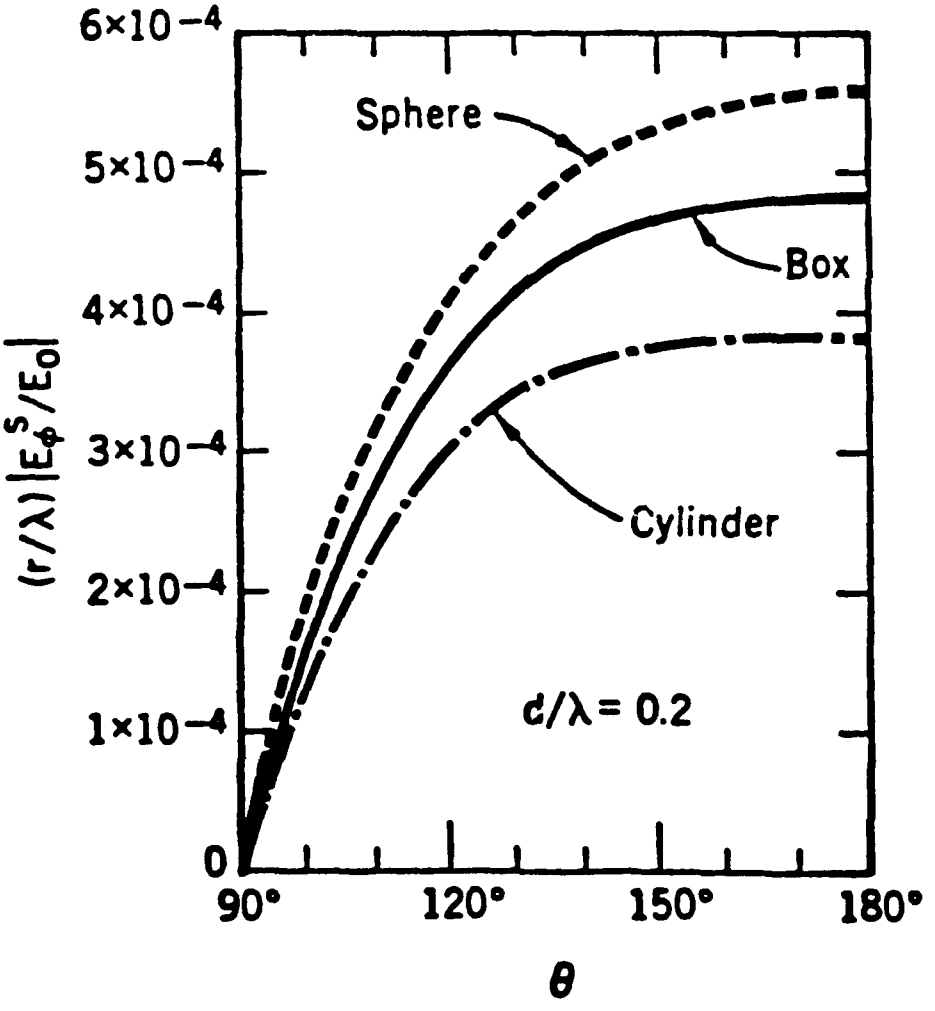

Figure 7.8 Scattered far-field for a cube (side = 0.1 λ), a circular cylinder (height = radius = 0.1084 λ), and a sphere (radius = 0.1241 λ) for normal incidence, TE polarization.

VIII. SUGGESTED FUTURE WORK

The additional work that NIST believes necessary may be broken down into two major tasks. What follows is a brief narrative describing these suggested tasks. Detailed discussions with Army personnel will be required in order to develop a suitable work statement that will meet the needs of the Army.

Task 1.

The first and largest task would be to modify the Army's existing mine detector test lanes at Fort Belvoir in order to install a set of five different rigid-matrix soil standard test lanes. The five different soil standards would simulate natural soils over a broad band of frequencies (approximately 10 MHz to 5 GHz for the nonmetallic object test lanes and 1 kHz to 10 MHz for the metallic object test lanes) as well as a broad range of ambient temperatures. As presently conceived, the five soil standards would simulate the following natural soil types: dry sand, damp loam, wet loam, high-conductivity sand, and high-permeability sand. The last two soil types are intended for testing metal detectors. The major subtasks necessary to accomplish this work are:

1. Engineering studies to choose the optimum material to serve as a rigid binding agent for the rigid-matrix soil standard bricks. Consultation with one or more polymer and/or cement chemists may be necessary to complete this study.

2. Fabrication experiments and electromagnetic constituent property measurements with experimental brick materials in order to learn how to make bricks that simulate the five soil types mentioned above, and that meet all of our other requirements (for example, strength, stability, homogeneity, toughness, and property accuracy).

3. Design and construction of standard and realistic replica mine targets, as necessary, to be embedded in bricks for the detector tests.

4. Development of techniques, based in either the frequency domain or the time domain, to calibrate the electromagnetic property values of both the soil bricks and the standard targets.

5. Design of the configuration of the test lane systems including such items as liner material, depth and volume requirements, electromagnetic field absorber material requirements, and maintenance requirements.

6. Fabrication of a sufficient number of bricks (with embedded targets) to meet the desired volume requirements of the test lanes.

7. Modification of the Army's existing mine test lanes facility.

8. Evaluation of the modified lanes to ensure that they meet requirements and specifications.

9. On-site technology transfer by adequate documentation and on-site training of Army personnel. (The Army will be responsible for providing personnel with adequate skills for training on the operation, calibration and maintenance of the test lanes.)

Task 2.

The other suggested task is the modification and automation of the Army's existing overhead trolley system so that the envisioned mine detector tests can be carried out automatically under computer control. With the required large number of tests, as outlined in chapter VII, automation of this system would speed up the testing process enormously. In addition, automation would remove the human element and thus make the tests more accurate and repeatable. The major subtasks for this suggested work are:

1. Analysis of the present overhead trolley system to determine what portions of the system, if any, could be incorporated into the new design.

2. Design of the trolley system including overhead rail structures, robotic arm, motion control systems, and computer system.

3. Construction and testing of a prototype system.

4. Development of necessary computer software for control of the system and mine detector testing.

5. Installation of the system over the test lanes at Fort Belvoir.

6. Testing and debugging of the system.

7. On-site technology transfer via adequate documentation and on-site training of Army personnel.

We think that if this suggested work is accomplished the Army would have a stable, accurate, automated mine detector test range that should more than meet the Army's needs, now and into the future. With the rigid-matrix technology for both soil standards and target standards, virtually all of the problems associated with natural soils, dry synthetic soils, or liquid synthetic soils will be eliminated. In addition, the entire system will be both flexible and expandable. The configuration of the test lanes would be easily changeable, simply by moving bricks and making simple program changes in the test software. New simulated soil types would be realized easily, simply by fabricating and installing additional bricks. In short, we are confident that this system will finally overcome most of the problems that the Army has endured for many years with respect to the evaluation of mine detectors.

BIBLIOGRAPHY

Afsar, M. N.; Birch, J. R.; Clarke, R. N. The measurement of properties of materials. Proc. IEEE; 1986; 74(1): 183-199.

Akimoto, S. Magnetic properties of ferromagnetic oxide minerals as a basis of rock magnetism. Adv. Phys.; 1957; 6(288).

Alvarez, R. Complex dielectric permittivity in rocks: a method for its measurement and analysis. Geophysics; 1973; 38: 920-940.

Barringer, A. R. The use of audio and radio frequency pulses for terrain sensing. Proc., 2nd Symposium on Remote Sensing of Environment, Center for Remote Sensing Information and Analysis, Willow Run Laboratories; University of Michigan; 1963: 201-214.

Barsis, A. P. Performance predictions for single tropospheric communication links and for several links in tandem. International Radio Consultative Committee worldwide minimum external noise levels, 0.1 Hz to 100 GHz; 1983. Report No. 3220-2.

Beckman, P. Probability in communication engineering. New York, NY: Harcourt, Brace and World, Inc.; 1967.

Bethe, H. A.; Schwinger, J. Perturbation theory of resonant cavities; 1943; NRDC Rpt. D2-117.

Birnbaum, G.; Franeau, J. Measurement of the dielectric constant and loss of solids and liquids by a cavity perturbation method. J. Appl. Phys.; 1949; 20: 817-818.

Bockris, J.; Gileady; Muller, K. Dielectric relaxation in the electric double layer. J. Chem. Physics; 1966; 44: 1445-1456.

Bottreau, A. M.; Dutuit, Y.; Moreau, J. On a multiple reflection time-domain method in dielectric spectroscopy: Application to the study of some normal primary alcohols. J. Chem. Phys.; 1977; 66(8): 3331-3336.

Broadhurst, M. G.; et al. A dielectric phantom material for electromagnetic radiation; 1986; NBS report for the Div. of Medical Engineering, Center for Devices and Radiological Health, Food and Drug Administration; 60 p.

Brumley, S. A.; et al. Far-field electromagnetic principles applied to mine detection. U.S. Army Belvoir R & D Center, Contract No. DAAK 70-86-C-0072; June 1987; Final Report.

Burrell, G. A.; Munk, B. A. The array scanning method and applying it to determine the impedance of linear antennas in a lossy half space. The Ohio State University ElectroScience Lab. Dept. of Electrical Engineering (prepared under Contract DAAG53-76-C-0179 for U.S. Army Mobility Equipment Research and Development Command, Ft. Belvoir, VA 22060); 1976; Technical Report 4460-1.

Burrell, G. A.; Peters, Jr., L.; Terzuoli, Jr., A. J. The propagation of electromagnetic video pulses with application to subsurface radar for tunnel application. The Ohio State University ElectroScience Lab, Dept. of Electrical Engineering (prepared under Contract DAAG53-76-C-0179 for U.S. Army Mobility Equipment Research and Development Command, Ft. Belvoir, VA 20060); Technical Report 4460-2.

Burrell, G. A.; Peters, Jr., L. Pulse propagation in lossy media using the low-frequency window for video pulse radar application. Proc. IEEE 67; 1979; No. 7.

Burrell, G. A.; Richmond, J. H.; Peters, Jr., L.; Tran, H. B. Acoustic, electromagnetic and elastic wave scattering -- Focus on T-matrix approach. A scattering model for detection of tunnels using video pulse radar in systems. New York: Pergamon Press; 1979: 667-683.

Bussey, H. E. Dielectric measurements in a shielded open circuit coaxial line. IEEE Trans. IM; 1980; IM-29(2): 120-124.

Bussey, H. E. Measurement of RF properties of materials: a survey. Proc. IEEE; 1967; 55: 1046-1053.

Caldecott, R.; et al. A radio frequency probe to measure solid electrical parameters; January 22, 1985; Final Report 715616-4; Ohio State University ElectroScience Lab., Columbus, Ohio.

Chan, L. C. Subsurface electromagnetic target characterization and identification. The Ohio State University; 1979; Ph.D. dissertation.

Chan, L. C.; Moffatt, D. L.; and Peters, Jr., L. A characterization of subsurface radar targets. Proc. IEEE 67; 1979; No. 7: 991-1001.

Chan, L. C.; Moffatt, D. L.; and Peters, Jr., L. Estimation of the complex natural resonances from a class of subsurface targets. Acoustic, electromagnetic, and elastic wave scattering--focus on T-matrix approach. New York: Pergamon Press; 1979: 453-463.

Chan, L. C.; Moffatt, D. L.; and Peters, Jr., L. Improved performance of a subsurface radar target identification system through antenna design. IEEE Trans. on Antennas and Prop.; 1981; AP-29(No. 2): 307-312.

Chan, L. C.; Moffatt, D. L.; and Peters, Jr., L. Subsurface radar target imaging estimates. IEEE Trans. on Antennas and Prop.; 1981; AP-29(No. 2): 413-418.

Cohn, G. I. Low frequency electromagnetic induction techniques; 1973; Tech. Essays, Army Countermine Study Report.

Cole, K. S.; Cole, R. H. Dispersion and absorption in dielectrics. J. Chem. Physics; 1941; 9: 341-351.

Conbau, G.; Schwering, F. On the guided propagation of electromagnetic wave beams. IRE Trans.; 1961; AP-9: 248-256.

Cook, R. J. Microwave cavity methods, in high frequency dielectric measurements; 1973; J. Chamberlain and G. W. Chantry, ed., IPC Science & Technology Press: 12-27.

Cook, R. J.; Jones, R. G.; Rosenberg, C. R. Comparison of cavity and open resonator measurements of permittivity and loss angle at 35 GHz. IEEE Trans.; 1974; IM-23: 438-442.

Cullen, A. L.; Nagenthiram, P.; Williams, A. D. Improvement in open resonator permittivity measurement. Electron. Letters; 1972; Vol. 8: 577-579.

Cullen, A. L.; Nagenthiram, P.; Williams, A. D. A variational approach to the theory of the open resonator. Proc. R. Soc. A.; 1972; 329: 153-169.

Cullen, A. L.; Yu, P. K. The accurate measurement of permittivity by means of an open resonator. Proc. R. Soc. A.; 1971; 325: 493-509.

Culshaw, W.; Anderson, M. V. Measurement of permittivity and dielectric loss with a millimeter wave Fabry-Perot interferometer. Proc. IEEE; 1962; 109(B), Suppl. 23: 820-826.

Dalton, F. N.; et al. Time-domain reflectometry: Simultaneous measurement of soil water content and electrical conductivity with a single probe. Science; June 1, 1984; 224: 989-990.

Davenport, W. B.; Root, W. L. Random signals and noise. New York, NY: McGraw-Hill Book Co.; 1970.

David, J. L. Relative permittivity measurements of a sand and clay soil in situ. Geological Survey of Canada; 1975; Paper 75-1C: 361-363.

Davidson, D. W.; Cole, R. H. Dielectric relaxation in glycerol propylene glycol, and n-propanol. J. Chem. Phys.; 1951; 29: 1484-1490.

Davis, C. W.; Peters, Jr., L. Characteristics of a video pulse radar system operating in the high frequency window at the Hazel A. mine near Gold Hill, Colorado. The Ohio State University ElectroScience Lab., Dept. of Electrical Engineering; 1979; Technical Report 784460-8.

Davis, C. W.; Peters, Jr., L. Application of a video pulse radar system to detect tunnels at the Curtis School Yard in Trumbull County, Ohio. The Ohio State University ElectroScience Lab., Dept. of Electrical Engineering; 1979; Technical Report 78440-7.

Davis, III, C. W. A computational model for subsurface propagation and scattering for antennas in the presence of a conducting half space. The Ohio State University ElectroScience Lab., Dept. of Electrical Engineering; 1979; Technical Report 479X-7.

Davis, J. L; Topp, G. C.; Omran, A. P. Measuring soil water content in situ using time-domain reflectometry techniques. Geological Survey of Canada; 1977; Paper 77-1B: 33-36.

Debye, P. Polar molecules. Dover Publications: New York; 1929.
Debye, P. Polar molecules. New York, NY: Chemical Catalog Co.; 1899.

Degenford, J. A quasi-optic technique for measuring dielectric loss tangents. IEEE Trans.; 1968; IM-17: 413-417.

Degenford, J.; Coleman, P. D. A quasi-optics perturbation technique for measuring dielectric constants. Proc. IEEE; 1966; 54: 520-522.

Dines, A.; Lytle, R. J. Computerized geophysical tomography. Proc. IEEE; 1979; 67: No. 7.

Dobson, M. C.; et al. Microwave dielectric behavior of wet soil. IEEE Trans. on Geosci. & Remote Sensing; January 1985; Vol. GE-23; 1: 35-46.

Dukhin, S. S. Dielectric properties of disperse systems in Matijevic, E. Surface and colloid science. E., ed. New York, NY: Wiley Interscience; 1969; v. 3: 83-166.

Falls, Bernard, A. Apparatus for measuring the electromagnetic impedance of soils; 1977.

Falls, R. A.; et al. EM soil properties in the VHF/UHF range. U.S. Army R & D Center; May 1972; Report 2030.

Fountain, L. S. Evaluation of the EM properties of soil materials; December 1984; Final Report, VSE Corp., Alexandria, VA.

Gabillard, R.; Degauge, P.; Wait, J. R. Subsurface electromagnetic telecommunication -- Review. IEEE Trans. on Communication Technology; 1971; Com-19: 1217-1228.

Gans, W. L.; Andrews, J. R. Time-domain automatic network analyzer for measurement of RF and microwave components; 1975; Nat. Bur. Stands. (U.S.) Tech. Note 672.

Gelengnse, M.; Barringer, A. R. Recent progress in remote sensing with audio and radio frequency pulses. Proc., 3rd Annual Symp. on Remote Sensing of Environment; 469-494.

Geyer, R. G. Suggested experimental parameters for land-mine detection performance evaluations; November 1987; Report for U.S. Army Belvoir Research and Development Center. Fort Belvoir, VA 22060-5606. Project No. 7232457.

Geyer, R. G. Magnetic susceptibility measurements for mine detecting; Report to U.S. Army, Ft. Belvoir, VA (Proj. 7232457); 10 p.

Goldman, S. Information theory. New York, NY: Prentice-Hall, Inc.; 1953.

Hancock, J. C.; Wintz, P. A. Signal detection theory. New York, NY: Prentice-Hall, Inc.; 1953.

Hasted, J. B. Aqueous dielectrics. London: Chapman and Hall; 1973. Note: 302 p.

Hayes, P. K. An on-site method for measuring the dielectric constant and conductivity of soils over a one gigahertz bandwidth. The Ohio State University ElectroScience Lab., Dept. of Electrical Engineering; Technical Report 582X-1.

Heiland, C. A. Geophysical exploration. Englewood Cliffs, New Jersey: Prentice Hall; 1940; (310-314).

Hill, D. A.; Cavcey, K. H. Coupling between two antennas separated by a planar interface. IEEE Trans. Geosci. Remote Sensing; July 1987; GE-25(4): 422-431.

Hill, David A. Electromagnetic scattering by buried objects of low contrast. IEEE Trans. Geosci. Remote Sensing; March 1988; GE-26(2): 195-203.

Hill, N. E.; Vaughn, W. E.; Price, A. H.; Davies, M. Dielectric properties and molecular behavior. London: Van Nostrand; 1969: 480 p.

Hoekstra, P.; Delaney, A. Dielectric properties of soils at UHF and microwave frequencies. J. of Geophysical Research 79; 1974; (No. 11): 1699-1708.

Hogg, R. V.; Craig, A. T. Introduction of mathematical statistics. New York, NY: MacMillan Co.; 1970.

Horner, F. Resonance methods of dielectric measurement at centimeter wavelengths. J. IRE; 1946; 93(III): 55-57.

Horner, F.; Harwood, J. An investigation of atmospheric radio noise at very low frequencies. J. IRE, 1956; 103B(743).

Izadian, J. An underground near-field antenna pattern range. The Ohio State University ElectroScience Lab., Dept. of Electrical Engineering; 1980.

Izadian, J. S. Two dimensional EM-scattering by buried penetrable noncircular cylinders using the method of moments. The Ohio State University; Ph.D. dissertation.

Izadian, J. S.; Peters, Jr., L.; and Richmond, J. H. Computation of scattering penetrable cylinders with improved numerical efficiency. IEEE Trans. on Geoscience; 1984.

Jesch, R. L. Dielectric measurements of five different soil textural types as functions of frequency and moisture content; 1978; NBSIR 78-896; 26 p.

Jones, R. G. Precise dielectric measurements at 35 GHz using an open microwave resonator. Proc. IEEE; 1976; 123(4): 284-290.

Jones, R. N.; Bussey, H. E.; Little, W. E.; Metzker, R. F. Electrical characteristics of corn, wheat, and soya in the 1-200 MHz range; 1978; Nat. Bur. Stand. (U.S.) NBSIR 78-897.

Jonscher, A. K. The interpretation of non-ideal dielectric admittance and impedance diagrams. Phys. Stat. Solutions (a); 1975; 32: 665-676.
Jonscher, A. K. The universal dielectric response, a review of data and their new interpretation. Chelsea Dielectric Group: University of London; 1979.

Kennaugh, E. M. The K-pulse concept. IEEE Trans. on Antennas and Prop.; 1981; AP-29(No. 2).

King, R. W.; Smith, G. S. Antennas in matter; Fundamentals, theory, and applications. Cambridge, MA: M.I.T. Press; 1981.

Knight, R. J. The use of complex plane plots in studying the electrical response of rocks. J. Geomag. Geoelectr.; 1983; 35: 767-776.

Kogelnik, H.; Li, T. Laser beams and resonators. Proc. IEEE; 1966; 54: 1312-1329.

Kottenstette, J. P.; Steffen, D. A. Planning for short pulse radar experiments; September 30, 1987; Final Report for U.S. Army Belvoir Research and Development Center, Fort Belvoir, VA 22060-5606; 109 p.

Kouyoumjian, R. G.; Peters, Jr., L.; Thomas, D. T. A modified geometrical optics method for scattering by dielectric bodies. IEEE Trans.; 1963; LAP-11: 690-703.

Kurosaki, S. The dielectric behavior of water sorbed on silica gel. J. Phys. Chem.2; 1954; 58: 320-324.

Lauber, N. R. Preliminary urban UHF/VHF radio noise intensity measurements in Ottawa, Canada. Proc., 2nd Symp. on EMC; 28-30 June, 1977; Montreux, Switzerland.

Lentz, R. R. Microwave detection of buried objects. Dept. of Electrical & Electronic Engineering, Queen Mary College, Mile End Road, London; May 1976; Contract Report AT-2042-059-RL.

Lentz, R. R. Detection of shallowly buried objects. Electr. Ltrs.; 1976; 12(22): 594-595.

Lerner, R. M. Ground radar system; 1974; U.S. Patent No. 3,831,173.

Lockner, D. A.; Byerlee, J. D. Complex resistivity measurements of confined rocks. J. Geophys. Res.; 1985; 90: 7837-7847.

Lundien, J. R. Terrain analysis by EM means: radar responses to laboratory prepared soil samples. U.S. Army Engineer Waterways Experiment Station, Vicksburg, MS; September 1966; Technical Report No. 3-693, Report 2.

Lytle, Jeffrey, R. Measurement of earth medium electrical characteristics: Techniques, results and applications; Lawrence Livermore National Laboratory; 1974.

Madden, T. R.; Cantwell, T. Induced polarization [Mining Geophysics], a review. A. W. Musgrave, ed. Soc. Explor. Geophys; 1967; 2: 373-400.

Maxwell, J. C. A treatise on electricity and magnetism: Dover Publishing; 1891.

McCafferty, E.; Zettlemayer, A. C. Absorption of water vapor on Faraday Soc. Discussions; 1971; 52: 239-254.

McWane, P. D. A look at the antenna radiation problem in the time domain. Ohio State University; 1972; Ph.D. dissertation.

Morey; 1974; U.S. Patent No. 3,806,795.

Nagata, T. Rock magnetism. Tokyo: Maruzen Press; 1961: 350 p.

Nakamura, H.; Mashimo, S.; Wada, A. Precise and easy method of TDR to obtain dielectric relaxation spectra in the GHz region. Japanese J. Appl. Phys.; 1982; 21(7): 1022-1024.

Nicolson, A. M.; Ross, G. F. Measurement of the intrinsic properties of materials by time-domain techniques. IEEE Trans. Instr. Meas.; 1970; IM-14(4).

Nolan, R. V.; et al. MERADCOM mine detection program: 1960-1980. U.S. Army, Ft. Belvoir; May 1980; Report No. 2294.

Olhoeft, G. R.; Frisillo, A. L.; Strangway, D. W. Electrical properties of lunar soil sample 15301. J. Geophys. Res.; 1974; 79: 1599-1604.

Owens, T. E. Cavity detection using VHF hole-to-hole electromagnetic techniques. Paper presented at Symposium on Tunnel Detection, Colorado School of Mines, Golden, CO; 1981.

Pelton, W. H.; Ward, S. H.; Hallof, P. G.; Sill, W. R.; Nelson, P. H. Mineral discrimination and removal of inductive coupling with multifrequency IP. Geophys; 1978; 43: 588-609.

Peters, Jr., L., and Richmond, J. H. Scattering from cylindrical nonhomogeneities in a lossy medium. Radio Science 17; 1982; (No. 5): 973-987.

Peters, Jr., L.; Burrell, G. A.; Tran, H. B. A scattering model for detection of tunnels using video pulse systems. The Ohio State University Electro-Science Lab., Dept. of Electrical Engineering; 1977; Technical Report 4460-3.

Peyrelasse, J.; Boned, C.; LePetit, J. P. Setting up of a time-domain spectroscopy experiment. Application to the study of the dielectric relaxation pentanol isomers. J. Phys. Sci. Instr.; 1981; 14: 1002-1008.

Probeck, Charles. R & D of a single-channel search head. U.S. Army Ft. Belvoir, Contract No. DA-44-009 ENG-1666: (Cook Electric Co., Chicago, IL); February 1956; Tech. Report.

Rubin, W. L.; DiFranco, J. V. Radar detection. Electro-technology; April 1964.

Saint-Amant, M.; Strangway, D. W. Dielectric properties of dry geologic materials. Geophysics; 1970; 35: 624-645.

Scott, W. R. Dielectric spectroscopy using shielded open-circuited coaxial lines and monopole antennas of general length. Ph.D. thesis, Georgia Inst. Tech.; 1985: 228 p.

Scott, Jr., W. R.; Smith, G. S. Error Analysis for Dielectric Spectroscopy Using Shielded Open-Circuited Coaxial Lines of General Length. Ph.D. Thesis, School of Electrical Engineering, Georgia Institute of Technology: Atlanta, GA: October 1985.

Scott, Jr., W. R.; Smith, G. S. Error Analysis for Dielectric Spectroscopy Using Shielded Open-Circuited Coaxial Lines of General Length. IEEE Trans. on Instr. & Meas.; June 1986; IM-35(2): 130-137.

Scott, Jr., W. R.; Smith, G. S. Dielectric spectroscopy using monopole antennas of general electrical length. IEEE Trans. on Antennas & Prop.; July 1986; AP-34(7): 919-929.

Shutko, A. M.; Rentov, E. M. Mixture formulas applied in estimation of dielectric and radiative characteristics of soils and ground at microwave frequencies; 1982; Vol. GE-20(No.): 29-32.

Skolnik, M. I. Introduction to radar systems. New York, NY: McGraw-Hill Book Co., Inc.; 1962.

Sluyters-Rehbach, M.; Sluyters, J. H. Sine wave methods in the study of electrode processes, in Electroanalytical Chemistry. A. J. Bard, ed., New York, NY: Marcel Dekker; 1970: 1-128

Smith, G. S.; Smith, W. R. A simple method for the in situ measurement of the electrical properties of the ground. 1987 IEEE AP-S International Symposium Digest, June 15-19 at Virginia Tech. (IEEE Catalog No. CH2435-6/87); 1987; Paper JA02-3: 242-245.

Smith, G. Antenna pattern performance near the interface of a dielectric medium. IEEE APS; 1983.

Smith, G. S.; King, R. W. P. Electric field probes in material media and their application in EMC. IEEE Trans. Electromagn. Compat.; 1975; EMC-17: 206-211.

Smith, G. S.; King, R. W. P. Electric field probes in material media and their application in EMC. IEEE Trans. Electromagn. Compat.; 1976; EMC-18: p. 130.

Smith, G. S.; Nordgard, J. D. Measurements of the electrical constitutive parameters of materials using antennas. IEEE Trans. Ant. prop.; 1985; 33(7): 783-792.

Smith, G. S.; Scott, Jr., W. R. A simple method for the In Situ Measurement of Electrical Properties of the Ground. 1987 Antennas and Propagation International Symposium Digest; June 1987; Vol. 1: 242-245.
Suggett, A. Time-domain methods, dielectric and related molecular processes. Chem. Soc., London; 1972; Vol. 1: 101-120.

Tribuzi, C. A. An antenna for use in an underground (HFW) radar system. The Ohio State University ElectroScience Lab., Dept. of Electrical Engineering; 1977; Technical Report 4460-4.

Tricoles, G.; et al. Near-field electromagnetic detection of mines. General Dynamics Electronics Div. Report No. R-87-013; August 1987; Final Report.

Van Gemert, M. J. C. High-frequency time-domain methods in dielectric spectroscopy. Phillips Res. Rpts.; 1973; 28: 530-572.

Volakis, J., and Peters, Jr., L. Elimination of undesired natural resonances for improved target identification. Paper presented at International Union of Radio Science, Quebec; 1980.

Volakis, J., and Peters, Jr., L. Improved identification of underground targets using video pulse radars by elimination of undesired natural resonances. IEEE Trans. on Antenna and Prop.; 1983; AP-31(No. 2).

Volakis, J. Improved identification of underground targets using video-pulse radars by elimination of undesired natural resonances; M.Sc. thesis, The Ohio State University.

von Hippel, A. R. Dielectric materials and applications. Cambridge Massachusetts Inst. Technology; 1954: 438 p.

von Hippel, A. R. Dielectric and waves. New York, NY: John Wiley & Sons; 1954: 284 p.

Wagner, K. W. Erklarung der dielektrischen Nachwirkungsvorgange auf Grund Maxwellscher verstellungen. Archiv. Electrotechnik; 1914; 2: 371.

Wait, J. R. A conducting sphere in a time-varying field. Geophysics; 1951; 16: 666.

Wait, James R. Mutual electromagnetic coupling of loops over a homogeneous ground. Geophysics XX; 1955; (No. 3): 630-637.

Wald, L. W. Modification of the HFW underground antenna based on experimental studies. The Ohio State University ElectroScience Lab., Dept. of Electrical Engineering; Technical Report 4460-6.

Ward, S. H. Electromagnetic theory for geophysical applications. Mining Geophys.; 1967; II: 78.

Watt, A. D.; Maxwell, E. L. Characterization of atmospheric noise from 1 to 100 kHz. Proc. IRE; June 1957: 787.

Williams, G.; Watts, D. C. Nonsymmetrical dielectric relaxation behavior arising from a simple empirical decay function. Trans. Faraday Soc.; 1970; 66: 80-85.

Williams, W. H.; et al. Elf: Computer automation and error correction for a microwave network analyzer. IEEE Trans. Instr. & Meas.; March 1988; 37(1): 95-100.

Wmyth, C. P. Dielectric relaxation times in molecular relaxation processes. London: The Chemical Society; 1966.

Woodward, P. M. Probability and information theory with application to radar. New York, NY: McGraw-Hill Book Co., Inc.; 1955.

Wyllie, G. Dielectric relaxation and molecular correlation in dielectric and related molecular processes. London: The Chemical Society; 1972.

Young, J. D.; Caldecott, R.; 1977; U.S. Patent No. 4,062,010.

Young, J. D.; Caldecott, R.; 1976; U.S. Patent No. 3,967,282.

International Radio Consultative Committee characteristics and applications of atmospheric radio noise data; 1983; Report No. 3220-2.

International Radio Consultative Committee worldwide minimum external noise levels, 0.1 Hz to 100 GHz; 1982; Report No. 670.

Measuring Dielectric Constant with the HP 8510 Network Analyzer. Product Note No. 8510-3, Hewlett-Packard Corp., Palo Alto, CA; August 1985.

Coupling Between Two Antennas Separated by a Planar Interface

D. A. Hill
K. H. Cavcey

Reprinted from: IEEE TRANSACTIONS ON GEOSCIENCE AND REMOTE SENSING, Vol. GE-25, No. 4, JULY 1987.

Coupling Between Two Antennas Separated by a Planar Interface

DAVID A. HILL, FELLOW, IEEE, AND KENNETH H. CAVCEY, MEMBER, IEEE

Abstract—The plane-wave spectrum technique is used to analyze the coupling between a pair of antennas separated by a planar interface. Multiple reflections between the antennas or between either antenna and the interface are included in the formulation. The formulation is used to model detection of buried objects, and a low-frequency metal detector example is analyzed in detail. For a transmitting loop and a buried oblate spheroid, the plane wave spectrum technique is shown to agree with well-known quasi-static approximations. Some experimental results from a 3-kHz metal detector are also shown.

I. Introduction

THE SUBJECT of radiation from an antenna in the presence of a half-space has a long history, and many results for electric and magnetic dipole sources have been summarized by Banos [1]. More recently, Smith [2] has used the plane-wave spectrum technique to study transmission into a lossy half-space. In this paper we use the plane-wave spectrum technique to describe the coupling between a pair of antennas located in different media separated by a planar interface. The approach is a generalization of Kerns' [3] plane-wave scattering matrix formulation for coupling between a pair of antennas located in a homogeneous medium.

The half-space geometry that we consider is useful in describing a number of important practical configurations. For example, in communicating with or locating trapped miners [4], [5], one antenna is located underground, and the other is usually above ground. Also, it might be desirable to do near-field planar scanning with the probe antenna in air for some transmitting antennas that are buried underground or submerged in water. Detection of subsurface objects [6] can be treated as a special case of this theory where the buried object is simply a passive scatterer.

The organization of this paper is as follows. In Section II we derive expressions for the coupling between a pair of general antennas separated by an interface and for the fields in each medium. In Section III we specialize the formulation to a case that is relevant for the detection of buried objects, and a low-frequency metal detector example is considered. The transmitting antenna in air is a small loop, and the buried object is a conducting oblate spheroid. We obtain specific numerical results for this case both from the plane-wave spectrum formulation of Section II and from quasi-static approximations, and the agreement is good. We also compare theoretical and experimental results for a metal detector operating at 3 kHz. Section IV contains conclusions and suggestions for other half-space problems that can be treated using the plane-wave spectrum approach.

Manuscript received May 19, 1986, revised October 7, 1986. This work was supported by the U.S. Army Belvoir Research & Development Center.

The authors are with Electromagnetic Fields Division, United States Department of Commerce, National Bureau of Standards, Boulder, CO 80303.

IEEE Log Number 8715154.

II. General Plane-Wave Scattering Formulation

The geometry for two antennas separated by a planar interface is shown in Fig. 1. The region $z < h$ has permeability μ and permittivity ϵ, and the region $z > h$ has permeability μ' and permittivity ϵ'. Both regions are isotropic, but ϵ and ϵ' can be complex to allow for loss. The time dependence is $\exp(-i\omega t)$.

Throughout this section we follow the notation and the formulation of Kerns [3] for coupling between a pair of antennas in a homogeneous medium. The primary difference resulting from the half-space geometry is the appearance of additional interaction terms between the antennas and the interface.

A. Plane-Wave Representations

We define region 1 to be a slab region ($z_1 < z < h$) between the antenna and the interface. In this region we can write the electric field $\bar{E}_1$ and the magnetic field $\bar{H}_1$ in terms of plane-wave spectra

$$\bar{E}_1(\bar{r}) = \int_{-\infty}^{\infty}\int_{-\infty}^{\infty} \sum_{m=1}^{2} \left[b_1(m, \bar{K})\, \bar{E}_m^+(\bar{K}, \bar{r}) + a_1(m, \bar{K})\, \bar{E}_m^-(\bar{K}, \bar{r}) \right] dk_x\, dk_y$$

$$\bar{H}_1(\bar{r}) = \int_{-\infty}^{\infty}\int_{-\infty}^{\infty} \sum_{m=1}^{2} \left[b_1(m, \bar{K})\, \bar{H}_m^+(\bar{K}, \bar{r}) + a_1(m, \bar{K})\, \bar{H}_m^-(\bar{K}, \bar{r}) \right] dk_x\, dk_y \quad (1)$$

where a_1 and b_1 are plane-wave coefficients, and $\bar{r}$ is the position vector. The integrations are taken over real values of the wavenumbers k_x and k_y. $\bar{K}$ is given by $\bar{K} = k_x \bar{e}_x + k_y \bar{e}_y$, where $\bar{e}_x$, $\bar{e}_y$, and $\bar{e}_z$ are unit vectors.

The plane wave fields, $\bar{E}_m^{\pm}$ and $\bar{H}_m^{\pm}$, are transverse electric (TE) for $m = 2$ or transverse magnetic (TM) for $m =$

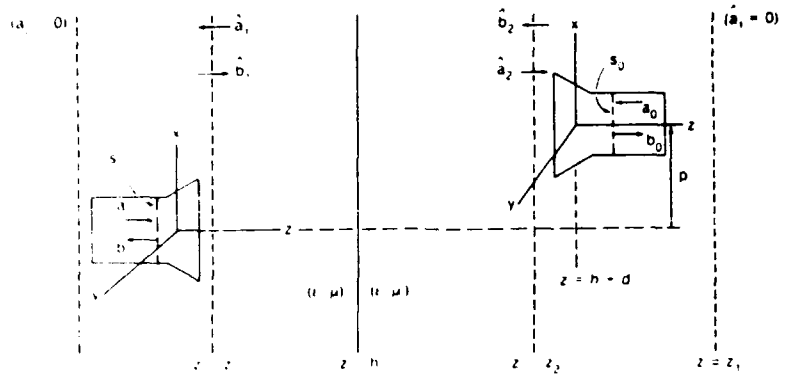

Fig. 1. Geometry for two antennas separated by a planar interface.

1. The propagation vector $\bar{k}^{\pm}$ can be written in the following form:

$$\bar{k}^{\pm} = \bar{K} \pm \gamma \bar{e}_z \tag{2}$$

where $\gamma = (k^2 - K^2)^{1/2}$, $k^2 = \omega^2 \mu\epsilon$, and $K^2 = \bar{K} \cdot \bar{K}$. The sign of the square root is chosen so that the imaginary part of γ is positive. If the imaginary part of γ is zero, then the sign is chosen so that γ is positive real. We define the following transverse unit vectors:

$$\bar{\kappa}_1 = \bar{K}/K$$

$$\bar{\kappa}_2 = \bar{e}_z \times \bar{\kappa}_1 \tag{3}$$

which are, respectively, in and perpendicular to the plane of $\bar{k}^{\pm}$ and $\bar{e}_z$. The TE plane-wave fields are given by

$$E_2^{\pm} = \bar{\kappa}_2 u^{\pm}$$

$$H_2^{\pm} = \left[\pm \eta_2 \bar{e}_z \times \bar{\kappa}_2 + K(\omega\mu)^{-1} \bar{e}_z \right] u^{\pm} \tag{4}$$

where $u^{\pm} = \exp(\pm i\bar{k}^{\pm} \cdot \bar{r})/(2\pi)$ and $\eta_2 = \gamma/(\omega\mu)$. The superscript $\pm$ refers to propagation in the $\pm z$ direction. The TM plane-wave fields are given by

$$E_1^{\pm} = \left[\bar{\kappa}_1 \mp K\gamma^{-1} \bar{e}_z \right] u^{\pm}$$

$$H_1^{\pm} = \pm \eta_1 \bar{e}_z \times \bar{\kappa}_1 u^{\pm} \tag{5}$$

where $\eta_1 = \omega\epsilon/\gamma$.

In some cases, only the transverse components of the fields are required. From (1)–(5), we can write

$$\bar{E}_t(\bar{r}) = \frac{1}{2\pi} \int \sum_m \left[b_1(m, \bar{K}) e^{i\gamma z} + a_1(m, \bar{K}) e^{-i\gamma z} \right] \bar{\kappa}_m e^{i\bar{K} \cdot \bar{R}} \, d\bar{K}$$

$$\bar{H}_t(\bar{r}) = \frac{1}{2\pi} \int \sum_m \left[b_1(m, \bar{K}) e^{i\gamma z} - a_1(m, \bar{K}) e^{-i\gamma z} \right] \bar{e}_z \times \bar{\kappa}_m \eta_m e^{i\bar{K} \cdot \bar{R}} \, d\bar{K} \tag{6}$$

where $\bar{r} = \bar{R} + z\bar{e}_z$ and subscript t denotes the transverse components. When z components are desired, they can be obtained from (1) or from the transverse components and Maxwell's equations. In (6) and throughout the rest of the paper, summation over the values 1 and 2 of the polarization index m and integration over the infinite k_x, k_y plane are understood.

We define region 2 to be a slab region ($-d < z' < z_2'$) between the other antenna and the interface. In this region we can write the transverse components of the fields in a manner analogous to (6)

$$\bar{E}_{2t}'(\bar{r}') = \frac{1}{2\pi} \int \sum_m \left[b_2'(m, \bar{K}) e^{-i\gamma' z'} + a_2'(m, \bar{K}) e^{i\gamma' z'} \right] \bar{\kappa}_m e^{i\bar{K} \cdot \bar{R}'} \, d\bar{K}$$

$$\bar{H}_{2t}'(\bar{r}') = \frac{1}{2\pi} \int \sum_m \left[b_2'(m, \bar{K}) e^{-i\gamma' z'} - a_2'(m, \bar{K}) e^{i\gamma' z'} \right] (-\bar{e}_z) \times \bar{\kappa}_m \eta_m' e^{i\bar{K} \cdot \bar{R}'} \, d\bar{K} \tag{7}$$

where $\bar{r}' = \bar{R}' + z'\bar{e}_z$, $\eta_1' = \omega\epsilon'/\gamma'$, $\eta_2' = \gamma'/\omega\mu'$, $\gamma' = (k'^2 - K^2)^{1/2}$, and $k'^2 = \omega^2\mu'\epsilon'$. We could write similar expressions for the fields in the regions, $z < z_2$ and $z' > z_1'$, but these regions contain no sources and do not affect the antenna coupling.

B. Antenna Characteristics

We begin with a description of the antenna on the left in Fig. 1. Because there are no waves incident from the left of the antenna ($a_2 = 0$), the scattering equations are written [3]

$$b_0 = S_{00} a_0 + \int_{\bar{L}} \sum_n S_{01}(n, \bar{L}) \, a_1(n, \bar{L}) \, d\bar{L}$$

$$b_1(m, \bar{K}) = S_{10}(m, \bar{K}) a_0 + \int_{\bar{L}} \sum_n S_{11}(m, \bar{K}; n, \bar{L}) \cdot a_1(n, \bar{L}) \, d\bar{L} \tag{8}$$

where a_0 and b_0 are coefficients of incoming and outgoing modes at the antenna feed, S_{00} represents backscattering observed at the feed, S_{01} represents the receiving characteristics of the antenna, S_{10} represents the transmitting characteristics, and S_{11} represents the scattering characteristics. For later work it is convenient to rewrite (8) in

the following short-hand notation:

$$b_0 = S_{00}a_0 + \hat{S}_{01}\hat{a}_1$$
$$\hat{b}_1 = \hat{S}_{10}a_0 + \hat{S}_{11}\hat{a}_1. \quad (9)$$

Here, $\hat{a}_1$ and $\hat{b}_1$ are column matrices representing $a_1(m, \bar{K})$ and $b_1(m, \bar{K})$ according to the values of m and $\bar{K}$. $\hat{S}_{01}$ is a row matrix, $\hat{S}_{10}$ is a column matrix, and $\hat{S}_{11}$ is a square matrix.

The antenna on the right in Fig. 1 can be treated in the same manner. In this case there are no waves incident from the right ($a_1' = 0$). For brevity we write only the short-hand scattering relationships

$$b_0' = S_{00}'a_0' + \hat{S}_{02}'\hat{a}_2'$$
$$\hat{b}_2' = \hat{S}_{20}'a_0' + \hat{S}_{22}'\hat{a}_2' \quad (10)$$

where a_0' and b_0' are coefficients of incoming and outgoing modes at the feed, S_{00}' represents backscattering at the feed, and $\hat{a}_2'$ and $\hat{b}_2'$ are column matrices of plane wave coefficients. $\hat{S}_{02}'$ is a row matrix representing the receiving characteristics of the antenna, $\hat{S}_{20}'$ is a column matrix representing the transmitting characteristics, and $\hat{S}_{22}'$ is a square matrix representing the scattering characteristics.

C. Solution for the Coefficients

The transverse field components must be continuous at the interface ($z = h$ or $z' = -d$)

$$\bar{E}_{1t}(\bar{R} + h\bar{e}_z) = \bar{E}_{2t}'(\bar{R} - \bar{P} - d\bar{e}_z)$$
$$\bar{H}_{1t}(\bar{R} + h\bar{e}_z) = \bar{H}_{2t}'(\bar{R} - \bar{P} - d\bar{e}_z) \quad (11)$$

where $\bar{P}$ is a transverse vector defined in Fig. 1. If we substitute (6) and (7) into (11), we obtain the following relationships for the coefficients:

$$a_1(m, \bar{K}) = R_{11}'b_1(m, \bar{K}) + T_{12}'b_2'(m, \bar{K})$$
$$a_2'(m, \bar{K}) = T_{21}'b_1(m, \bar{K}) + R_{22}'b_2'(m, \bar{K}). \quad (12)$$

The superscript t on the coefficients indicates that they are translated reflection and transmission coefficients

$$R_{11}' = R_{11}e^{i2\gamma h}, \qquad T_{12}' = T_{12}e^{i(\gamma h + \gamma' d - \bar{K}\cdot\bar{P})}$$
$$T_{21}' = T_{21}e^{i(\gamma h + \gamma' d + \bar{K}\cdot\bar{P})}, \qquad R_{22}' = R_{22}e^{i2\gamma' d} \quad (13)$$

where

$$R_{11} = \frac{\eta_m - \eta_m'}{\eta_m + \eta_m'}, \qquad T_{12} = \frac{2\eta_m'}{\eta_m + \eta_m'}$$
$$T_{21} = \frac{2\eta_m}{\eta_m' + \eta_m}, \qquad R_{22} = \frac{\eta_m' - \eta_m}{\eta_m' + \eta_m}. \quad (14)$$

The quantities in (14) are easily identified as plane-wave reflection and transmission coefficients.

We can rewrite (12) in short-hand notation as we did in (9) and (10)

$$\hat{a}_1 = \hat{R}_{11}'\hat{b}_1 + \hat{T}_{12}'\hat{b}_2'$$
$$\hat{a}_2' = \hat{T}_{21}'\hat{b}_1 + \hat{R}_{22}'\hat{b}_2'. \quad (15)$$

Here, $\hat{R}_{11}'$, $\hat{T}_{12}'$, $\hat{T}_{21}'$, and $\hat{R}_{22}'$ are all square diagonal matrices. The physical interpretation of (12) or (15) is that any plane-wave incident on the interface is reflected and refracted with the same polarization and transverse wavenumber. There is no mode conversion, and this is the principal advantage of using plane-wave expansions for the half-space geometry of Fig. 1.

From (9), (10), and (15), we have six equations in eight unknowns, four scalars (a_0, b_0, a_0', and b_0'), and four column matrices ($\hat{a}_1$, $\hat{b}_1$, $\hat{a}_2'$, and $\hat{b}_2'$). These equations have been derived from conditions on the transverse fields at $z = z_1$, $z = h$, and $z' = z_2'$. To solve the system completely, we need two more equations, and these could be obtained at the antenna terminals, S_0 and S_0'. An alternative is to eliminate the column matrices from the six equations and obtain the scattering matrix of the "system two-port," which has its terminals at S_0 and S_0' and is defined by the equations [3]

$$b_0 = M_{00}a_0 + M_{00'}a_0'$$
$$b_0' = M_{0'0}a_0 + M_{0'0'}a_0'. \quad (16)$$

After considerable manipulation of (9), (10), and (15), we obtain

$$M_{00} = S_{00} + \hat{S}_{01}[\hat{1} - \hat{R}_{11}'\hat{S}_{11} - \hat{T}_{12}'\hat{S}_{22}'(\hat{1} - \hat{R}_{22}'\hat{S}_{22}')^{-1} \cdot \hat{T}_{21}'\hat{S}_{11}]^{-1}[\hat{R}_{11}' + \hat{T}_{12}'\hat{S}_{22}'(\hat{1} - \hat{R}_{22}'\hat{S}_{22}')^{-1}\hat{T}_{21}']\hat{S}_{10}$$
$$M_{00'} = \hat{S}_{01}[\hat{1} - \hat{R}_{11}'\hat{S}_{11} - \hat{T}_{12}'\hat{S}_{22}'(\hat{1} - \hat{R}_{22}'\hat{S}_{22}')^{-1}\hat{T}_{21}'\hat{S}_{11}]^{-1} \cdot \hat{T}_{12}'(\hat{1} - \hat{S}_{22}'\hat{R}_{22}')^{-1}\hat{S}_{20}'$$
$$M_{0'0} = \hat{S}_{02}'[\hat{1} - \hat{R}_{22}'\hat{S}_{22}' - \hat{T}_{21}'\hat{S}_{11}(\hat{1} - \hat{R}_{11}'\hat{S}_{11})^{-1}\hat{T}_{12}\hat{S}_{22}']^{-1} \cdot \hat{T}_{21}'(\hat{1} - \hat{S}_{11}\hat{R}_{11})^{-1}\hat{S}_{10}$$
$$M_{0'0'} = S_{00}' + \hat{S}_{02}'[\hat{1} - \hat{R}_{22}'\hat{S}_{22}' - \hat{T}_{21}'\hat{S}_{11}(\hat{1} - \hat{R}_{11}'\hat{S}_{11})^{-1} \cdot \hat{T}_{12}'\hat{S}_{22}']^{-1}[\hat{R}_{22}' + \hat{T}_{21}'\hat{S}_{11}(\hat{1} - \hat{R}_{11}\hat{S}_{11})^{-1}\hat{T}_{12}']\hat{S}_{20}' \quad (17)$$

where $\hat{1}$ is an identity matrix and the superscript -1 indicates an inverse.

This completes the formal solution for the interaction between arbitrary antennas separated by an interface, but several comments are in order. The scattering parameters of the system in (17) contain several inverses. If we make the system discrete and of finite dimension, then the inverses in (17) can be interpreted as inverse matrices and standard matrix methods apply. All of the inverses are of the following form that can be expanded in a geometric series:

$$(\hat{1} - \hat{A})^{-1} = \hat{1} + \hat{A} + \hat{A}^2 + \hat{A}^3 + \cdots \quad (18)$$

where higher powers of the matrix $\hat{A}$ can be interpreted as multiple interactions. If we neglect such multiple interactions in (17), then the scattering parameters of the system take on the following forms:

$$M_{00} \approx S_{00} + \hat{S}_{01}(\hat{R}_{11}' + \hat{T}_{12}'\hat{S}_{22}'\hat{T}_{21}')\hat{S}_{10}$$
$$M_{00'} \approx \hat{S}_{01}\hat{T}_{12}'\hat{S}_{20}'$$

$$M_{0'0} \approx \hat{S}'_{02}\hat{T}'_{21}\hat{S}_{10}$$

$$M_{0'0'} \approx \hat{S}'_{00} + \hat{S}'_{02}[\hat{R}'_{22} + \hat{T}'_{21}\hat{S}_{11}\hat{T}'_{12}]\hat{S}'_{20}. \quad (19)$$

Both M_{00} and $M_{0'0}$ contain three terms that represent reflections from the antenna terminals, the interface, and the opposite antenna. $M_{00'}$ and $M_{0'0'}$ contain one term that represents transmission through the interface. Multiple interactions can be included by expanding the inverses as in (18). If the two media have the same constitutive parameters, then the reflection coefficients ($\hat{R}'_{11}$ and $\hat{R}'_{22}$) go to zero, and the results in (17) reduce to those of Kerns [3] for a homogeneous medium.

III. Detection of Buried Objects

To model the case of detection of buried objects, we set ϵ and μ equal to their free space values (ϵ_0 and μ_0) and set ϵ' and μ' equal to values for lossy ground. This means that ϵ' is typically complex

$$\epsilon' = \epsilon_r + i\sigma/\omega \quad (20)$$

where ϵ_r is the real permittivity of the ground and σ is the conductivity of the ground. Most soils are approximately nonmagnetic, and we can set μ' equal to the free space permeability μ_0. A detailed study by Cook and Carts [7] found this to be a good approximation for most soil types except for some coastal sands. We also replace the right-hand antenna in Fig. 1 by a passive scatterer. Scattering by buried objects has been treated by the transition matrix formalism [8], by the unimoment method [9], and by the moment method [10].

A. Simplification for a Passive Scatterer

To treat the case of a passive buried scatterer, we remove the terminals from the right antenna in Fig. 1. The scatterer is then completely characterized by its scattering characteristics $\hat{S}'_{22}$, and (10) simplifies to

$$\hat{b}'_2 = \hat{S}'_{22}\hat{a}'_2. \quad (21)$$

Also, the "system two-port" relations in (16) are replaced by

$$b_0 = M_{00}a_0 \quad (22)$$

where M_{00} is still given by (17).

For detection systems that receive and transmit with the same antenna, (22) provides an adequate description because it yields the received signal b_0. However, if a separate antenna is used for reception, then we need to know the fields above the ground that will excite the receiving antenna. The total fields in the slab region between the ground and the transmitting antenna ($z_1 < z < h$) are given by (1), and the transverse components are given by (6). The plane wave coefficients for this region are determined from simultaneous solution of (9), (15), and (21). If we neglect multiple interaction terms, then (23) simplifies to

$$\hat{a}_1 \approx (\hat{R}'_{11} + \hat{T}'_{12}\hat{S}'_{22}\hat{T}'_{21})\hat{S}_{10}a_0$$

$$\hat{b}_1 \approx \hat{S}_{10}a_0. \quad (24)$$

The two terms for $\hat{a}_1$ represent reflection from the ground and scattering from the buried object. The single term for $\hat{b}_1$ represents direct transmission from the antenna. Multiple interaction terms can be obtained by expanding the inverses as in (18).

If the receiving antenna is located above the transmitting antenna, then we also need the field expressions for negative z. However, the fields in this region contain only upgoing plane-waves, and the plane-wave coefficients resulting from ground reflection and scattering from the buried target are given by $\hat{a}_1$ in (23) for any value of $z < h$. To obtain the total field above the antenna, we only need to add the direct field from the antenna.

B. Low-Frequency Example

In Fig. 2 the geometry of Fig. 1 is specialized to the case of a horizontal loop transmitting antenna and a small passive scatterer. This geometry is relevant to common metal detectors and to metal mine detectors.

The small loop antenna has area A and carries a uniform current I. Thus, it radiates like a z-directed magnetic dipole of magnetic moment IA. Kerns [3, p. 128] has given the transmitting spectrum of a small loop, and we can write the transmitting characteristics as

$$S_{q0}(1, \bar{K}) = 0$$

$$S_{q0}(2, \bar{K}) = \frac{i\omega\mu A}{4\pi}\frac{K}{(k^2 - K^2)^{1/2}} \quad (25)$$

where $q = 1$ or 2. We have arbitrarily defined $a_0 = I$. From (25) we see that the small loop radiates only TE fields ($m = 2$) and the transmitting characteristics are the same below ($z > 0$, $q = 1$) or above ($z < 0$, $q = 2$) the loop. For a small loop we can neglect scattering and set

$$S_{11} \approx 0. \quad (26)$$

Because we do not anticipate receiving with the transmitting loop, we do not need to specify S_{00} and S_{01}.

We assume that the buried scatterer is electrically small and that it scatters like a pair of electric and magnetic dipoles [11]. The equivalent electric and magnetic dipole moments $\bar{p}_e$ and $\bar{p}_m$ can be written as

$$\bar{p}_e = \bar{\bar{\alpha}}_e \cdot \bar{E}'$$

$$\bar{p}_m = \bar{\bar{\alpha}}_m \cdot \bar{H}' \quad (27)$$

where $\bar{\bar{\alpha}}_e$ and $\bar{\bar{\alpha}}_m$ are electric and magnetic polarizability

$$\hat{a}_1 = [\hat{I} - \hat{R}'_{11}\hat{S}_{11} - \hat{T}'_{12}\hat{S}'_{22}(\hat{I} - \hat{R}'_{22}\hat{S}'_{22})^{-1}\hat{T}'_{21}\hat{S}_{11}]^{-1} \cdot [\hat{R}'_{11} + \hat{T}'_{12}\hat{S}'_{22}(\hat{I} - \hat{R}'_{22}\hat{S}'_{22})^{-1}\hat{T}'_{21}]\hat{S}_{10}a_0$$

$$\hat{b}_1 = [\hat{I} - \hat{R}'_{11}\hat{S}_{11} - \hat{T}'_{12}\hat{S}'_{22}(\hat{I} - \hat{R}'_{22}\hat{S}'_{22})^{-1}\hat{T}'_{21}\hat{S}_{11}]^{-1}\hat{S}_{10}a_0. \quad (23)$$

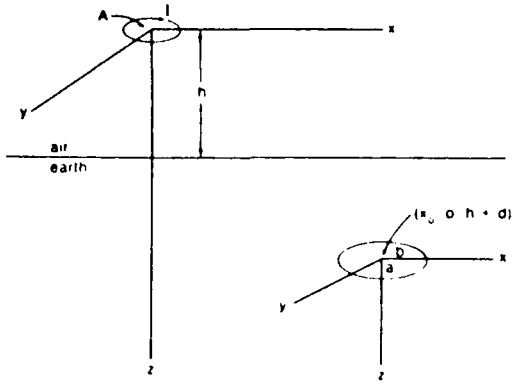

Fig. 2. Geometry for a loop antenna in air and a buried oblate spheroid.

dyads and $\bar{\bar{E}}'$ and $\bar{\bar{H}}'$ are the incident electric and magnetic fields in the absence of the scatterer. To use the polarizability results in the plane-wave scattering matrix formulation, we need to derive the scattering matrix $\hat{S}_{22}'$ from (27), and this is done in Appendix A. Kerns [3] has treated the special case of a small dielectric sphere where $\bar{\bar{\alpha}}_e$ reduces to a scalar and $\bar{\bar{\alpha}}_m$ is zero.

C. Quasi-Static Approach

For sufficiently low frequencies, the wavenumbers k and k' are approximately zero, and the fields of the small loop are approximately those of a static magnetic dipole. This type of approximation is best obtained by quasi-static approximations to Sommerfeld integrals [12], and the mathematical details are given in Appendix B. Here we present only the final results.

The magnetic field in air produced by the loop antenna is

$$H_{1x}^a \approx \frac{IA}{4\pi r^3}\frac{3xz}{r^2}$$

$$H_{1y}^a \approx \frac{IA}{4\pi r^3}\frac{3yz}{r^2}$$

$$H_{1z}^a \approx \frac{IA}{4\pi r^3}\left(\frac{3z^2}{r^2} - 1\right) \tag{28}$$

where $r = (x^2 + y^2 + z^2)^{1/2}$. The electric field is negligible because it is proportional to frequency (see Appendix B). For observation points that are very close to the loop in terms of the loop radius, the magnetic dipole approximation is not accurate, and this limitation is discussed in Appendix C.

The buried object is an oblate spheroid located at the origin of the primed coordinate with its axis aligned with the z axis. We consider an oblate spheroid because it is a realistic object whose electric and magnetic polarizabilities are known [13]. Here, we require only the magnetic polarizability because the incident electric field is negligible. For perfect conductivity, the magnetic polarizability is [3]

$$\bar{\bar{\alpha}}_m = \alpha_{mx}\bar{e}_x\bar{e}_x + \alpha_{my}\bar{e}_y\bar{e}_y + \alpha_{mz}\bar{e}_z\bar{e}_z \tag{29}$$

where $\alpha_{mx} = \alpha_{my} = -2V/(1 + L)$, $\alpha_{mz} = -V/(1 - L)$, $V = \frac{4}{3}\pi ab^2$, and

$$L = \frac{ab^2}{(b^2 - a^2)^{3/2}}\left\{\frac{(b^2 - a^2)^{1/2}}{a} - \tan^{-1}\left[\frac{(b^2 - a^2)^{1/2}}{a}\right]\right\}.$$

As indicated in Fig. 2, a is the semiminor axis, and b is the semimajor axis. For the special case of a sphere ($a = b$), (29) reduces to

$$\alpha_{mx} = \alpha_{my} = \alpha_{mz} = -2\pi a^3. \tag{30}$$

If we locate the prime coordinate origin at $x = x_0$, $y = 0$, $z = h + d$, then the incident field at the center of the spheroid is [12]

$$H_x' \approx \frac{IA}{4\pi r_i^3}\frac{3x_0(h + d)}{r_i^2}$$

$$H_y' = 0$$

$$H_z' \approx \frac{IA}{4\pi r_i^3}\left[\frac{3(h + d)^2}{r_i^2} - 1\right] \tag{31}$$

where $r_i = [x_0^2 + (h + d)^2]^{1/2}$. Thus the induced magnetic dipole moment is

$$p_{mx} = \alpha_{mx}H_x', \quad p_{my} = 0$$

$$p_{mz} = \alpha_{mz}H_z' \tag{32}$$

where α_{mx} and α_{my} are given by (29), and H_x' and H_z' are given by (31). The fields scattered by the spheroid are then given by (see Appendix B)

$$H_x^s \approx \frac{1}{4\pi r_s^3}\left\{p_z\frac{3(z - d - h)(x - x_0)}{r_s^2} + p_x\left[\frac{3(x - x_0)^2}{r_s^2} - 1\right]\right\}$$

$$H_y^s \approx \frac{1}{4\pi r_s^3}\left\{p_z\frac{3(z - h - d)y}{r_s^2} + p_x\frac{3(x - x_0)y}{r_s^2}\right\}$$

$$H_z^s \approx \frac{1}{4\pi r_s^3}\left\{p_z\left[\frac{3(z - h - d)^2}{r_s^2} - 1\right] + p_x\frac{3(x - x_0)(z - h - d)}{r_s^2}\right\} \tag{33}$$

where $r_s = [(x - x_0)^2 + y^2 + (z - d - h)^2]^{1/2}$.

At this point it is useful to do a numerical comparison between the plane-wave scattering-matrix formulation of Section II and the quasi-static approximation. Because we are modeling both the loop antenna and the oblate spheroid scatterer as magnetic dipoles, it is sufficient to compare the two methods for calculating the incident magnetic field of the loop (magnetic dipole) source. Fig. 3 shows the x and z components of the incident magnetic field as a function of x calculated by the two methods. The quasi-static curves are obtained from (31) and are

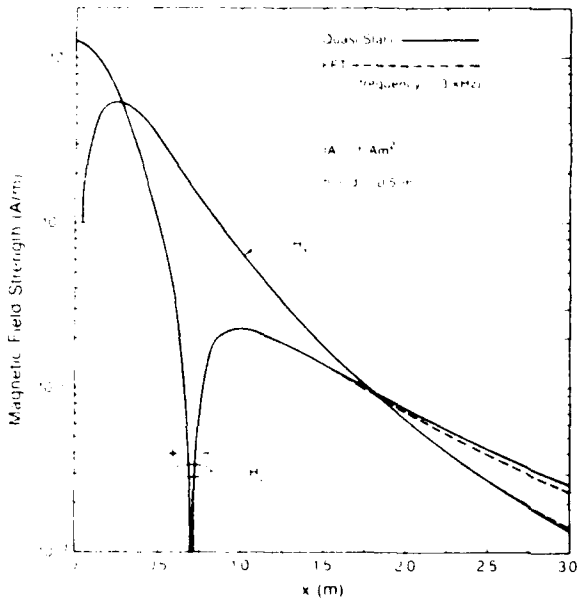

Fig. 3. Comparison of the magnetic field of a small loop calculated by FFT and by quasi-static approximations.

valid for r_1 much less than a free-space wavelength. The other curves are obtained by substituting the transmitting spectrum given by (25) into the plane-wave spectrum results of Section II. The two-dimensional integrals on wavenumbers k_x and k_y are evaluated by two-dimensional fast Fourier transform (FFT). The FFT evaluation is very efficient and has been used for related problems involving sources over the earth [14]. The agreement between the two methods is very good for $x < 2$ m, and this range can be extended by including more samples in the FFT. However, the field values are so small for $x > 2$ m that this range is of little interest. The main point of Fig. 3 is that the plane-wave spectrum representation is easily evaluated by FFT and is accurate even in the quasi-static region. In near-field antenna scanning [3], the plane-wave representation is generally used in the radiating near field (distances somewhat greater than a wavelength). The frequency of 3 kHz is typical of metal detectors, but the magnetic field is essentially independent of frequency for such low frequencies.

Because the FFT and quasi-static approximation give essentially the same results, we use the simpler quasi-static approximation in the remaining calculations for low-frequency metal detectors. Fig. 4 shows a typical example for the direct antenna field and the field scattered by a buried oblate spheroid. An obvious difficulty in detecting the buried scatterer is that the direct field is much larger than the scattered field, even for a sizable buried object ($a = 5$ cm and $b = 15$ cm). This problem is usually overcome by nulling out the direct field and by moving the source closer to the earth (smaller h). There are many ways to accomplish the nulling, and one method is described in the following section.

D. A Practical Metal Detector

One type of mine detector uses a single transmitting loop and four receiving loops as shown in Fig. 5. The

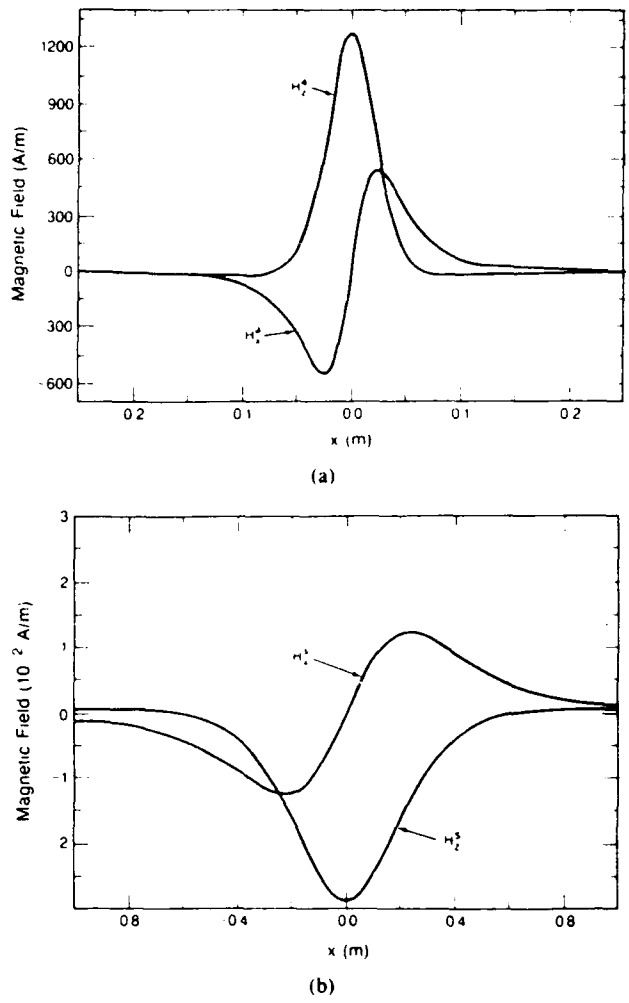

Fig. 4. Horizontal variation of (a) the incident magnetic field of a small loop and (b) the magnetic field scattered by an oblate spheroid. Parameters: $IA = 1$ A · m², $y = 0$, $z = 5$ cm, $h + d = 50$ cm, $x_0 = 10$ cm, $a = 5$ cm, and $b = 15$ cm.

detector sums the output of the four loops, but two of the polarities are reversed. Because of the detector symmetry, the direct field of transmitting loop (or any other symmetrical field, such as a reflection from smooth ground) produces a zero output. Hence the desired nulling of the strong direct field is achieved.

When a buried scatterer is present, the total received voltage V_r can be written

$$V_r = K(H^s_{z1} - H^s_{z2} + H^s_{z3} - H^s_{z4}) \qquad (34)$$

where $K = i\omega\mu_0 N_r A_r$, N_r is the number of turns in the receiving loops, and A_r is the area of the receiving loops. In our theoretical model we assume that the four receiving loops are identical and that the transmitting and receiving loops can be modeled as magnetic dipoles. The transmitting loop is actually fairly large, and the magnetic dipole approximation is not good if the detector is located too close to the scatterer. The scattered magnetic fields, $H^s_{z1} - H^s_{z4}$, in (34) are the scattered fields evaluated at the four loop centers. We model the buried object as an oblate spheroid, and the scattered fields are calculated as indicated in (29)–(33).

The experiment was conducted in a sandbox where the

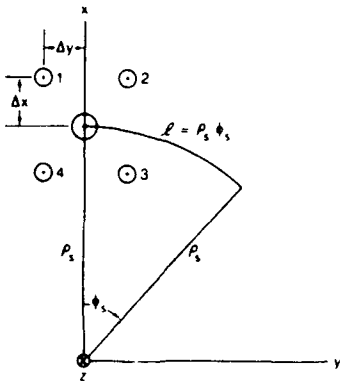

Fig. 5. Geometry for a metal detector with a central transmitting loop and four receiving loops. The detector is swept in an arc of radius ρ_s in the $z = 0$ plane.

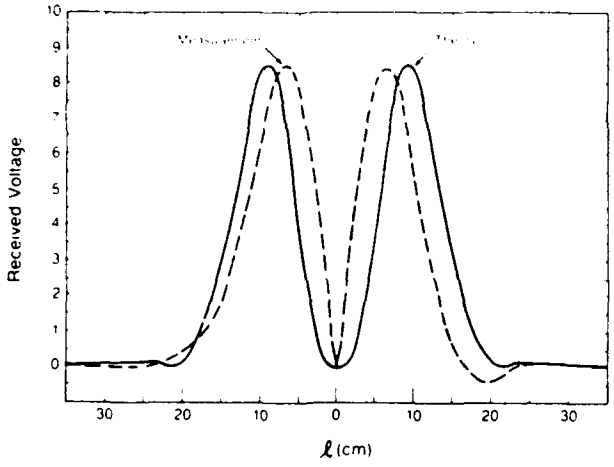

Fig. 6. Comparison of theoretical and measured received voltage for a metal detector swept over a buried copper penny. Parameters: $h = d = 7.5$ cm, $\Delta x = 7.62$ cm, $\Delta y = 5.72$ cm, $\rho_s = x_0 = 1.13$ m, $a = 0.5$ mm, and $h = 9$ mm.

detector was moved in an arc to simulate the mine detector sweep technique. A copper penny was buried at a depth of 7.5 cm in dry sand, and the mine detector was maintained at a constant height of 7.5 cm above the surface of the sand. We did not measure the dielectric constant of the sand at the detector frequency of 3 kHz, but the sand was found to have little effect on the sweep waveform. This is in agreement with the quasi-static approximations of the previous section. The arc radius of the detector path was 1.13 m, and the receiving loops were offset by $\Delta x = 7.62$ cm and $\Delta y = 5.72$ cm. We modeled the copper penny as a perfectly conducting oblate spheroid of major axis 18 mm and minor axis 1 mm. A comparison of the theoretical and measured sweep curves is shown in Fig. 6. The arc distance l is defined in Fig. 5. Only a relative amplitude comparison is attempted because the value of the constant K in (34) is not known for the detector that was used in the measurement. Both curves have a null for the detector directly over the scatterer. The theoretical curve is symmetrical, and the measured curve is fairly symmetrical. The main differences are that the theoretical curve has a broader null and has a greater separation between the peaks. The measured null would probably be broader if it

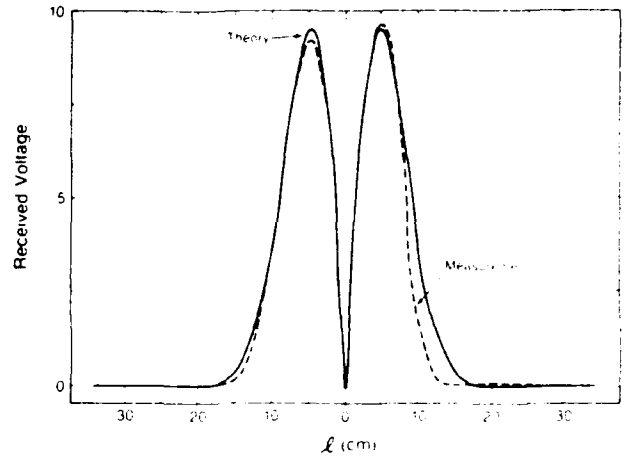

Fig. 7. Comparison of theoretical and measured received voltage for a metal detector swept over a copper penny. Parameters: $h = 15$ cm, $d = 0$, $\Delta x = 7.62$ cm, $\Delta y = 5.72$ cm, $\rho_s = 1.13$ m, $x_0 = \rho_s + \Delta x$, $a = 0.5$ mm, and $h = 9$ mm.

were possible to balance the four loop outputs more precisely.

In Fig. 7 a second comparison is shown where the penny is now on the surface ($d = 0$) and the detector is raised to maintain the same vertical separation ($h = 15$ cm). Also, the penny location is moved farther out ($x_0 = \rho_s + \Delta x$) so that two receiving coils pass over the penny. With the penny offset from the center of the detector, both the theory and experiment show a sharp null, and the overall agreement is very good. The null is sharp because only coils 1 and 2 contribute significantly to the total received voltage in (34). We have made comparisons for other values of x_0, and we generally find good agreement for $x_0 \neq \rho_s$ where the balance of the four receiving loops is less critical.

IV. Conclusions

We have used the plane-wave spectrum technique to analyze the coupling between a pair of antennas separated by a planar interface. The results are similar to those of Kerns [3], but there are additional multiple interactions that involve the planar interface. We have treated the case of detection of buried targets by replacing one of the antennas by a buried passive scatterer. We have analyzed the case of a loop transmitter and a buried oblate spheroid in detail and have compared theoretical and experimental results for a low-frequency metal detector.

The formulation in Section I is quite general and could be applied to many antenna or scattering problems. The required antenna or scatterer characteristics could be determined by any available method, such as the unimoment method [9], or even experimentally. We could also treat near-field scanning of a buried antenna where we wish to determine the transmitting characteristics $\hat{S}_{20}$ of the buried antenna. Similarly, the scattering characteristics $\hat{S}_{22}$ of a buried scatterer could be determined by scanning the scattered fields above the earth. We are currently modeling the problem of a UHF detector over a buried dielectric sphere, and we are using the plane-wave spectrum theory

to evaluate the importance of multiple reflections between the detector or the scatterer and the interface.

Appendix A
S'_{22} for Small Scatterers

For electrically small scatterers, we can split S'_{22} into two terms

$$S'_{22}(m, \bar{K}; n, \bar{L}) = S'_{22e}(m, \bar{K}; n, \bar{L}) + S'_{22m}(m, \bar{K}; n, \bar{L}) \quad \text{(A1)}$$

where S'_{22e} is due to the induced electric dipole moment and S'_{22m} is due to the induced magnetic dipole moment. The actual expression for S'_{22} is most easily obtained by starting with the vector-dyadic form of the scattering matrix of the second kind [3]. This dyadic form can be split in the same manner as in (A1)

$$\bar{\bar{s}}'_{22}(\bar{K}, \bar{L}) = \bar{\bar{s}}'_{22e}(K, L) + \bar{\bar{s}}'_{22m}(\bar{K}, \bar{L}) \quad \text{(A2)}$$

where subscripts e and m again refer to the induced electric and magnetic dipole moments. The dyadic scattering matrix $\bar{\bar{s}}'_{22}$ relates the vector coefficients of the incoming and outgoing plane waves as follows:

$$\bar{b}'_2(\bar{K}) = \int \bar{\bar{s}}'_{22}(\bar{K}, \bar{L}) \cdot \bar{a}'_2(\bar{L})\, d\bar{L}. \quad \text{(A3)}$$

The vector plane wave coefficients are related to the scalar coefficients by

$$\bar{b}'_2(\bar{K}) = b'_2(1, \bar{K})(\bar{\kappa}_1 + K\gamma'^{-1}\bar{e}_z) + b'_2(2, \bar{K})\bar{\kappa}_2$$

$$\bar{a}'_2(\bar{L}) = a'_2(1, \bar{L})(\bar{\kappa}_{L1} - L\gamma'^{-1}_L\bar{e}_z) + a'_2(2, \bar{L})\bar{\kappa}_{L2}. \quad \text{(A4)}$$

The subscript L on γ' and $\bar{\kappa}$ refers to an incoming plane wave with transverse wavenumber L.

By using the spectrum for an electric dipole [3], we can write

$$\bar{\bar{s}}'_{22e}(\bar{K}, \bar{L}) = \frac{ik^2}{8\pi^2\gamma'}\bar{\bar{\Pi}}(\bar{k}') \cdot \bar{\bar{\alpha}}_e \cdot \bar{\bar{\Pi}}(\bar{l}') \quad \text{(A5)}$$

where $\bar{\bar{\Pi}}(\bar{k}') = \bar{\bar{I}} - \bar{k}'\bar{k}'k'^{-2}$, $\bar{\bar{I}}$ is the identity dyad, and $\bar{l}'$ is the incoming propagation vector. This result is consistent with Kerns' result for a small dielectric sphere [3] where $\bar{\bar{\alpha}}_e$ is proportional to $\bar{\bar{I}}$. By using the spectrum for a magnetic dipole [3], we can also write

$$\bar{\bar{s}}'_{22m}(\bar{K}, \bar{L}) = \frac{1}{8\pi^2 i\gamma'}\bar{k}' \times \bar{\bar{\alpha}}_m \times \bar{l}'. \quad \text{(A6)}$$

By using the definitions in (A4) and the results in (A5) and (A6), we can obtain S'_{22}

$$S'_{22}(1, \bar{K}; 1, \bar{L}) = \bar{\kappa}_1 \cdot \bar{\bar{s}}'_{22}(\bar{K}, \bar{L}) \cdot (\bar{\kappa}_{L1} - L\gamma'^{-1}_L\bar{e}_z)$$

$$S'_{22}(1, \bar{K}; 2, \bar{L}) = \bar{\kappa}_1 \cdot \bar{\bar{s}}'_{22}(\bar{K}, \bar{L}) \cdot \bar{\kappa}_{L2}$$

$$S'_{22}(2, \bar{K}; 1, \bar{L}) = \bar{\kappa}_2 \cdot \bar{\bar{s}}'_{22}(\bar{K}, \bar{L}) \cdot (\bar{\kappa}_{L1} - L\gamma'^{-1}_L\bar{e}_z)$$

$$S'_{22}(2, \bar{K}; 2, \bar{L}) = \bar{\kappa}_2 \cdot \bar{\bar{s}}'_{22}(\bar{K}, \bar{L}) \cdot \bar{\kappa}_{L2}. \quad \text{(A7)}$$

This completes the derivation of S'_{22} for an electrically small scatterer in terms of its electric and magnetic polarizabilities.

Appendix B
Quasi-Static Approximations to Sommerfeld Integrals

An alternate formulation for the geometry in Fig. 2 can be obtained in terms of Sommerfeld integrals [8]. This formulation is equivalent to the plane wave spectrum formulation except that the double integrals over k_x and k_y are cast into polar form. For the simple source and scatterer of Fig. 2, the azimuthal integral can be done analytically, and only a single integral over the radial wavenumber remains.

We first consider the fields of the loop source in the absence of the scatterer. The fields in air ($z < h$) can be derived in terms of a magnetic Hertz vector with only a z component Π_z^*, which can be split into primary Π_z^{*p} and reflected Π_z^{*r} terms [8]

$$\Pi_z^* = \Pi_z^{*p} + \Pi_z^{*r} \quad \text{(B1)}$$

where

$$\Pi_z^{*p} = IA\frac{e^{ikr}}{4\pi r}$$

$$\Pi_z^{*r} = \frac{IA}{4\pi}\int_0^\infty u^{-1}J_0(\lambda\rho)\,R(\lambda)e^{-u(z+2h)}\lambda\,d\lambda$$

$$R(\lambda) = \frac{u - u'}{u + u'},\quad u = (\lambda^2 - k^2)^{1/2},\quad u' = (\lambda^2 - k'^2)^{1/2}$$

$$\rho = (x^2 + y^2)^{1/2}$$

and J_0 is the zero-order Bessel function. The magnetic and electric field components are given by

$$H_z = \left(\frac{\partial^2}{\partial z^2} + k^2\right)\Pi_z^*$$

$$H_\rho = \frac{\partial^2}{\partial\rho\partial z}\Pi_z^*$$

$$E_\phi = -i\omega\mu\frac{\partial\Pi_z^*}{\partial\rho}. \quad \text{(B2)}$$

In the quasi-static approximation, we assume that all relevant dimensions are small in terms of the free-space wavelength. This is equivalent to setting k equal to zero or $u \approx \lambda$. This approximation in (B1) and (B2) yields the inverse distance cubed fields given in (28). If in addition displacement currents are negligible and k' times the relevant dimensions is small, we can approximate u' by

$$u' \approx \lambda\left(1 - \frac{k'^2}{2\lambda^2}\right) \approx \lambda - \frac{i\omega\mu\sigma}{2\lambda}. \quad \text{(B3)}$$

Substitution of (B3) into (B1) and (B2) yields the following approximations for the reflected field components [8]:

$$H_z^r \approx \frac{i\omega\mu\sigma IA}{16\pi r_r}$$

$$H_\rho^r \approx \frac{-i\omega\mu\sigma IA}{16\pi\rho}\left(1 - \frac{2h - z}{r_r}\right)$$

$$E_\phi^r \approx \frac{\omega^2\mu^2\sigma IA}{16\pi}\frac{r_r - (2h - z)}{\rho} \quad \text{(B4)}$$

where

$$r = \left[\rho^2 + (2h - z)^2\right]^{1/2}.$$

The reflected field in (A11) is small compared to the primary field if the following inequality holds:

$$\omega\mu\sigma r_1^2 \ll 1. \tag{B5}$$

This inequality normally holds for the low frequencies used by metal detectors, and the reflected field can be neglected as in (28).

The transmitted fields in the earth can also be derived from a magnetic Hertz vector with only a z component [8]

$$\Pi_z^{se} = \frac{IA}{4\pi}\int_0^\infty u'^{-1} J_0(\lambda\rho)\, T(\lambda) e^{-uh + u'(z-h)}\lambda\, d\lambda \tag{B6}$$

where

$$T(\lambda) = \frac{2u'}{u + u'}.$$

If we make the same quasi-static approximations ($k \approx k' \approx 0$) in (B6), then the transmitted fields have the inverse distance cubed dependence as shown in (31).

The magnetic dipole moments induced in the oblate spheroid are given in (29). The fields reradiated by these dipole moments can also be written as Sommerfeld integrals, and the same quasi-static approximations can be made. The resultant scattered fields in air are also inverse distance cubed fields, and the field expressions are given in (33).

Appendix C
Magnetic Dipole Approximation

The magnetic dipole approximation for a small loop is particularly convenient because it allows the quasi-static magnetic field to be written in the simple inverse distance cubed form shown in (28). The magnetic field of a circular loop can be written in integral form [15], but in general the integral must be evaluated numerically. However, the field on the loop axis ($x = y = 0$) can be evaluated analytically in the following form [14]:

$$H = \frac{IA}{2\pi(r_1^2 + z^2)^{3/2}} \tag{C1}$$

where r_1 is the loop radius, I is the loop current, and A is the loop area ($= \pi r_1^2$). The magnetic dipole approximation on the z axis is

$$H_{zd} = \frac{IA}{2\pi|z|^3}. \tag{C2}$$

It is clear that (C1) and (C2) are equivalent for $z^2 >> r_1^2$, but that (C2) approaches infinity as z approaches zero.

A comparison of the two results is shown in Fig. 8. The magnetic dipole approximation is poor for $z < 2r_1$, but improves rapidly for $z > 2r_1$. The results are similar for points off the loop axis (x or $y \neq 0$). Consequently the magnetic dipole approximation can be used for observation points located at least two loop radii from the center of the loop.

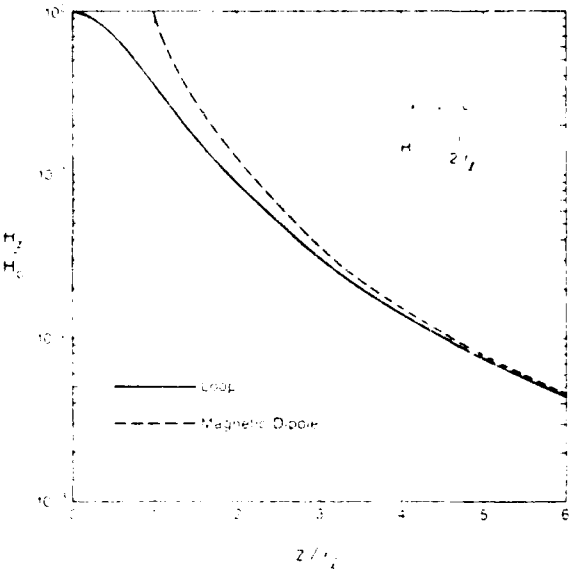

Fig. 8. Axial magnetic field for a circular loop and a magnetic dipole.

Acknowledgment

The authors would like to thank W. K. Klemperer for performing the measurements and R. L. Lewis and R. C. Wittmann for their comments on the manuscript.

References

[1] A. Banos, Jr., *Dipole Radiation in the Presence of a Conducting Half-Space*. New York: Pergamon, 1966.
[2] G. S. Smith, "Directive properties of antennas for transmission into a material half space," *IEEE Trans. Antennas Propagat.*, vol. AP-32, pp. 232-246, 1984.
[3] D. M. Kerns, *Plane Wave Scattering-Matrix Theory of Antennas and Antenna-Antenna Interactions*, National Bureau of Standards Monograph 162. Washington, DC: U.S. Government Printing Office, 1981.
[4] D. G. Large, L. Ball, and A. J. Farstad, "Radio transmission to and from underground coal mines—Theory and experiment," *IEEE Trans. Commun.*, vol. COM-21, pp. 194-202, 1973.
[5] J. R. Wait and D. A. Hill, "Fields of a horizontal loop of arbitrary shape buried in a two-layer earth," *Radio Sci.*, vol. 15, pp. 903-912, 1980.
[6] D. L. Moffatt and R. J. Puskar, "A subsurface electromagnetic pulse radar," *Geophys.*, vol. 41, pp. 506-518, 1976.
[7] J. C. Cook and S. L. Carts, Jr., "Magnetic effects and properties of typical topsoils," *J. Geophys. Res.*, vol. 67, pp. 815-828, 1962.
[8] G. Kristensson, "Electromagnetic scattering from buried inhomogeneities—A general three-dimensional formalism," *J. Appl. Phys.*, vol. 51, pp. 3486-3500, 1980.
[9] H. S. Chang and K. K. Mei, "Scattering of electromagnetic waves by buried and partly buried bodies of revolution," *IEEE Trans. Geosci. Remote Sensing*, vol. GE-23, pp. 596-605, 1985.
[10] X. B. Xu and C. M. Butler, "Current induced by TE excitation on a conducting cylinder located near the planar interface between two semi-infinite half-spaces," *IEEE Trans. Antennas Propagat.*, vol. AP-34, pp. 880-890, 1986.
[11] H. C. van de Hulst, *Light Scattering by Small Particles*. New York: Wiley, 1957.
[12] J. R. Wait, *Geo-Electromagnetism*. New York: Academic, 1982.
[13] R. E. Collin, *Field Theory of Guided Waves*. New York: McGraw-Hill, sec. 12.4, 1960.
[14] J. Lajoie, J. Alfonso-Roche, and G. F. West, "EM response of an arbitrary source on a layered earth: A new computational approach," *Geophys.*, vol. 40, pp. 773-789, 1975.
[15] J. R. Wait, "Mutual coupling of loops lying on the ground," *Geophys.*, vol. 19, pp. 290-296, 1954.

David A. Hill (M'72-SM'76-F'87) was born in Cleveland, OH, on April 21, 1942. He received the B.S.E.E. and M.S.E.E. degrees from Ohio University in 1964 and 1966, respectively, and the Ph.D. degree in electrical engineering from Ohio State University in 1970.

Since 1970, he has been a member of the Boulder scientific community. From 1970 to 1971, he was a Visiting Fellow with the Cooperative Institute for Research in Environmental Sciences where he worked on pulse propagation. From 1971 to 1982, he was with the Institute for Telecommunication Sciences where he worked on theoretical problems in antennas and propagation. Since 1982, he has been in the Electromagnetic Fields Division of the National Bureau of Standards where he has been working on EMC/EMI problems. He is also a Professor Adjoint in the Department of Electrical and Computer Engineering of the University of Colorado.

Dr. Hill is a member of URSI Commissions B, E, and F. He has served as a Technical Editor for the IEEE TRANSACTIONS ON GEOSCIENCE AND REMOTE SENSING and is now an Associate Editor for the IEEE TRANSACTIONS ON ANTENNAS AND PROPAGATION.

Kenneth H. Cavcey (S'82-M'84) was born in Columbia, MO, in 1956. He received the B.S. degree in physics from The University of Missouri—Columbia in 1968 and the M.S. and Ph.D. degree in electrical engineering in 1977 and 1986, respectively.

After teaching on The University of Missouri—Columbia faculty as an Instructor in Electrical Engineering from 1980 to 1984, he joined the Electromagnetic Fields Division of the National Bureau of Standards in Boulder, CO, where he is presently employed.

Dr. Cavcey is a member of the IEEE Antennas and Propagation Society.

Electromagnetic Scattering by Buried Objects of Low Contrast

DAVID A. HILL, FELLOW, IEEE

Abstract- We use the Born approximation to derive the plane-wave scattering matrix for objects of low dielectric contrast. For general shapes a numerical integration over the volume of the scatterer is required, but analytical expressions are derived for a sphere, a circular cylinder, and a rectangular box (parallelepiped). The plane-wave scattering-matrix theory is used to account for the air–earth interface. Numerical results are presented for the scattered near field and far field for plane-wave excitation. The scattered fields are weak for low-contrast objects, but the near-field results have application to electromagnetic detection of buried objects.

I. Introduction

THE ANALYSIS of electromagnetic scattering by buried objects [1]-[4] is complicated by the presence of the air–earth interface. The plane-wave scattering-matrix formulation [5] provides a convenient means for combining the source, scattering, and interface effects and for including interactions. However, it requires knowing the full plane-wave scattering matrix [6] for the buried object for all incident and scattered plane waves. For scatterers of arbitrary shape where numerical methods are generally required to determine the scattering characteristics, this requires a large amount of computation.

In this paper we use the Born approximation (also called the Rayleigh–Gans approximation [7]) to obtain an approximate expression for the scattering matrix of the buried object in terms of an integral over the volume of the object. For simple shapes (such as a sphere, a circular cylinder, or a rectangular box), the volume integral can be evaluated analytically to obtain a closed-form expression for the scattering matrix. The Born approximation requires small contrast between the electrical properties of the buried object and the earth. This requirement is fairly restrictive, but the low-contrast case is important [8] because it represents a difficult detection situation. For example, the detection of plastic mines in dry, sandy soil is difficult because of the low dielectric contrast [9].

The organization of this paper is as follows. In Section II we review the plane-wave scattering-matrix formulation for the geometry of a buried scatterer [5]. In Section III we use the Born approximation to derive the plane-wave scattering matrix for a buried object of low contrast. Specific results are given for a sphere, a circular cylinder, and a rectangular box. In Section IV we present numerical results for the scattered field above the earth when the incident field is a plane wave. Conclusions and recommendations for further work are contained in Section V.

Manscript received March 3, 1987, revised September 11, 1987. This work was supported by the U.S. Army Belvoir Research & Development Center.

The author is with the Electromagnetic Fields Division, National Bureau of Standards, U.S. Department of Commerce, Boulder, CO 80303.

IEEE Log Number 8718450

II. Plane-Wave Scattering-Matrix Formulation

The geometry for a scatterer located in a half space is shown in Fig. 1. The unprimed coordinate system (x, y, z) has its origin at the interface $(z = 0)$, and the primed coordinate system (x', y', z') is centered at the scatterer. The region $z < 0$ has permittivity ϵ and permeability μ, and the region $z > 0$ has permittivity ϵ' and permeability μ'. Both regions are isotropic, but ϵ and ϵ' can be complex to allow for loss. The time dependence is $\exp(-i\omega t)$.

The more general problem, which includes the source antenna, has been formulated in [5]. In this section we extract only those results from [5] that are needed to analyze the scattering problem. Throughout this paper we follow the notation of Kerns [6].

A. Plane-Wave Representations

We define region 1 to be a homogeneous half space, $z < 0$. In this region we can write the electric field $\boldsymbol{E}_1$ as an integral of the plane-wave spectrum

$$\boldsymbol{E}_1(\boldsymbol{r}) = \int_{-\infty}^{\infty}\int \sum_{m=1}^{2} \left[b_1(m, \boldsymbol{K})\, \boldsymbol{E}_m^+(\boldsymbol{K}, \boldsymbol{r}) + a_1(m, \boldsymbol{K})\, \boldsymbol{E}_m^-(\boldsymbol{K}, \boldsymbol{r}) \right] dk_x\, dk_y \qquad (1)$$

where a_1 and b_1 are plane-wave coefficients, and $\boldsymbol{r}$ is the position vector. A similar expression can be written for the magnetic field [5]. The integrations are taken over real values of the wavenumbers k_x and k_y. $\boldsymbol{K}$ is given by $\boldsymbol{K} = k_x \boldsymbol{e}_x + k_y \boldsymbol{e}_y$, where $\boldsymbol{e}_x$, $\boldsymbol{e}_y$, and $\boldsymbol{e}_z$ are unit vectors.

The plane-wave field $\boldsymbol{E}_m^{\pm}$ is transverse magnetic (TM) for $m = 1$ or transverse electric (TE) for $m = 2$. The propagation vector $\boldsymbol{k}^{\pm}$ can be written in the following form:

$$\boldsymbol{k}^{\pm} = \boldsymbol{K} \pm \gamma \boldsymbol{e}_z \qquad (2)$$

where $\gamma = (k^2 - K^2)^{1/2}$, $k^2 = \omega^2 \mu \epsilon$, and $K^2 = \boldsymbol{K} \cdot \boldsymbol{K}$.

The sign of the square root is chosen so that the imaginary part of γ is positive. If the imaginary part of γ is

Electromagnetic Scattering by Buried Objects of Low Contrast

David A. Hill

Reprinted from
IEEE TRANSACTIONS ON GEOSCIENCE AND REMOTE SENSING
Vol. 26, No. 2, March 1988

Electromagnetic Scattering by Buried Objects of Low Contrast

DAVID A. HILL, FELLOW, IEEE

Abstract—We use the Born approximation to derive the plane-wave scattering matrix for objects of low dielectric contrast. For general shapes a numerical integration over the volume of the scatterer is required, but analytical expressions are derived for a sphere, a circular cylinder, and a rectangular box (parallelepiped). The plane-wave scattering-matrix theory is used to account for the air–earth interface. Numerical results are presented for the scattered near field and far field for plane-wave excitation. The scattered fields are weak for low-contrast objects, but the near-field results have application to electromagnetic detection of buried objects.

I. Introduction

THE ANALYSIS of electromagnetic scattering by buried objects [1]–[4] is complicated by the presence of the air–earth interface. The plane-wave scattering-matrix formulation [5] provides a convenient means for combining the source, scattering, and interface effects and for including interactions. However, it requires knowing the full plane-wave scattering matrix [6] for the buried object for all incident and scattered plane waves. For scatterers of arbitrary shape where numerical methods are generally required to determine the scattering characteristics, this requires a large amount of computation.

In this paper we use the Born approximation (also called the Rayleigh–Gans approximation [7]) to obtain an approximate expression for the scattering matrix of the buried object in terms of an integral over the volume of the object. For simple shapes (such as a sphere, a circular cylinder, or a rectangular box), the volume integral can be evaluated analytically to obtain a closed-form expression for the scattering matrix. The Born approximation requires small contrast between the electrical properties of the buried object and the earth. This requirement is fairly restrictive, but the low-contrast case is important [8] because it represents a difficult detection situation. For example, the detection of plastic mines in dry, sandy soil is difficult because of the low dielectric contrast [9].

The organization of this paper is as follows. In Section II we review the plane-wave scattering-matrix formulation for the geometry of a buried scatterer [5]. In Section III we use the Born approximation to derive the plane-wave scattering matrix for a buried object of low contrast. Specific results are given for a sphere, a circular cylinder, and a rectangular box. In Section IV we present numerical results for the scattered field above the earth when the incident field is a plane wave. Conclusions and recommendations for further work are contained in Section V.

Manscript received March 3, 1987, revised September 11, 1987. This work was supported by the U.S. Army Belvoir Research & Development Center.

The author is with the Electromagnetic Fields Division, National Bureau of Standards, U.S. Department of Commerce, Boulder, CO 80303.

IEEE Log Number 8718450.

II. Plane-Wave Scattering-Matrix Formulation

The geometry for a scatterer located in a half space is shown in Fig. 1. The unprimed coordinate system (x, y, z) has its origin at the interface $(z = 0)$, and the primed coordinate system (x', y', z') is centered at the scatterer. The region $z < 0$ has permittivity ϵ and permeability μ, and the region $z > 0$ has permittivity ϵ' and permeability μ'. Both regions are isotropic, but ϵ and ϵ' can be complex to allow for loss. The time dependence is $\exp(-i\omega t)$.

The more general problem, which includes the source antenna, has been formulated in [5]. In this section we extract only those results from [5] that are needed to analyze the scattering problem. Throughout this paper we follow the notation of Kerns [6].

A. Plane-Wave Representations

We define region 1 to be a homogeneous half space, $z < 0$. In this region we can write the electric field $\boldsymbol{E}_1$ as an integral of the plane-wave spectrum

$$\boldsymbol{E}_1(\boldsymbol{r}) = \int_{-\infty}^{\infty}\int \sum_{m=1}^{2} \left[b_1(m, \boldsymbol{K})\, \boldsymbol{E}_m^+(\boldsymbol{K}, \boldsymbol{r}) + a_1(m, \boldsymbol{K})\, \boldsymbol{E}_m^-(\boldsymbol{K}, \boldsymbol{r}) \right] dk_x\, dk_y \qquad (1)$$

where a_1 and b_1 are plane-wave coefficients, and $\boldsymbol{r}$ is the position vector. A similar expression can be written for the magnetic field [5]. The integrations are taken over real values of the wavenumbers k_x and k_y. $\boldsymbol{K}$ is given by $\boldsymbol{K} = k_x \boldsymbol{e}_x + k_y \boldsymbol{e}_y$, where $\boldsymbol{e}_x$, $\boldsymbol{e}_y$, and $\boldsymbol{e}_z$ are unit vectors.

The plane-wave field $\boldsymbol{E}_m^{\pm}$ is transverse magnetic (TM) for $m = 1$ or transverse electric (TE) for $m = 2$. The propagation vector $\boldsymbol{k}^{\pm}$ can be written in the following form:

$$\boldsymbol{k}^{\pm} = \boldsymbol{K} \pm \gamma \boldsymbol{e}_z \qquad (2)$$

where $\gamma = (k^2 - K^2)^{1/2}$, $k^2 = \omega^2 \mu \epsilon$, and $K^2 = \boldsymbol{K} \cdot \boldsymbol{K}$.

The sign of the square root is chosen so that the imaginary part of γ is positive. If the imaginary part of γ is

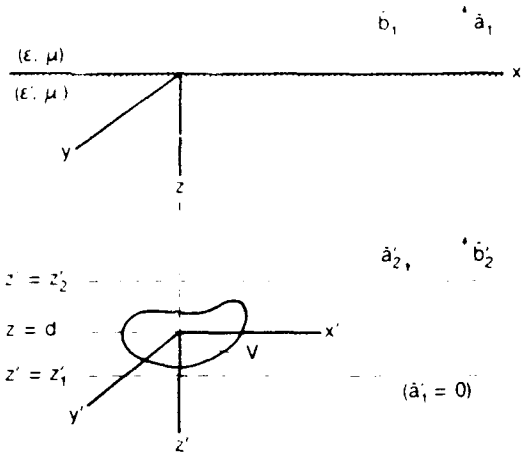

Fig. 1. Geometry for a scatterer located in a half space.

zero, then the sign is chosen so that γ is positive real. We define the following transverse unit vectors:

$$\boldsymbol{\kappa}_1 = \boldsymbol{K}/K \quad \text{and} \quad \boldsymbol{\kappa}_2 = \boldsymbol{e}_z \times \boldsymbol{\kappa}_1 \tag{3}$$

which are respectively in and perpendicular to the plane of $\boldsymbol{k}^{\pm}$ and $\boldsymbol{e}_z$. The TM plane-wave field is given by

$$\boldsymbol{E}_1^{\pm} = (\boldsymbol{\kappa}_1 \mp K\gamma^{-1}\boldsymbol{e}_z)u^{\pm} \tag{4}$$

where $u^{\pm} = \exp(i\boldsymbol{k}^{\pm} \cdot \boldsymbol{r})/(2\pi)$. The superscript $\pm$ refers to propagation in the $\pm z$ direction. The TE plane-wave field is given by

$$\boldsymbol{E}_2^{\pm} = \boldsymbol{\kappa}_2 u^{\pm}. \tag{5}$$

In some cases, only the transverse components of the electrical field are required. From (1)–(5), we can write

$$\boldsymbol{E}_{1t}(\boldsymbol{r}) = \frac{1}{2\pi}\int \sum_m \left[b_1(m, \boldsymbol{K})e^{i\gamma z} + a_1(m, \boldsymbol{K})e^{-i\gamma z}\right]\boldsymbol{\kappa}_m e^{i\boldsymbol{K}\cdot\boldsymbol{R}}\, d\boldsymbol{K} \tag{6}$$

where $\boldsymbol{r} = \boldsymbol{R} + z\boldsymbol{e}_z$ and subscript t denotes the transverse components. When z components are desired, they can be obtained from (1) or from the transverse components and Maxwell's equations. In (6) and throughout the rest of this paper, summation over the values 1 and 2 of the polarization index m and integration over the infinite k_x, k_y plane are understood.

We define region 2 to be a slab region ($-d < z' < z'_2$) between the scatterer and the interface. In this region we can write the transverse electric field in a manner analogous to (6)

$$\boldsymbol{E}'_{2t}(\boldsymbol{r}') = \frac{1}{2\pi}\int \sum_m \left[b'_2(m, \boldsymbol{K})\exp(-i\gamma' z') + a'_2(m, \boldsymbol{K})\exp(i\gamma' z')\right]\boldsymbol{\kappa}_m \cdot \exp(i\boldsymbol{K}\cdot\boldsymbol{R}')\, d\boldsymbol{K} \tag{7}$$

where $\boldsymbol{r}' = \boldsymbol{R}' + z'\boldsymbol{e}_z$, $\gamma' = (k'^2 - K^2)^{1/2}$, and $k'^2 = \omega^2\mu'\epsilon'$. We could write a similar expression for the field in the region, $z' > z'_1$, but this region contains no sources and does not affect the scattering.

B. Scattering Matrix

The plane-wave scattering matrix S'_{22} of the buried object relates the coefficients of the incoming and outgoing plane waves. The outgoing plane wave coefficients b'_2 can be written [6]

$$b'_2(m, \boldsymbol{K}) = \int_L \sum_n S'_{22}(m, \boldsymbol{K}; n, \boldsymbol{L})\, a'_2(n, \boldsymbol{L})\, d\boldsymbol{L} \tag{8}$$

where n and $\boldsymbol{L}$ represent the polarization and transverse wavenumbers of the incoming plane waves. We could write a similar expression for the coefficients b'_1 of the plane waves scattered in the positive z' direction, but we are not concerned with the fields in the region, $z' > z'_1$. For general scatterers, the calculation of S'_{22} is a big job. However, for objects of low contrast the Born approximation simplifies the calculations, as shown in Section III.

For later work it is convenient to rewrite (8) in the following shorthand notation [6]:

$$\hat{b}'_2 = \hat{S}'_{22}\hat{a}'_2. \tag{9}$$

Here $\hat{S}'_{22}$ is a square matrix representing $S'_{22}(m, \boldsymbol{K}; n, \boldsymbol{L})$ according to the values of m, n, $\boldsymbol{K}$, and $\boldsymbol{L}$. Similarly, $\hat{b}'_2$ and $\hat{a}'_2$ are column matrices representing $b'_2(m, \boldsymbol{K})$ and $a'_2(n, \boldsymbol{L})$.

C. Scattered Field in Region 1

For detection of buried objects, we are interested primarily in the scattered fields in region 1 that is normally free space. In (1), b_1 is the coefficient of the incident plane waves, and a_1 is the coefficient of the scattered plane waves. Thus, we need to determine a_1 in terms of b_1. This can be done by matching the fields at the interface ($z = 0$) and using the scattering matrix relationship in (8) or (9). The result in shorthand notation is [5]

$$\hat{a}_1 = \hat{R}'_{11}\hat{b}_1 + \hat{T}'_{12}\hat{S}'_{22}(\hat{1} - \hat{R}'_{22}\hat{S}'_{22})^{-1}\hat{T}'_{21}\hat{b}_1. \tag{10}$$

Here $\hat{1}$ is the identity matrix, $\hat{R}'_{11}$ and $\hat{R}'_{22}$ are diagonal reflection-coefficient matrices, $\hat{T}'_{12}$ and $\hat{T}'_{21}$ are diagonal transmission-coefficient matrices, and the superscript t indicates translation. The expressions for the diagonal elements are [5]

$$R'_{11} = R_{11}, \quad R'_{22} = R_{22}e^{i2\gamma' d}$$
$$T'_{12} = T_{12}e^{i\gamma' d}, \quad T'_{21} = T_{21}e^{i\gamma' d} \tag{11}$$

where

$$R_{11} = \frac{\eta_m - \eta'_m}{\eta_m + \eta'_m}, \quad R_{22} = \frac{\eta'_m - \eta_m}{\eta'_m + \eta_m}$$
$$T_{12} = \frac{2\eta'_m}{\eta_m + \eta'_m}, \quad T_{21} = \frac{2\eta_m}{\eta_m + \eta'_m}. \tag{12}$$

The quantities in (12) are plane-wave reflection and transmission coefficients, and the admittances are given by

$$\eta_1 = \omega\epsilon/\gamma, \quad \eta_2 = \gamma/(\omega\mu)$$
$$\eta'_1 = \omega\epsilon'/\gamma', \quad \eta'_2 = \gamma'/(\omega\mu'). \tag{13}$$

The physical interpretation of (10) is clear. The first term represents specular reflection ($\hat{R}'_{11}$) of the incident field ($\hat{b}_1$) from the planar interface. The second term is caused by the buried object. It involves transmission into the lower medium ($\hat{T}'_{21}$), scattering by the buried object ($\hat{S}'_{22}$), and transmission back into region 1 ($\hat{T}'_{12}$). The inverse factor represents multiple reflections between the buried object and the interface. The multiple reflections can be shown explicitly if we expand the inverse in a geometric series

$$(\hat{1} - \hat{R}'_{22}\hat{S}'_{22})^{-1} = \hat{1} + \hat{R}'_{22}\hat{S}'_{22} + (\hat{R}'_{22}\hat{S}'_{22})^2 + \cdots . \quad (14)$$

If we have weak scattering as in the low-contrast case, then multiple reflections can be neglected, and the first term in (14) is sufficient. In this case, (10) reduces to

$$\hat{a}_1 \approx \hat{R}'_{11}\hat{b}_1 + \hat{T}'_{12}\hat{S}'_{22}\hat{T}'_{21}\hat{b}_1. \quad (15)$$

III. Born Approximation

The geometry for a homogeneous scatterer of permittivity ϵ_s imbedded in a homogeneous medium of permittivity ϵ' is shown in Fig. 2. We assume no magnetic contrast so that both media have magnetic permeability μ'. The refractive index n of the scatterer is

$$n = (\epsilon_s/\epsilon')^{1/2} \quad (16)$$

and n can be complex because both ϵ' and ϵ_s can be complex. The Born approximation is valid under the following conditions [7]:

$$|n - 1| \ll 1 \quad \text{and} \quad s|k'(n-1)| \ll 1 \quad (17)$$

where $k' = \omega(\mu'\epsilon')^{1/2}$ and s is the maximum linear dimension of the scatterer. (The Born approximation is also called the Rayleigh–Gans approximation [7], but we will use Born in this paper to avoid confusion with Rayleigh scattering discussed in Appendix B.) Under the above conditions, the electric field within the scatterer is equal to the incident field $\boldsymbol{E}^i$. The scattered field can be computed as the field radiated by the equivalent current density $\boldsymbol{J}_e$ located within the scatterer volume

$$\boldsymbol{J}_e(\boldsymbol{r}_s) = -i\omega\epsilon'(n^2 - 1)\,\boldsymbol{E}^i(\boldsymbol{r}_s). \quad (18)$$

In this section we will use (18) to derive the scattering matrix for scatterers of low contrast.

A. Scatterers of Arbitrary Shape

Although we require the scattering matrix S'_{22} as defined in (8), we find it easier to derive the dyadic scattering matrix s'_{22} first. The two forms contain the same information, and the derivation of S'_{22} in terms of the dyadic scattering matrix is given in Appendix A. The dyadic scattering matrix relates the vector coefficients of the incoming and outgoing plane waves as follows [6]:

$$\boldsymbol{b}'_2(\boldsymbol{K}) = \int \boldsymbol{s}'_{22}(\boldsymbol{K}, \boldsymbol{L}) \cdot \boldsymbol{a}'_2(\boldsymbol{L})\, d\boldsymbol{L}. \quad (19)$$

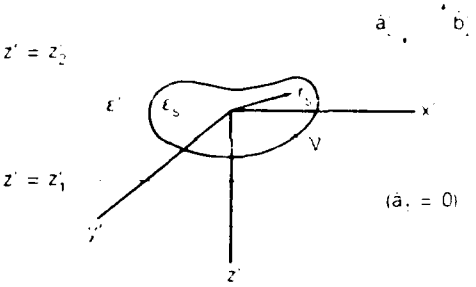

Fig. 2. Geometry for a scatterer of permittivity ϵ_s.

The vector plane-wave coefficients are related to the scalar coefficients by

$$\boldsymbol{b}'_2(\boldsymbol{K}) = b'_2(1, \boldsymbol{K})\,(\boldsymbol{\kappa}_1 + K\gamma'^{-1}\boldsymbol{e}_z) + b'_2(2, \boldsymbol{K})\,\boldsymbol{\kappa}_2 \quad (20)$$

$$\boldsymbol{a}'_2(\boldsymbol{L}) = a'_2(1, \boldsymbol{L})\,(\boldsymbol{\kappa}_{L1} - L\gamma'^{-1}_L\boldsymbol{e}_z) + a'_2(2, \boldsymbol{L})\,\boldsymbol{\kappa}_{L2}. \quad (20)$$

The subscript L on γ' and $\boldsymbol{\kappa}$ refers to an incoming plane wave with transverse wavenumber $\boldsymbol{L}$.

Kerns [6, pp. 124–129] has presented a general formalism for the scattering matrix, and we follow his approach and notation in our application of the Born approximation. We assume that the incident field is a plane wave of the form

$$\boldsymbol{E}^i(\boldsymbol{r}') = \frac{\boldsymbol{a}'_2(\boldsymbol{L})}{2\pi}\exp(i\boldsymbol{l}'^{+}\cdot\boldsymbol{r}'), \quad \text{where } \boldsymbol{l}'^{+} = \boldsymbol{L} + \gamma'_L\boldsymbol{e}_z. \quad (21)$$

Then the integral in (19) reduces to a dot product [6]

$$\boldsymbol{b}'_2(\boldsymbol{K}) = \boldsymbol{s}'_{22}(\boldsymbol{K}, \boldsymbol{L}) \cdot \boldsymbol{a}'_2(\boldsymbol{L}). \quad (22)$$

If we substitute (21) into (18), the equivalent current density of the scatterer is

$$\boldsymbol{J}_e(\boldsymbol{r}_s) = \frac{-i\omega\epsilon'(n^2 - 1)\,\boldsymbol{a}'_2(\boldsymbol{L})}{2\pi}\exp(i\boldsymbol{l}'^{+}\cdot\boldsymbol{r}_s). \quad (23)$$

The task now is to derive an expression for $\boldsymbol{b}'_2$ in terms of $\boldsymbol{J}_e$ so that we can identify the form of $\boldsymbol{s}'_{22}$. Kerns [6, pp. 124–127] has already derived the plane-wave spectrum of the fields radiated by prescribed currents in a volume. If we substitute (23) into his result and perform some algebra, we obtain

$$\boldsymbol{b}'_2(\boldsymbol{K}) = \frac{ik'^2(n^2 - 1)\,I_V}{8\pi^2\gamma'}\,\boldsymbol{\pi}(\boldsymbol{k}'^{-})\cdot\boldsymbol{\pi}(\boldsymbol{l}'^{+})\cdot\boldsymbol{a}_2(\boldsymbol{L}) \quad (24)$$

where

$$I_V = \int_V \exp[i(\boldsymbol{l}'^{+} - \boldsymbol{k}'^{-})\cdot\boldsymbol{r}_s]\, d\boldsymbol{r}_s$$

and V is the volume of the scatterer. The projection operator $\boldsymbol{\pi}$ in (24) is defined as [6]

$$\boldsymbol{\pi}(\boldsymbol{k}) = \boldsymbol{1} - \boldsymbol{kk}/k^2 \quad (25)$$

where $\mathbf{1}$ is the unit dyad. From (22) and (24), we can identify the dyadic scattering matrix

$$s'_{22}(\boldsymbol{K}, \boldsymbol{L}) = \frac{ik'^2(n^2 - 1)I_V}{8\pi^2\gamma'} \pi(\boldsymbol{k}'^-) \cdot \pi(\boldsymbol{l}'^+). \quad (26)$$

The equivalent scalar form S'_{22} is given in Appendix A.

The form of the dyadic scattering matrix for low-contrast scatterers is similar to that for a small dielectric sphere [6], and analytical and numerical comparisons are given in Appendix B. All of the shape dependence is contained in I_V, and I_V is evaluated for some specific shapes in the next section. For very small scatterers, I_V is approximately equal to the volume V, and s'_{22} is proportional to $(n^2 - 1)V$. This simple dependence is consistent with measurements of the scattered field (and detectability) of plastic mines buried in dry sandy soil [9].

B. Scatterers of Simple Shape

In general, I_V as given by (24) must be evaluated numerically. However, for some simple shapes the integration can be performed analytically. In this section we evaluate I_V for a rectangular box (parallelepiped), a circular cylinder, and a sphere. We first rewrite I_V in the following equivalent form:

$$I_V = \int_V \exp(i\boldsymbol{p} \cdot \boldsymbol{r}_s)\, d\boldsymbol{r}_s \quad (27)$$

where

$$\boldsymbol{p} = \boldsymbol{l}'^+ - \boldsymbol{k}'^- = p_x\boldsymbol{e}_x + p_y\boldsymbol{e}_y + p_z\boldsymbol{e}_z.$$

Both p_x and p_y are real, but p_z can be complex because γ'_l and γ' can be complex.

The geometry for a rectangular box of dimensions 2a by 2b by 2c is shown in Fig. 3(a). For this shape, (27) can be rewritten as

$$I_V = \int_{-c}^{c}\int_{-b}^{b}\int_{-a}^{a} \exp\left[i(p_x x' + p_y y' + p_z z')\right] \cdot dx'\, dy'\, dz'. \quad (28)$$

The integrations in (28) are easily performed to yield

$$I_V = V \frac{\sin(p_x a)}{p_x a} \frac{\sin(p_y b)}{p_y b} \frac{\sin(p_z c)}{p_z c}, \quad \text{where } V = 8abc. \quad (29)$$

For an electrically small box, all of the sine arguments are small, and I_V approaches V.

The geometry for a circular cylinder of height $2h$ and radius a_c is shown in Fig. 3(b). For this shape, (27) can be rewritten as

$$I_V = \int_{-h}^{h}\int_0^{2\pi}\int_0^{a_c} \exp\left\{i\left[\rho'(p_x\cos\phi' + p_y\sin\phi') + p_z z'\right]\right\} \rho'\, d\rho'\, d\phi'\, dz'. \quad (30)$$

The z' integration can be performed to yield a sine function, and the ϕ' integration can be performed to yield a zero-order Bessel function [10]

$$I_V = 4\pi h \frac{\sin(p_z h)}{(p_z h)} \int_0^{a_c} J_0(u\rho')\,\rho'\, d\rho', \quad \text{where } u = (p_x^2 + p_y^2)^{1/2}. \quad (31)$$

The ρ' integration can be performed by using recurrence relations [10] to yield a first-order Bessel function

$$I_V = V \frac{J_1(ua_c)}{(ua_c/2)} \frac{\sin(p_z h)}{(p_z h)}, \quad \text{where } V = 2h\pi a_c^2. \quad (32)$$

For an electrically small cylinder, the arguments of the Bessel function and sine are small, and I_V approaches V.

The geometry for a sphere of radius a_s is shown in Fig. 3(c). For this geometry, (27) can be written in spherical coordinates

$$I_V = \int_0^{a_s}\int_0^{2\pi}\int_0^{\pi} \exp\left\{ir'\left[\sin\theta'(p_x\cos\phi' + p_y\sin\phi') + p'_z\cos\theta'\right]\right\} \cdot r'^2\sin\theta'\, d\theta'\, d\phi'\, dr'. \quad (33)$$

Because of the spherical symmetry, we can perform the θ' and ϕ' integrations to yield

$$I_V = 4\pi \int_0^{a_s} \frac{\sin(vr')}{vr'} r'^2\, dr', \quad \text{where } v = (p_x^2 + p_y^2 + p_z^2)^{1/2}. \quad (34)$$

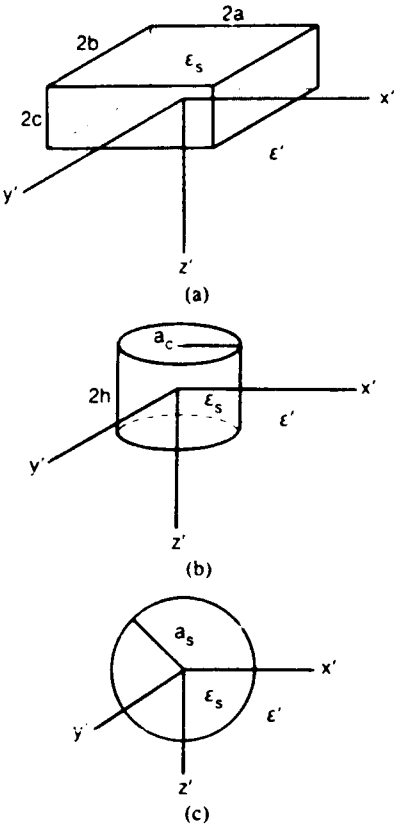

Fig. 3. Geometry for scatterers of special shape centered at the origin: (a) rectangular box (parallelepiped), (b) circular cylinder, (c) sphere.

The r' integration can be evaluated using integration by parts, and the final result for I_V is

$$I_V = V \frac{\sin(va_s) - va_s \cos(va_s)}{(va_s)^3/3},$$

where $V = 4\pi a_s^3/3$. (35)

For an electrically small sphere, the arguments of the sine and cosine functions are small, and I_V approaches V.

The expressions for the cylinder in (32) and the sphere in (35) are in agreement with previous Born approximation results [7], but the notation is different. The validity of the Born approximation has been studied numerically by Kerker *et al.* [11] for dielectric spheres. They compared plane-wave scattering as given by the Born approximation results in (35) with the exact Mie series [7, ch. 9] for wide ranges of values of n and $|k'|a$ and generated plots of the errors of the Born approximation. Their results show a useful range of values where the Born approximation is within 10 percent of the Mie series results. All of our specific cases for spherical scatterers in Section IV fall within this region where the Born approximation error is less than 10 percent. We have no exact solution for rectangular boxes or cylinders of finite length, but we can expect similar ranges of validity because the shape does not appear in the criteria of validity in (17).

Since we have the scattering matrix for three different shapes, it is possible to derive the scattering matrix for a variety of shapes (such as a cylinder on a box) by superposition. For the box and the cylinder, we have assumed that a flat face is parallel to the $x'y'$ plane. It is possible to treat arbitrary orientation by introducing appropriate coordinate rotations.

IV. Numerical Results for Plane-Wave Incidence

The geometry of plane-wave incidence is shown in Fig. 4. The incident plane wave can have either TM (parallel) or TE (perpendicular) polarization. For TM polarization, the incident electric field $\boldsymbol{E}^i$ is

$$\boldsymbol{E}^i = \boldsymbol{e}_{\theta_i} E_0 \exp(i\boldsymbol{k}_i \cdot \boldsymbol{r}) \quad (36)$$

where

$$\boldsymbol{k}_i = \boldsymbol{K}_i + \boldsymbol{e}_z k \cos\theta_i,$$

$$\boldsymbol{K}_i = k \sin\theta_i (\boldsymbol{e}_x \cos\phi_i + \boldsymbol{e}_y \sin\phi_i),$$

θ_i and ϕ_i are incident elevation and azimuth angles, $\boldsymbol{e}_{\theta_i}$ is a unit vector in the θ_i direction, and E_0 is a constant. For the incident TM field in (36), the corresponding b_1 coefficients in (1) are

$$b_1(1, \boldsymbol{K}) = 2\pi E_0 \cos\theta_i \, \delta(\boldsymbol{K} - \boldsymbol{K}_i)$$

$$\text{and } b_1(2, \boldsymbol{K}) = 0. \quad (37)$$

For TE polarization, the incident electric field is

$$\boldsymbol{E}^i = \boldsymbol{e}_{\phi_i} E_0 e^{i\boldsymbol{k}_i \cdot \boldsymbol{r}} \quad (38)$$

where $\boldsymbol{e}_{\phi_i}$ is a unit vector in the ϕ_i direction. For the incident TE field in (38), the corresponding b_1 coefficients

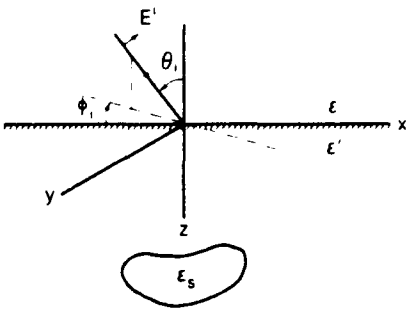

Fig. 4. Geometry for plane-wave incidence.

in (1) are

$$b_1(1, \boldsymbol{K}) = 0$$

$$\text{and } b_1(2, \boldsymbol{K}) = 2\pi E_0 \delta(\boldsymbol{K} - \boldsymbol{K}_i). \quad (39)$$

The second term in (15) represents the field scattered into region 1 from the buried object, and we define it as

$$\hat{a}_1^s = \hat{T}_{12}' \hat{S}_{22}' \hat{T}_{21}' \hat{b}_1. \quad (40)$$

In Section A we present numerical results for the scattered far field, and in Section B we present numerical results for the scattered near field. In both sections we show only the field scattered from the buried object and do not include the specular reflection from the planar interface.

A. Scattered Far Field

The geometry for the scattered far field is shown in Fig. 5. When kr is large, the scattered field can be evaluated asymptotically [6, p. 58]

$$\boldsymbol{E}_1^s \sim ik|\cos\theta| \frac{e^{ikr}}{r} \cdot \left[a_1^s(1, \boldsymbol{K})(-k/\gamma)\boldsymbol{e}_\theta + a_1^s(2, \boldsymbol{K})\boldsymbol{e}_\phi\right]\Big|_{\boldsymbol{K}=k\boldsymbol{R}/r}. \quad (41)$$

For all of the numerical results, we set the permeability equal to the free-space value everywhere. For region 1 we set the permittivity ϵ equal to the free-space value. For region 2 we set the complex relative permittivity $\epsilon'/\epsilon = 3.0 + i\,0.1$, and this value is representative of fairly dry sand [12]. For the buried object we set the complex relative permittivity $\epsilon_s/\epsilon = 2.9 + i\,0.05$. This value is representative of some plastics and explosives and satisfies the low-contrast condition in (17). Since the scattered field strength is proportional to $|n^2 - 1|$, results for other values of ϵ_s can be obtained easily. The azimuthal incidence angle ϕ_i is zero in all cases.

The normalized scattered field strength for $\phi = 0$ as a function of θ is shown in Figs. 6–10 for various cases. The relevant dimensions are normalized to the free-space wavelength λ ($= 2\pi/k$). For a typical frequency of 600 MHz, $\lambda = 50$ cm. In all cases, the buried object has a volume of $0.008\lambda^3$.

The dependence on the burial depth of a cube is shown in Fig. 6 for normal incidence ($\theta_i = 0$). For $d/\lambda = 0.1$,

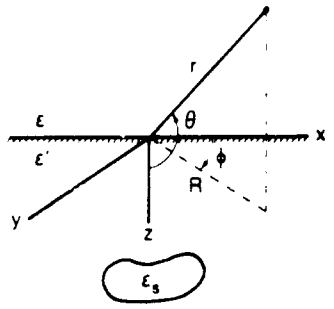

Fig. 5. Geometry for the scattered far-field.

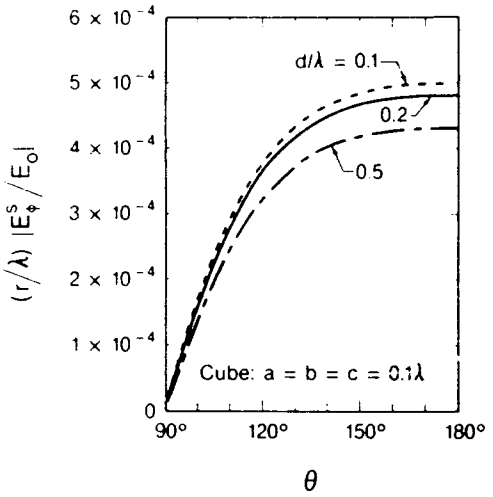

Fig. 6. Scattered far field for a cube located at various depths d. Normal incidence ($\theta_i = 0$).

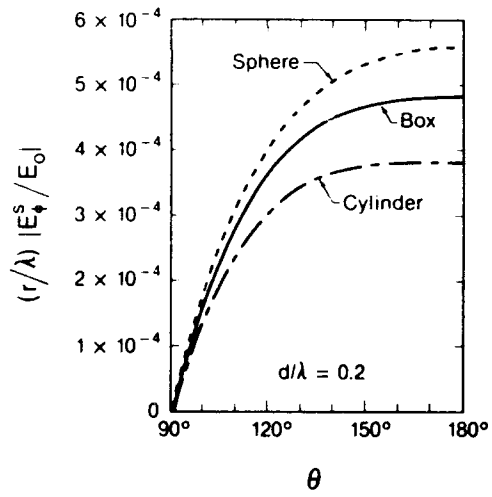

Fig. 7. Scattered far field for a cube ($a = b = c = 0.1\ \lambda$), a circular cylinder ($h = a_c = 0.1084\ \lambda$), and a sphere ($a_s = 0.1241\ \lambda$) for normal incidence. All have equal volumes ($V = 0.008\ \lambda^3$).

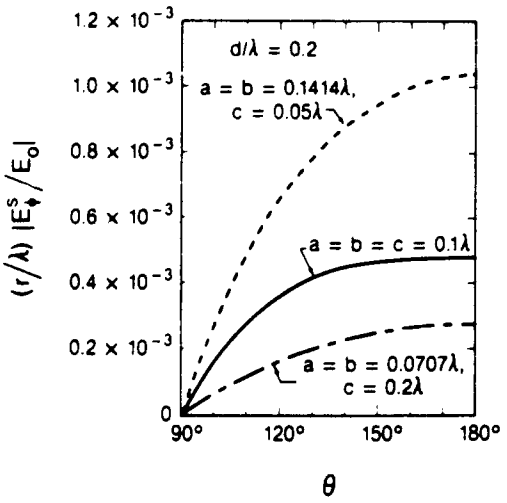

Fig. 8. Scattered far field for equal-volume boxes of various dimensions for normal incidence.

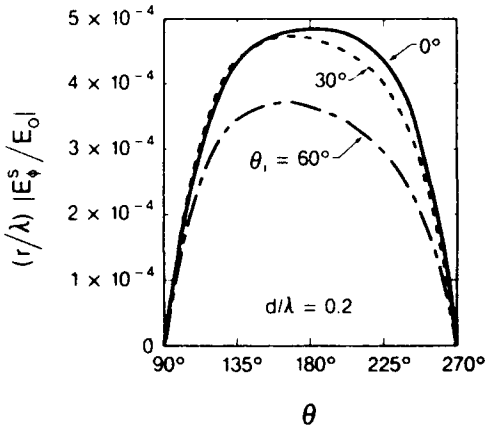

Fig. 9. Scattered far field for a cube for TE incidence at various angles θ_i.

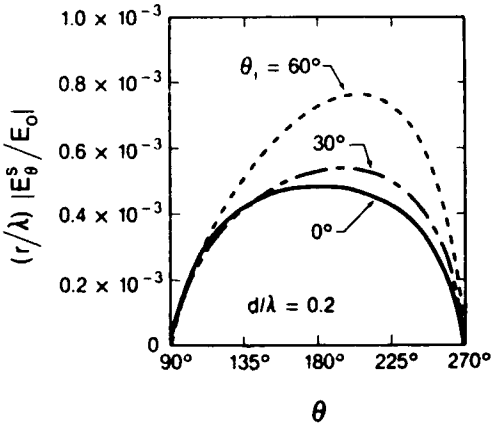

Fig. 10. Scattered far field for a cube for TM incidence at various angles θ_i.

the upper surface of the cube is flush with the interface. Results for a sphere, a cube, and a cylinder are shown in Fig. 7, and there is some shape dependence. Results for a cube, a flattened box, and an elongated box are shown in Fig. 8. The flattened box has the largest scattered field because of the $\sin(p_z c)/(p_z c)$ factor in (29).

The effect of incidence angle is shown in Figs. 9 and 10. For TE polarization in Fig. 9, the curves lose their symmetry for $\theta_i \neq 0$, and the peak is shifted toward the specular direction. However, the general field level decreases because of a decrease in the transmission coefficient (T_{21}) of the incident field. For TM polarization in Fig. 10, the peaks are shifted in the opposite direction, and this is a result of the polarization properties of the scattering matrix as given by (26). In all cases, the scat-

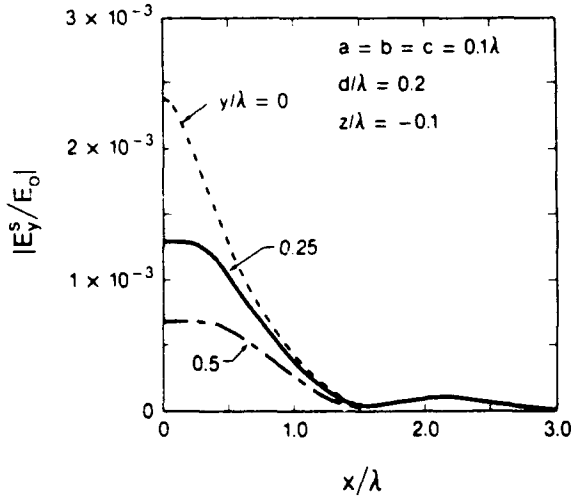

Fig. 11. Scattered near field for a cube for normal incidence

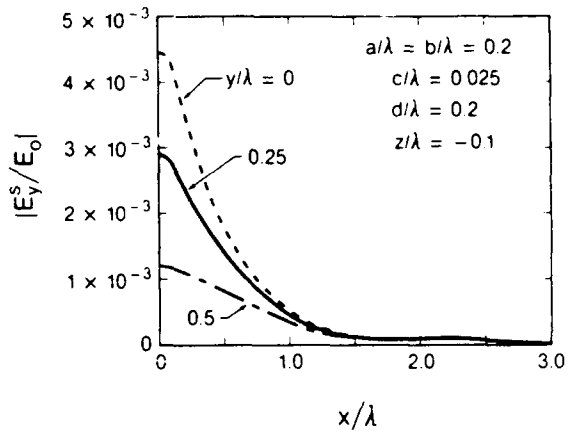

Fig. 12. Scattered near field for a rectangular box for normal incidence.

tered far field is zero at the interface ($\theta = 90°$), and this is consistent with calculations by other methods [4].

B. Scattered Near Field

The scattered near field is of interest in detection where the receiving antenna is located near the interface. From (6) and (40), the transverse components of the scattered near field are

$$\boldsymbol{E}^s_{1t}(r) = \frac{1}{2\pi}\int \sum_m \boldsymbol{\kappa}_m a^s_1(m, \boldsymbol{K}) \exp(-i\gamma z) \cdot \exp\left[i(k_x x + k_y y)\right] dk_x\, dk_y. \quad (42)$$

A similar expression for the z component can be obtained from (1). For a fixed value of z, the double integration over k_x and k_y can be approximated [13] by a two-dimensional fast Fourier transform (2D FFT). Thus, a rectangular grid of field values at discrete values of x and y is computed rapidly by 2D FFT.

In Figs. 11–16, we show the normalized magnitude of E^s_y as a function of x for TE polarization. There are also small x and z components, but the y component is dominant. The y component is the one of interest in detection systems when y-directed dipoles are used for transmitting and receiving.

The near field for several values of y at a height of 0.1 λ above the interface is shown in Fig. 11. The peak value occurs directly above the buried cube for normal incidence ($\theta_i = 0$). The scattered field is small compared to the incident field because of the low dielectric contrast. The scattered field is somewhat larger for the flattened box in Fig. 12.

The depth dependence is illustrated in Fig. 13. The response is decreased and stretched out as the depth is increased. The height dependence is shown in Fig. 14, and this is important for liftoff considerations of real detectors. It is most desirable to locate the receiving antenna as close to the interface as possible.

The effect of the incidence angle is shown in Fig. 15 for a rectangular box scatterer. For $\theta_i \neq 0$, the peak field

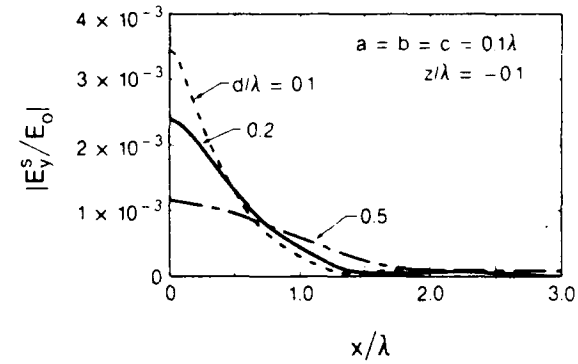

Fig. 13. Scattered near field for a cube located at various depths for normal incidence.

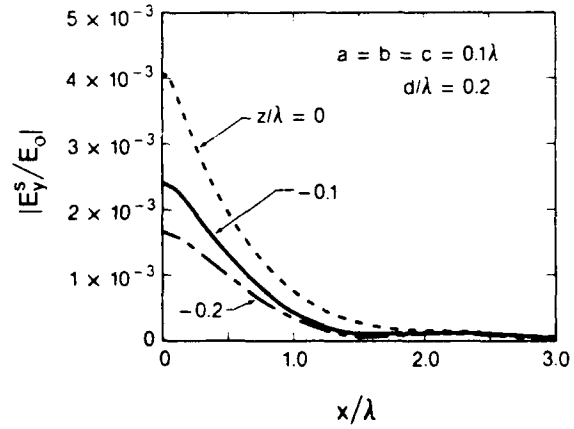

Fig. 14. Scattered near field for a cube at various heights above the interface for normal incidence.

is no longer located directly over the scatterer, but is shifted in the specular direction. This shift in the peak field also occurs for other values of y as shown in Fig. 16.

V. Conclusions

We have used the Born approximation to obtain the scattering matrix for buried objects of low contrast. For general shapes a numerical integration over the volume of the object is required, but for some special shapes (sphere, circular cylinder, and rectangular box) the integration can be done analytically.

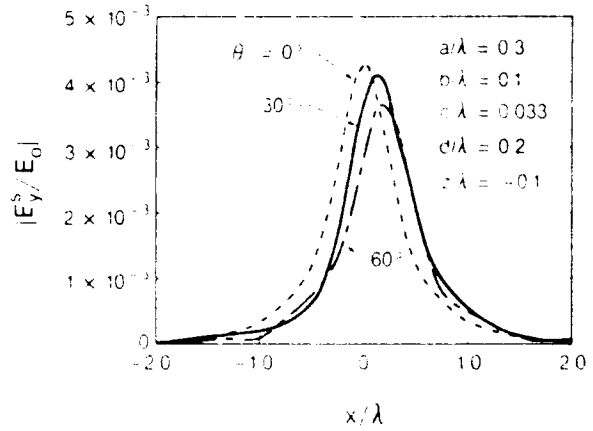

Fig. 15. Scattered near field for a rectangular box for various incidence angles.

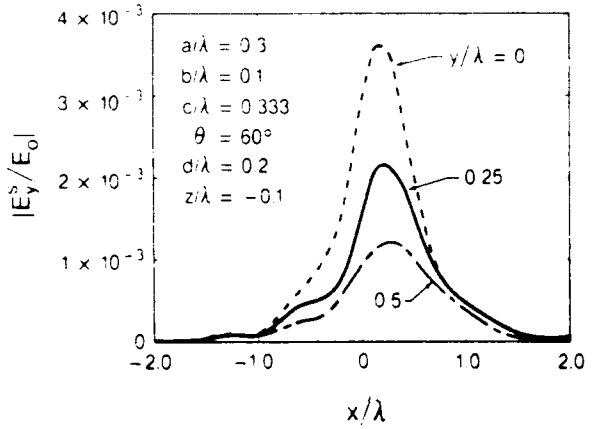

Fig. 16. Scattered near field for a rectangular box for oblique incidence.

We have used the plane-wave scattering-matrix formulation to compute the scattering from buried objects of low contrast. Numerical results have been presented for the scattered far field and near field. Near fields are calculated using 2D FFT, and no Sommerfeld integral evaluations are required. The scattered fields are fairly weak because of the low dielectric contrast, but this is an important case in detection of buried objects.

A number of extensions to this work would be useful. Rather than plane-wave incidence, we could treat the incident field from the transmitting antenna of an actual detector by using the plane-wave scattering matrix theory [5]. The plane-wave characteristics of the receiving antenna could also be included in the calculations. This would allow comparison with UHF detection measurements for dielectric objects buried in sand. Other object shapes could be analyzed by combining the simple shapes studied in this paper. It would also be interesting to carry this approach over to the time domain [14].

Appendix A
Scalar Form of S'_{22}

We first rewrite the dyadic scattering matrix of (26) in the following form:

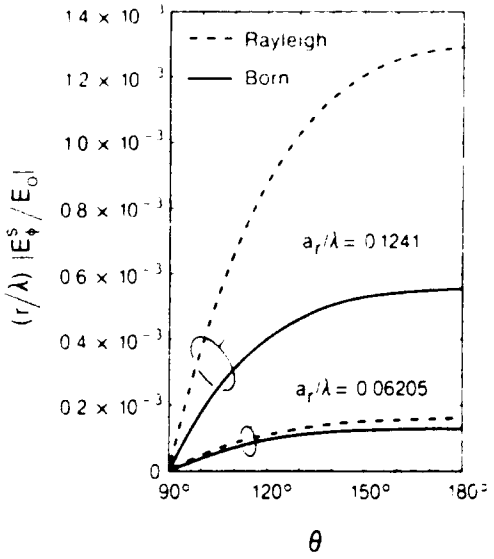

Fig. 17. Comparison of Rayleigh and Born approximations for far field scattered by a sphere at depth $d = 0.2\ \lambda$, for normal incidence.

$$s'_{22}(\boldsymbol{K}, \boldsymbol{L}) = f_{22}\pi(\boldsymbol{k}'^{-}) \cdot \pi(\boldsymbol{l}'^{-}),$$

$$\text{where } f_{22} = \frac{ik'^2(n^2-1)I_V}{8\pi^2\gamma'}. \quad \text{(A1)}$$

The conversion from s'_{22} to S'_{22} is given by Kerns [6], and in general it involves several dot products of vectors and dyads. However, for the special form of s'_{22} in (A1), S'_{22} reduces to

$$S'_{22}(1, \boldsymbol{K}; 1, \boldsymbol{L}) = \frac{k'_z}{l'_z}\, \boldsymbol{e}_{\text{par}}(\boldsymbol{k}'^{-}) \cdot \boldsymbol{e}(\boldsymbol{l}'^{+}) f_{22}$$

$$S'_{22}(1, \boldsymbol{K}, 2, \boldsymbol{L}) = \frac{k'_z}{k'}\, \boldsymbol{e}_{\text{par}}(\boldsymbol{k}'^{-}) \cdot \boldsymbol{\kappa}_2(\boldsymbol{L}) f_{22}$$

$$S'_{22}(2, \boldsymbol{K}; 1, \boldsymbol{L}) = \frac{k'}{l'_z}\, \boldsymbol{\kappa}_2(\boldsymbol{K}) \cdot \boldsymbol{e}_{\text{par}}(\boldsymbol{l}'^{+}) f_{22}$$

$$\text{and } S'_{22}(2, \boldsymbol{K}; 2, \boldsymbol{L}) = \boldsymbol{\kappa}_2(\boldsymbol{K}) \cdot \boldsymbol{\kappa}(\boldsymbol{L}) f_{22}. \quad \text{(A2)}$$

The parallel unit vectors in (A2) are defined as [6]

$$\boldsymbol{e}_{\text{par}}(\boldsymbol{k}'^{-}) = \boldsymbol{\kappa}_2(\boldsymbol{K}) x \frac{\boldsymbol{k}'^{-}}{k'} \quad \text{and} \quad \boldsymbol{e}_{\text{par}}(\boldsymbol{l}'^{+}) = \boldsymbol{\kappa}_2(\boldsymbol{L}) x \frac{\boldsymbol{l}'^{+}}{l'}. \quad \text{(A3)}$$

Appendix B
Comparison with Rayleigh Scattering for a Sphere

In Rayleigh scattering [7, Sec. 6.1], the electrical size of the scatterer is small compared to the wavelength in the surrounding medium ($|k'|a_s << 1$). Under this condition, the dyadic scattering matrix for a dielectric sphere is [6, p. 130]

$$s'_{22}(\boldsymbol{K}, \boldsymbol{L}) = f_{22R}\pi(\boldsymbol{k}'^{-}) \cdot \pi(\boldsymbol{l}'^{+}),$$

$$\text{where } f_{22R} = \frac{3ik'^2(n^2-1)V}{8\pi^2\gamma'(n^2+2)}. \quad \text{(B1)}$$

Comparing (A1) and (B1), we see that the dyadic function is the same, but the scalar functions are slightly different. The ratio of the scalar functions is

$$I_{2,R}/I_{22} = \frac{3I}{(n^2+2)I_1}. \tag{B2}$$

For low contrast $n^2 \approx 1$, and for small $|k'|a_s$, $I_1 \approx V$. Under these conditions, the ratio in (B2) is approximately 1, and the Rayleigh and Born approximations agree.

A numerical comparison for scattering by a buried sphere is shown in Fig. 17. The permittivities and the depth of the sphere are the same as in Fig. 7. For $a_s/\lambda = 0.1241$, $k' a_s \approx 1.35$, and Rayleigh scattering is not valid. For $a_s/\lambda = 0.06205$, $k' a_s \approx 0.675$, and Rayleigh scattering is nearly valid. For this case, the Born and Rayleigh curves in Fig. 17 are in fairly close agreement.

Acknowledgment

The authors would like to thank W. K. Klemperer and R. G. Geyer for useful discussions.

References

[1] M. Kaveh, R. K. Mamin, P. Degauque, and R. Gabillard, "Numerical modeling for electromagnetic remote sensing of inhomogeneities in the ground," *Proc. IEEE*, vol. 67, pp. 1009–1015, 1979.

[2] G. Kristensson, "Electromagnetic scattering from buried inhomogeneities—a general three dimensional formalism," *J. Appl. Phys.*, vol. 51, pp. 3486–3500, 1980.

[3] S. F. Mahmoud, S. M. Ali, and J. R. Wait, "Electromagnetic scattering from a buried cylindrical inhomogeneity inside a lossy earth," *Radio Sci.*, vol. 16, pp. 1285–1298, 1981.

[4] H. S. Chang and K. K. Mei, "Scattering of electromagnetic waves by buried and partly buried bodies of revolution," *IEEE Trans. Geosci. Remote Sensing*, vol. GE-23, pp. 596–605, 1985.

[5] D. A. Hill and K. H. Cavcey, "Coupling between two antennas separated by a planar interface," *IEEE Trans. Geosci. Remote Sensing*, vol. GE-25, pp. 422–431, 1987.

[6] D. M. Kerns, *Plane Wave Scattering Matrix Theory of Antennas and Antenna Antenna Interactions*. Washington, D.C.: NBS Monograph 162, 1981.

[7] H. C. van de Hulst, *Light Scattering by Small Particles*. New York: Wiley, 1957.

[8] W. H. Carter, "Inverse scattering in the first Born approximation," *Optical Engineering*, vol. 23, pp. 204–209, 1984.

[9] R. C. Weaver, U.S. Army Belvoir Research, Development & Engineering Center, Fort Belvoir, VA, private communication.

[10] M. Abramowitz and I. A. Stegun, *Handbook of Mathematical Functions*, (Applied Mathematics Series 55). Washington, DC: NBS, 1964.

[11] M. Kerker, W. A. Farone, and E. Matijevic, "Applicability of Rayleigh-Gans scattering to spherical particles," *J. Opt. Soc. Amer.*, vol. 53, pp. 758–759, 1963.

[12] A. R. Von Hippel, *Dielectric Materials and Applications*. New York: Technology Press of M.I.T., 1954.

[13] A. Q. Howard, Jr., "On approximating Fourier integral transforms by their discrete counterparts in certain geophysical applications," *IEEE Trans. Antennas Propagat.*, vol. AP-23, pp. 264–266, 1975.

[14] D. Quak and A. T. de Hoop, "Time domain Born approximation to the far-field scattering of plane electromagnetic waves by a penetrable object," *Radio Sci.*, vol. 21, pp. 815–821, 1986.

David A. Hill (M'72–SM'76–F'87) was born in Cleveland, OH, on April 21, 1942. He received the B.S.E.E. and M.S.E.E. degrees from Ohio University in 1964 and 1966, respectively, and the Ph.D. degree in electrical engineering from Ohio State University in 1970.

Since 1970 he has been a member of the Boulder scientific community. From 1970 to 1971 he was a Visiting Fellow with the Cooperative Institute for Research in Environmental Sciences where he worked on pulse propagation. From 1971 to 1982 he was with the Institute for Telecommunication Sciences where he worked on theoretical problems in antennas and propagation. Since 1982 he has been in the Electromagnetic Fields Division of the National Bureau of Standards where he has been working on EMC/EMI problems. He is also a Professor Adjoint in the Department of Electrical and Computer Engineering of the University of Colorado.

Dr. Hill is a member of URSI Commissions B, E, and F. He has served as a Technical Editor for the IEEE TRANSACTIONS ON GEOSCIENCE AND REMOTE SENSING and is now an Associate Editor for the IEEE TRANSACTIONS ON ANTENNAS AND PROPAGATION.

Fields of Horizontal Currents Located Above the Earth

David A. Hill

APPENDIX
III C

Reprinted from
IEEE TRANSACTIONS ON GEOSCIENCE AND REMOTE SENSING
Vol. 26, No. 6, November 1988

Fields of Horizontal Currents Located Above the Earth

DAVID A. HILL, FELLOW, IEEE

Abstract—The plane-wave spectrum technique is used to derive the fields of horizontal currents located in a horizontal plane above the earth. The far field is derived asymptotically, and the near field is computed by two-dimensional fast Fourier transform. Specific numerical results are presented for a pair of oppositely directed dipoles, and the results have application to detection of buried objects. When the antenna is located at low heights, the field is enhanced in the earth and decreased in air.

I. Introduction

RADIATION from antennas near the earth has been studied by many investigators, and Banos [1] has summarized many of the results for Hertzian electric and magnetic dipole sources. More recently Smith [2] has used the plane-wave spectrum technique to study transmission into a lossy half space. Hill and Cavcey [3] have used the related plane-wave, scattering-matrix technique [4] to include interactions between antennas separated by a planar interface and between an antenna and an interface.

In this paper we specialize the scattering-matrix technique [3] to the case of an antenna with horizontal currents located in a horizontal plane over a horizontal, air–earth interface. This case includes many of the antenna types, such as horizontal loops [5] and dipoles [6], which are used in detection of buried objects.

The organization of this paper is as follows. In Section II we derive the plane-wave spectrum of the primary fields of horizontal currents in free space. In Section III we obtain the transmitted and reflected fields from the previous results in [3]. In Section IV we obtain the plane-wave spectrum of the fields of oppositely directed dipoles of finite length. This type of antenna has a null in a vertical plane to reduce strong ground reflections and has been used for detection of buried objects. Section V contains numerical results for the far field and the near field of oppositely directed dipoles. The near fields in the earth are of particular interest in detection of buried objects. Section VI contains conclusions and recommendations for further study, and the Appendix contains an analytical expression for the ratio of the field strength in the earth to the field strength in air.

Manuscript received October 19, 1987; revised May 12, 1988. This work was supported by the U.S. Army Belvoir Research and Development Center.

The author is with the Electromagnetic Fields Division, National Bureau of Standards, Boulder, CO 80303.

IEEE Log Number 8823376.

II. Primary Fields

The geometry for horizontal currents located in a plane ($z = 0$) above a half space is shown in Fig. 1. We assume that the electric surface current density $\boldsymbol{J}_s(\boldsymbol{R}_s)$ is known, and the time dependence is exp $(-i\omega t)$. The interface is located at $z = h$, and a primed coordinate system ($x' = x$, $y' = y$, $z' = z - h$) has its origin at the interface. The complex permittivity ϵ and permeability μ of the region, $z < h$, are arbitrary, but will later be set equal to their free-space values. The formulation and notation will follow [3] and [4] fairly closely.

In the region $z < h$ the primary electric field $\boldsymbol{E}_q^p$ can be written as a spectrum of plane waves [4]

$$\boldsymbol{E}_q^p(r) = \int_{-\infty}^{\infty}\int \sum_{m=1}^{2} b_q(m, \boldsymbol{K})\, \boldsymbol{E}_m^{\pm}(\boldsymbol{K}, r)\, dk_x\, dk_y \quad (1)$$

where r is the position vector, and the subscript q takes the value 1 for $z > 0$ and 2 for $z < 0$. For $q = 1$, we take the positive superscript of $\boldsymbol{E}_m$, and for $q = 2$, the negative superscript. The integrations are taken over real values of the wavenumbers k_x and k_y, and $\boldsymbol{K}$ is given by $\boldsymbol{K} = k_x \boldsymbol{e}_x + k_y \boldsymbol{e}_y$, where $\boldsymbol{e}_x$, $\boldsymbol{e}_y$, and $\boldsymbol{e}_z$ are unit vectors. An expression similar to (1) can be written for the magnetic field, but in this paper we are interested primarily in the electric field.

The plane-wave field $\boldsymbol{E}_m^{\pm}$ is a transverse to the propagation vector. $\boldsymbol{E}_m^{\pm}$ is transverse magnetic (TM) for $m = 1$ or transverse electric (TE) for $m = 2$. The propagation vector $k^{\pm}$ can be written

$$\boldsymbol{k}^{\pm} = \boldsymbol{K} \pm \gamma \boldsymbol{e}_z \quad (2)$$

where $\gamma = (k^2 - K^2)^{1/2}$, $k^2 = \omega^2 \mu\epsilon$, and $K^2 = \boldsymbol{K} \cdot \boldsymbol{K}$.

The sign of γ is chosen so that the imaginary part of γ is positive. If the imaginary part of γ is zero, then the sign is chosen so that γ is positive real. We define the following transverse (to z) unit vectors

$$\boldsymbol{\kappa}_1 = \boldsymbol{K}/K \quad \text{and} \quad \boldsymbol{\kappa}_2 = \boldsymbol{e}_z \times \boldsymbol{\kappa}_1 \quad (3)$$

which are respectively in and perpendicular to the plane $\boldsymbol{k}^{\pm}$ and $\boldsymbol{e}_z$. The TM plane-wave field is given by

$$\boldsymbol{E}_1^{\pm}(\boldsymbol{K}, r) = (\boldsymbol{\kappa}_1 \mp K\gamma^{-1}\boldsymbol{e}_z) u^{\pm} \quad (4)$$

where $u^{\pm} = \exp(i\boldsymbol{\kappa}^{\pm} \cdot r)/(2\pi)$.

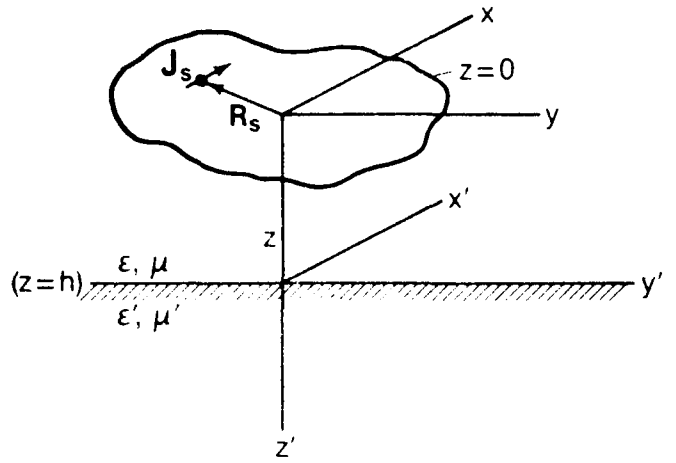

Fig. 1. Geometry for horizontal surface currents in the plane $z = 0$ at a height h above the interface.

The TE plane-wave field is given by

$$\boldsymbol{E}_2^{\pm}(\boldsymbol{K}, \boldsymbol{r}) = \boldsymbol{\kappa}_2 u^{\pm}. \tag{5}$$

The scalar coefficient $b_q(m, \boldsymbol{K})$ in (1) can be written in terms of a vector coefficient

$$b_q(m, \boldsymbol{K}) = \boldsymbol{\kappa}_m \cdot \boldsymbol{b}_q(\boldsymbol{K}). \tag{6}$$

Kerns [4, pp. 124–127] has derived the vector coefficient in terms of an integral over the source current. For the geometry in Fig. 1, we can write his result in the form

$$\boldsymbol{b}_q(\boldsymbol{K}) = -(k^2/\gamma)\, \boldsymbol{\pi}(k^{\pm}) \cdot \boldsymbol{U}(\boldsymbol{K}) \tag{7}$$

where $\boldsymbol{U}(\boldsymbol{K}) = 1/4\pi\omega\epsilon \int \boldsymbol{J}_s(\boldsymbol{R}_s)\, e^{-i\boldsymbol{K}\cdot\boldsymbol{R}_s}\, d\boldsymbol{R}_s$.
The projection operator $\boldsymbol{\pi}$ in (7) is defined as [4]

$$\boldsymbol{\pi}(k^{\pm}) = \mathbf{1} - \boldsymbol{k}^{\pm}\boldsymbol{k}^{\pm}/k^2 \tag{8}$$

where 1 is the unit dyad.

III. Reflected and Transmitted Fields

In the region, $z < h$, the reflected electric field $\boldsymbol{E}_1^r$ can be written in a form similar to (1)

$$\boldsymbol{E}_1^r(r) = \int_{-\infty}^{\infty}\int \sum_{m=1}^{2} a_1(m, \boldsymbol{K})\, \boldsymbol{E}_m^-(\boldsymbol{K}, \boldsymbol{r})\, dk_x\, dk_y. \tag{9}$$

The coefficient a_1 has been derived in [3]

$$a_1(m, \boldsymbol{K}) = R_{11}^t b_1(m, \boldsymbol{K}). \tag{10}$$

The superscript t indicates that R_{11}^t is a translated reflection coefficient

$$R_{11}^t = R_{11} e^{i2\gamma h} \tag{11}$$

where

$$R_{11} = \frac{\eta_m - \eta_m'}{\eta_m + \eta_m'},\ \eta_1 = \omega\epsilon/\gamma,\ \eta_2 = \gamma/(\omega\mu),$$

$$\eta_1' = \omega\epsilon'/\gamma',\ \eta_2' = \gamma'/(\omega\epsilon'),$$

$$\gamma' = (k'^2 - K^2)^{1/2},\ \text{and}\ k'^2 = \omega^2\mu'\epsilon'.$$

The total field $\boldsymbol{E}(\boldsymbol{r})$ in the region, $z < h$, is the sum of the primary and reflected fields: $\boldsymbol{E}(\boldsymbol{r}) = \boldsymbol{E}_q^p(\boldsymbol{r}) + \boldsymbol{E}_1^r(\boldsymbol{r})$.

In the lower medium, $z' > 0$ or $z > h$, the transmitted electric field $\boldsymbol{E}_2^t$ can be written in a form similar to (1)

$$\boldsymbol{E}_2^t(\boldsymbol{r}') = \int_{-\infty}^{\infty}\int \sum_{m=1}^{2} a_2^t(m, \boldsymbol{K})\, \boldsymbol{E}_m'^{+}(\boldsymbol{K}, \boldsymbol{r}')\, dk_x\, dk_y. \tag{12}$$

The plane-wave field $\boldsymbol{E}_m'^{+}$ is given by

$$\boldsymbol{E}_1'^{+}(\boldsymbol{K}, \boldsymbol{r}') = (\boldsymbol{\kappa}_1 - K\gamma'^{-1}\boldsymbol{e}_z)u'^{+} \quad \text{and}$$

$$\boldsymbol{E}_2'^{+}(\boldsymbol{K}, \boldsymbol{r}') = \boldsymbol{\kappa}_2 u_2'^{+} \tag{13}$$

where

$$u'^{+} = \exp(i\boldsymbol{k}'^{+} \cdot \boldsymbol{r}')/(2\pi) \quad \text{and} \quad \boldsymbol{k}'^{+} = \boldsymbol{K} + \gamma'\boldsymbol{e}_z.$$

The coefficient a_2^t has been derived in [3]

$$a_2^t(m, \boldsymbol{K}) = T_{21}^t b_1(m, \boldsymbol{K}). \tag{14}$$

The superscript t again indicates translation

$$T_{21}^t = T_{21} e^{i\gamma h} \tag{15}$$

where

$$T_{21} = \frac{2\eta_m}{\eta_m' + \eta_m}.$$

IV. Oppositely Directed Dipoles

A transmitting antenna of particular interest in detection of buried objects at shallow depths is shown in Fig. 2. The antenna consists of two x-directed dipoles of length L fed in opposition and separated by a distance s. This type of antenna has a null in the xz plane even when it is located over a homogeneous half space or a horizontally stratified half space. We do not consider the receiving antenna in this paper, but it is normally an x-directed dipole located at the origin. Thus it will respond to inhomogeneities that are asymmetrical with respect to the xz plane, but not to a homogeneous or horizontally stratified earth. In this paper our interest is in the near fields to see how buried objects will be illuminated.

We assume sinusoidal current distributions on the oppositely directed dipoles that can be represented by the following surface current distribution:

$$\boldsymbol{J}_s(\boldsymbol{R}_s) = \boldsymbol{e}_x \frac{I_0 \sin\left[k\left(\frac{L}{2} - |x_s|\right)\right]}{\sin(kL/2)} \cdot [\delta(y_s - s/2) - \delta(y_s + s/2)] \tag{16}$$

where I_0 is the feed current of each dipole and δ is the Dirac delta function. It would be possible to solve for the current distribution on a pair of wire antennas over the ground by the method of moments [7], but the classical sinusoidal current approximation [8] is adequate for our field calculations as indicated in Section V.

If we substitute (16) into (7) and carry out the $\boldsymbol{R}_s$ inte-

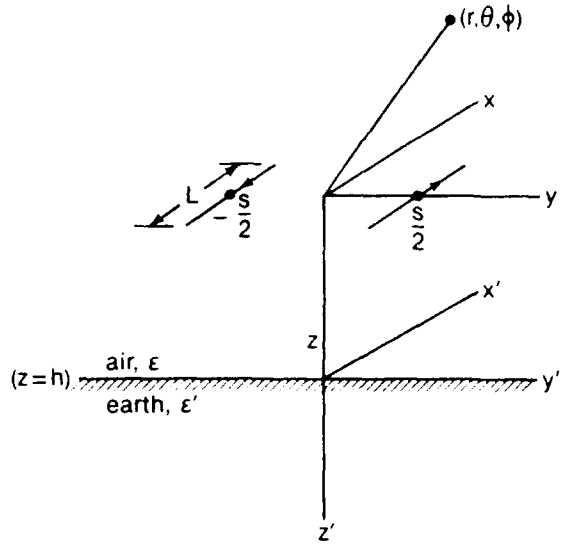

Fig. 2. Geometry for oppositely directed dipoles at a height h above the earth.

gration, we obtain the following result for $\boldsymbol{U}(\boldsymbol{K})$:

$$\boldsymbol{U}(\boldsymbol{K}) = \frac{\boldsymbol{e}_x I_0}{\pi i\omega\epsilon \sin(kL/2)} \sin(k_y s/2) \cdot \frac{k[\cos(k_x L/2) - \cos(kL/2)]}{k^2 - k_x^2}. \quad (17)$$

As given by (17), $\boldsymbol{U}(\boldsymbol{K})$ is indeterminate at $k_x = \pm k$. This special case can be evaluated directly from (7) and (16) to yield

$$\boldsymbol{U}(\boldsymbol{K})\big|_{k_x = \pm k} = \frac{\boldsymbol{e}_x I_0 L}{4\pi i\omega\epsilon} \sin(k_y s/2). \quad (18)$$

Thus $\boldsymbol{U}(\boldsymbol{K})$ for the current distribution in (16) is even in k_x, odd in k_y, and well behaved for all $\boldsymbol{K}$.

V. Numerical Results

In this section we obtain far-field and near-field results for the oppositely directed dipoles located in air over a lossy earth. We assume that the magnetic permeability of both the air and earth is that of free space, $\mu = \mu' = \mu_0$, and that the permittivity of air is that of free space, $\epsilon = \epsilon_0$. The dipole length L and separation s are: $L = s = 0.2735\ \lambda$, where λ is the free-space wavelength ($= 2\pi/k$). This corresponds to a physical length and separation of 21.59 cm at a frequency of 380 MHz.

A. Far Field

We first consider the electric field in air ($z < h$). When kr is large, $\boldsymbol{E}(r)$ can be evaluated asymptotically [4, p. 58]

$$\boldsymbol{E}(r) \sim ik|\cos\theta| \frac{e^{ikr}}{r} \left\{ [b_2(1, \boldsymbol{K}) + a_1(1, \boldsymbol{K})] \frac{\boldsymbol{e}_\theta}{\cos\theta} + b_2(2, \boldsymbol{K})\boldsymbol{e}_\phi \right\}\Big|_{\boldsymbol{K} = k\boldsymbol{R}/r} \quad (19)$$

where $\boldsymbol{e}_\theta$ and $\boldsymbol{e}_\phi$ are unit vectors in standard spherical coordinates (r, θ, ϕ).

The far field in the earth can also be evaluated asymptotically. When $|k'|r'$ is large, the transmitted field is [4, p. 58]

$$\boldsymbol{E}_2'(\boldsymbol{r}') \sim i\gamma' \frac{e^{ik'r'}}{r'} \left\{ a_2'(1, \boldsymbol{K})(k'/\gamma')\boldsymbol{e}_\theta + a_2'(2, \boldsymbol{K})\boldsymbol{e}_\phi \right\}\Big|_{\boldsymbol{K} = k'\boldsymbol{R}/r'} \quad (20)$$

where $\boldsymbol{e}_\theta$ and $\boldsymbol{e}_\phi$ are unit vectors in the primed spherical coordinate system (r', θ', ϕ'). When k' is complex, the far field in the earth has exponential decay in addition to spherical spreading, and Smith [2] has factored out this exponential decay in his definition of the far-field pattern.

To verify that the assumed current distribution in (16) is an adequate model for a detector with oppositely directed dipoles, we first compared theoretical and measured far-field patterns for free space conditions ($\epsilon' = \epsilon$). The measurements were performed in an anechoic chamber in the far field of the oppositely directed dipoles. A dipole probe was used to measure the electric field strength. Fig. 3 shows the H-plane ($\phi = 90°$) pattern, and the agreement is very good for the dominant horizontal component. The theory predicts no vertical component of electric field, but the measurement shows a vertical component about 20 dB below the horizontal component.

Fig. 4 shows the E-plane pattern ($\theta = 90°$), and the agreement is not as good. Again there is a measured vertical component of electric field about 20 dB down that is not predicted by the theory. Part of the problem is that the detector dipoles have some end loading, and there is a circuit board in the plane of the dipoles. We tried assuming a constant current to take account of the end loading, but the sinusoidal current in (16) provided better agreement in the far-field pattern. The poorer agreement in the E-plane pattern is not a serious problem for our application because most of the interest is in the H-plane pattern (far field and near field).

In Fig. 5 we show the H-plane pattern for three antenna heights over a lossless earth ($\epsilon'/\epsilon = 4.0$). (We use θ to represent either θ or θ' because in the far field they are equal. Because the z-axis is pointed down, θ values greater than 90° represent the pattern in air and θ values less than 90° represent the pattern in the earth.) The electric field has only an x-component in the H-plane, and we multiply E_x by the normalization factor $r/(I_0\eta)$ to make it dimensionless. The sharp cusps at the critical angle, $\theta = \sin^{-1}[(\epsilon/\epsilon')^{1/2}] = 30°$, have also been observed in the numerical results of Smith [2]. If we wish to maximize the field in the earth and minimize the field in air, then it is best to make h as small as possible. This has been done for a crossed-dipole system [6]. The reason for minimizing the field in air is to reduce reflections from above-ground objects.

In Fig. 6 we show the H-plane pattern for three real values of ϵ'/ϵ. The free-space case ($\epsilon'/\epsilon = 1$) shows equal fields in air and earth, but an increase in ϵ'/ϵ in-

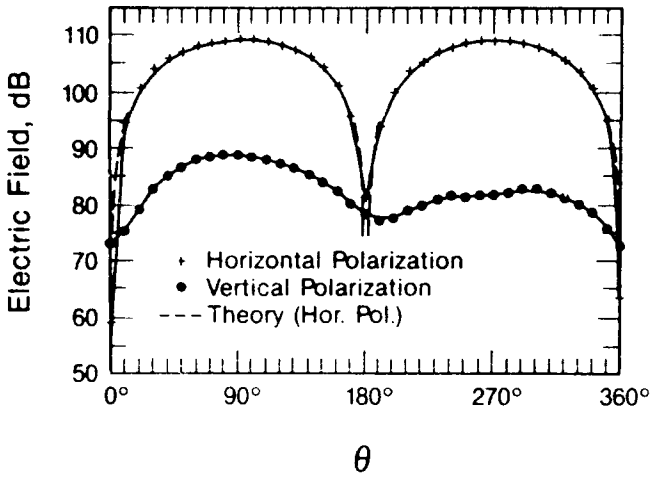

Fig. 3. Comparison of measured and theoretical H-plane patterns for oppositely directed dipoles in free space.

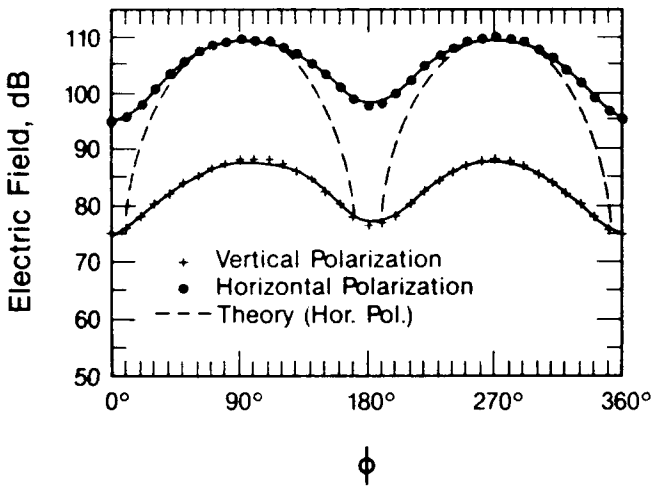

Fig. 4. Comparison of measured and theoretical E-plane patterns for oppositely directed dipoles in free space.

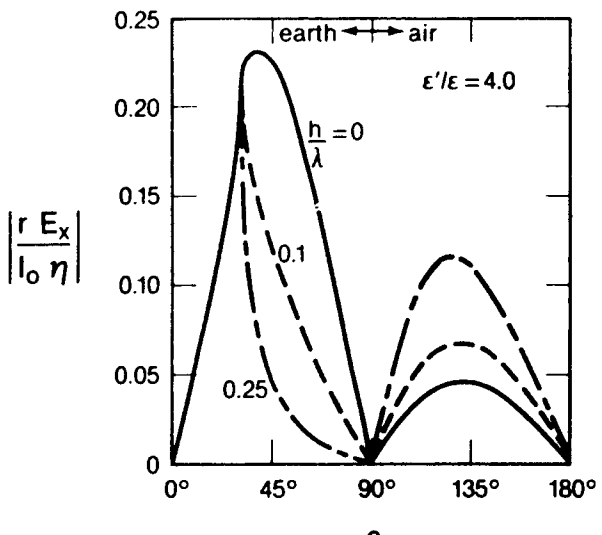

Fig. 5. H-plane pattern of oppositely directed dipoles at various heights above the earth.

creases the fields in the earth and decreases the fields in air. The case, $\epsilon'/\epsilon = 4.0$, is representative of dry soil, and the case, $\epsilon'/\epsilon = 80.0$, is representative of water. For

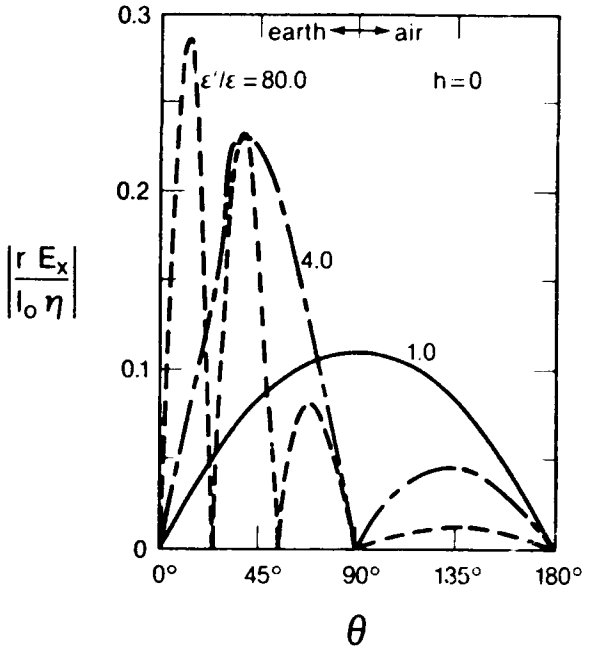

Fig. 6. H-plane pattern of oppositely directed dipoles located at the air-earth interface for various earth permittivities.

$\epsilon'/\epsilon \neq 1$, there is a null along the interface ($\theta = 90°$) because the reflected and primary fields cancel. The multiple lobes in the earth for $\epsilon'/\epsilon = 80.0$ are a result of the $\sin(k_y s/2)$ factor in (17). For antennas that do not have a null in the vertical directions ($\theta = 0°, 180°$), the Appendix contains a simple result for the ratio of the far field in earth and in air.

B. Near Field

The near fields are actually of more interest than the far fields in the detection of buried objects at shallow depths (typically less than a skin depth in the earth). From Sections II and III, we see that all field components require evaluation of two-dimensional integrals of the form

$$\int_{-\infty}^{\infty}\int F(\boldsymbol{K})\, e^{i(k_x x + k_y y)}\, dk_x\, dk_y,$$

where $F(\boldsymbol{K})$ depends on the particular component and region. The double integration over k_x and k_y can be approximated [9], [10] by a two-dimensional fast Fourier transform (2D FFT).

The x-component of the electric field E_x is dominant both in the earth and in the air, and in this section we give numerous results for the normalized, dimensionless x-component, $E_{xn} = \lambda E_x/(I_0\eta)$. All plots show only the magnitude of E_{xn} because the phase is of less interest. In all cases E_{xn} has a null at $y = 0$, and only positive values of y are shown because $|E_{xn}|$ is even in y.

Figs. 7–10 show $|E_{xn}|$ for an antenna height h of 0.1 λ over a low-loss earth ($\epsilon'/\epsilon = 4.0 + i0.1$). Figs. 7 and 8 show the effect of the offset distance x from the antenna centerline ($x = 0$) on the fields in earth and air. The field in the earth is about twice that in air, and the x and y

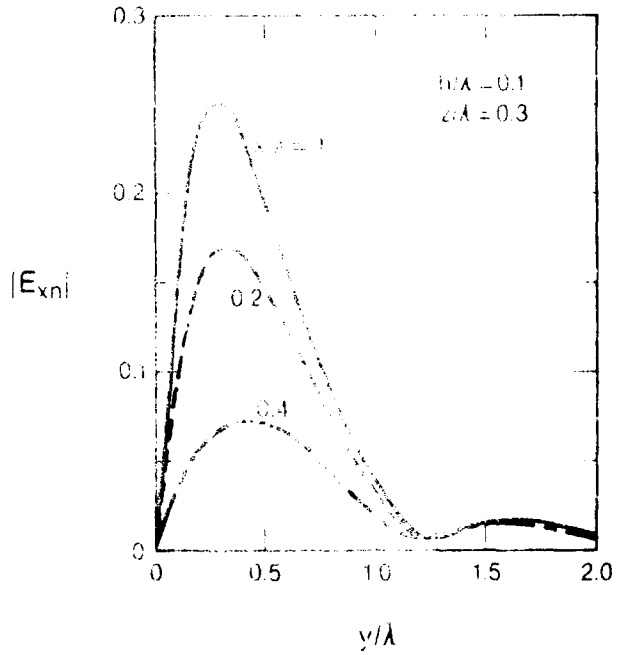

Fig. 7. Normalized electric field in the earth at various x locations. Complex earth permittivity: $\epsilon'/\epsilon = 4.0 + i0.1$.

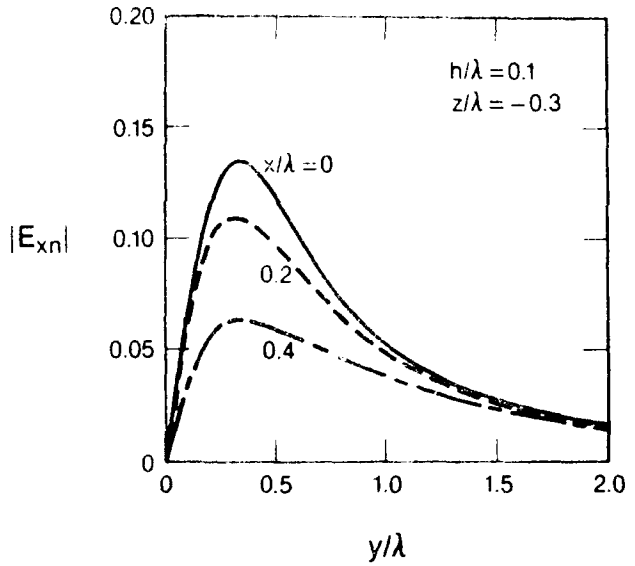

Fig. 8. Normalized electric field in air at various x locations. Complex earth permittivity: $\epsilon'/\epsilon = 4.0 + i0.1$.

variations are about the same. Figs. 9 and 10 show the field decay with depth in the earth and with height in the air. The curve for $z/\lambda = -0.1$ in Fig. 10 has a sharp peak for the point near the antenna ($y \approx s/2$).

Figs. 11 and 12 show the effect of antenna height on the field at a fixed depth, $z - h$, in the earth and a fixed height, $h - z$, in air. As with the far-field patterns, a decrease in antenna height causes a desirable increase in the fields in the earth and decrease in the fields in air.

Fig. 13 shows the effect of increasing loss in the earth. Fig. 14 shows the effect of increasing the dielectric constant of the earth. An increase in the dielectric constant shifts the peak toward the origin because the field is refracted toward the vertical direction.

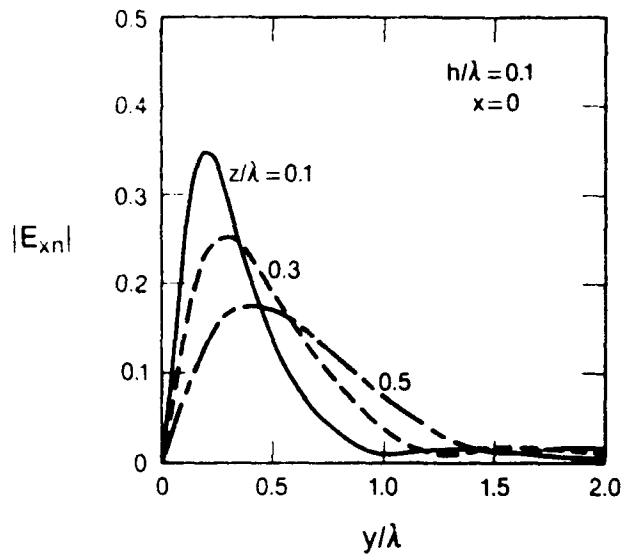

Fig. 9. Normalized electric field at various depths in the earth. Complex earth permittivity: $\epsilon'/\epsilon = 4.0 + i0.1$.

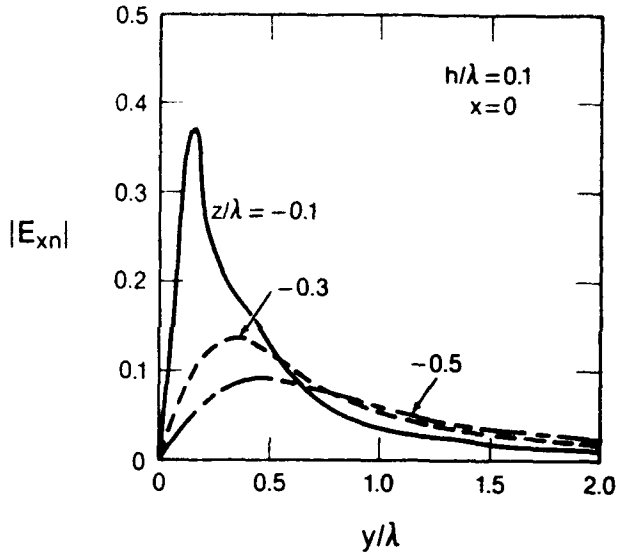

Fig. 10. Normalized electric field at various heights in air. Complex earth permittivity: $\epsilon'/\epsilon = 4.0 + i0.1$.

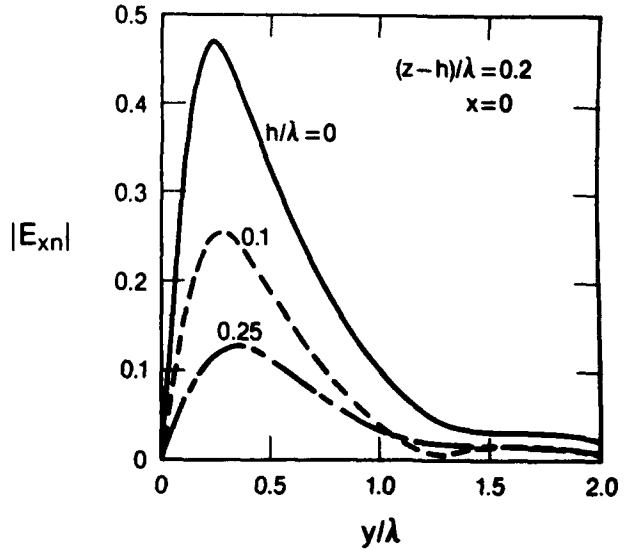

Fig. 11. Normalized electric field in the earth for various antenna heights. Complex earth permittivity: $\epsilon'/\epsilon = 4.0 + i0.1$.

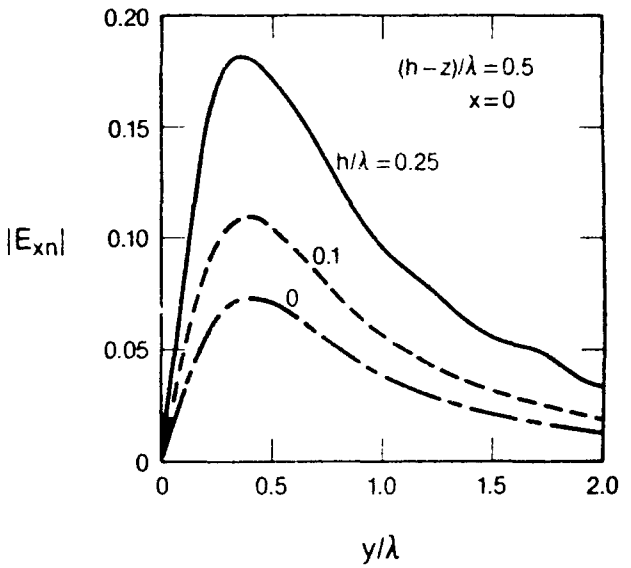

Fig. 12. Normalized electric field in air for various antenna heights. Complex earth permittivity $\epsilon'/\epsilon = 4.0 + i0.1$.

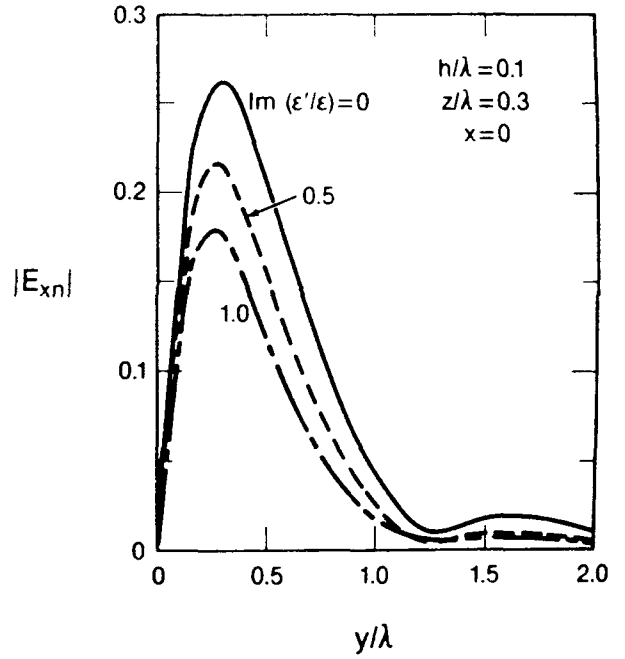

Fig. 13. Normalized electric field in the earth for various values of Im (ϵ'/ϵ). Earth permittivity: Re $(\epsilon'/\epsilon) = 4.0$.

VI. Conclusion

We have used the plane-wave spectrum technique to derive expressions for the near fields and far fields of horizontal electric currents located above the earth. The far fields are evaluated asymptotically, and the near fields are calculated using 2D FFT. The 2D FFT technique is fast and simple, and it avoids Sommerfeld integral evaluations that are usually associated with antennas near an interface [7].

Specific numerical results have been generated for the far fields and near fields of oppositely directed dipoles located above the earth. This antenna configuration is of particular interest in detection of buried objects. Locating the antenna close to the earth enhances the field in the earth and decreases the field in air, and this effect holds for the near field and the far field.

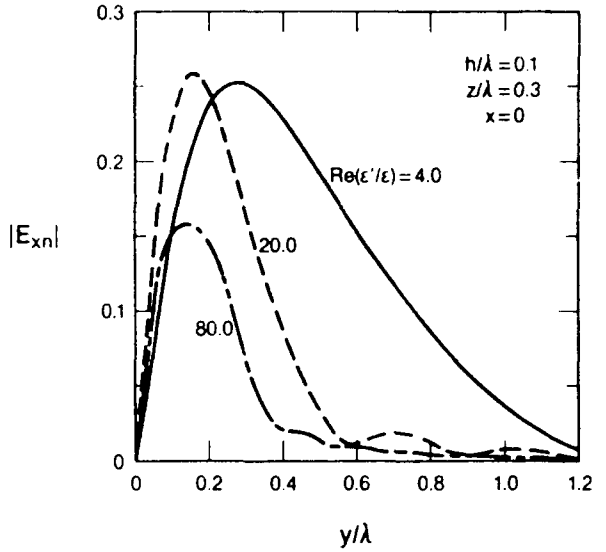

Fig. 14. Normalized electric field in the earth for various values of Re (ϵ'/ϵ). Imaginary part of earth permittivity: Im $(\epsilon'/\epsilon) = 0.1$.

A number of extensions to this work would be useful. A buried scattering object [11] and a receiving antenna could be included in the theory to assess the overall detection effectiveness. The required plane-wave, scattering-matrix theory has already been developed to handle such cases [3]. Other antenna configurations could be analyzed, and the effect of the ground on the input impedance could be studied as a function of antenna height [12].

Appendix—Front-to-Back Ratio

We define the front-to-back ratio FBR(h) as the magnitude of the ratio of the far field in the earth to the far field in air for the directions normal to the interface ($\theta' = 0$ and $\theta = 180°$). This definition is not useful for antennas that have nulls normal to the interface as in the case of oppositely directed dipoles. As in Section V, we considered the special case, $\mu' = \mu = \mu_0$ and $\epsilon = \epsilon_0$. From (19) and (20), we can derive the following:

$$\mathrm{FBR}(h) = \frac{k' T_{21} e^{ik'r'}}{k(1 + R'_{11})} \qquad \text{(A1)}$$

where the expression is evaluated at $K = 0$. The exponential factor occurs because the earth is lossy. The height dependence is contained in R'_{11} as seen in (11). When $h = 0$, (A1) simplifies to

$$\mathrm{FBR}(0) = \left|(\epsilon'/\epsilon)^{1/2} e^{ik'r'}\right|. \qquad \text{(A2)}$$

When ϵ' is real, there is no exponential decay, and (A1) reduces to

$$\mathrm{FBR}(h) = \left|k' T_{21} / [k(1 + R'_{11})]\right| \qquad \text{(A3)}$$

where the expression is again evaluated at $K = 0$. If in addition $h = 0$, (A3) reduces to

$$\mathrm{FBR}(0) = (\epsilon'/\epsilon)^{1/2}. \qquad \text{(A4)}$$

This remarkably simple result is consistent with the nu-

merical results of Smith [2] for a horizontal dipole located at the interface. The result in (A4) can also be derived by reciprocity.

ACKNOWLEDGMENT

The author would like to thank W. K. Klemperer and G. Tricoles for useful discussions.

REFERENCES

[1] A. Banos, Jr., *Dipole Radiation in the Presence of a Conducting Half-Space*. New York: Pergamon, 1966.
[2] G. S. Smith, "Directive properties of antennas for transmission into a material half-space," *IEEE Trans. Antennas Propagat.*, vol. AP-32, pp. 232-246, 1984.
[3] D. A. Hill and K. H. Cavcey, "Coupling between two antennas separated by a planar interface," *IEEE Trans. Geosci. Remote Sensing*, vol. GE-25, pp. 422-431, 1987.
[4] D. M. Kerns, *Plane-Wave Scattering-Matrix Theory of Antennas and Antenna-Antenna Interactions*, National Bureau of Standards Monograph 162, Washington: U.S. Government Printing Office, 1981.
[5] G. S. Smith and L. N. An, "Loop antennas for directive transmission into a material half space," *Radio Sci.*, vol. 18, pp. 664-674, 1983.
[6] L. C. Chan, L. Peters, Jr., and D. L. Moffat, "Improved performance of a subsurface radar target identification system through antenna design," *IEEE Trans. Antennas Propagat.*, vol. AP-29, pp. 307-311, 1981.
[7] G. J. Burke, E. K. Miller, J. N. Brittingham, D. L. Lager, R. J. Lytle, and J. T. Okada, "Computer modeling of antennas near the ground," *Electromagnetics*, vol. 1, pp. 29-49, 1981.
[8] E. C. Jordan and K. G. Balmain, *Electromagnetic Waves and Radiating Systems*. Englewood Cliffs, NJ: Prentice-Hall, 1968, sec. 10.06.
[9] A. Q. Howard, Jr., "A canonical solution to the three-dimensional electromagnetic prospecting problem," *Radio Sci.*, vol. 10, pp. 461-471, 1975.
[10] ——, "On approximating Fourier integral transforms by their discrete counterparts in certain geophysical applications," *IEEE Trans. Antennas Propagat.*, vol. AP-23, pp. 264-266, 1975.
[11] D. A. Hill, "Electromagnetic scattering by buried objects of low contrast," *IEEE Trans. Geosci. Remote Sensing*, vol. 26, pp. 195-203, 1988
[12] K. Moore, R. Hayward, J. Nilles, E. Rope, and G. Tricoles, "Phase switched interferometer for nearfield detection of buried ojects," in *IEEE AP S Int. Symp. Dig.*, (Blacksburg, VA), pp. 1054-1055, 1987.

David A. Hill (M'72-SM'76-F'87) was born in Cleveland, OH on April 21, 1942. He received the B.S.E.E. and M.S.E.E. degrees from Ohio University, Athens, in 1964 and 1966, respectively, and the Ph.D. degree in electrical engineering from Ohio State University, Columbus, in 1970.

Since 1970 he has been a member of the Boulder scientific community. From 1970 to 1971 he was a Visiting Fellow with the Cooperative Institute for Research in Environmental Sciences where he worked on pulse propagation. From 1971 to 1982 he was with the Institute for Telecommunication Sciences where he worked on theoretical problems in antennas and propagation. Since 1982 he has been in the Electromagnetic Fields Division of the National Bureau of Standards where he has been working on EMC/EMI problems. He is also a Professor Adjoint in the Department of Electrical and Computer Engineering of the University of Colorado.

Dr. Hill is a member of URSI Commissions B, E, and F. He has served as a Technical Editor for the IEEE TRANSACTIONS ON GEOSCIENCE AND REMOTE SENSING and is now an Associate Editor for the IEEE TRANSACTIONS ON ANTENNAS AND PROPAGATION.

Near-Field Detection of Buried Dielectric Objects

DAVID A. HILL

APPENDIX
III D

Reprinted from
IEEE TRANSACTIONS ON GEOSCIENCE AND REMOTE SENSING
Vol. 27, No. 4, July 1989

Near-Field Detection of Buried Dielectric Objects

DAVID A. HILL, FELLOW, IEEE

Abstract—The plane-wave scattering-matrix method is used to compute the response of a detector to a buried dielectric scatterer. The Born approximation is used to derive the scattering matrix for scatterers of small dielectric contrast, but the general theory is not limited to such cases. Specific numerical results are generated for a UHF dipole detector swept over a buried dielectric cube. The maximum response is obtained when the detector is located at the air–earth interface, and the response decays rapidly with detector height. The sweep curves are symmetrical in the horizontal direction and have a null when the detector is directly over the object. An experimental curve for a free-space environment has the same qualitative features.

I. Introduction

THE analysis of scattering by buried objects [1]–[3] is complicated by the presence of the air–earth interface. The problem becomes even more complicated when the characteristics of the transmitting and receiving antennas are included [4], [5]. The plane-wave scattering-matrix method [6] provides a convenient means of combining the source, receiver, scatterer, and interface effects in a self-consistent formulation [7].

In this paper we use the plane-wave scattering-matrix method to study the detection of buried objects by a detector that is swept over the earth's surface at a low height. Numerical results are obtained for a UHF detector that consists of oppositely directed transmitting dipoles [8] and a single receiving dipole. The buried dielectric target is a homogeneous rectangular box of arbitrary dimensions [9]. The scattering matrix for this particular target is derived by using the Born approximation for a low dielectric contrast.

The organization of this paper is as follows: In Section II we review the plane-wave scattering-matrix theory for the detection application [7] and obtain an approximate expression for the received signal as a function of detector position. In Section III we derive the required plane-wave transmitting and receiving characteristics for the UHF dipole detector. In Section IV we carry-out the scattering-matrix calculations and present sweep curves for the UHF detector for various parameters. An experimental sweep curve is also shown for a free-space environment. Conclusions and recommendations for further work are contained in Section V.

Manuscript received July 15, 1988; revised February 10, 1989. This work was supported by the U.S. Army Belvoir Research and Development Center.

The author is with the Fields and Interference Metrology Group, Electromagnetic Fields Division, National Institute of Standards and Technology, Boulder, CO 80303.

IEEE Log Number 8928101.

II. Plane-Wave Scattering-Matrix Theory

The geometry of a detector in air and a buried scatterer is shown in Fig. 1. The air has permittivity ϵ_0, the earth has permittivity ϵ', and the permeability is μ_0 everywhere. The detector can consist of either a single antenna or separate transmitting and receiving antennas, and it is located at a height h above the earth. The scatterer is located at a depth d and a horizontal offset P.

The general notation and the formal scattering-matrix solution for the fields and the received signal are contained in [7], and here we will only extract the results that are necessary for our detector application. The column matrices $\hat{a}_1$ and $\hat{b}_1$ contain the coefficients of the upgoing and downgoing plane waves in the region between the detector and the interface. Similarly, the column matrices $\hat{b}_2'$ and $\hat{a}_2'$ contain the coefficients of the upgoing and downgoing plane waves in the region between the scatterer and the air–earth interface.

The receiving and transmitting characteristics of the detector are specified by

$$b_0 = \hat{S}_{01}\hat{a}_1 \quad \text{and} \quad \hat{b}_1 = \hat{S}_{10}a_0 \tag{1}$$

where a_0 and b_0 are coefficients of incoming and outgoing modes at the detector feed, $\hat{S}_{01}$ is a row matrix representing the receiving characteristics of the detector, and $\hat{S}_{10}$ is a column matrix representing the transmitting characteristics of the detector. Here we have assumed that the reflection coefficient at the detector feed and the scattering matrix of the detector are negligible.

The scattering characteristics of the buried object are specified by

$$\hat{b}_2' = \hat{S}_{22}'\hat{a}_2' \tag{2}$$

where $\hat{S}_{22}'$ is a square matrix representing the scattering characteristics of the buried object. The results in [7] apply to general scatterers, but here we assume that the scatterer is homogeneous and has complex permittivity ϵ_s which does not depart markedly from ϵ'. For this case the scattering matrix $\hat{S}_{22}'$ has been derived using the Born approximation [9]. This weak-scattering case is applicable to detection of plastic mines in dry soil [10].

The general solution for the received signal b_0 in [7] contains the effects of multiple reflections between the scatterer and the interface. For our case of weak scattering we neglect multiple reflections, and the result in [7] reduces to

$$b_0 = \hat{S}_{01}\hat{R}_{11}'\hat{S}_{10}a_0 + \hat{S}_{01}\hat{T}_{12}\hat{S}_{22}'\hat{T}_{21}\hat{S}_{10}a_0. \tag{3}$$

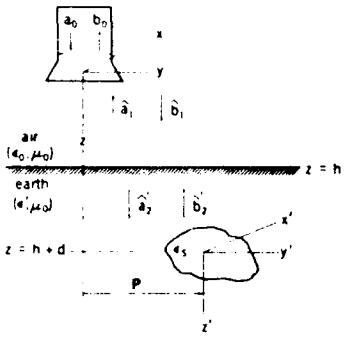

Fig. 1. Geometry for a detector over a buried dielectric object.

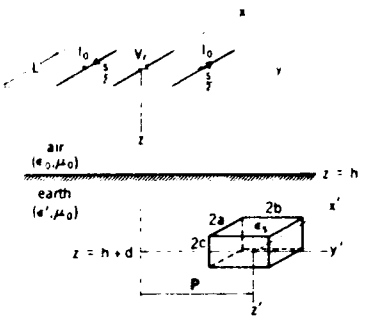

Fig. 2. Geometry for a dipole detector over a buried dielectric box.

The first term in (3) represents reflection of the air–earth interface and is independent of the buried scatterer. Most detectors are designed to null out this ground-reflected signal either by placing the receiving element at a null of the field [8] or by using a cross-polarized receiving element [11]. Consequently, we will assume that the first term in (3) is zero, and the ratio of the received to the incident signal is

$$b_0/a_0 = \hat{S}_{01}\hat{T}'_{12}\hat{S}'_{22}\hat{T}'_{21}\hat{S}_{10}. \tag{4}$$

The right side of (4) has a simple physical interpretation. $\hat{S}_{10}$ represents transmission from the detector into air, $\hat{T}'_{21}$ represents transmission from air into the earth, $\hat{S}'_{22}$ represents scattering from the buried object, $\hat{T}'_{12}$ represents transmission from the earth into air, and $\hat{S}_{01}$ represents reception at the detector.

The square diagonal matrices $\hat{T}'_{21}$ and $\hat{T}'_{12}$ have diagonal elements of the following form for $\exp(-i\omega t)$ time dependence:

$$T'_{21} = T_{21}e^{i(\gamma h + \gamma' d + \boldsymbol{K}\cdot\boldsymbol{P})} \quad \text{and} \quad T'_{12} = T_{12}e^{i(\gamma h + \gamma' d - \boldsymbol{K}\cdot\boldsymbol{P})}. \tag{5}$$

Here T_{21} and T_{12} are Fresnel transmission coefficients, and the superscript indicates translation as given by the exponential factors. The transverse wavenumber $\boldsymbol{K}$ is given by

$$\boldsymbol{K} = k_x\boldsymbol{e}_x + k_y\boldsymbol{e}_y \tag{6}$$

where $\boldsymbol{e}_x$, $\boldsymbol{e}_y$, and $\boldsymbol{e}_z$ are unit vectors. The horizontal offset $\boldsymbol{P}$ of the scatterer is given by

$$\boldsymbol{P} = P_x\boldsymbol{e}_x + P_y\boldsymbol{e}_y. \tag{7}$$

The z components of the wavenumbers are given by

$$\gamma = (k^2 - k_x^2 - k_y^2)^{1/2} \quad \text{and} \quad \gamma' = (k'^2 - k_x^2 - k_y^2)^{1/2} \tag{8}$$

where $k^2 = \omega^2\mu_0\epsilon_0$ and $k'^2 = \omega^2\mu_0\epsilon'$.

Detectors are normally moved at a constant height above the earth. To generate sweep curves (detector response as a function of horizontal position) we need to calculate b_0/a_0 from (4) for varying values of the horizontal offset $\boldsymbol{P}$. This calculation involves multiplication of large matrices, but fortunately $\hat{S}_{10}$, $\hat{S}'_{22}$, and $\hat{S}_{01}$ are independent of $\boldsymbol{P}$. Thus only $\hat{T}'_{21}$ and $\hat{T}'_{12}$ need to be recalculated for each value of $\boldsymbol{P}$. The numerical evaluation of (4) will be discussed in more detail in Section IV.

III. Dipole Detector

A UHF dipole detector of particular interest in detection of buried objects at shallow depths is shown in Fig. 2. The transmitting antenna consists of two x-directed dipoles of length L fed in opposition and separated by a distance s. The x-directed receiving dipole of length L is located at the center of the detector ($y = z = 0$) which is in the null of the transmitting antenna. Thus the detector will respond to inhomogenieties that are asymmetrical with respect to the xz plane, but not to a homogeneous or horizontally stratified earth.

A. Transmitting Antenna

The transmitting antenna has been analyzed previously [8] for a sinusoidal current assumption. It would be possible to solve for the current distribution on a pair of wires over the ground by the method of moments [12], but the classical sinusoidal current approximation [13] is adequate for our detector calculations. A major advantage of the sinusoidal current assumption is that it allows us to obtain an analytical expression for the transmission matrix $\hat{S}_{10}$.

The coefficients of the outgoing plane waves $b_1(m, \boldsymbol{K})$ are given by [8, eq. (6)]. For linear antennas it is more convenient to normalize the transmission matrix to the input current I_0 rather than a mode coefficient a_0 as indicated in Fig. 1. Thus we can define the elements $S_{10}(m, \boldsymbol{K})$ of the transmission matrix $\hat{S}_{10}$ as

$$S_{10}(m, \boldsymbol{K}) = b_1(m, \boldsymbol{K})/I_0 \tag{9}$$

where $b_1(m, \boldsymbol{K})$ is given by [8, eq. (6)]. In (9), m takes on values of 1 for transverse magnetic (TM) polarization, and values of 2 for transverse electric (TE) polarization. The transverse wavenumbers k_x and k_y in $\boldsymbol{K}$ take on real values from $-\infty$ to ∞.

B. Receiving Antenna

We assume that the receiving dipole also has a sinusoidal current [13]:

$$I(x) = \frac{\sin\left\{k[(L/2) - |x|]\right\}}{\sin(kL/2)}, \quad |x| < L/2. \tag{10}$$

For an incident field E^i, the open-circuit received voltage V_r can be determined from the induced EMF method [13]:

$$V_r = -\int_{-L/2}^{L/2} e_x \cdot E^i\big|_{y=z=0} I(x)\,dx. \tag{11}$$

To determine the elements $S_{01}(m, K)$ of the receiving matrix $\hat{S}_{01}$, we let the incident field in (11) be either a TM or a TE plane wave. Thus we have

$$e_x \cdot E^i\big|_{y=z=0} = \frac{e_x \cdot \kappa_m}{2\pi} e^{ik_x x}. \tag{12}$$

The transverse unit vectors κ_m are [6]

$$\kappa_1 = (k_x e_x + k_y e_y)/K \quad \text{and} \quad \kappa_2 = (k_y e_x - k_x e_y)/K \tag{13}$$

where $K = |K|$. For linear antennas we find it more convenient to define the receiving matrix in terms of the received voltage V_r rather than a mode amplitude. Thus we set $S_{01}(m, K) = V_r$. If we substitute (10), (12), and (13) into (11) and carry out the x integration, we obtain the final result

$$S_{01}\begin{pmatrix}1, K\\ 2\end{pmatrix} = \frac{-kk_x}{\pi K(k^2 - k_x^2)\sin(kL/2)} \cdot \left[\cos(k_x L/2) - \cos(kL/2)\right]. \tag{14}$$

When $k_x^2 = k^2$, (14) is indeterminate and the limiting result is

$$S_{01}\begin{pmatrix}1, K\\ 2\end{pmatrix} = -k_x L/(4\pi K). \tag{15}$$

In (14) and (15), the x subscript on k corresponds to $m = 1$, and the y subscript corresponds to $m = 2$.

IV. Numerical and Experimental Results

In this section we present numerical results for the geometry shown in Fig. 2. We simulate sweep curves by varying P_y while holding constant the detector height h, the scatterer depth d, and the x offset P_x. The computed quantity is the ratio of the received voltage V_r to the input current I_0:

$$V_r/I_0 = \hat{S}_{01}\hat{T}'_{12}\hat{S}'_{22}\hat{T}'_{21}\hat{S}_{10}. \tag{16}$$

The result in (16) is the same as (4) except that $\hat{S}_{01}$ and $\hat{S}_{10}$ have been defined in terms of voltage and current as indicated in the previous section. The quantity V_r/I_0 is the mutual impedance between the transmitting antennas and receiving antennas and has units of ohms. It is zero in the symmetrical environment of free space or a homogeneous half-space, but is unbalanced by the presence of any asymmetries.

The buried target is modeled as a rectangular box (parallelepiped) of dimensions $2a \times 2b \times 2c$ and complex dielectric constant ϵ_s. As indicated in Fig. 2, the faces of the box are parallel to the xy, yz, and xz planes. The scattering matrix $\hat{S}'_{22}$ for this target has been derived for the low contrast case [9], and we will not reproduce the result here. The bulk of the computing in evaluation of (16) is the filling of $\hat{S}'_{22}$ and the associated matrix multiplications. $\hat{S}'_{22}$ is a square $(N \times N)$ matrix where N is determined by the sampling in k_x and k_y. If N_k is the number of samples required for k_x (and k_y), then $N = 2N_k^2$ where the 2 factor is due to the two polarizations (TM and TE). This means that $\hat{S}'_{22}$ contains $N^2 = 4N_k^4$ elements, which is typically a very large number. Fortunately, $\hat{S}_{01}$ is a row matrix, $\hat{S}_{10}$ is a column matrix, and both matrices contain only $2N_k^2$ elements. Also, both $\hat{T}'_{12}$ and $\hat{T}'_{21}$ are diagonal matrices that contain only $2N_k^2$ nonzero elements. A computer program was written to evaluate (16), and the convergence was studied by varying the step size and the maximum values of k_x and k_y.

The magnitude of V_r/I_0 versus P_y is shown in Figs. 3–5 for a number of different parameters. All dimensions are normalized to the free space wavelength λ, and the actual frequency of operation for this type of detector is typically 380 MHz, which corresponds to a wavelength of 78.9 cm. The detector dimensions are $L = s = 0.2735\ \lambda = 21.6$ cm. For ground constants we choose $\epsilon'/\epsilon_0 = 3.5 + i0.1$, which represents fairly dry soil. For target dimensions we choose $2a = 2b = 2c = 0.126\ \lambda$, which equals 10 cm. The complex dielectric constant is $\epsilon_s/\epsilon_0 = 3.0 + i0.05$, which represents a fairly low-loss material such as plastic or wood.

In Fig. 3 we show the effect of offset distance P_x on the sweep curves. All curves have a null at $P_y = 0$ and are symmetrical in P_y, and the response falls off as P_x is increased. In Fig. 4 we show the effect of the scatterer depth d on the sweep curves. For $d/\lambda = 0.063$, the top surface of the cube is flush with the air–earth interface. For increasing d, the response decreases. In Fig. 5 we show the effect of detector height h on the sweep curves, and the response decreases rapidly with increasing h. All of the results in Figs. 3–5 are consistent with the scattering results in [9] and the antenna results in [8]. For soil with a higher moisture content, both the real and imaginary parts of ϵ' will be larger, and some results for the increased attenuation of the transmitted field have been given in [8].

Some experimental work was performed for the UHF detector in Fig. 2 for the same physical dimensions ($L = s = 21.6$ cm). The detector suffered from lack of sensitivity and an imperfect balance. However, its performance improved somewhat when the operating frequency was increased from 380 to 430 MHz. An experimental curve for a spherical target in a free-space environment ($\epsilon'/\epsilon_0 = 1$) is shown in Fig. 6. The sphere diameter was 9.85 cm, and the sphere material was nylon ($\epsilon_s/\epsilon_0 \approx 3.0$). The height of the detector above the surface of the sphere was 1.2 cm. Since the Born approximation is not valid for such a large contrast ($\epsilon_s/\epsilon' \approx 3.0$), we did not attempt a direct comparison with the theory. However, the main features of the theoretical and experimental

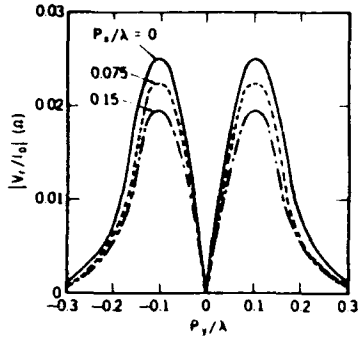

Fig. 3. Sweep curves for various offset distances P_x. Parameters: $h/\lambda = 0.1$ and $d/\lambda = 0.126$.

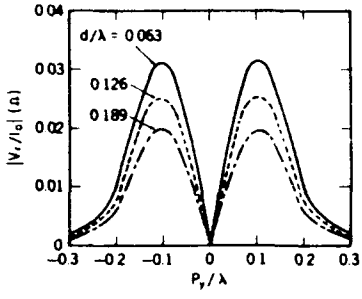

Fig. 4. Sweep curves for various target depths d. Parameters: $h/\lambda = 0.1$ and $P_x = 0$.

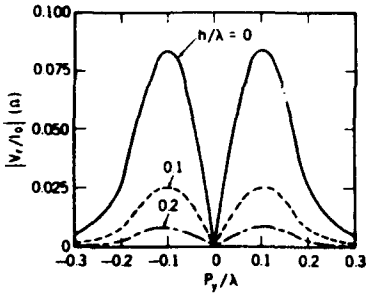

Fig. 5. Sweep curves for various detector heights h. Parameters: $d/\lambda = 0.126$ and $P_x = 0$.

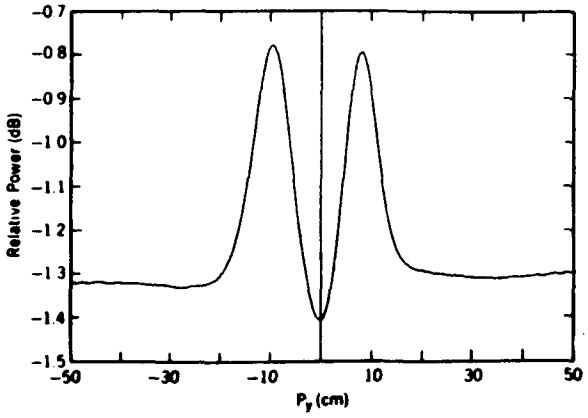

Fig. 6. Experimental sweep curve for a dielectric sphere in free space. Parameters: frequency = 432 MHz, $\epsilon_r/\epsilon_0 = 3.0$, and $P_x = 0$.

curves are the same, and the locations of the peaks are approximately the same ($P_y \approx \pm 8$ cm). The experimental curve is not quite symmetrical and the unbalance of the detector results in a baseline value (large $|P_y|$) that is not zero. The null value for $P_y = 0$ is actually lower than the baseline value.

V. Conclusions

We have used the plane-wave scattering-matrix formulation to compute the response of a dipole detector to a buried dielectric scatterer. The computations involve a large number of evaluations of the scattering matrix of the buried rectangular box, but the evaluation of Sommerfeld integrals usually associated with antennas near an interface [12] is avoided.

The numerical results in Figs. 3–5 indicate that the sweep curves are symmetrical and have a null directly over the buried target. Experimental results in Fig. 6 show the same qualitative features. The results in Fig. 5 show that the detector should be located as close as possible to the earth for maximum response.

A number of extensions to this work would be useful. The importance of multiple reflections between the detector, the buried target, and the air–earth interface could be studied using the complete formulation in [7]. Also, a quantitative study of the errors caused by truncating the range of the horizontal wavenumbers k_x and k_y would be useful for further numerical work. Larger dielectric targets with higher contrast could be treated and the effects of target resonances [14] on the frequency response could be studied. Other antenna configurations could be analyzed and the effect of the ground on the input impedance could be studied as a function of antenna height [15]. A related problem is the effect of surface roughness and volume clutter on the detector response. A more accurate experimental study of the UHF detector over various earths and targets would also be very useful and would provide a more complete comparison with the theory.

Acknowledgment

I would like to thank Dr. W. K. Klemperer for providing the experimental results.

References

[1] G. Kristensson, "Electromagnetic scattering from buried inhomogeneities—A general three-dimensional formalism," *J. Appl. Phys.*, vol. 51, pp. 3486–3500, 1980.

[2] S. F. Mahmoud, S. M. Ali, and J. R. Wait, "Electromagnetic scattering from a buried cylindrical inhomogeneity inside a lossy earth," *Radio Sci.*, vol. 16, pp. 1285–1298, 1981.

[3] H. S. Chang and K. K. Mei, "Scattering of electromagnetic waves by buried and partly buried bodies of revolution," *IEEE Trans. Geosci. Remote Sensing*, vol. GE-23, pp. 596–605, July 1985.

[4] M. Cauterman, J. L. Martin, P. Degauge, and R. Gabillard, "Numerical modeling for electromagnetic remote sensing of inhomogeneities in the ground," *Proc. IEEE*, vol. 67, pp. 1009–1015, 1979.

[5] P. A. Eaton and G. W. Hohmann, "An evaluation of electromagnetic methods in the presence of geologic noise," *Geophysics*, vol. 52, pp. 1106–1126, 1987.

[6] D. M. Kerns, *Plane-Wave Scattering-Matrix Theory of Antennas and Antenna-Antenna Interactions*. Washington, DC: NBS Monog. 162, 1981.

[7] D. A. Hill and K. H. Cavcey, "Coupling between two antennas sep-

arated by a planar interface," *IEEE Trans. Geosci. Remote Sensing*, vol. GE-25, pp. 422-431, July 1987.
[8] D. A. Hill, "Fields of horizontal currents located above the earth," *IEEE Trans. Geosci. Remote Sensing*, vol. 26, pp. 726-732, Nov. 1988.
[9] D. A. Hill, "Electromagnetic scattering by buried objects of low contrast," *IEEE Trans. Geosci. Remote Sensing*, vol. 26, pp. 195-203, Mar. 1988.
[10] R. C. Weaver, private communication, 1987.
[11] L. C. Chan, L. Peters, Jr., and D. L. Moffat, "Improved performance of a subsurface radar target identification system through antenna design," *IEEE Trans. Antennas Propagat.*, vol. AP-29, pp. 307-311, 1981.
[12] G. J. Burke *et al.*, "Computer modeling of antennas near the ground," *Electromagn.*, vol. 1, pp. 29-49, 1981.
[13] E. C. Jordan and K. G. Balmain, *Electromagnetic Waves and Radiating Systems*. Englewood Cliffs, NJ: Prentice-Hall, 1968.
[14] L. C. Chan, D. L. Moffat, and L. Peters, "A characterization of subsurface radar targets," *Proc. IEEE*, vol. 67, pp. 991-1000, 1979.
[15] K. Moore, R. Hayward, J. Nilles, E. Rope, and G. Tricoles, "Phase switched interferometer for nearfield detection of buried objects," *IEEE AP-S Int. Symp. Dig.* (Blacksburg, VA), pp. 1054-1055, 1987.

David A. Hill (M'72-SM'76-F'87) was born in Cleveland, OH, on April 21, 1942. He received the B.S.E.E. and M.S.E.E. degrees from Ohio University, Athens, in 1964 and 1966, respectively, and the Ph.D. degree in electrical engineering from Ohio State University, Columbus, in 1970.

Since 1970 he has been a member of the Boulder scientific community. From 1970 to 1971 he was a Visiting Fellow with the Cooperative Institute for Research in Environmental Sciences, where he worked on pulse propagation. From 1971 to 1982 he was with the Institute for Telecommunication Sciences, where he worked on theoretical problems in antennas and propagation. Since 1982 he has been in the Electromagnetic Fields Division of the National Bureau of Standards, where he has been working on EMC/EMI and remote-sensing problems. He is also a Professor Adjoint in the Department of Electrical and Computer Engineering of the University of Colorado.

Dr. Hill is a member of URSI Commissions B, E, and F. He has served as a Technical Editor for the IEEE TRANSACTIONS ON GEOSCIENCE AND REMOTE SENSING and is now an Associate Editor for the IEEE TRANSACTIONS ON ANTENNAS AND PROPAGATION.

APPENDIX VI.A BASIC Program to Print Out Values of Mu and Epsilon

```
110!Last Revision August 7, 1987  11:21
115!This program calculates the relative mu and epsilon of a
116!     material from
120!S-parameter results obtained from the HP8510 network analyzer.
125!Written by Eric J. Vanzura (303) 497-5752   6/26/1987
130     GOSUB Init
135     GOSUB Load_matrix
140     GOSUB Calc_rotation
145     GOSUB Calc_dielectric
150     GOSUB Print_results
155     GOSUB Save_results
160     GOTO End
165!
170! ////////////////////////////////////////////////////////////
175!
180 Init:!
185     OUTPUT KBD USING "#,K";"SCRATCH KEY"&CHR$(255)&CHR$(69)
190     DEG
195     OPTION BASE 1
200     INTEGER I,J,Use_s11,Datacount,Bad_number
205     REAL Samplelength,L1,L2,Rot1,Rot2,Lairline,Test
210     DIM Test$[160]
215     Datacount=201
220     Samplelength=.095     !METERS
225     Lairline=.0994
230     L2=.002
235     L1=Lairline-Samplelength-L2
240     GOSUB Init_expt
245     ALLOCATE A(Datacount,9),B(Datacount,2),Lam0(Datacount),
                Prompt$[40],Id$[40]
250     ALLOCATE OPTION S11(Datacount),S12(Datacount),S21(Datacount),
                S22(Datacount)
255     ALLOCATE OPTION Gam1(Datacount),Gam2(Datacount),
        Gam(Datacount),K(Datacount),Lam(Datacount),T(Datacount)
260     ALLOCATE OPTION Mu(Datacount),Eps(Datacount)
265*
270     COM /Files/ Sourcedisk$[20],Diskout$[20],Diskdrive$[20],
        Filename$[10]
275     COM /Bugs/ INTEGER Bug1,Bug2,Bug3,Printer,Printer_on
280     Printer=701
285     Printer_on=0
290     Prty=VAL(SYSTEM$("SYSTEM PRIORITY"))+1
295     DISP CHR$(129);" DO YOU WANT TO USE (S11,S21) DATA OR
        (S22,S12) DATA? ";
300     DISP CHR$(128)
305     ON KEY 4 LABEL "S11,S21 DATA",Prty GOSUB Use_s11_yes
310     ON KEY 5 LABEL "S22,S12 DATA",Prty GOSUB Use_s11_no
315     Done=0
320     LOOP
325     EXIT IF Done
330     END LOOP
335     RETURN
340 !
```

```
355 Init_expt:!
360 Enter_datacount:OUTPUT KBD USING "#,K";Datacount
365    LINPUT "ENTER number of frequencies in datafile",Test$
370    CALL Test_real(Test,Test$,51.,401.,Bad_number)
375    IF Bad_number THEN GOTO Enter_datacount
380    Datacount=INT(Test)
385 Enter_airline:!
390    OUTPUT KBD USING "#,K";Lairline
395    LINPUT "ENTER length of airline (meters)",Test$
400    CALL Test_real(Test,Test$,.01,.5,Bad_number)
405    IF Bad_number THEN GOTO Enter_airline
410    Lairline=Test
415 Enter_sample:!
420    OUTPUT KBD USING "#,K";Samplelength
425    LINPUT "ENTER sample length (meters)",Test$
430    CALL Test_real(Test,Test$,.001,Lairline,Bad_number)
435    IF Bad_number THEN GOTO Enter_sample
440    Samplelength=Test
445 Enter_l1:!
450    OUTPUT KBD USING "#,K";L1
455    LINPUT "ENTER distance from Port 1 interface to
       sample (meters)",Test$
460    CALL Test_real(Test,Test$,0.,.5,Bad_number)
465    IF Bad_number THEN GOTO Enter_l1
470    L1=Test
475 Enter_l2:!
480    OUTPUT KBD USING "#,K";L2
485    LINPUT "ENTER distance from Port 2 interface to
       sample (meters)",Test$
486    CALL Test_real(Test,Test$,0.,.5,Bad_number)
490    IF Bad_number THEN GOTO Enter_l2
495    L2=Test
500    RETURN
505 !
510 ! ////////////////////////////////////////////////////////////
515 !
520 Use_s11_yes:OFF KEY
525    Use_s11=1
530    Done=1
535    RETURN
540 !
545 ! ////////////////////////////////////////////////////////////
550 !
555 Use_s11_no:OFF KEY
560    Use_s11=0
565    Done=1
570    RETURN
575 !
580 ! ////////////////////////////////////////////////////////////
585 !
590 Load_matrix:!
595    Prompt$="8510 S-PARAMETER DATA"
600    CALL Select_disk(Prompt$)
605    CALL Enterfilename("CAT",Prompt$)
610    IF Filename$="" THEN
```

```
615         CAT Diskdrive$
620         CALL Enterfilename("ABORT",Prompt$)
625         IF Filename$="" THEN
630             BEEP
635             DISP "PROGRAM ABORTED"
640             STOP
645         END IF
650     END IF
655     DISP CHR$(129);" GETTING DATA FROM DISK ";CHR$(128)
660     ASSIGN @Datapath TO Filename$&Diskdrive$
665     ENTER @Datapath;A(*)
670     ASSIGN @Datapath TO *
675     FOR I=1 TO Datacount
680*
685*
690*
695*
700     NEXT I
705     IF Printer_on THEN PRINTER IS Printer
710     PRINT "FREQ          S11            S21            S22
         S12"
715     FOR I=1 TO Datacount STEP INT(Datacount/10)
720         PRINT USING "2D.2D,4X,4(2(SD.3D),2X)";A(I,1),S11(I),
            S21(I),S22(I),S12(I)
725     NEXT I
730     PRINTER IS 1
735     RETURN
740 !
745 ! ////////////////////////////////////////////////////////////
750 !
755 Calc_rotation:!
760     DISP CHR$(129);" CALCULATING PHASE ROTATIONS L1=";L1;" ";
        CHR$(128)
765     FOR I=1 TO Datacount
770         Lam0(I)=.29979/A(I,1)     !METERS
775         Rot1=360*L1/Lam0(I)
780         Rot2=360*L2/Lam0(I)
785*
790*
795         S11(I)=S11(I)*(Phase1^2)
800         S21(I)=S21(I)*(Phase1*Phase2)
805         S12(I)=S12(I)*(Phase1*Phase2)
810         S22(I)=S22(I)*(Phase2^2)
815     NEXT I
820     DISP " S11 AND S22 SHOULD NOW BE VERY CLOSE TO EQUAL ";
              CHR$(128)
825     IF Printer_on THEN PRINTER IS Printer
830     PRINT "FREQ (GHz)          S11                S22
           S11-S22       ANGLE(S11-S22)"
835     FOR I=1 TO Datacount STEP INT(Datacount/30)
840*
845     NEXT I
846     PRINT " S11 AND S22 SHOULD NOW BE VERY CLOSE TO EQUAL ";
          CHR$(128)
850     PRINTER IS 1
```

```
855     RETURN
860 !
865 ! ////////////////////////////////////////////////////////////
870 !
875 Calc_dielectric:!
880 Cd:!
885     DISP CHR$(129);" CALCULATING COMPLEX MU AND EPSILON ";
        CHR$(128)
890     FOR I=1 TO Datacount
895         IF Use_s11 THEN
900             K(I)=(S11(I)^2-S21(I)^2+1)/(2*S11(I))
905         ELSE
910             K(I)=(S22(I)^2-S12(I)^2+1)/(2*S22(I))
915         END IF
920*
925*
930         IF ABS(Gam1(I))<1 THEN
935             IF ABS(Gam2(I))<1 THEN
940                 BEEP
945                 DISP "GAM1(";I;") AND GAM2(";I;") ARE BOTH LESS
                        THAN 1 !?"
950                 PAUSE
955             ELSE
960                 Gam(I)=Gam1(I)
965             END IF
970         ELSE
975             IF ABS(Gam2(I))>1 THEN
980                 BEEP
985                 DISP "GAM1(";I;") AND GAM2(";I;") ARE BOTH
                        GREATER THAN 1 !?"
990                 PAUSE
995             ELSE
1000                Gam(I)=Gam2(I)
1005            END IF
1010        END IF
1015        IF Use_s11 THEN
1020        T(I)=(S11(I)+S21(I)-Gam(I))/(1-(S11(I)+S21(I))*Gam(I))
1025        ELSE
1030        T(I)=(S22(I)+S12(I)-Gam(I))/(1-(S22(I)+S12(I))*Gam(I))
1035        END IF
1040*
1045        Mu(I)=Lam0(I)*(1+Gam(I))/(Lam(I)*(1-Gam(I)))
1050        Eps(I)=Lam0(I)^2/(Lam(I)^2*Mu(I))
1055    NEXT I
1060    RETURN
1065!
1070! ////////////////////////////////////////////////////////////
1075!
1080 Print_results:!
1085    Prty=VAL(SYSTEM$("SYSTEM PRIORITY"))+1
1090    DISP CHR$(129);" DO YOU WANT A PRINTOUT OF MU AND
        EPSILON DATA? ";CHR$(128)
1095    ON KEY 5 LABEL "PRINT TO SCREEN",Prty GOSUB Prnt_to_screen
1100    ON KEY 7 LABEL "PRINT TO PRINTER",Prty GOSUB Prnt_to_printer
1105    ON KEY 6 LABEL "NO",Prty GOSUB Done_return
```

```
1110    Done=0
1115    LOOP
1120    EXIT IF Done
1125    END LOOP
1130    OFF KEY
1135    RETURN
1140!
1145! ////////////////////////////////////////////////////////////
1150!
1155 Prnt_to_screen:OFF KEY
1160    PRINTER IS 1
1165    GOSUB Prnt_results
1170    RETURN
1175!
1180! ////////////////////////////////////////////////////////////
1185!
1190 Prnt_to_printer:OFF KEY
1195    PRINTER IS Printer
1200    GOSUB Prnt_results
1205    RETURN
1210!
1215! ////////////////////////////////////////////////////////////
1220!
1225 Prnt_results:OFF KEY
1230    PRINT "Freq (GHz)   Mu                          Epsilon"
1235    IF Printer_on THEN
1240        FOR I=1 TO Datacount
1245            PRINT USING "2D.4D,2(4X,2(S3D.4D,2X))";A(I,1),
                            Mu(I),Eps(I)
1250        NEXT I
1255    ELSE
1260        FOR I=1 TO Datacount STEP INT(Datacount/20)
1265            PRINT USING "2D.4D,2(4X,2(S3D.4D,2X))";A(I,1),
                            Mu(I),Eps(I)
1270        NEXT I
1275    END IF
1280    PRINTER IS 1
1285    Done=1
1290    RETURN
1295!
1300! ////////////////////////////////////////////////////////////
1305!
1310 Save_results:!
1315    FOR I=1 TO Datacount
1320        B(I,1)=A(I,1)
1325    NEXT I
1330    Prty=VAL(SYSTEM$("SYSTEM PRIORITY"))+1
1335    DISP "SAVE MU (PERMEABILTY) RESULTS?"
1340    ON KEY 5 LABEL "YES",Prty GOSUB Save_mu
1345    ON KEY 6 LABEL "NO",Prty GOSUB Done_return
1350    Done=0
1355    LOOP
1360    EXIT IF Done
1365    END LOOP
1370    OFF KEY
```

```
1375   DISP "SAVE EPSILON (PERMITTIVITY) RESULTS?"
1380   ON KEY 5 LABEL "YES",Prty GOSUB Save_eps
1385   ON KEY 6 LABEL "NO",Prty GOSUB Done_return
1390   Done=0
1395   LOOP
1400   EXIT IF Done
1405   END LOOP
1410   OFF KEY
1415   RETURN
1420!
1425! ////////////////////////////////////////////////////////////
1430!
1435 Save_mu:OFF KEY
1440   Prompt$="REAL PART OF MU RESULTS"
1445   CALL Select_disk(Prompt$)
1450   IF Diskdrive$="NO DISK" THEN GOTO Save_im_mu
1455   Id$=""
1460   CALL Enter_id(Id$,Prompt$)
1465   IF Id$="" THEN GOTO Save_im_mu
1470   CALL Enterfilename("ABORT",Prompt$)
1475   IF Filename$="" THEN GOTO Save_im_mu
1480   FOR I=1 TO Datacount
1485*
1490   NEXT I
1495   CALL Save_file(B(*),Datacount,Id$)
1500   PRINT "REAL PART OF MU SAVED"
1505 Save_im_mu:!
1510   Prompt$="IMAGINARY PART OF MU RESULTS"
1515   !CALL Select_disk(Prompt$)
1520   IF Diskdrive$="NO DISK" THEN GOTO Save_mu_rtn
1525   !Id$=""
1530   !CALL Enter_id(Id$,Prompt$)
1535   IF Id$="" THEN GOTO Save_mu_rtn
1540   CALL Enterfilename("ABORT",Prompt$)
1545   IF Filename$="" THEN GOTO Save_mu_rtn
1550   FOR I=1 TO Datacount
1555*
1560   NEXT I
1565   CALL Save_file(B(*),Datacount,Id$)
1570   PRINT "IMAGINARY PART OF MU SAVED"
1575 Save_mu_rtn:Done=1
1580   RETURN
1585!
1590! ////////////////////////////////////////////////////////////
1595!
1600 Save_eps:OFF KEY
1605   Prompt$="REAL PART OF EPSILON RESULTS"
1610   !CALL Select_disk(Prompt$)
1615   IF Diskdrive$="NO DISK" THEN GOTO Save_im_eps
1620   !Id$=""
1625   !CALL Enter_id(Id$,Prompt$)
1630   IF Id$="" THEN GOTO Save_im_eps
1635   CALL Enterfilename("ABORT",Prompt$)
1640   IF Filename$="" THEN GOTO Save_im_eps
1645   FOR I=1 TO Datacount
```

```
1650*
1655    NEXT I
1660    CALL Save_file(B(*),Datacount,Id$)
1665    PRINT "REAL PART OF EPSILON SAVED"
1670 Save_im_eps:!
1675    Prompt$="IMAGINARY PART OF EPSILON RESULTS"
1680    !CALL Select_disk(Prompt$)
1685    IF Diskdrive$="NO DISK" THEN GOTO Save_ep_rtn
1690    !Id$=""
1695    !CALL Enter_id(Id$,Prompt$)
1700    IF Id$="" THEN GOTO Save_ep_rtn
1705    CALL Enterfilename("ABORT",Prompt$)
1710    IF Filename$="" THEN GOTO Save_ep_rtn
1715    FOR I=1 TO Datacount
1720*
1725    NEXT I
1730    CALL Save_file(B(*),Datacount,Id$)
1735    PRINT "IMAGINARY PART OF EPSILON SAVED"
1740 Save_ep_rtn:Done=1
1745    RETURN
1750!
1755! ////////////////////////////////////////////////////////////////
1760!
1765 Done_return:!
1770    Done=1
1775    RETURN
1780!
1785! ////////////////////////////////////////////////////////////////
1790!
1795 End:!
1796    DISP "Program finished. Have a nice day."
1800    END
1805!
1810! ************************************************************
1815!
1820    SUB Enterfilename(Ac$,OPTIONAL Prompt$)
1825 Enterfilename:      !
1830        COM /Files/ Sourcedisk$,Diskout$,Diskdrive$,Filename$
1835        INTEGER I,Ascii_num
1840        DIM Test$[160]
1845        SELECT NPAR
1850        CASE 1
1855            DISP " ENTER the FILE NAME ";
1860        CASE 2
1865            DISP " ENTER the FILE NAME for ";Prompt$;
1870        END SELECT
1875        SELECT Ac$
1880        CASE "CAT"
1885            DISP " ... (ENTER alone to CAT) ";
1890        CASE "ABORT"
1895            DISP " ... (ENTER alone to ABORT) ";
1900        CASE "VALID"
1905        END SELECT
1910        LINPUT Test$
1915        Test$=TRIM$(Test$)
```

```
1920        IF LEN(Test$)=0 THEN
1925            SELECT Ac$
1930            CASE "VALID"
1935                DISP "You MUST enter the FILE NAME now."
1940                BEEP
1945                WAIT 1.8
1950                GOTO Enterfilename
1955            CASE "ABORT","CAT"
1960                GOTO Abortline
1965            CASE ELSE
1970                DISP "Ac$=";Ac$;" in SUB Enterfilename"
1975                BEEP
1980                PAUSE
1985            END SELECT
1990        END IF
1995        IF LEN(Test$)>10 THEN
2000            BEEP
2005            DISP "ERROR in NAME ENTRY--up to 10 chars, you have ";
2010            DISP LEN(Test$);" "
2015            WAIT 1.8
2020            OUTPUT 2 USING "#,K,K";"?#";Test$
2025            GOTO Enterfilename
2030        END IF
2035        Filename$=Test$
2040        FOR I=1 TO LEN(Filename$)
2045            Ascii_num=NUM(Filename$[I])
2050            SELECT Ascii_num
2055            CASE 65 TO 90,95,97 TO 122,48 TO 57
2060                !Allowed characters
2065            CASE ELSE
2070                BEEP
2075                DISP "ERROR in NAME ENTRY--ILLEGAL CHARACTERS,
                          TRY AGAIN."
2080                WAIT 1.8
2085                OUTPUT 2 USING "#,K,K";"?#";Filename$
2090                GOTO Enterfilename
2095            END SELECT
2100        NEXT I
2105        SUBEXIT
2110 Abortline:Filename$=""
2115        SUBEXIT
2120    SUBEND
2125    !
2130    ! ************************************************************
2135    !
2140    SUB Select_disk(OPTIONAL Prompt$)
2145 Select_disk:OFF KEY
2150        COM /Files/ Sourcedisk$,Diskout$,Diskdrive$,Filename$
2155        INTEGER Prty
2160        Prty=VAL(SYSTEM$("SYSTEM PRIORITY"))+1
2165        IF NPAR=1 THEN
2170            DISP " SELECT DISK DRIVE for ";Prompt$;" ... NO
                      DISK to abort. "
2175        ELSE
2180            DISP " SELECT DISK DRIVE .... NO DISK to abort. "
```

```
2185        END IF
2190        ON KEY 0 LABEL "NO DISK",Prty GOSUB No_disk
2195        ON KEY 1 LABEL "9133H  V0 ^V1",Prty GOSUB Hard9133h0
2200        ON KEY 11,Prty GOSUB Hard9133h1
2205        ON KEY 2 LABEL "9133H  Floppy",Prty GOSUB Floppy9133h
2210        ON KEY 3 LABEL "9133XV Hard",Prty GOSUB Hard9133xv
2215        ON KEY 4 LABEL "9133XV Floppy",Prty GOSUB Floppy9133x
2220        IF Sys_id$[1,4]<>"S300" THEN
2225        ON KEY 5 LABEL "LEFT Internal",Prty GOSUB Left_internal
2230        ON KEY 6 LABEL "RIGHT Internal",Prty GOSUB Right_internal
2235        END IF
2240        ON KEY 7 LABEL "9125   Floppy",Prty GOSUB Floppy9125
2245        ON KEY 8 LABEL "9122   Left",Prty GOSUB Floppy9122l
2250        ON KEY 9 LABEL "9122   Right",Prty GOSUB Floppy9122r
2255        LOOP
2260        EXIT IF Done
2265        END LOOP
2270        SUBEXIT
2275 Left_internal:Diskdrive$=":HP9153,700,0"
2280        GOTO Diskselected
2285 Right_internal:Diskdrive$=":INTERNAL,4,0"
2290        GOTO Diskselected
2295 Hard9133xv:Diskdrive$=":HP9133,700,0"
2300        GOTO Diskselected
2305 Floppy9133x:Diskdrive$=":HP9133,702,0"
2310        GOTO Diskselected
2315 Hard9133h0:Diskdrive$=":,700,0,0"
2320        GOTO Diskselected
2325 Hard9133h1:Diskdrive$=":,700,0,1"
2330        GOTO Diskselected
2335 Floppy9133h:Diskdrive$=":,700,1"
2340        GOTO Diskselected
2345 Floppy9122r:Diskdrive$=":,707,1"
2350        GOTO Diskselected
2355 Floppy9122l:Diskdrive$=":,707,0"
2360        GOTO Diskselected
2365 Floppy9125:Diskdrive$=":,704,0"
2370        GOTO Diskselected
2375 No_disk:Diskdrive$="NO DISK"
2380 Diskselected:OFF KEY
2385        Done=1
2390        RETURN
2395    SUBEND
2400    !
2405    ! ********************************************************8
2410    !
2415    SUB Enter_id(Id$,OPTIONAL Return_test$)
2420 Enter_id:!
2425    !
2430    !LAST REVISION  30/SEPT/86
2435        OPTION BASE 1
2440        COM /Bugs/ INTEGER Bug1,Bug2,Bug3,Printer,Printer_on
2445    !
2450        DIM Test$[160]
2455        INTEGER N
```

```
2460        N=LEN(Id$)
2465        Test$=Id$
2470        SELECT Id$
2475        CASE ""
2480            !OUTPUT NOTHING
2485        CASE ELSE
2490            OUTPUT 2 USING "K,#";Test$
2495        END SELECT
2500        SELECT NPAR
2505        CASE 1    !NO Return_test$ given
2510        DISP CHR$(129);"Please ENTER a description (<= 40 chrs).";
2515        DISP CHR$(128);
2520        CASE ELSE
2525        DISP CHR$(129);"Please ENTER a description (<= 40 chrs) ";
2530        DISP CHR$(128);
2535            SELECT Return_test$
2540            CASE Id$
2545                DISP " for THIS ID";
2550            CASE "ABORT"
2555                DISP " CLR LN/ ENTER to ABORT."
2560            CASE ELSE
2565                DISP " for ";Return_test$;
2570            END SELECT
2575        END SELECT
2580        LINPUT Test$
2585        DISP ""
2590        Test$=TRIM$(Test$)
2595        N=LEN(Test$)
2600        SELECT N
2605        CASE >40
2610        DISP "Length of data_id$ too long. You entered ";N;
2615        DISP " characters. Try again."
2620            BEEP
2625            WAIT 1.5
2630            IF NPAR=2 THEN
2635                IF Id$<>Return_test$ THEN
2640                    OUTPUT 2 USING "#,K";Test$
2645                END IF
2650            END IF
2655            GOTO Enter_id
2660        CASE =0
2665            IF NPAR>1 THEN
2670                IF Return_test$="ABORT" THEN
2675                    Id$=Test$   !=""
2680                    SUBEXIT
2685                END IF
2690            END IF
2695            DISP "You must ENTER SOMETHING or you'll ";
2700            DISP "never get out of this."
2705            BEEP 1000,.3
2710            WAIT 1.8
2715            GOTO Enter_id
2720        CASE ELSE
2725             !Everything ok
2730        END SELECT
```

```
2735        Id$=Test$
2740     SUBEND
2745 !
2750 ! ******************************************************
2755 !
2760     SUB Save_file(T_f(*),INTEGER Datacount,Id$)
2765 Save_file:   !
2770        COM /Files/ Sourcedisk$,Diskout$,Diskdrive$,Filename$
2775        ON ERROR CALL Errortrap
2780        Diskspace=INT((3500+(Datacount*16))/256)+1
2785        CREATE BDAT Filename$&Diskdrive$,Diskspace,256
2790!       CREATE ASCII Filename$&Diskdrive$,Diskspace*2
2795        ASSIGN @Datapath TO Filename$&Diskdrive$
2800        OUTPUT @Datapath;"N"
2805        OUTPUT @Datapath;TRIM$(Id$)
2810        OUTPUT @Datapath;Datacount
2815        OUTPUT @Datapath;Datacount
2820        OUTPUT @Datapath;T_f(*)
2825        ASSIGN @Datapath TO *
2830        OFF ERROR
2835     SUBEND
2840!
2845! ************************************************************
2850!
2855     SUB Errortrap
2860 Errortrap:       !Trap disk errors here
2865        COM /Files/ Sourcedisk$,Diskout$,Diskdrive$,Filename$
2870        DIM File$[20],Test$[160],What$[20],Ac$[5]
2875        BEEP 400,.6
2880        SELECT ERRN
2885        CASE 54
2890            DISP "DUPLICATE FILE NAME:  ";Filename$;
2895            DISP "....PURGE old one? (Y/N)";
2900            LINPUT What$
2905            SELECT What$[1,1]
2910            CASE "Y","y"
2915                PURGE Filename$&Diskdrive$
2920            CASE ELSE
2925                Ac$="VALID"
2930                Prompt$=""
2935                CALL Enterfilename(Ac$)
2940            END SELECT
2945        CASE 52,53
2950            DISP "Improper FILE NAME --- ENTER NEW FILE NAME";
2955            OUTPUT 2 USING "#,K,K";"?#";Filename$
2960            LINPUT Filename$
2965            Filename$=TRIM$(Filename$)
2970        CASE 56
2975            DISP "FILE:  ";Filename$;" is not on this disk,
                      please insert";
2980            DISP " correct disk"
2985            PAUSE
2990        CASE 64
2995            DISP "This disk is full, PLEASE insert clean disk"
3000            PAUSE
```

```
3005        CASE 56
3010            DISP "DATA INPUT disk must be in drive!!  ";
3015            DISP "...CONTINUE when ready."
3020            PAUSE
3025        CASE 72,73,76
3030            DISP Diskdrive$;
3035            DISP " is not available, type correct";
3040            DISP " unit specifier (ie. ':,707,0').";
3045            OUTPUT 2 USING "K,#";Diskdrive$
3050            LINPUT Diskdrive$
3055        CASE 80
3060            DISP "CHECK DISK drive door!"
3065            PAUSE
3070        CASE ELSE
3075            DISP ERRM$;" 'CONTINUE' when fixed"
3080            PAUSE
3085        END SELECT
3090        DISP CHR$(12)
3095        SUBEXIT
3100    SUBEND
3105    !
3110    ! ************************************************************
3115    !
3120    SUB Test_real(Test,Test$,Low,High,INTEGER Bad_number)
3125 Test_real:!
3130        Bad_number=0
3135        ON ERROR GOSUB Trap_bad_number
3140        IF Bad_number THEN RETURN
3145        Test=VAL(TRIM$(Test$))
3150        OFF ERROR
3155        SELECT Test
3160        CASE <Low
3165            BEEP 1000,.3
3170            DISP " Number entered is TOO LOW. ";
3175            DISP " LOWEST allowable number is ";Low
3180            WAIT 2.1
3185            Bad_number=1
3190        CASE >High
3195            BEEP 1000,.3
3200            DISP " Number entered is TOO HIGH. ";
3205            DISP " HIGHEST allowable number is ";High
3210            WAIT 2.1
3215            Bad_number=1
3220        CASE ELSE
3225            Bad_number=0
3230     ! Number within limits
3235        END SELECT
3240        SUBEXIT
3245!
3250! ////////////////////////////////////////////////////////////
3255 !
3260 Trap_bad_number:!
3265        SELECT ERRN
3270        CASE 15,32
3275  DISP CHR$(129);"What you ENTERED is not a number! Try again. ";
```

```
3280            DISP CHR$(128)
3285            Bad_number=1
3290            WAIT 1.7
3295            LINPUT "Please ENTER the number you wish",Test$
3300        CASE ELSE
3305            DISP ERRN,ERRM$
3310            BEEP 850,.5
3315            Bad_number=1
3320            PAUSE
3325        END SELECT
3330        RETURN
3335    SUBEND
```

Appendix VI B: Automatic Network Analyzer ϵ and μ Measurement System

The ANA approach is based on inverting the measured reflection S_{11} and transmission S_{21} from and through a section of material filled air line. These are then inverted to determine ϵ and μ. The analysis is straightforward and is repeated here for convenience. We follow the notation used in [HP Ap Note].

In terms of the normal plane wave reflection (Γ) and transmission (T) coefficients, S_{11} and S_{21} are given by

$$S_{11}(\omega) = \frac{(1 - T^2)\Gamma}{1 - T^2\Gamma^2} . \qquad 6\text{-(B1)}$$

and

$$S_{21}(\omega) = \frac{(1 - \Gamma^2)T}{1 - T^2\Gamma^2} ,$$

where

$$\Gamma = \frac{Z - Z_o}{Z + Z_o} ,$$

and

$$T = e^{-\gamma d} . \qquad 6\text{-(B2)}$$

Inverting (B1) yields

$$\Gamma = K \pm (K^2 - 1) ,$$

where

$$K = \frac{\{S_{11}^2(\omega) - S_2^2(\omega)\} + 1}{2S_{11}(\omega)} , \qquad 6\text{-(B3)}$$

and

$$T = \frac{\{S_{11}(\omega) + S_{21}(\omega)\} - \Gamma}{1 - \{S_{11}(\omega) + S_{21}(\omega)\}\Gamma}$$

(2) We find that $$\mu_r/\epsilon_r = \left(\frac{1 + \Gamma}{1 - \Gamma}\right)^2 = x$$

and $$\mu_r\epsilon_r = -\left(\frac{1}{k_o d} \ln\left(\frac{1}{\Gamma}\right)\right)^2 = y \,. \qquad \text{6-(B4)}$$

It follows that $$\epsilon_r = (y/x)^{1/2} \,,$$

and $$\mu_r = (xy)^{1/2} \,.$$

NIST-114A
(REV. 3-89)

U.S. DEPARTMENT OF COMMERCE
NATIONAL INSTITUTE OF STANDARDS AND TECHNOLOGY

BIBLIOGRAPHIC DATA SHEET

1. PUBLICATION OR REPORT NUMBER
NISTIR 89-3915R

2. PERFORMING ORGANIZATION REPORT NUMBER

3. PUBLICATION DATE
March 1990

4. TITLE AND SUBTITLE

Suggested Methods and Standards for Testing and Verification of Electromagnetic Buried Object Detectors

5. AUTHOR(S)

William L. Gans, Richard G. Geyer, and Wilfred K. Klemperer

6. PERFORMING ORGANIZATION (IF JOINT OR OTHER THAN NIST, SEE INSTRUCTIONS)

U.S. DEPARTMENT OF COMMERCE
NATIONAL INSTITUTE OF STANDARDS AND TECHNOLOGY
~~GAITHERSBURG, MD 20899~~ Boulder, Colorado 80303-3328

7. CONTRACT/GRANT NUMBER

8. TYPE OF REPORT AND PERIOD COVERED

9. SPONSORING ORGANIZATION NAME AND COMPLETE ADDRESS (STREET, CITY, STATE, ZIP)

U.S. Army Belvoir Research, Development, and Engineering Center
Fort Belvoir, Virginia 22060-5606

10. SUPPLEMENTARY NOTES

[ ] DOCUMENT DESCRIBES A COMPUTER PROGRAM; SF-185, FIPS SOFTWARE SUMMARY, IS ATTACHED.

11. ABSTRACT (A 200-WORD OR LESS FACTUAL SUMMARY OF MOST SIGNIFICANT INFORMATION. IF DOCUMENT INCLUDES A SIGNIFICANT BIBLIOGRAPHY OR LITERATURE SURVEY, MENTION IT HERE.)

This is an interim report to sponsor on work performed by NIST personnel from January 1, 1985, to September 30, 1988. A brief overview of the theory of the electromagnetic properties of soils is presented, followed by an equally brief review of existing technologies for the detection of buried objects using electromagnetics. Suggested methods are then presented for realizing adequate target and soil standards and for testing procedures for buried object detectors that use these standards. Suggested instrumentation methodologies for verifying (calibrating) the target and soil standards are also presented along with an appendix containing reprints of selected relevant papers and an extensive bibliography.

12. KEY WORDS (6 TO 12 ENTRIES; ALPHABETICAL ORDER; CAPITALIZE ONLY PROPER NAMES; AND SEPARATE KEY WORDS BY SEMICOLONS)

buried object; conductivity; electromagnetic detection; mine; mine detector; permeability; permittivity; remote sensing

13. AVAILABILITY

[ ] UNLIMITED

[X] FOR OFFICIAL DISTRIBUTION. DO NOT RELEASE TO NATIONAL TECHNICAL INFORMATION SERVICE (NTIS).

[ ] ORDER FROM SUPERINTENDENT OF DOCUMENTS, U.S. GOVERNMENT PRINTING OFFICE, WASHINGTON, DC 20402.

[ ] ORDER FROM NATIONAL TECHNICAL INFORMATION SERVICE (NTIS), SPRINGFIELD, VA 22161.

14. NUMBER OF PRINTED PAGES
238

15. PRICE

ELECTRONIC FORM